

A Thesis Submitted for the Degree of PhD at the University of Warwick

Permanent WRAP URL:

<http://wrap.warwick.ac.uk/104986>

Copyright and reuse:

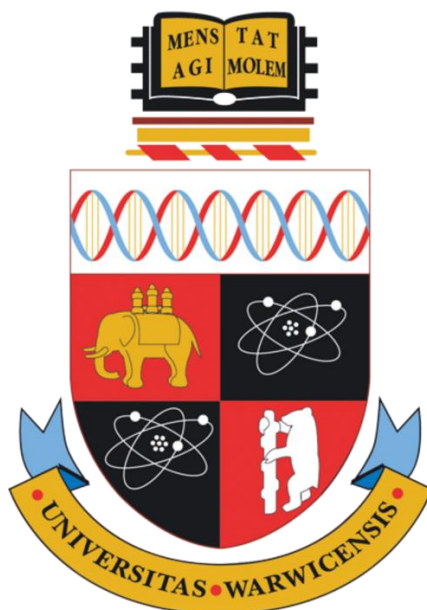
This thesis is made available online and is protected by original copyright.

Please scroll down to view the document itself.

Please refer to the repository record for this item for information to help you to cite it.

Our policy information is available from the repository home page.

For more information, please contact the WRAP Team at: wrap@warwick.ac.uk



Electron Paramagnetic Resonance Techniques for Pharmaceutical Characterization and Drug Design

by

Claudio Vallotto

Thesis

Submitted to the University of Warwick

for the degree of

Doctor of Philosophy

Department of Chemistry

August 2017



Contents

Title page	i
Contents	ii
List of Figures	ix
Acknowledgments.....	xv
Declaration and published work	xvi
Abstract.....	xix
Abbreviations and symbols.....	xx
Chapter 1 Principles of EPR	1
1.1 Uses of EPR	1
1.2 The Zeeman effect	2
1.3 The spin Hamiltonian.....	3
1.4 The g-factor.....	4
1.5 Hyperfine interaction	4
1.6 Multi-frequency EPR	6
1.7 Spin trapping	8
1.7.1 Spin trapping reaction	8
1.7.2 Choice of spin trapping agent	8
1.8 References.....	10
Chapter 2 Sterilization of Pharmaceuticals.....	13
2.1 Sterilization in the pharmaceutical industry.....	13
2.1.1 Dry heat sterilization.....	13
2.1.2 Steam sterilization.....	14
2.1.3 Ethylene oxide sterilization.....	14
2.1.4 Filtration sterilization	14
2.2 Radiation sterilization	14
2.2.1 Ionising radiation	15

2.2.2 γ -irradiation sterilization	15
2.2.3 γ -sterilization of pharmaceuticals	16
2.3 EPR in the detection of pharmaceutical degradants.....	17
2.4 Pharmaceutical excipients.....	17
2.5 Motivation of study.....	19
2.6 Thesis outline	20
2.7 References.....	21
Chapter 3 Experimental Methods	24
3.1 Experimental	24
3.1.1 Materials.....	24
3.2 Crystal growth.....	24
3.2.1 Deuteration.....	24
3.3 γ -irradiation.....	25
3.3.1 Room temperature irradiation	25
3.3.2 γ -irradiation in liquid nitrogen	25
3.3.3 Removal of quartz background signal.....	26
3.4 X-irradiation.....	26
3.5 Instrumentation	27
3.5.1 The EPR spectrometer	27
3.5.1.1 W-band EPR	29
3.5.1.2 mm-wave EPR	29
3.5.2 Low temperature	30
3.5.3 Spin trapping.....	31
3.5.3.1 Phosphate buffer solution.....	32
3.5.3.2 Sample preparation	33
3.5.4 ENDOR.....	33
3.5.5 ^1H NMR.....	33
3.5.6 ESI-MS analysis.....	34
3.5.7 XRF.....	34

3.6 Quantitative EPR	34
3.6.1.1 Quantification of persistent radicals in the solid state.....	35
3.6.1.2 Quantification of spin adducts	36
3.7 EPR simulations.....	37
3.8 References.....	38
Chapter 4 Irradiation of L-histidine Free Base	40
4.1 Introduction.....	40
4.1.1 Use of L-histidine in parenteral formulations	40
4.1.2 Scavenging properties of histidine	41
4.1.3 Solid state radicals	41
4.1.4 Spin trapped L-histidine radicals	41
4.2 Experimental	42
4.2.1 Instrumentation	42
4.2.2 Sample preparation	42
4.2.2.1 Growth and analysis of L-histidine single crystals	42
4.2.2.2 Spin trapping experiments.....	43
4.2.3 EPR Simulations	44
4.3 Results.....	44
4.3.1 Non-irradiated L-histidine powder control	44
4.3.2 γ -irradiated L-histidine powder EPR spectra	44
4.3.3 X-ray vs γ -ray irradiation.....	46
4.3.4 Single crystal analysis.....	47
4.3.5 Single crystal roadmaps	49
4.3.6 Multi-frequency EPR	54
4.3.7 Cold irradiation	56
4.3.7.1 Carboxyl radical.....	56
4.3.7.2 Formation of the deamination radical – 120 K	60
4.3.7.3 Rearrangement of the deamination radical – 120 K to r.t.	61
4.3.8 Dissolution experiments.....	63

4.3.8.1 Spin trapping with MNP	63
4.3.8.2 Radical regeneration	65
4.3.8.3 XRF analysis on the metal needles	70
4.3.9 MS analysis	70
4.3.10 Liquid NMR analysis	73
4.4 Discussion	74
4.4.1 Solid state persistent radicals at r.t.	74
4.4.2 Low temperature stable species	75
4.4.3 Dissolution experiments.....	76
4.4.4 Recombination of radicals in solution.....	78
4.5 Conclusions	80
4.6 References	80
Chapter 5 Irradiation of D-mannitol	85
5.1 Introduction	85
5.1.1 Industrial use of D-mannitol	85
5.1.2 Mannitol in lyophilized formulations.....	86
5.1.3 Therapeutic properties of D-mannitol.....	86
5.1.4 EPR studies on D-mannitol	86
5.2 Experimental	87
5.2.1 Sample preparation	87
5.2.1.1 Growth and analysis of D-mannitol single crystal	87
5.2.1.2 Spin trapping experiments.....	88
5.2.2 EPR simulations	88
5.3 Results	89
5.3.1 Non-irradiated D-mannitol powder control	89
5.3.2 γ -irradiated D-mannitol powder EPR spectra	89
5.3.3 Multi-frequency EPR	91
5.3.4 Cold irradiation	92
5.3.4.1 Radical I – 80 K	92

5.3.4.2	Radical II – 120 K.....	94
5.3.4.3	Radical III – 170 K.....	98
5.3.4.4	170 – 200 K.....	101
5.3.4.5	200 – 240 K.....	103
5.3.4.6	240 – 260 K.....	106
5.3.4.7	260 – 295 K.....	108
5.3.5	CW ENDOR	110
5.3.6	Dissolution experiments.....	110
5.3.6.1	Spin trapping with MNP	110
5.3.6.2	Testing radical regeneration for D-mannitol.....	113
5.3.6.3	Spin trapping with DMPO	114
5.3.7	MS analysis	114
5.3.8	¹ H NMR analysis.....	117
5.4	Discussion.....	118
5.4.1	Evolution of the radicals from nitrogen temperature to r.t.....	118
5.4.1.1	Detection of radical I at 77 K.....	118
5.4.1.2	Formation of radical II at 120 K	122
5.4.1.3	Formation of radical III at 170 K	123
5.4.1.4	Decrease of concentration of radical II and III at 200 K.....	124
5.4.1.5	Dominant β -proton coupling at 240 K	124
5.4.1.6	Spectral evolution at 260 K.....	126
5.4.1.7	R.t. persistent species	126
5.4.2	Spin trapping experiments	127
5.4.3	MS.....	128
5.4.4	NMR	129
5.5	Conclusions.....	129
5.6	References.....	130
Chapter 6	Photoactivation of a Platinum(IV) Anticancer Complex	134
6.1	Introduction.....	134

6.1.1 Cancer	134
6.1.2 Metallo-organic compounds.....	135
6.1.3 Pt-based chemotherapeutics	135
6.1.3.1 Pt ^{II} complexes.....	135
6.1.3.2 Second generation of Pt ^{II} complexes.....	137
6.1.3.3 Pt ^{IV} complexes.....	138
6.1.4 Targeted delivery	139
6.1.5 Phototherapy	139
6.1.6 Photo-chemotherapy	141
6.1.6.1 Pt ^{IV} diiodo complexes	141
6.1.6.2 Pt ^{IV} diazo complexes.....	142
6.1.6.3 Photo-degradation pathways of complex 13.....	144
6.1.6.4 Reactivity of azidyl radicals towards amino acids	145
6.1.6.5 Photo-irradiation in the presence of melatonin	146
6.2 Experimental	147
6.2.1 Materials.....	148
6.2.2 Sample preparation	148
6.2.3 Instrumentation	148
6.2.3.1 EPR spectroscopy	148
6.2.3.2 Irradiation.....	148
6.2.4 EPR simulations.....	149
6.3 Results.....	150
6.3.1 L-tryptophan.....	150
6.3.1.1 Spin trapping of complex 13 with MNP	150
6.3.1.2 Spin trapping of L-trp radical with blue light	152
6.3.1.3 Spin trapping of L-trp radical with green light	155
6.3.2 Melatonin	157
6.3.2.1 Spin trapping of melatonin radical (EtOH 20%) with blue light	157
6.3.2.2 Spin trapping of melatonin radical (H ₂ O) with blue light	161

6.3.2.3	Photo-activation of complex 13 with MLT at longer wavelengths.....	164
6.3.2.4	Detection of hydroxyl radicals	164
6.3.3	L-histidine	168
6.3.4	Pentagastrin.....	169
6.3.4.1	Spin trapping with MNP in the presence of pentagastrin.....	169
6.3.4.2	Spin trapping with DMPO	170
6.4	Discussion	174
6.4.1	Detection of MNP-indole radicals	174
6.4.2	Formation of hydroxyl radical	176
6.4.3	Longer wavelength of activation.....	176
6.4.4	Photo-protective effect of pentagastrin	176
6.4.5	Hyperfine coupling constants.....	177
6.4.6	Mechanism of photo-activation of complex 13	178
6.4.7	Amino acid radicals	178
6.5	Conclusions.....	179
6.6	References.....	180
Chapter 7	Conclusions and Future Work.....	188
7.1	Conclusions.....	188
7.2	Future work.....	192
7.3	References.....	193

List of Figures

Figure 1.1 The electron Zeeman effect.	3
Figure 1.2 The effect of the magnetic field of a nucleus on the field experienced by an electron spin.	5
Figure 1.3 Mesomeric structures of a nitroxide radical.	8
Figure 1.4 The nitroso spin trap MNP and the nitron spin trap DMPO.	9
Figure 1.5 Trapping of a radical (R^{\bullet}) species by a nitron compound.	9
Figure 1.6 Trapping of a radical (R^{\bullet}) species by a nitroso compound.	9
Figure 2.1 Summary of γ -sterilization published literature	15
Figure 3.1 γ -irradiated quartz tube before and after annealing with a flame torch	26
Figure 3.2 Schematic representation of the X-ray diffractometer.	27
Figure 3.3 Diagram of the componets of a typical EPR spectrometer.	28
Figure 3.4 Schematic representation of the setup used for the low temperature EPR.	30
Figure 3.5 The field distribution in a TM_{110} cylindrical cavity.	31
Figure 3.6 The field distribution in a TE_{011} cylindrical cavity.	32
Figure 3.7 Calibration curve for TEMPO.	36
Figure 3.8 Calibration curve for TEMPOL.	37
Figure 4.1 Chemical structure of L-histidine.	40
Figure 4.2 Crystallographic structure of the single crystal of L-his.	43
Figure 4.3 Radiation dose dependence of r.t. γ -irradiated L-his powder.	45
Figure 4.4 CW EPR microwave power saturation spectra of r.t. γ -irradiated L-his powder. ...	46
Figure 4.5 Effect of the radiation source on the EPR spectrum.	47
Figure 4.6 X-band EPR spectrum of L-his single crystal.	48
Figure 4.7 Radiolytic deamination of L-his.	48
Figure 4.8 EPR spectrum from crushed X-irradiated L-his single crystal.	49
Figure 4.9 Roadmap of the r.t. γ -irradiated L-his single crystal (c axis perp. to B_0).	51

Figure 4.10 Roadmap of the r.t. γ -irradiated L-his single crystal (b axis perp. to B_0).	52
Figure 4.11 Roadmap of the r.t. γ -irradiated L-his single crystal (a axis perp. to B_0).	53
Figure 4.12 Multi-frequency EPR analysis of X-irradiated L-his powder.....	54
Figure 4.13 Simulation of multi-frequency EPR data of X-irradiated L-his powder.....	55
Figure 4.14 X-band EPR spectrum of single crystal of L-his and L-his powder γ -irradiated in liquid nitrogen and acquired at 80 K.....	57
Figure 4.15 Roadmap spectrum of the γ -irradiated single crystal of L-his at 80 K.	58
Figure 4.16 Formation of the carboxylic anion.....	58
Figure 4.17 Microwave power saturation spectra of L-his single crystal at 80 K.	59
Figure 4.18 Microwave power saturation spectra of L-his powder at 80 K.....	59
Figure 4.19 Annealing of γ -irradiated L-his single crystal to 120 K.	60
Figure 4.20 Annealing of γ -irradiated L-his powder from 80 K to 120 K.....	61
Figure 4.21 Annealing of γ -irradiated L-his powder from 120 K to 170 K.....	62
Figure 4.22 Annealing of γ -irradiated L-his powder from 170 K to r.t.	62
Figure 4.23 Formation of a transient species at 200 K.	63
Figure 4.24 Control X-band EPR spectra.	64
Figure 4.25 Spin trapping of irradiated L-his.....	64
Figure 4.26 Regeneration of L-his radical in solution.	66
Figure 4.27 Regeneration of the deamination radical at different time intervals.....	66
Figure 4.28 Kinetics of formation of L-his spin adduct with glass pipette.....	68
Figure 4.29 Kinetics of formation of L-his spin adduct with syringe with needle	68
Figure 4.30 Simulation of deamination radical and hydroxyl radical spin adducts.	69
Figure 4.31 Background subtracted XRF spectra for the metal needles.	70
Figure 4.32 Positive mode MS analysis of γ -irradiated L-his.....	71
Figure 4.33 Negative mode MS analysis of γ -irradiated L-his.	71
Figure 4.34 ^1H -NMR analysis of non-irradiated L-his.	73
Figure 4.35 ^1H -NMR analysis of 250 kGy γ -irradiated L-his.....	74
Figure 4.36 Scheme of regeneration of the deamination radical through Fenton reaction.	77

Figure 4.37 Suggested decomposition scheme for histidine from irradiation in solution.....	79
Figure 5.1 Chemical structure of D-mannitol.	85
Figure 5.2 Structures of D-mannitol and sorbitol.	86
Figure 5.3 Crystallographic structure of the single crystal of D-mannitol.....	88
Figure 5.4 Radiation dose dependence of γ -irradiated D-mannitol powder.....	90
Figure 5.5 Microwave power saturation spectra of γ -irradiated D-mannitol powder.	90
Figure 5.6 Multi-frequency EPR analysis of X-irradiated D-mannitol powder.....	91
Figure 5.7 CW EPR spectra of D-mannitol crystals and powders at 80 K.	92
Figure 5.8 Roadmap of partially deuterated D-mannitol single crystal at 80 K	93
Figure 5.9 Simulation of CW EPR spectrum of D-mannitol single crystal at 80 K	93
Figure 5.10 Annealing of γ -irradiated D-mannitol crystal from 80 K to 120 K.	94
Figure 5.11 Comparison between the EPR spectra of single crystal at 80 K and 120 K	95
Figure 5.12 CW EPR spectra of D-mannitol crystals and powders at 120 K.	95
Figure 5.13 Roadmap of D-mannitol single crystal at 120 K and 80 K.....	96
Figure 5.14 Simulation of CW EPR spectrum of D-mannitol single crystal at 120 K	97
Figure 5.15 Annealing of γ -irradiated D-mannitol crystal from 120 K to 170 K.	98
Figure 5.16 Roadmap of D-mannitol single crystal at 170 K and 120 K.....	99
Figure 5.17 CW EPR spectra of D-mannitol crystals and powders at 170 K.	99
Figure 5.18 Simulation of CW EPR spectrum of D-mannitol single crystal at 170 K	100
Figure 5.19 Annealing of γ -irradiated D-mannitol crystal from 170 K to 200 K.	101
Figure 5.20 CW EPR spectra of D-mannitol crystals and powders at 200 K.	102
Figure 5.21 Simulation of CW EPR spectrum of D-mannitol single crystal at 200 K	102
Figure 5.22 Annealing of γ -irradiated D-mannitol crystal from 200 K to 240 K.	104
Figure 5.23 Roadmap of D-mannitol crystal at 240 K and partially saturated spectrum.....	105
Figure 5.24 CW EPR spectra of D-mannitol crystals and powders at 240 K.	105
Figure 5.25 Annealing of γ -irradiated D-mannitol crystal from 240 K to 260 K.	106
Figure 5.26 CW EPR spectra of D-mannitol crystals and powders at 260 K.	107
Figure 5.27 Roadmap of D-mannitol crystal at 260 K and partially saturated spectrum.....	107

Figure 5.28 Annealing of γ -irradiated D-mannitol crystal from 260 K to 295 K.	108
Figure 5.29 CW EPR spectra of D-mannitol crystals and powders at 295 K.	109
Figure 5.30 Roadmap of protonated and partially deuterated D-mannitol crystal at 295 K..	109
Figure 5.31 Microwave power saturation spectra of γ -irradiated D-mannitol crystals.....	110
Figure 5.32 Control X-band EPR spectra..	111
Figure 5.33 Spin trapping of irradiated D-mannitol with MNP.....	112
Figure 5.34 Spin trapping of irradiated D-mannitol in MNP with 0.01 mT mod. ampl.	113
Figure 5.35 Dissolution of mannitol powder in water with later addition of MNP.	113
Figure 5.36 Spin trapping of irradiated D-mannitol with DMPO	114
Figure 5.37 Positive mode MS analysis of γ -irradiated D-mannitol.....	115
Figure 5.38 Negative mode MS analysis of γ -irradiated D-mannitol.	116
Figure 5.39 ^1H -NMR analysis of non-irradiated D-mannitol.	117
Figure 5.40 ^1H -NMR analysis of 250 kGy γ -irradiated D-mannitol.....	118
Figure 5.41 Influence of the dihedral angle ϕ on the β -proton coupling.	120
Figure 5.42 Proposed chemical structures for radical I.....	120
Figure 5.43 Newman projections along C3–C4 and C4–C3.....	121
Figure 5.44 Proposed chemical structures for radical II.	123
Figure 5.45 Molecule of D-mannitol highlighting intermolecular short contact bonds.....	123
Figure 5.46 Proposed chemical structures for radical III.	124
Figure 5.47 Double integrated area of the paramagnetic species detected in the range 80–200 K corrected by the Curie law.	125
Figure 5.48 Fraction of the paramagnetic species detected in the range 80–200 K assuming the total radical concentration to be constant.....	126
Figure 5.49 Proposed mechanism for radical rearrangement through to β -elimination.....	128
Figure 6.1 Splitting of the d-orbitals of a square-planar Pt^{II} (d^8) complex with strong donor ligands.....	136
Figure 6.2 Structures of cis-platin and trans-platin.....	136
Figure 6.3 Hydrolysis of CDDP.....	136

Figure 6.4 Structure of the second generation Pt ^{II} complexes carboplatin and oxaliplatin....	137
Figure 6.5 Splitting of the d-orbitals of an octahedral Pt ^{IV} (d ⁶) complex with strong donor ligands.....	138
Figure 6.6 Structure of the Pt ^{IV} octahedral complex satraplatin.	138
Figure 6.7 Depth of penetration of different wavelengths.	140
Figure 6.8 Structures of early photo-activable Pt ^{IV} -diiodo complexes.	141
Figure 6.9 Structures of platinum(IV) diamine diazo complexes.	142
Figure 6.10 Structure of mono-pyridine, bis-pyridine and bis-pyridine-TEMPO platinum(IV) diazo complexes.....	143
Figure 6.11 UV-visible spectra of complex 13	145
Figure 6.12 Multiple degradation pathways of photo-activated complex 13	145
Figure 6.13 Reaction pathways between the azidyl radical and L-trp	146
Figure 6.14 Setup of the X-band EPR cavity for the irradiation experiments.	149
Figure 6.15 Photo-activation of complex 13 in the presence of MNP	151
Figure 6.16 Photo-activation of complex 13 in the presence of MNP and simulated MNP-N ₃ spin adduct	152
Figure 6.17 Photo-activation of complex 13 in the presence of MNP and L-trp (blue light)	153
Figure 6.18 Photo-activation of complex 13 in the presence of MNP and L-trp and simulated MNP-trp spin adduct.....	154
Figure 6.19 Kinetics of formation of the MNP-trp spin adduct (blue light).	154
Figure 6.20 Photo-activation of complex 13 in the presence of MNP and L-trp (green light)	156
Figure 6.21 Kinetics of formation of the MNP-trp spin adduct (blue light).	157
Figure 6.22 Spin trapping of MLT with MNP (blue light)	158
Figure 6.23 Photo-activation of complex 13 in the presence of MNP and MLT (20% EtOH) (blue light).....	159
Figure 6.24 Spin trapping of MLT radical using either 0.1 mT or 0.01 mT mod. ampl.	159

Figure 6.25 Photo-activation of complex 13 in the presence of MNP and MLT (20% EtOH) and simulated MNP-MLT spin adduct	160
Figure 6.26 Kinetics of formation of the MNP-MLT (20% EtOH) spin adduct (blue light).	161
Figure 6.27 Photo-activation of complex 13 in the presence of MNP and MLT (H ₂ O) (blue light).....	162
Figure 6.28 Kinetics of formation of the MNP-MLT (H ₂ O) spin adduct (blue light).	163
Figure 6.29 Kinetics of formation of the MNP-MLT (20% EtOH) spin adduct (green light).	164
Figure 6.30 Photo-activation of complex 13 in the presence of MNP and EtOH (blue light).	165
Figure 6.31 Photo-activation of complex 13 in the presence of MNP and EtOH and simulated MNP-EtOH spin adduct.....	166
Figure 6.32 Kinetics of formation of the MNP-EtOH spin adduct (blue light)..	167
Figure 6.33 Photo-activation of complex 13 in the presence of MNP and L-his.....	168
Figure 6.34 Photo-activation of complex 13 in the presence of MNP and pentagastrin (blue light).....	169
Figure 6.35 Photo-activation of complex 13 in the presence of MNP and pentagastrin (summed scans).....	170
Figure 6.36 Photo-activation of complex 13 in the presence of DMPO and pentagastrin (blue light).....	171
Figure 6.37 Photo-activation of complex 13 in the presence of DMPO 70% (DMF) and simulated DMPO-N ₃ spin adduct.....	172
Figure 6.38 Kinetics of formation of the DMPO-N ₃ spin adduct in the presence and absence of pentagastrin.	173
Figure 6.39 Reaction between the azidyl radical and indole derivatives.	174

Acknowledgments

First and foremost, I would like to thank my supervisors Prof. Mark Newton and Dr. Chris Wedge for their constant guidance, support and encouragement throughout my PhD.

My thanks go to Helen Williams for her kind supervision, for hosting me in AstraZeneca and getting me involved in many activities. Thanks also to Lotta Salmela and Matthew Molloy for their assistance during my time in Macclesfield, and to Prof. Per-Ola Norrby for the helpful discussions on radical chemistry.

I also want to thank Prof. Damien Murphy for the insightful discussions, scientific and non-scientific, and for inviting me to Cardiff. Thanks also to Dr. Emma Richards for the time she dedicated to the long ENDOR experiments in Cardiff.

Thanks to Prof. Peter Sadler for involving me in his exciting studies and for his contagious scientific enthusiasm, and to Jenny and Venkat for providing me with such interesting compounds to play with.

I also need to thank Dr. Igor Gromov and Dr. Maik Icker for assistance with the high frequency EPR experiments. Thanks also to Dr. Ruth Edge and Dr. David Walker for assistance with irradiation, and to Dr. Zoe Ayres for the XRF analysis.

I am grateful to Prof. Balaraman Kalyanaraman for allowing me to visit the Medical College of Wisconsin, and I would like to thank Jacek Zielonka and Jeannette Vasquez Vivar for teaching me the secrets of the art of spin trapping.

I would also like to thank all the past and present members of the EPR group in Warwick, Ben I, Ben II, Matthew, Mika, Angelo, Sinead, Chris, Anton, Colin, Phil, Enrik and Guy for their help and support.

A special thank goes to the CAS-IDP people. It has been a pleasure to share this journey with you, learning so much one from the other. Thanks to Prof. Alison Rodger for guiding us all through this wonderful experience.

Last but not least, I want to thank all the people that have been sending their love and support from overseas: my family, my friends, and Elena.

Declaration and published work

I declare that the work presented in this thesis is my own except where stated otherwise, and was carried out entirely at the University of Warwick, during the period of September 2013 to August 2017, under the supervision of Prof. Mark Newton and Dr. Christopher Wedge. The research reported here has not been submitted, either wholly or in part, in this or any other academic institution for admission to a higher degree.

Some parts of the work reported and other work not reported in this thesis have been published, as listed below. It is anticipated that further parts of this work will be submitted for publication in due course.

Published papers

Vallotto, C., Williams, H.E., Murphy, D.M., Ayres, Z.J., Edge, R., Newton, M.E. & Wedge, C.J. *An Electron Paramagnetic Resonance (EPR) spectroscopy study on the γ -irradiation sterilization of the pharmaceutical excipient L-histidine: regeneration of the radicals in solution.* Int. J. Pharm. 533, 315-319 (2017).

Papers in preparation for submission

Vallotto, C., Shaili, S., Shi, S., Butler, J.S., Wedge, C.J., Newton, M.E. & Sadler P.J. *Photoactivatable platinum anticancer complex generates tryptophan radicals.* To be submitted to Chem. Comm. (2017).

Conference presentations

1. Vallotto, C., Williams, H.E., Murphy, D.M., Wedge, C.J. and Newton, M.E, *Sterilization by γ -irradiation: evaluating the effects on pharmaceutical excipients*, 50th RSC ESR Conference, Oxford (UK), poster presentation (2017).

2. Vallotto, C., Williams, H.E., Murphy, D.M., Wedge, C.J. and Newton, M.E., *Sterilization by γ -irradiation: evaluating the effects on pharmaceutical excipients*, Xth Conference of the European Federation of EPR groups (EFEPR), Turin (Italy), poster presentation (2016).
3. Vallotto, C., Williams, H.E., Murphy, D.M., Wedge, C.J. and Newton, M.E., *Sterilization by γ -irradiation: evaluating the effects on pharmaceutical excipients*, The 58th Annual Rocky Mountain Conference on Magnetic Resonance, Breckenridge, Colorado (USA), poster presentation (2016).
4. Vallotto, C., Williams, H.E., Wedge, C.J. and Newton, M.E., *Electron paramagnetic resonance techniques for pharmaceutical characterisation and drug design*, CAS-IDP Networking Meeting, Taormina (Italy), poster presentation (2016).
5. Vallotto, C., Williams, H.E., Murphy, D.M., Wedge, C.J. and Newton, M.E., *Sterilization by γ -irradiation: evaluating the effects on pharmaceutical excipients*, Emerging Analytical Professionals, Fareham (UK), oral presentation (2016).
6. Vallotto, C., Williams, H.E., Murphy, D.M., Wedge, C.J. and Newton, M.E., *Sterilization by γ -irradiation: evaluating the effects on pharmaceutical excipients*, APS 6th International PharmSci Conference 2015, Nottingham (UK), poster presentation (2015).
7. Vallotto, C., Williams, H.E., Murphy, D.M., Wedge, C.J. and Newton, M.E., *Sterilization by γ -irradiation: evaluating the effects on pharmaceutical excipients*, 48th RSC ESR Conference, Southampton (UK), poster presentation (2015).
8. Vallotto, C., Williams, H.E., Wedge, C.J. and Newton, M.E., *Electron paramagnetic resonance techniques for pharmaceutical and biopharmaceutical characterisation*. CAS-IDP Networking Meeting, University of Warwick (UK), oral and poster presentation (2015).
9. Vallotto, C., Williams, H.E., Wedge, C.J. and Newton, M.E., *Electron paramagnetic resonance techniques for pharmaceutical and biopharmaceutical characterisation*, CAS-IDP Networking Meeting, London (UK), oral and poster presentation (2014).
10. Vallotto, C., Wedge, C.J. and Newton, M.E., *Electron paramagnetic resonance techniques for pharmaceutical and biopharmaceutical characterisation*, CAS-IDP Networking Meeting, Venice (Italy), oral and poster presentation (2014).
11. Vallotto, C., Breeze B.G., Dale, M.W., Wedge, C.J. and Newton, M.E., *Spin-polarization kinetics of negatively charged nitrogen vacancy centres by time resolved EPR spectroscopy*. 47th RSC ESR Conference, Dundee (UK), poster presentation (2014).

12. Vallotto, C., Wedge, C.J. and Newton, M.E., *Electron paramagnetic resonance techniques for pharmaceutical and biopharmaceutical characterisation*, CAS-IDP Networking Meeting, University of Warwick (UK), oral presentation (2013).

Claudio Vallotto

August 2017

Abstract

This thesis aims to explore the applicability of Electron Paramagnetic Resonance (EPR) spectroscopy in the pharmaceutical field. EPR is a powerful biophysical tool that allows the detection and characterisation of paramagnetic species, such as free organic radicals and metal complexes. EPR is widely used across all disciplines but to date has been much underutilised in the pharmaceutical industry.

In the first part of this work, EPR techniques were applied to characterise the degradation products originating from irradiation sterilization of two common excipients, L-histidine and D-mannitol. Radicalic degradants can form as a result of several degradation pathways and industrial processes, including γ -radiation sterilization. A quantification of the radical species formed upon γ -irradiation was performed, indicating a much higher radical concentration for D-mannitol compared to L-histidine at pharmaceutically relevant irradiation doses. Cold irradiation analysis allowed the study of the low temperature stable species and their evolution into the r.t. stable ones. Three low temperature persistent radical species of D-mannitol were identified for the first time. The reactivity of the radicals in solution was also investigated. Spin trapping experiments allowed trapping of radicals from both L-histidine and D-mannitol. An unusual, and potentially hazardous, radical regeneration mechanism was observed for L-histidine, which was suggested to be due to the sterile metal needles used for transferring the sample solution in the EPR tubes.

The second part of this work was concerned with the investigation of the radicalic mechanism of action of a promising photo-activable platinum(IV) anticancer complex. It has been previously suggested that the cytotoxicity of the said compound is associated to the photo-release of azidyl radicals, which can be quenched in the presence of the amino acid L-tryptophan. By the use of the spin trapping methodology, an intermediate indole radical was isolated and identified from photo-activation of the anticancer complex in the presence of both L-tryptophan and melatonin. The same photo-protective effect was observed also in the presence of a tryptophan-containing peptide. Thus, this work contributed to the overall understanding on photo-irradiated platinum anticancer complexes and their generated photo-products.

Abbreviations and symbols

A	Adenine
a	Hyperfine splitting constant
ACN	Acetonitrile
API	Active Pharmaceutical Ingredient
AR	Androgen Receptor
B_0	Static magnetic field
B_I	Magnetic field induced by a nucleus
B_m	Modulation amplitude
CDDP	<i>Cis</i> -diamminedichloroplatinum(II)
CW	Continuous Wave
D.I.	Double integrated
DACH	Diaminocyclohexane
DMF	Dimethylformamide
DMPO	5,5-dimethyl-1-pyrroline-N-oxide
DPPH	2,2-diphenyl-1-picrylhydrazyl
DTBN	Di- <i>tert</i> -butyl nitroxide
E^0	Standard electrode potential
ED	Energy Dispersive
EDTA	Ethylenediaminetetraacetic acid
EGF	Epidermal Growth Factor
EMR	Electron Magnetic Resonance
ENDOR	Electron Nuclear DOuble Resonance
EPR	Electron Paramagnetic Resonance
ESI	Electron Spray Irradiation

ESR	Electron Spin Resonance
ETO	Ethylene oxide
EtOH	Ethanol
ΔE	Energy difference between two spin states
FDA	Food and Drug Administration
FR	Folate Receptor
FT	Fourier Transform
G	Guanine
g	g-factor
G	Receiver gain
GC	Gas Chromatography
g_e	g-factor of the free electron
GSH	Glutathione
h	Planck's constant
HPLC	High Performance Liquid Chromatography
HR-MS	High Resolution Mass Spectrometry
HSP	Heat Shock Protein
I	Nuclear spin quantum number
IC ₅₀	Half maximal inhibitory concentration
J	J coupling constant
L-his	L-histidine
L-trp	L-tryptophan
LMCT	Ligand-to-metal charge transfer
lw _{pp}	Peak-to-peak linewidth
m/z	Mass-to-charge ratio
MLT	Melatonin
MMR	Mismatch Repair
MNP	2-methyl-2-nitrosopropane

MS	Mass Spectrometry
m_s	Spin state of an electron, projection of electron spin along B_0
MW	Microwave
N	Number of scans
NER	Nucleotide Excision Repair
NMR	Nuclear Magnetic Resonance
P	Microwave power
p.b.	Phosphate buffer
PDT	Photodynamic Therapy
ppm	Parts per million
PS	Photo-sensitiser
PSU	Power Supply Unit
PVC	Polyvinyl chloride
Q	Quality factor of the resonator
r.t.	Room temperature
RNS	Reactive Nitrogen Species
ROS	Reactive Oxygen Species
S	Electron spin quantum number
S/N	Signal-to-noise ratio
SAL	Sterility Assurance Level
ST	Spin Trap
T	temperature
t	Conversion time
TEMPO	2,2,6,6-tetramethyl-piperidine-1-oxyl
TEMPOL	4-hydroxyl-2,2,6,6-tetramethyl-piperidine-1-oxyl
TfR	Transferrin Receptor
UHPLC	Ultra-high performance liquid chromatography
USP	United States Pharmacopoeia

WHO	World Health Organization
XRF	X-ray Fluorescence
ZFS	Zero Field Splitting
φ	Dihedral angle
μ_{B}	Bohr magneton
μ_{N}	Nuclear magnetic moment
η	Filling factor
ν	Frequency of the electromagnetic radiation in Hertz
τ_{c}	Tumbling correlation time

Chapter 1

Principles of EPR

In this Chapter, the background theory behind the Electron Paramagnetic Resonance (EPR) techniques used in this work is presented. Far from representing a comprehensive background of all the areas covered, the following sections will provide sufficient elements for a full understanding of the results presented in the upcoming chapters.

1.1 Uses of EPR

EPR, also known as ESR (Electron Spin Resonance) or EMR (Electron Magnetic Resonance) is a powerful technique for the study of paramagnetic species, which include transition metal ions, defect centres and free radicals. The concept of EPR is very similar to the more familiar Nuclear Magnetic Resonance (NMR) technique, both dealing with the interaction between electromagnetic radiation and magnetic moments, which for NMR arise from nuclei while for EPR arise from electrons.¹

Modern applications of EPR can be found across all the disciplines, from chemistry to physics, to medicine and biology. In the polymer industry, EPR is used to study polymerisation reactions and polymer stability.²⁻⁴ EPR has also been successfully applied to study the kinetics of chemical reactions involving paramagnetic species.^{5,6} In medicine, EPR provides unique insights into the redox biochemistry of several conditions related to oxidative stress.⁷ EPR techniques for *in vivo* oximetry allow characterisation of a wealth of physiological and pathophysiological systems with minimal invasiveness and high precision.⁸ Important applications of EPR are also found in catalysis.^{9,10} EPR finds applications also in the food industry, where it is used for the study of food antioxidant properties,^{11,12} of flavour stability of beer^{13,14} and to assess the effects of industrial processes such as radiation sterilization¹⁵⁻¹⁷ and thermal treatment on foodstuffs.¹⁸

To date, EPR has been much underutilised in the pharmaceutical industry. Nonetheless, several studies have shown the potential of this technique in this field. EPR has been used to study the radical species formed from oxidative degradation¹⁹ and photodegradation²⁰ of active

pharmaceutical ingredients (APIs) in the solid state, as well as the oxidation of various pharmaceutical compounds in solution with the spin trapping methodology.^{21–23} EPR techniques have also been used for studying the effects of irradiation on drug delivery systems.^{24,25} EPR spectroscopy also finds applications in drug design, for the development of pharmaceutical compounds which rely on a radical-based mechanism of action.^{26–28}

In the sections below the fundamental theory of EPR is discussed in order to provide key notions for the understanding of the work presented in the following chapters.

1.2 The Zeeman effect

The *Zeeman effect* describes the interaction of an unpaired electron with a magnetic field B_0 . When an electron is placed in a magnetic field, the magnetic moment of the electron μ_e will either align *with* the magnetic field (parallel state, lower energy) or *against* the magnetic field (antiparallel state, higher energy). Since the electron possesses a spin $S = 1/2$, and considering the negative charge of the electron, the parallel state is characterised by a magnetic quantum number $m_s = -1/2$ and the antiparallel state by a $m_s = +1/2$. The energy difference between these two states is defined as:²⁹

$$\Delta E = g \mu_B B_0 \quad \Delta m_s = g \mu_B B_0 \quad \text{Eq. 1.1}$$

where: g is the g-factor (see section 1.4); μ_B is the Bohr magneton, the natural unit for expressing the electron's magnetic moment; $\Delta m_s = 1$.

In EPR, the energy required to drive a transition between the two spin states can be provided by an electromagnetic radiation and is given by:

$$\Delta E = h \nu = g \mu_B B_0 \quad \text{Eq. 1.2}$$

where: h is the Planck's constant and ν is the frequency of the applied electromagnetic radiation, typically microwaves (MW). Accordingly, in the absence of a magnetic field ($B_0 = 0$) the two spin states are degenerate so that no energy difference can be measured (Figure 1.1). Instead, as the applied magnetic field increases ($B_0 \neq 0$), the energy of the two spin states linearly diverges with the field.

Differently from modern NMR spectroscopy, where all the NMR transitions are simultaneously excited by a short radiofrequency pulse and the resulting signal is Fourier transformed to produce a time-domain spectrum (FT-NMR), most of modern EPR spectrometers continue to operate in continuous wave (CW), with the electromagnetic radiation kept constant and the

magnetic field being swept. Applications of FT-EPR are in fact limited by the impossibility of applying sufficiently wide bandwidth pulses to drive all EPR transitions at the same time, and by the difficulties in detecting the resulting signal after the deadtime. In CW EPR, when the magnetic field reaches a value for which the energy difference between the two spin states matches the energy of the electromagnetic radiation, also defined as “field of resonance”, the energy is absorbed and an EPR signal is detected (Figure 1.1). The study of such energy transitions with EPR spectroscopy can provide a wealth of information on paramagnetic species. On the contrary, systems where electrons occur in pairs (diamagnetic), will present a net magnetic moment equal to zero and therefore will be EPR silent.

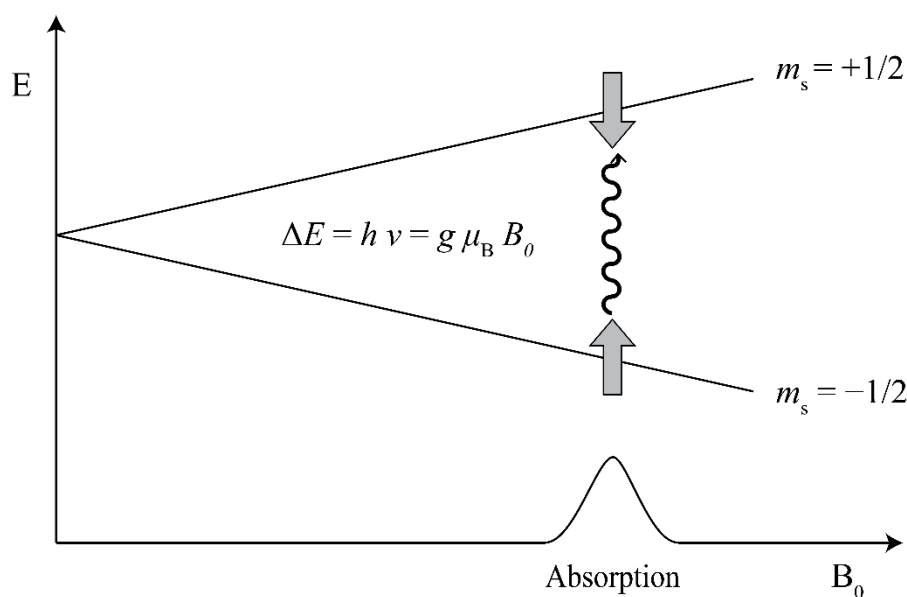


Figure 1.1 The electron Zeeman effect for a $S = 1/2$ system subjected to an increasing B_0 (figure adapted from ref. 29).

1.3 The spin Hamiltonian

A system consisting of a single electron spin is the simplest case that can be considered. The effects of the presence of additional electron and nuclear spins in the system are described by the spin Hamiltonian \hat{H} . A simplified version of the spin Hamiltonian, relevant for this work, is described by:¹

$$\hat{H} = \underbrace{\mu_B \mathbf{S} \cdot \mathbf{g} \cdot \mathbf{B}_0}_1 + \underbrace{\mathbf{S} \cdot \mathbf{D} \cdot \mathbf{S}}_2 + \underbrace{\sum_{i=1}^N \mathbf{S} \cdot \mathbf{A} \cdot \mathbf{I}_i}_3 - \underbrace{\mu_N g_N \mathbf{I}_N \cdot \mathbf{B}_0}_4 + \underbrace{\mathbf{I}_N \cdot \mathbf{P}_N \cdot \mathbf{I}_N}_5 \quad \text{Eq. 1.3}$$

The terms labelled from 1 to 5 represent:

1. Electronic Zeeman interaction
2. Zero-field interaction (for $S \geq 1$)
3. Hyperfine interaction
4. Nuclear Zeeman interaction, significantly smaller than its electronic counterpart
5. Quadrupole interaction (for $I \geq 1$), often weaker than both the electronic Zeeman and hyperfine interactions.

Considering that the spin systems studied in this thesis are characterised by $S = 1/2$, the spin Hamiltonian can be simplified as follows:

$$H = \mu_B \mathbf{S} \cdot \mathbf{g} \cdot \mathbf{B}_0 + \sum_{i=1}^N \mathbf{S} \cdot \mathbf{A} \cdot \mathbf{I}_i - \mu_N g_N \mathbf{I}_N \cdot \mathbf{B}_0$$

Eq. 1.4

1.4 The g-factor

The g-factor is for EPR the analogue of the chemical shift (δ) for NMR. This parameter is independent on the microwave frequency and therefore represents a unique fingerprint for paramagnetic species. The g-factor is described in Eq. 1.5.

$$g = h \nu / \mu B_0$$

Eq. 1.5

For carbon-centred radicals, the value of g is usually close to the value of the free electron $g_e = 2.0023$, while heteroatoms shift the g-factor to different values. As an example, an unpaired electron in the proximity of an oxygen atom gives g -values in the range of 2.004–2.006. Metal ions can instead be characterised by very different g -factors, shifted to both lower (*e.g.* 1.9 for the vanadyl ion) and higher values (*e.g.* 2.3 for Cu^{2+}) compared to g_e .²⁹ For paramagnetic species with partially or totally restricted motion, such as radicals trapped in crystalline reticulate or in viscous liquids, g -anisotropy might be observed, meaning that the g -factor, and therefore the appearance of the EPR spectrum, depends on the orientation of the paramagnetic species with respect to the magnetic field.

1.5 Hyperfine interaction

A second important parameter that characterises EPR spectra is the hyperfine interaction. The hyperfine splitting represents the equivalent of the J coupling in NMR. Certain nuclei in a

molecule possess a nuclear magnetic moment μ_N , which produces a local magnetic field at the electron, B_I . Such magnetic field can either oppose or add to the magnetic field of the laboratory magnet. When B_I adds to the external magnetic field, the field of resonance is thereby lowered; instead, when B_I opposes to the magnetic field, the field of resonance is found at higher values.

An example is given in Figure 1.2. For an electron coupling to a nucleus with spin $I = 1/2$ such as hydrogen, the EPR absorption signal splits into two distinct signals, each of them B_I away from the original signal. The hyperfine splitting constant a^H represents the distance between these two peaks, therefore corresponding to $2B_I$. An additional spin $1/2$ nucleus would then split each line into two additional lines. Therefore, for a set of n spin $1/2$ nuclei coupled to the electron, the total number of lines in the spectrum will be 2^n . The general rule defines that, for n symmetry equivalent nuclei of spin I , the number of hyperfine lines in the EPR spectrum is equal to $2nI + 1$.

The nuclear hyperfine interaction can reveal a wealth of information regarding the surroundings of the unpaired electron. The interpretation of the hyperfine splitting can determine the identity and number of atoms coupling to the electron, thus allowing in some cases to unveil the molecular structure of the paramagnetic species. Similarly to the g -factor, the hyperfine splitting displays anisotropy in solid and viscous liquid samples depending on the geometry of the molecule.

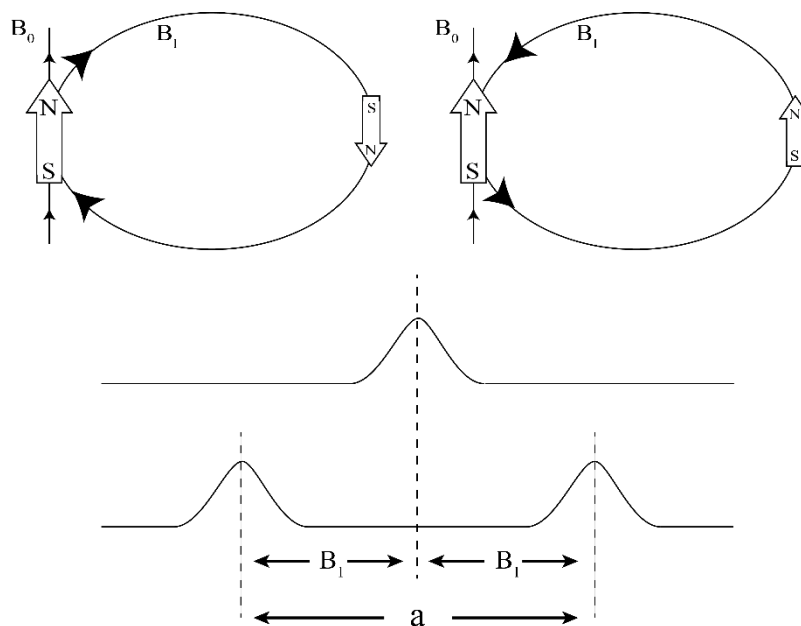


Figure 1.2 The effect of the magnetic field of a nucleus on the field experienced by an electron spin. The local magnetic field from the nucleus either opposes to or enhances the field of the laboratory magnet, causing the splitting of the EPR lines (adapted from ref. 29).

1.6 Multi-frequency EPR

Most EPR experiments are performed at X-band, *ca.* 9–10 GHz. The choice of this frequency has both historical and practical reasons. Historically, the development of RADAR during World War II made a surplus of X-band military equipment available to the early EPR pioneers in the 1950s.¹

From a practical side, X-band is a rather convenient frequency for EPR experiments. Firstly, the fields required for running experiments at this frequency can conveniently be obtained from electromagnets. Additionally, in terms of sensitivity, EPR at X-band represents a good compromise between the sample size (*ca.* 3 cm wavelengths) and the Boltzmann factor. In fact, an increasing of the Boltzmann factor and sample size results in an increased spectrometer sensitivity. Unfortunately, the effect of the frequency on these two factors is diametrically opposite. In fact, as the Boltzmann factor is higher at higher frequencies, the sample size decreases, and vice versa. At X-band, a not very high Boltzmann factor is counterbalanced by a relatively large sample size, thus making X-band analyses convenient in terms of sensitivity.

The analysis of a sample at multiple frequencies can provide extremely valuable information. As it can be deduced from **Eq. 1.3**, the appearance of an EPR spectrum is determined by both magnetic field dependent (the electronic and nuclear Zeeman) and magnetic field independent (hyperfine interaction and ZFS) components. Multi-frequency studies allow resolving the contributions from these two types of interaction, thus implementing the understanding of the paramagnetic species under study.

High frequencies are generally defined as frequencies higher than X-band, while low frequencies represent the frequency below ~9 GHz. The most commonly used bands are listed in Table 1.1.

Each of the Hamiltonian parameters offers specific information on the samples under study. The analysis of the g-factor provides information over the identity of the paramagnetic species, together with insights on the electronic state and symmetry of the paramagnetic site. The nuclear hyperfine interactions allow determination of the identity, number and distance of the nuclei in proximity to the paramagnetic centre. The zero-field splitting (ZFS) can also give important information on systems with $S \geq 1$, but it is not the case of this work and therefore will not be discussed further.

Table 1.1 Field for resonance for a $g = 2.0023$ sample at different microwave frequencies.

Microwave band	Microwave frequency (GHz)	Field of resonance for $g = g_e$ (mT)	Sample tube O.D. (mm)
L	1	36	30
S	3	107	
X	9.8	350	4
K	24	856	
Q	34	1213	2
W	94	3354	0.9
mm-wave	263	9384	0.3

At high frequencies the field dependent term is emphasised and becomes more dominant. High frequencies can be convenient for identifying multiple paramagnetic species characterised by a similar g -factor. Indeed, the difference in field of resonance ΔB will be approximately proportional to the microwave frequency, thereby making possible to distinguish species with similar g -factors, as long as ΔB becomes greater than the linewidth. Also, high frequencies might allow the anisotropic components of a spectrum to be distinguished, giving valuable information on the symmetry of the paramagnetic centre.

On the contrary, at low frequencies the magnetic field independent components are dominating the spectrum. Therefore, at low enough frequencies it can be possible to extract information on the nuclear hyperfine coupling of the system, as the g -anisotropy is less accentuated.

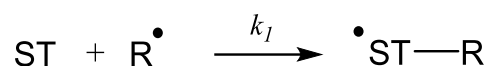
Theoretically, going very low or very high in frequency should allow a direct determination of the Hamiltonian parameters such as g -factor and hyperfine coupling components. In practice, this is rarely obtained as several factors can interfere with the analysis, including linewidths, anisotropy and second order effects (at lower frequencies). A solution to this problem is to perform experiments at multiple frequencies, thus obtaining a data set with all the limiting cases that can allow extraction of the required spin Hamiltonian parameters through spectral simulation.

1.7 Spin trapping

1.7.1 Spin trapping reaction

Free radicals are known to be involved in a number of metabolic processes, thus drawing a great interest in biology and medicine. EPR is generally considered the gold standard for the detection of free radicals. Nevertheless, direct detection of these paramagnetic species is often impeded by multiple factors. Firstly, their concentration may be below the detection limit of the spectrometer. Additionally, if their spin relaxation times are too short, their linewidth will be too broad to be observable, which is the case of *e.g.* hydroxyl radical ($\cdot\text{OH}$) or singlet oxygen ($\text{O}_2^{\cdot-}$).^{30–32}

Spin trapping is a technique that has been developed to overcome these limitations. It consists in the addition reaction of the radical of interest (R^\cdot) to a diamagnetic compound, the spin trap (ST), in order to produce a relatively long-lived free radical product, the spin adduct (ST-R^\cdot).^{30,33}



This is usually a nitroxide, which is a relatively stable chemical species thanks to the mesomeric stabilization of the unpaired electron (Figure 1.3).³⁰ Once formed, the spin adduct would then hopefully accumulate to a high enough concentration to be studied by EPR. Therefore, spin trapping is a valuable technique for the study of free radicals where direct detection of the paramagnetic species is not possible.

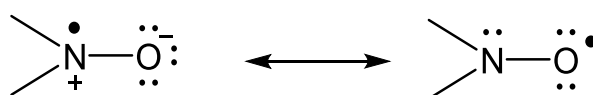


Figure 1.3 Mesomeric structures of a nitroxide with the unpaired electron localized on the nitrogen atom (left) and the oxygen atom (right).

1.7.2 Choice of spin trapping agent

Two kinds of spin trapping agents are available, the nitron and nitroso spin traps. They have the ability to trap carbon-, nitrogen-, oxygen- and sulphur-based radicals. Nitron compounds, such as DMPO (Figure 1.4), DEMPO, PBN, POBN are typically used for the detection of oxygen-centred radicals (Figure 1.5).³⁴ The radical adds to the carbon atom adjacent to the nitron nitrogen, inducing the formation of relatively stable spin adducts. The hyperfine

splitting parameter of the β -hydrogen can also provide considerable information about the radical trapped.³⁰

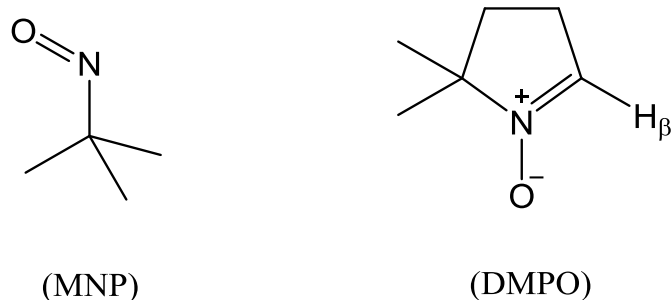


Figure 1.4 The nitroso spin trap 2-methyl-2-nitroso propane (MNP, left) and the nitron spin trap 5,5-dimethyl-1-pyrroline N-oxide (DMPO, right).

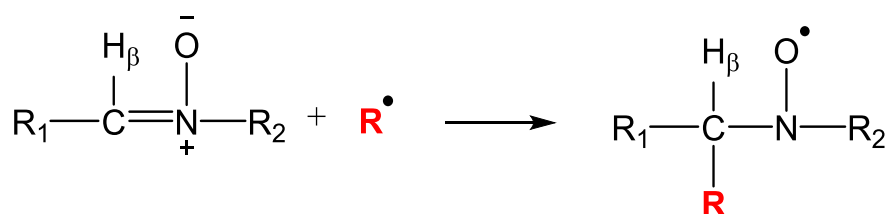


Figure 1.5 Trapping of a radical (R^\bullet) species by a nitron compound.

Nitroso compounds, such as MNP (Figure 1.4), can provide much more information in the hyperfine splitting parameters than the nitron compounds, as the radical binds directly to the nitroso nitrogen (Figure 1.6). On the other hand, adducts formed from reaction with oxygen-centred radicals are quite unstable, so they are mostly utilised for the trapping of carbon-centred species.³⁰ This work focused in particular on the use of the nitroso spin trapping agent MNP for the trapping of carbon-centred radicals.

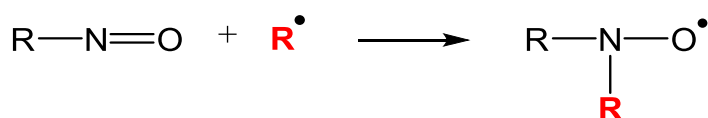


Figure 1.6 Trapping of a radical (R^\bullet) species by a nitroso compound.

1.8 References

1. Weil, J. A. & Bolton, J. R. *Electron paramagnetic resonance: elementary theory and practical applications*. (John Wiley & Sons, Hoboken, New Jersey, 2007).
2. Fischer, H. Applications of Electron Spin Resonance in Polymer Chemistry. *Proc. R. Soc. Lond. A. Math. Phys. Sci.* **302**, 321–327 (1968).
3. Yamada, B., Westmoreland, D. G., Kobatake, S. & Konosu, O. ESR spectroscopic studies of radical polymerization. *Prog. Polym. Sci.* **24**, 565–630 (1999).
4. Hinderberger, D. in *EPR Spectroscopy* (eds. Drescher, M. & Jeschke, G.) 67–89 (Springer Berlin Heidelberg, 2012).
5. Schubert, E., Hett, T., Schiemann, O. & Nejatyjahromy, Y. EPR studies on the kinetics of the α -hydroxyethyl radical generated by Fenton-like chemistry. *J. Magn. Reson.* **265**, 10–15 (2016).
6. Lobrutto, R., Van Camp, H. L., Scholes, C. P. & King, T. E. Electron Paramagnetic Resonance- (EPR-) resolved kinetics of cryogenic nitric oxide recombination to cytochrome c oxidase and myoglobin. *Biophysical J.* **45**, 473–479 (1984).
7. Spasojevi, I. Electron Paramagnetic Resonance - A Powerful Tool of Medical Biochemistry in Discovering Mechanisms of Disease and Treatment Prospects. *J. Med. Biochem.* **29**, 175–188 (2010).
8. Gallez, B. & Baudalet, C. Assessment of tumor oxygenation by electron paramagnetic resonance : principles and applications. *NMR Biomed.* **17**, 240–262 (2004).
9. Van Doorslaer, S. & Murphy, D. M. in *EPR Spectroscopy* (eds. Drescher, M. & Jeschke, G.) 1–39 (Springer Berlin Heidelberg, 2012).
10. Morra, E., Giamello, E. & Chiesa, M. EPR approaches to heterogeneous catalysis . The chemistry of titanium in heterogeneous catalysts and photocatalysts. *J. Magn. Reson.* **280**, 89–102 (2017).
11. Frankel, E. N. Antioxidants in lipid foods and their impact on food quality. *Food Chem.* **57**, 51–55 (1996).
12. Morsy, M. A. & Khaled, M. M. Novel EPR characterization of the antioxidant activity of tea leaves. *Spectrochim. Acta Part A Mol. Biomol. Spectrosc.* **58**, 1271–1277 (2002).

13. Uchida, M., Suga, S. & Ono, M. Improvement for oxidative flavor stability of beer: rapid prediction method for beer flavor stability of electron spin resonance spectroscopy. *Am. Soc. Brew. Chem.* (1996).
14. Burns, C. S., Heyerick, A., Keukeleire, D. De & Forbes, M. D. E. Mechanism for Formation of the Lightstruck Flavor in Beer Revealed by Time-Resolved Electron Paramagnetic Resonance. *Chem. Eur. J.* **7**, 4553–4561 (2001).
15. Stachowicz, W., Burlínska, G., Michalik, J., Dziedzic-Gocławska, A. & Ostrowski, K. The EPR detection of foods preseeded with the use of ionizing radiation. *Radiat. Phys. Chem.* **46**, 771–777 (1995).
16. Polovka, M., Brezová, V. & Šimko, P. EPR spectroscopy: A tool to characterize gamma-irradiated foods. *J. Food Nutr. Res.* **46**, 75–83 (2007).
17. Raffi, J., Yordanov, N. D., Chabane, S., Douifi, L. & Gancheva, V. Identification of irradiation treatment of aromatic herbs, spices and fruits by electron paramagnetic resonance and thermoluminescence. **56**, 409–416 (2000).
18. Bidzińska, E., Dyrek, K., Fortuna, T., Łabanowska, M. & Pietrzyk, S. EPR Studies of Thermally Treated Oxidized Corn. **56**, 461–468 (2004).
19. Williams, H. E., Loades, V. C., Claybourn, M. & Murphy, D. M. Electron paramagnetic resonance spectroscopy studies of oxidative degradation of an active pharmaceutical ingredient and quantitative analysis of the organic radical intermediates using partial least-squares regression. *Anal. Chem.* **78**, 604–608 (2006).
20. Williams, H. E. & Claybourn, M. Predicting the photostability characteristics of active pharmaceutical ingredients using electron paramagnetic resonance spectroscopy. **38**, 200–208 (2012).
21. Lamy-Freund, M. T., Ferreira, V. F. N. & Shirley, S. Mechanism of inactivation of the polyene antibiotic amphotericin B. *J. Antibiot. (Tokyo)*. **38**, 753–757 (1985).
22. Auclair, C., Hyland, K. & Paoletti, C. Autoxidation of the Antitumor Drug 9-Hydroxyellipticine and Its Derivatives. *J. Med. Chem.* **26**, 1438–1444 (1983).
23. Vasquez-vivar, J. & Augusto, O. ESR detection of free radical intermediates during autoxidation of 5-hydroxyprimaquine. *Free Radic. Res. Commun.* **9**, 383–389 (1990).
24. Claybourn, M., Gray, H., Murphy, D. M., Purnell, I. J. & Rowlands, C. C. Electron magnetic resonance study of gamma-irradiated poly (lactide-co-glycolide)

- microspheres. *J. Control. Release* **91**, 431–438 (2003).
25. Bushell, J. A., Claybourn, M., Williams, H. E. & Murphy, D. M. An EPR and ENDOR study of α - and β -radiation sterilization in poly (lactide-co-glycolide) polymers and microspheres. *J. Control. Release* **110**, 49–57 (2005).
26. Butler, J. S., Woods, J. A., Farrer, N. J., Newton, M. E. & Sadler, P. J. Tryptophan Switch for a Photoactivated Platinum Anticancer Complex. *J. Am. Chem. Soc.* **134**, 16508–16511 (2012).
27. Butler, J. S. Photodecomposition Pathways for Photoactivatable Platinum (IV) Anticancer Complexes. (PhD Thesis, University of Warwick, 2014).
28. Venkatesh, V., Wedge, C. J., Romero-Canelón, I., Habtemariam, A. & Sadler, P. J. Spin-labelled photo-cytotoxic diazido platinum(IV) anticancer complex. *Dalt. Trans.* **45**, 13034–13037 (2016).
29. Eaton, G. R., Eaton, S. S., Barr, D. P. & Weber, R. T. *Quantitative EPR*. (Springer Science & Business Media, New York, 2010).
30. Buettner, G. R. Spin Trapping - Electron-Spin-Resonance Parameters of Spin Adducts. *Free Radic. Bio. Med.* **3**, 259–303 (1987).
31. Kalyanaraman, B., Mottley, C. & Mason, R. P. A Direct Electron Spin Resonance and Spin-trapping Investigation of Peroxyl Free Radical Formation by Hematin/Hydroperoxide Systems. *J. Biol. Chem.* **253**, 3855–3858 (1983).
32. Yadav, K. D. & Pospisil, P. Evidence on the Formation of Singlet Oxygen in the Donor Side Photoinhibition of Photosystem II: EPR Spin- Trapping Study. *PLoS One* **7**, (2012).
33. Janzen, E. G. Spin Trapping. *Acc. Chem. Res.* **4**, 31–40 (1971).
34. Makino, K., Hagiwara, T. & Murakami, A. Z. A. A Mini Review: Fundamental Aspects of Spin Trapping with DMPO. *Radiat. Phys. Chem.* **37**, 657–665 (1991).

Chapter 2

Sterilization of Pharmaceuticals

The first part of this work focuses on the characterisation of the degradants formed from irradiation sterilization of pharmaceutical excipients. In this Chapter, a description of the procedures used for the sterilization of drug products in the pharmaceutical industry is presented. The role of EPR spectroscopy in the detection of degradation products from pharmaceuticals is also outlined. At the end of the Chapter, the motivation for study and a thesis outline are also presented.

2.1 Sterilization in the pharmaceutical industry

In microbiology, the term sterilization defines the process of inactivation of microorganisms. The effectiveness of a sterilization process is measured in relation to the sterility assurance level (SAL), which is a parameter that defines the probability of the survival of one viable microorganism in a unit being subjected to the sterilization process. Currently, a SAL of 10^{-6} is the standard generally accepted by the pharmacopoeias,¹ meaning that the probability of survival of a viable microorganism in a sterilized product must not be higher than one in a million. A product that has been subject of such process is defined as “sterile”. The oldest and most recognised method for assuring sterility is heat, but many other sterilization processes have been developed, and will be shortly described in the following paragraphs.

2.1.1 Dry heat sterilization

Dry heat is often used in the pharmaceutical industry and represents the method of choice for the sterilization of heat-stable materials. These usually include items such as glassware, stainless-steel equipment, closed containers, powders and oils.² Compared to steam sterilization (see next paragraph) it generally requires higher temperatures and/or longer exposure times. The times and temperatures required for reaching the desired SAL varies depending on the pharmacopoeia of reference. As an example, according to the U.S. Pharmacopoeia (USP) items that undergo dry heat sterilization should be kept at a temperature of 160–170 °C for a period of 2 to 4 hours.³

2.1.2 Steam sterilization

Also known as autoclaving, steam sterilization is the most widely used sterilization method. It consists of exposing the products to a defined combination of temperature and humidity such as to inactivate the microorganisms. Typically, materials are exposed to pressurised saturated steam at 121 °C for 15 minutes, but temperature and time can vary depending on the stability of the materials to sterilize.⁴ Nevertheless, this method is unsuitable for the sterilization of heat- or moisture-sensitive compounds and active ingredients.

2.1.3 Ethylene oxide sterilization

An alternative for the sterilization of heat-sensitive materials is represented by ethylene oxide (EtO) sterilization. This highly reactive gas is typically used at lower temperatures compared to dry heat and steam sterilization (*ca.* 50 – 60 °C) and in the presence of water.⁴ EtO is mainly used for the sterilization of medical devices, and only secondarily for pharmaceutical products. Packaging of the sterilized material is limited to that allowing penetration of the gas. Important issues related the use of this sterilization method concern safety in the industrial site and safety of the sterilized materials. In fact, some packaging materials have been shown to retain the gas representing a potential hazard. Therefore, the residual EtO has necessarily to be removed, usually through post sterilization aeration with sterile air, in order to avoid direct contact of the gas which has been classified as carcinogenic and mutagenic.⁴

2.1.4 Filtration sterilization

Filtration is a safe technique that consists in the physical removal of microorganisms and can be an alternative for aqueous solutions of thermolabile substances. However, this procedure doesn't allow processing of the product in its final packaged form (terminal processing) and as such requires operation in aseptic conditions, therefore resulting in a rather costly and complex process.^{4,5}

2.2 Radiation sterilization

Commercial radiation sterilization has been used for more than 60 years, since the first electron accelerator that was developed by the Ethicon Division of Johnson & Johnson in New Jersey in 1956 for the commercial radiation sterilization of surgical sutures.⁶ Currently, approximately 50% of disposable medical devices in North America are radiation sterilized⁶ and the demand for the radiation sterilization of single-use medical devices in the United States grows at a rate of approximately 7% per year.⁷

2.2.1 Ionising radiation

Radiation can be classified as either ionising or non-ionising, the former having sufficient energy to cause the release of orbital electrons from atoms and disruption of covalent bonds. Electron beams, X-rays and γ -rays are all forms of ionising radiations, while UV, visible, IR and radiofrequencies are all non-ionising radiations.

Both UV and IR are utilised for sterilization purposes, the former exerting its germicidal action by excitation of atoms at cellular level and the latter by heat generation. However, the penetrating power of these non-ionising radiation types is rather low and makes them not suitable for terminal sterilization.

2.2.2 γ -irradiation sterilization

Amongst the different types of radiation, γ -sterilization is gaining popularity, covering in 2003 approximately 40% of the sterilization market and being the method of choice for the sterilization of single-use medical devices.⁸ Part of its success relies on the progressive decrease in the use of EtO as a terminal sterilization method and on the development of radiation-stable polymers for packaging, such as polyvinyl chloride (PVC), polycarbonates and polypropylene, which are able to prevent the brittleness and brown-yellow post-sterilization coloration.⁸ This tendency is reflected in scientific literature, with works on ‘gamma sterilization’ being increasingly published over the last 40 years (Figure 2.1).

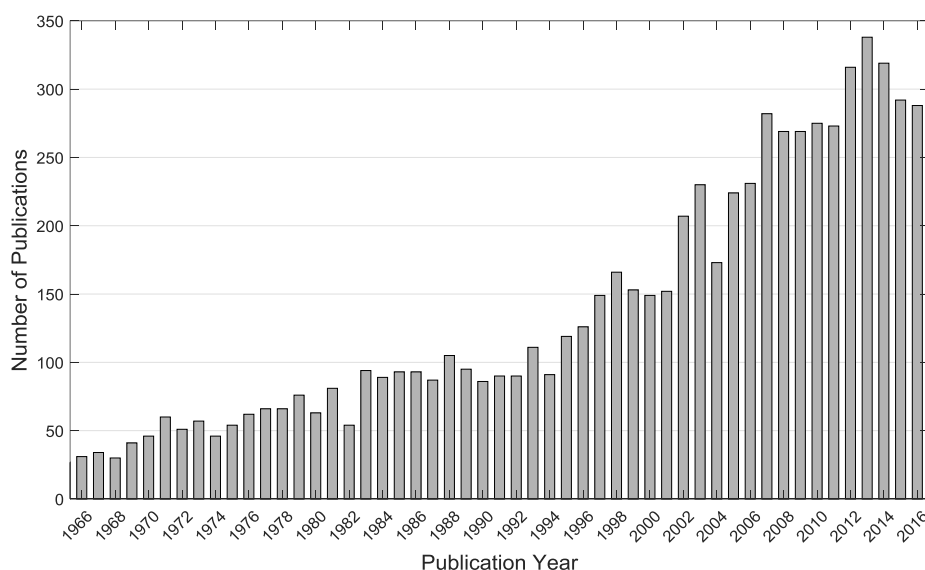


Figure 2.1 Summary of gamma sterilization published literature (from ref. 9).

The interaction of γ -rays with matter is a process that can be divided into three stages:³

1. The physical stage ($\sim 10^{-18} - 10^{-15}$ s): involves the absorption of the energy of the ionising radiation by the irradiated material. The effect of such energy transfer is the production of electronically excited molecules, ions and free electrons.
2. The physio-chemical stage ($\sim 10^{-14} - 10^{-12}$ s): during this stage the excited molecules and ions dissipate their energy through a number of processes including bond rupture, luminescence and transfer of energy to neighbouring molecules. At this stage, free radicals are formed.
3. The chemical stage ($\sim 10^{-12} - 10^{-3}$ s): ions and radicals formed in the previous stage react with other molecules. Examples of reactions at this stage include atomic abstraction, radical recombination, oxidation, depolymerisation, crosslinking and addition to π -bonds.^{3,4}

The lethal action of ionising radiations has been proposed to be due to disruption of DNA, occurring either directly (target theory), or indirectly by interaction of DNA with newly formed free radicals (diffusion theory).

An irradiation dose of 25 kGy is generally accepted to assure sterility,³ although lower doses can be used, depending on the bioburden of the components, in order to reduce the impact of the sterilization process on the sterilized materials.¹⁰

The use of γ -irradiation for sterilization purposes has numerous advantages in respect to the other methods.^{5,11,12} To begin, it enables the sterilization of thermolabile or chemically reactive drugs. Its high penetrating power allows terminal sterilization of the products, assuring better sterility and less pitfalls than non-terminal processes and a higher penetration compared to electron beams and X-rays. Cost wise, it is also more convenient than processes such as filtration and working in aseptic conditions. On the other hand, γ -sterilization can produce chemical and physical alterations in the irradiated material, which must be assessed to ensure the safety of the sterilized products.¹³

2.2.3 γ -sterilization of pharmaceuticals

As the popularity of γ -irradiation sterilization increases, the interest in the γ -sterilization of pharmaceutical products is also constantly growing. Numerous reviews have been published in the past, covering the effects of γ -sterilization on several APIs and drug delivery systems^{4,5,12-18} and will not be here reported. From the said reviews, it clearly emerges that the effects of γ -sterilization on pharmaceutical compounds are rather varied and therefore difficult to predict. In fact, it is not possible to make predictions on the impact of radiation sterilization on a molecular structural base, as just minor changes in the molecular structure can have significant

influence in the outcome of the sterilization.¹¹ Thus, the impact of radiation sterilization on a specific compound must be assessed every single time.

2.3 EPR in the detection of pharmaceutical degradants

As described in **Chapter 1**, electron paramagnetic resonance (EPR) is the technique of choice for the study of free radicals. Since the interaction of γ -rays and matter results in the formation of free radicals, EPR spectroscopy has been used in the past to provide proof of whether a drug has been irradiated or not.^{19–21} Radicals can originate from processes other than irradiation, and unirradiated samples often present an EPR signal.^{11,19} Materials exposed to UV radiation can in fact give an EPR signal,^{22,23} likewise mechanistic actions such as grinding or milling can produce EPR active species.^{24–26} The difference is usually given by the intensity of the EPR signal, which is much higher in γ -irradiated materials. In fact, UV radiation induces the production of paramagnetic species only on the surface of the irradiated material, while for thermal processes the radical yield is rather low.²⁰

Other techniques have been utilized to characterize degradation products formed upon irradiation of pharmaceuticals, but all show some limitations. Thermoluminescence, for example, can be used to analyse irradiated products in the solid state by detecting radio-induced ions trapped in the solid matrix. Some signals are characteristic of irradiated drugs, but depending on the compound under study the relevant peaks can be one or multiple, and can be dose dependent or not. Therefore, each compound is a different case and requires a specific study. In case of mixtures, it also would not be possible to unequivocally attribute the detected signal to one component or another, hence a general detection protocol cannot be produced.^{20,21} Protocols for the detection of irradiated foodstuffs containing lipids with gas phase chromatography (GC) can potentially be applied to lipid containing formulations, *e.g.* creams. However, the complexity of such products does not usually allow the use of this technique, which cannot distinguish more than three/four different lipids at the same time.²¹

2.4 Pharmaceutical excipients

The formulation of a drug product involves the use of excipients, which represent the non-active part of the drug that is included in the manufacturing process or contained in a finished pharmaceutical product dosage form.²⁷ These pharmaceutically inactive substances are needed to improve the properties of the drug, either by enhancing the therapeutic effect of the API or

by facilitating the manufacturing process.²⁸ Parenteral (*i.e.* injectable) products, which are the subject of the first part of this thesis, are often formulated as freeze-dried cakes. These cakes are obtained through a process called freeze-drying, also known as lyophilisation. This process consists of freezing the solution that contains all the ingredients of the formulation, followed by removal of (most of) the water content, initially by sublimation and later by desorption. This procedure allows formulation of drugs which are thermolabile or unstable in aqueous solutions.^{3,27} The lyophilised cake is then reconstituted in a physiological solution immediately prior to injection into the patient.

A summary of the types and functions of the most common freeze-dried excipients is reported in Table 2.1:

Table 2.1 Summary of types and functions of freeze-dried excipients.

Excipient	Functions	Examples
Bulking agents	Act as filling material	Mannitol, lactose, sucrose, trehalose, sorbitol, glucose
Buffering agents	Control the pH of the reconstituted solution	Histidine, citric acid, sodium citrate, sodium phosphate, tris base, arginine
Solubilising agents	Aid the reconstitution of the drug	EDTA, alpha cyclodextrin, polysorbate 80
Antimicrobials	Prevent microbial growth during shelf life	Benzyl alcohol, phenol, methyl paraben
Tonicity modifiers	Make solution isotonic with human plasma	Dextran, mannitol, glycerol

Typically, the total amount of excipients in a dosage form is greater than the amount of the API(s). The choice of excipients in a formulation is paramount, as they can both stabilise or destabilise the product.¹⁹ Indeed, the action of a pharmaceutical product depends on the stability not only of the APIs, but also of the excipients. Adverse effects can in fact be caused by excipients or their impurities, either directly or by reaction with the active part of the drug.²⁹ Thus, assessing the stability of these inactive components after they undergo potentially

destructive industrial processes is crucial to determine the safety of the processed pharmaceutical product.

2.5 Motivation of study

This thesis aims to explore the applicability of EPR spectroscopy in areas of pharmaceutical R&D where this powerful tool is still much underutilised.

Several industrial pharmaceutical processes result in degrading the products being processed to some extent. Often, the energy released in the said processes induces the formation of radicalic degradants. In particular, sterilization with γ -rays can form free radicals in relatively high concentrations.^{3,4,13} The safety of these highly reactive species must be assessed to avoid adverse effects following administration of the drug product to the patient. γ -sterilization is of particular interest for a variety of parenteral drugs which are thermolabile and as such cannot be sterilized with the classic autoclaving process. Since the effects of γ -sterilization cannot be predicted beforehand, as even very similar compounds usually have rather different responses to irradiation, the stability of each new irradiated pharmaceutical product must be assessed. Nevertheless, the number of excipients that can be utilised in parenteral formulations is limited. Thus, having a complete characterisation of the degradants formed upon irradiation of the most common excipients would be a great advantage towards the study of a multi-component system.

EPR is considered the gold standard for the study of free radicals, being characterised by a high sensitivity and specificity towards paramagnetic species. This technique therefore allows to quantify, identify and assess the reactivity of free radicals produced upon γ -sterilization of parenteral drugs. Interestingly, it was shown that the same radical species are detected in starches after γ -irradiation, UV radiation or grinding.^{20,21} Hence, it appears that the characterization of the degradation products originated from γ -irradiation is not only limited to the study of this pharmaceutical process, but is in fact useful for a number of processes in the pharmaceutical industry. In the first part of this work, the effects of γ -sterilization on two very common excipients, L-histidine and D-mannitol, are studied.

Approximately 50% of anticancer treatments nowadays involve the use of platinum-based compounds.³⁰ Despite many important results in the development of this class of anticancer drugs, the development of resistance remains a major issue and pushes to the search for new anticancer candidates.³¹ *trans,trans,trans*-[Pt(N₃)₂(OH)₂(pyridine)₂] is a promising photo-activable diazo anticancer compound, which has been shown to have a dual mechanism of action involving both platination to DNA and oxidative attack carried out by photo-released

azidyl radicals.³² Additionally, the cytotoxic activity of this platinum(IV) complex was found to be tuned by the presence of L-tryptophan, an effect that was ascribed to the quenching of azidyl radicals by this aromatic amino acid with consequent formation of a transient L-tryptophan radical, although such species had not been previously detected. EPR spin trapping methodology offers the possibility to unveil the details of the interaction between these transient species, leading to an increased mechanistic understanding of the activity of the platinum(IV) compound to improve the drug design of such anticancer drugs. Additionally, EPR studies can help to identify the intracellular target of the photo-released azidyl radicals, which to date remains unknown.

2.6 Thesis outline

An outline of the remainder of this thesis is as follows:

- In addition to the theoretical basis for the experiments performed that has been discussed in Chapter 1 and the background information of this chapter, Chapter 3 provides the experimental aspects of the techniques used in this thesis. Details on the instrumentation used and on the experimental procedures are outlined.
- Chapter 4 discusses the effects of γ -irradiation on the amino acid L-histidine. Solid state irradiated crystals and powders are studied with EPR in the range of 77–295 K. Particular focus is given to the spin trapping experiments, reporting an unusual regeneration mechanism of the radical species in solution.
- Chapter 5 focuses on studying the irradiation effects on the excipient D-mannitol, characterising the radical species formed at low temperature and following their evolution into the r.t. stable species. Spin trapping experiments are also reported, together with data from complementary techniques.
- In Chapter 6, a short introduction to metallo-organic anticancer compounds is presented. The chapter then investigates the mechanism of action of a promising photo-activable anticancer Pt-complex, with the identification of transient intermediates through spin trapping experiments. The target of photo-released RNS is also studied.
- Finally, Chapter 7 offers a summary of the presented work and the direction of future investigations.

2.7 References

1. Woedtke, T. von & Kramer, A. The limits of sterility assurance. *GMS Krankenhhyg. Interdiszip.* **3**, 1–10 (2008).
2. Kupiec, T. C., Matthews, P. & Ahmad, R. Dry-heat sterilization of parenteral oil vehicles. *Int. J. Pharm. Compd.* **4**, 223–224 (2000).
3. Schulman, S. G. & Achey, P. M. *Encyclopedia of Pharmaceutical Technology*. **6**, (Marcel Dekker, New York, 2007).
4. Gopal, N. G. S. Radiation sterilization of pharmaceuticals and polymers. *Radiat. Phys. Chem.* **12**, 35–50 (1978).
5. Hasanain, F., Guenther, K., Mullett, W. M. & Craven, E. Gamma sterilization of pharmaceuticals - A review of the irradiation of excipients, active pharmaceutical ingredients, and final drug product formulations. *PDA J. Pharm. Sci. Technol.* **68**, 113–137 (2014).
6. Morrissey, R. F. & Herring, C. M. Radiation sterilization: past, present and future. *Radiat. Phys. Chem.* **63**, 217–221 (2002).
7. Masfield, J. Reflections on the evolution and current status of the radiation industry. *Radiat. Phys. Chem.* **71**, 8–15 (2004).
8. Hemmerich, K., Masfield, J. & Nelson, J. R. Sterilization methods stand the test of time. *Med. Device Diagnostic Ind.* **26**, 132–145 (2004).
9. www.cas.org/products/scifinder (date accessed 01/08/17).
10. Association for the Advancement of Medical Instrumentation. *ANSI/AAMI/ISO 11137-2:2013: Sterilization of health care products–radiation–Part 2: Establishing the sterilization dose*. (USA, February, 2013).
11. Ambroz, H. B., Kornacka, E. M., Marciniak, B., Ogrodowczyk, M. & Przybytniak, G. K. EPR study of free radicals in some drugs γ -irradiated in the solid state. **58**, (2000).
12. Jacobs, G. P. & Wills, P. A. Recent developments in the radiation sterilization of pharmaceuticals. *Int. J. Radiat. Appl. Instrumentation. Part C. Radiat. Phys. Chem.* **31**, 685–691 (1988).
13. Jacobs, G. P. A review: radiation sterilization pharmaceuticals. **26**, 133–142 (1985).

14. Jacobs, G. P. Radiation Sterilization of Parenterals. 1–7 (2007). at <http://www.pharmtech.com/pharmtech/Aseptic+processing/Radiation-Sterilization-of-Parenterals/ArticleStandard/Article/detail/423948>
15. Jacobs, G. P. A review of the effects of gamma radiation on pharmaceutical materials. *J. Biomater. Appl.* **10**, 59–96 (1995).
16. Razem, D. & Katusin-Razem, B. The effects of irradiation on controlled drug delivery / controlled drug release systems. *Radiat. Phys. Chem.* **77**, 288–344 (2008).
17. Clough, R. L. High-energy radiation and polymers : A review of commercial processes and emerging applications. *Nucl. Instruments Methods Phys. Res. B* **185**, 8–33 (2001).
18. Sintzel, M. B., Merkli, A., Tabatabay, C. & Gurny, R. Influence of Irradiation Sterilization on Polymers Used as Drug Carriers- A Review. *Drug Dev. Ind. Pharm.* **23**, 857–878 (1997).
19. Aleksieva, K. & Yordanov, N. D. EPR investigation of some gamma-irradiated excipients. *Radiat. Eff. Defects Solids* **167**, 685–689 (2012).
20. Raffi, J. *et al.* Electron spin resonance - Thermoluminescence studies on irradiated drugs and excipients. *Radiat. Phys. Chem.* **63**, 705–707 (2002).
21. Raffi, J. *et al.* Electron paramagnetic resonance of radicals induced in drugs and excipients by radiation or mechanical treatments. *Spectrochim. Acta - Part A Mol. Biomol. Spectrosc.* **58**, 1313–1320 (2002).
22. Zhang, S., Xie, J., Zhang, J., Zhao, J. & Jiang, L. Electron spin resonance studies on photosensitized formation of hydroxyl radical by C-phycocyanin from *Spirulina platensis*. **1426**, 205–211 (1999).
23. K.J. Reszka, P. Bilski, C.-F. Chignell, J. D. Free radical reactions photosensitized by the human lens component, kynurenine: an EPR and spin trapping investigation. *Free Radic. Biol. Med.* **20**, 23–34 (1996).
24. T. Kudo, H. H. Formation of mechano-radicals in D-glucose and lactose. *Carbohydr. Res.* **103**, 7–14 (1982).
25. M. Desrosiers, M. Simic, F. Eichmiller, A. Johnston, R. B. Mechanically-induced Generation of Radicals in Tooth Enamel. *Appl. Radiat. Isot.* **40**, 1195–1197 (1989).
26. A. Marino, R. B. Mechanically induced free radicals in bone. *Nature* **218**, 466–467

- (1968).
27. Pikal, M. J. & Costantino, H. R. *Lyophilization of Biopharmaceuticals. Biotechnology: Pharmaceutical Aspects* **2**, (AAPS Press, Arlington, VA, 2004).
 28. García-Arieta, A. Interactions between active pharmaceutical ingredients and excipients affecting bioavailability: impact on bioequivalence. *Eur. J. Pharm. Sci.* **65**, 89–97 (2014).
 29. Katdare, A. *Excipient Development for Pharmaceutical, Biotechnology, and Drug Delivery Systems. Informa Healthcare USA, Inc* (2006).
 30. Johnstone, T. C., Park, G. Y. & Lippard, S. J. Understanding and Improving Platinum Anticancer Drugs - Phenanthriplatin. *Anticancer Res.* **34**, 471–6 (2014).
 31. Martin, L. P., Hamilton, T. C. & Schilder, R. J. Platinum resistance: The role of DNA repair pathways. *Clin. Cancer Res.* **14**, 1291–1295 (2008).
 32. Butler, J. S., Woods, J. A., Farrer, N. J., Newton, M. E. & Sadler, P. J. Tryptophan Switch for a Photoactivated Platinum Anticancer Complex. *J. Am. Chem. Soc.* **134**, 16508–16511 (2012).

Chapter 3

Experimental Methods

In this Chapter the main materials, experimental procedures and instrumentation used throughout the thesis will be described. More specific experimental details will be discussed in the following chapters.

3.1 Experimental

3.1.1 Materials

L-histidine free base, D-mannitol, deuterium oxide (D_2O , $\geq 99.96\%$), acetonitrile (ACN), 2-methyl-2-nitrosopropane (MNP) in the form of dimer, ethylenediaminetetraacetic acid (EDTA) were all purchased from Sigma Aldrich. 5,5-Dimethyl-1-pyrroline-N-oxide (DMPO) was purchased from Enzo Life Sciences. DMPO and MNP dimer were stored at $-20\text{ }^{\circ}\text{C}$. Ethanol (99.7–100%) absolute and toluene were purchased from VWR.

3.2 Crystal growth

Single crystals were grown from saturated aqueous solutions by slow evaporation at room temperature (r.t.). Saturated solutions were prepared by mixing an excess of powder to Milli-Q water. The solutions were then filtered with $0.22\text{ }\mu\text{m}$ Millipore syringe filters and transferred into crystallising dishes. The dishes were covered with a pierced aluminium foil and left to desiccate at r.t. until complete evaporation of the water. The structures of the crystals were determined by single crystal X-ray diffraction on a *Rigaku Oxford Diffraction Gemini R*.

3.2.1 Deuteration

In order to obtain partially deuterated samples, powders were dissolved in D_2O and subsequently reprecipitated by slow addition of ethanol under mild stirring. The powders were then filtered with a filter funnel. The procedure was repeated for a total of 3 times, after which

the powders were left to desiccate until complete evaporation of the residual solvent. Part of the powders were dissolved once again in D₂O to form a saturated solution, and were left to crystallise as previously described. Partially deuterated crystals and powders were stored in sealed vials containing nitrogen gas. The procedure resulted in the deuteration of fast proton exchange chemical groups such as amino, carboxyl and hydroxide groups.

3.3 γ -irradiation

All γ -irradiations were performed at Dalton Cumbrian Facility (UK) using a Foss Therapy Model 812 ⁶⁰Co self-contained high dose rate γ -irradiator.

3.3.1 Room temperature irradiation

Powder and crystal samples were sealed in headspace glass vials with PTFE/butyl septa and evacuated. γ -irradiation was performed supplying a dose rate of approximately 2.3 kGy/h, which was measured by a Radcal 10X6-0.18 ion chamber. Samples received a total dose of either 25, 125 or 250 kGy, with an estimated error of $\pm 5\%$ of the total irradiation dose.

3.3.2 γ -irradiation in liquid nitrogen

Samples were inserted in 4 mm o.d. EPR quartz tubes (Wilmad-LabGlass 707-SQ-250M), which were flame sealed after being evacuated for a few minutes. As crystals grow preferentially in one direction forming plates, they could be inserted in the quartz tubes only in one orientation, hence low temperature experiments could not be performed along all the three orientations of the crystal samples. The sample tubes were then tied together by means of cable ties, and placed at the centre of a liquid nitrogen dewar. A polystyrene lid with a hole in the centre was placed at the top of the dewar to keep the tubes in position. The dewar was then filled with liquid nitrogen and placed in the irradiation chamber. The samples were irradiated while submerged in liquid nitrogen for a total dose of approximately 25 kGy, with an irradiation rate of approximately 2.3 kGy/h. The nitrogen dewar was periodically refilled to keep the samples always submerged in liquid nitrogen. Before each refilling, the samples were temporarily moved into a second liquid nitrogen dewar, while the liquid nitrogen left in the first dewar was eliminated as ozone (O₃) can form with γ -irradiation in open air¹ and can result in explosions.² When the irradiation was completed, samples were quickly transferred into a transportable *Statebourne Bio 10* nitrogen dewar and transported back to the laboratory for the EPR analysis.

3.3.3 Removal of quartz background signal

As the irradiation of quartz results in the formation of a number of EPR-active defects which can interfere with the analysis,³ the tubes were annealed by using the sliding technique.⁴ Samples were slid to the other end of the EPR quartz tube and the empty end of the tube was annealed with a oxygen/propane flame torch, resulting in the elimination of the quartz EPR signal (Figure 3.1). The samples were then slid back to the original position. During this operation, the samples were kept in liquid nitrogen in order to maintain their temperature at 77 K.

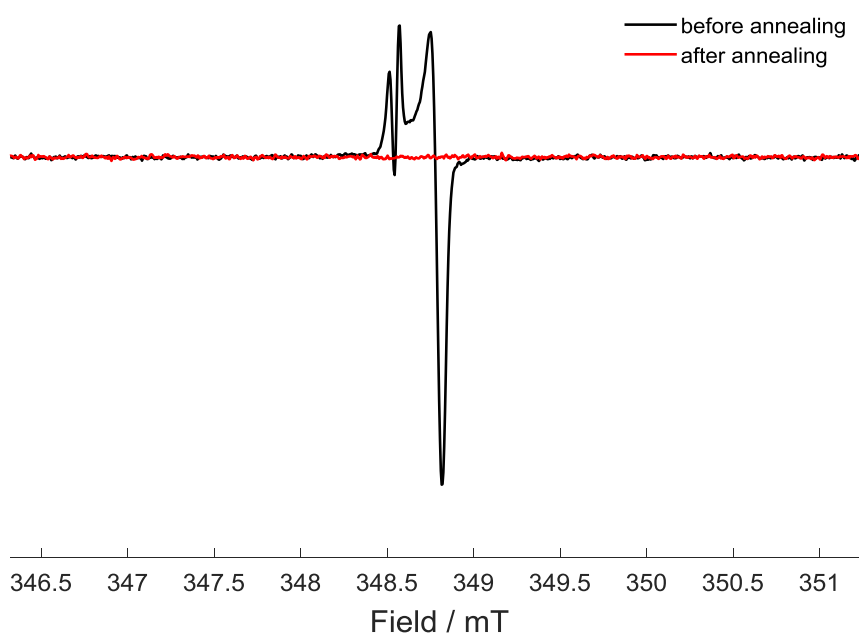


Figure 3.1 γ -irradiated quartz tube before (black) and after (red) annealing with a flame torch for *ca.* 30 seconds.

3.4 X-irradiation

X-irradiation was performed in normal atmosphere on a *Bruker D5005* Cu K α X-ray powder diffractometer. The radiation dose rate varied depending on the position of the anode X-ray tube in respect to the sample holder. During a standard X-ray diffraction experiment, both the X-ray source and the detector are rotating about a specific angle in respect to the sample, in order to obtain a diffraction pattern. In our experiment, the X-ray source was kept fixed in position for all the duration of the irradiation. When irradiating powder samples, the tube was positioned to make an angle of 60° with the plane of the sample holder, such as to irradiate as much surface of the sample holder as possible. Instead, when irradiating crystals, the position

of the X-ray tube was changed to an angle of 80° , thus concentrating the beam into the centre of the sample holder, where the crystal sample was positioned (Figure 3.2).

To quantify the irradiation dose rate for each of the two configurations, alanine pellets were X-irradiated for either 0.5, 1 and 2 hours. The EPR signal intensity, directly proportional to the irradiation dose received, was measured on a *Bruker Alanine Dosimeter Reader*. The dose rate in the powder configuration (60° to the plane of the sample holder) was found to be of 0.67(7) kGy/h, while the dose rate in the crystal configuration (80°) was 0.72(7) kGy/h.

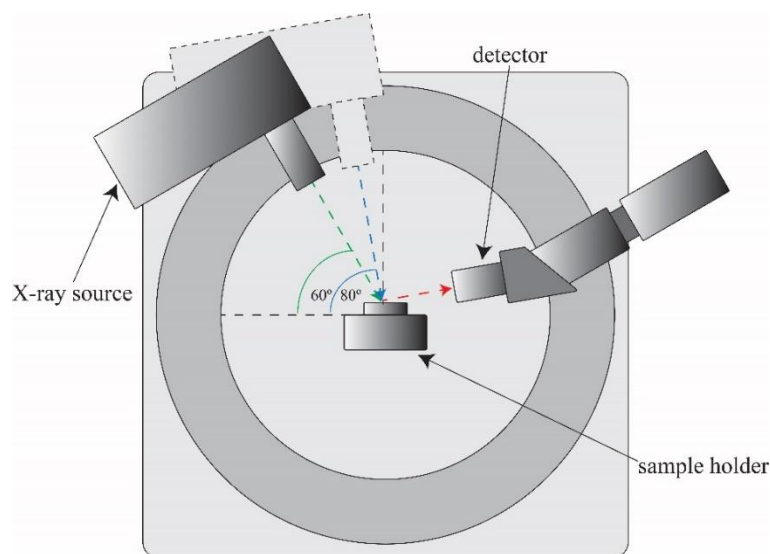


Figure 3.2 Schematic representation of the X-ray diffractometer, showing the rotation of the X-ray source in respect to the sample holder, depending on the type of sample to irradiate. For the irradiation procedure the position of the detector was not relevant.

3.5 Instrumentation

3.5.1 The EPR spectrometer

The main components of a continuous wave (CW)-EPR spectrometer are reported in Figure 3.3. An iron-core electromagnet provides a homogeneous magnetic field at the sample. A variable power supply unit (PSU) in the console controls the magnets and allows the magnetic field to be swept steadily and reproducibly through the magnetic field range of interest. As the magnetic field produced is not inherently linear to the current and affected by hysteresis, a temperature-stabilised Hall probe is mounted inside the magnet. The probe is calibrated against a known NMR signal and allows accurate control of the field by correcting the current generated through a feedback loop. A 2,2-diphenyl-1-picrylhydrazyl (DPPH) standard was used for

calibration of the g-factor. The microwave frequency was recorded on each spectrometer using an EIP-545A microwave frequency counter.

The microwave bridge contains both the microwave source, generally a Gunn diode, and the detector. The microwave source provides microwaves at a stable frequency and power. Specific microwave frequencies are classified into bands, as discussed previously. The microwave power can be controlled by an attenuator. After attenuation, the microwaves go through a circulator, a three port device that allows transmission of microwaves from one port to the next in rotation, thus directing the radiation to the resonator. The resonator is defined as “critically coupled” when the maximum power is transferred from the microwave source to the resonator. The EPR spectrometer detects the changes in amount of microwave radiation reflected back from the cavity. The reflected microwaves are directed to the detector diode through the circulator. Microwaves are also sent to the detector via a reference arm, which is used to bias the detector allowing it to operate in its linear regime. The current is therefore converted into a digital signal with an analogue-to-digital converter. Before digitalization of the signal, phase sensitive detection is employed to increase the sensitivity.

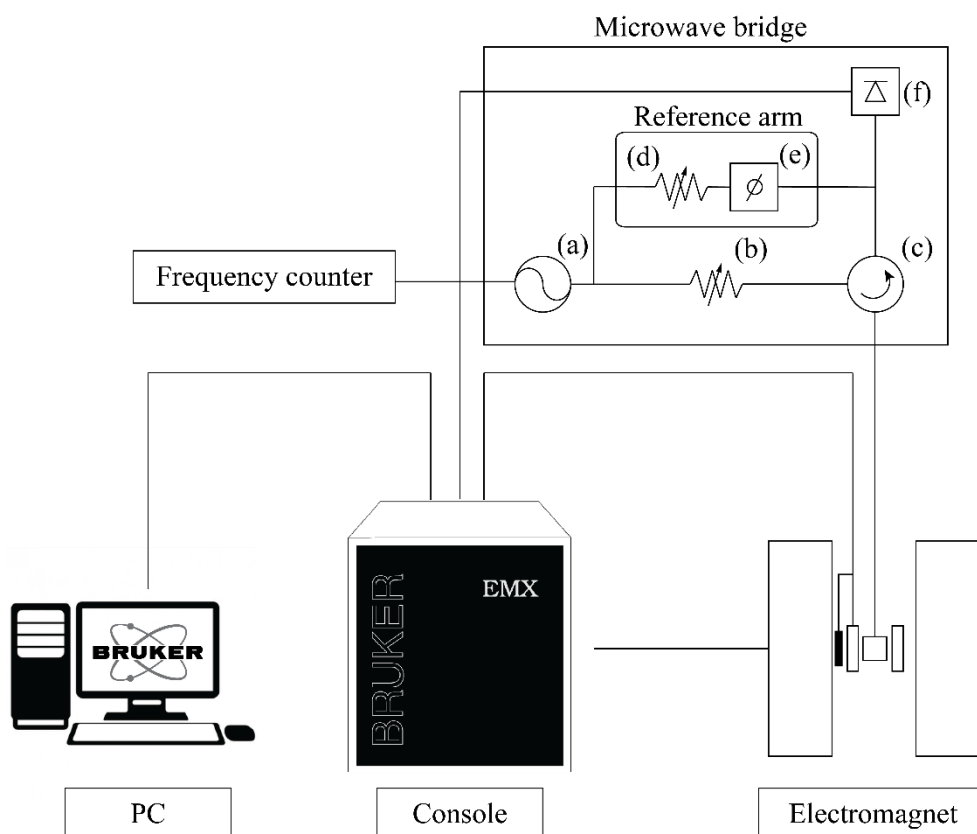


Figure 3.3 Diagram of the components of a typical EPR spectrometer. The components of the microwave bridge include (a) source, (b) high-power attenuator, (c) circulator, (d) bias attenuator, (e) phase shifter, (f) diode detector. Partially adapted from ref. 5.

The magnetic field is modulated at typically 100 kHz, causing modulation of the EPR signal. A lock-in amplifier allows demodulation of the signal to extract the component in phase with the field modulation. The signal amplitude at the modulation frequency is proportional to the slope of the EPR absorption signal, thus the detected signal is displayed as the first derivative of the absorption.

In order to increase the sensitivity of the EPR experiment, the sample is placed in the resonator. Resonators are components of the spectrometer that possess the ability to increase the signal by concentrating the microwave magnetic field at the sample while minimising the microwave electric field at this position. Several types of resonators are available, including cavity resonators, dielectric and loop gap resonators.

The cavity resonator is a metallic chamber of size comparable to the wavelength of the applied microwaves. Coupling to an X-band cavity is obtained by varying the effective size of a hole called the iris, which controls how much of the microwave power is allowed into the cavity and how much is reflected back. This is done by the iris by matching the impedances (*i.e.* the resistance to the waves) of the cavity and the waveguide. The effective size of the iris is varied by varying the position of an iris screw. When the impedances are matched, the cavity is critically coupled. When the sample absorbs microwave energy, the impedance of the cavity changes and the cavity is no longer critically coupled. Consequently, the microwaves are reflected back to the detector, resulting in an EPR signal.

3.5.1.1 W-band EPR

W-band experiments were performed on a *Bruker Elexsys E680* FT/CW EPR spectrometer operating at 94 GHz. The setup of the W-band EPR spectrometer includes a custom resonator characterised by a horizontal sample access and a *Bruker* 300 MHz NMR magnet. Powder samples were meticulously crushed in a mortar in order to facilitate the insertion into 0.9 mm o.d. Suprasil EPR sample tubes (Wilma-LabGlass WG-213ST9S-RB), which were then placed in the resonator for the r.t. analysis.

3.5.1.2 mm-wave EPR

Millimeter-wave experiments were performed on a *Bruker Elexsys E780* EPR spectrometer operating at 263 GHz. The system is equipped with a quasi-optical front end featuring reflection and induction detection. The standard probe head was used in non-resonant configuration, with the sample inserted in a standard X-band tube. The signal was detected in quadrature, providing the real/imaginary, dispersion/absorption signals in CW. The acquisition of the data in the

correct phase was found to be challenging, thus the phase was adjusted afterwards in MATLAB by manually minimising the imaginary signal.

3.5.2 Low temperature

Low temperature experiments were conducted on a *Bruker EMX CW* spectrometer operating at X-band (9.8 GHz) using a *Bruker VT 2000* variable temperature unit equipped with a heating element (Figure 3.4). To operate at cryogenic temperatures, nitrogen gas was flowed into a long copper tube arranged in coils which were inserted in a liquid nitrogen dewar and submerged in liquid nitrogen. The cooled nitrogen gas was passed over a long quartz transfer line containing a heating element, positioned below the resonator. The gas was directed into a quartz insert in the resonator, where the sample was placed. A second nitrogen line was connected to the back of the waveguide and r.t. nitrogen gas was flowed through the resonator to prevent condensation and keep temperature constant. The temperature was monitored by means of a thermocouple located below the resonator, feeding back to the temperature control unit. In order to analyse samples previously γ -irradiated in liquid nitrogen, the system was pre-cooled down to *ca.* 80 K.

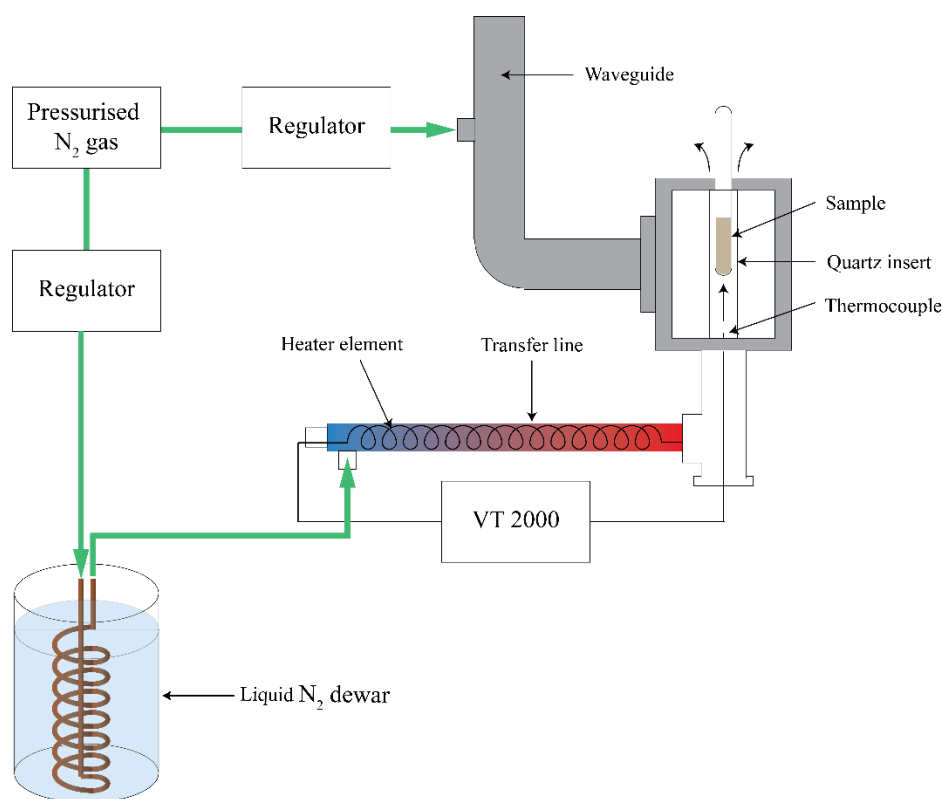


Figure 3.4 Schematic representation of the setup used for the low temperature EPR experiments, with key components labelled.

The samples were thereafter quickly transferred from the storage liquid nitrogen dewar into the cooled EPR cavity. Annealing of the samples in steps allowed monitoring of the evolution of the EPR spectra from (assumed) primary radical species into secondary, tertiary, quaternary species and so on. A uniaxial goniometer placed at the top of the cavity allowed the acquisition of roadmaps for the analysis of single crystals.

3.5.3 Spin trapping

All EPR spectra were recorded at room temperature (*ca.* 291 K) on a *Bruker EMX* CW spectrometer operating at X-band (9.8 GHz). Either a flat cylindrical cavity (ER 4103TM) operating in the TM_{110} mode, or a super high Q cylindrical cavity (ER 4122SHQE) operating in the TE_{011} mode was used. Both of these cavities are particularly suited for the analysis of so called lossy samples, *i.e.* exhibiting a high dielectric loss such as water containing samples.^{6,7} The interaction of the electric field of the microwaves with lossy samples causes the samples to be heated by the absorption of microwaves, reducing the Q of the cavity and the sensitivity of the spectrometer as a consequence. Cylindrical cavities are therefore designed in such a way to minimize the interaction between the sample and the microwave electric field, while maximizing the interaction with the magnetic field. The mode of the cavities is illustrated in Figure 3.5 and Figure 3.6.

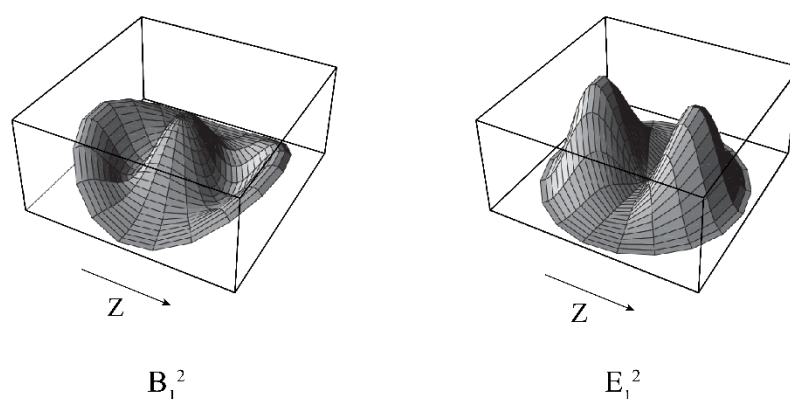


Figure 3.5 The field distribution in a TM_{110} cylindrical cavity (reproduced from ref. 8).

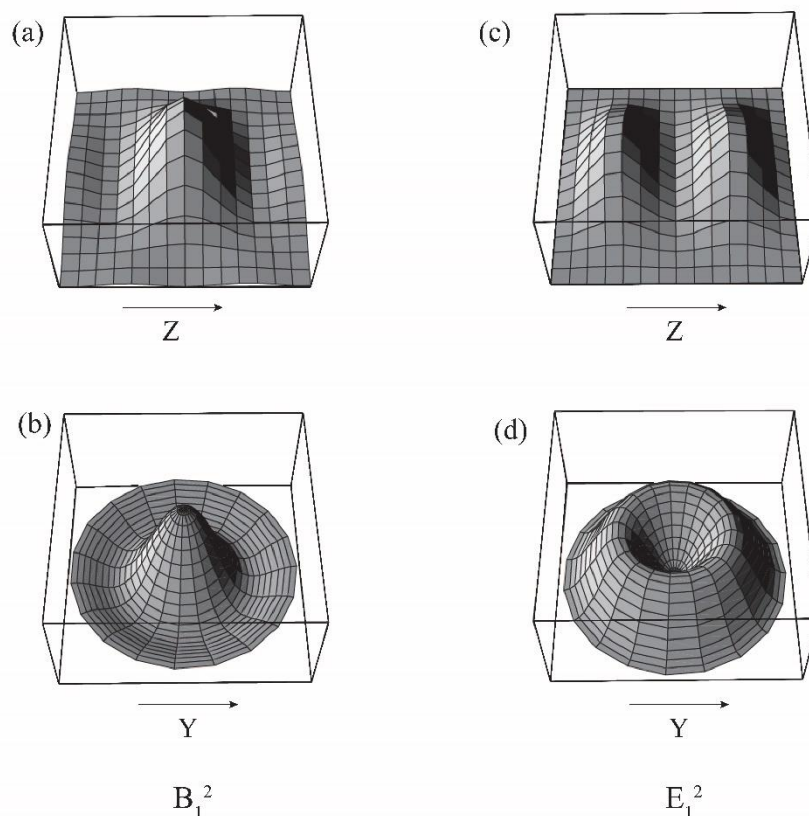


Figure 3.6 The field distribution in a TE_{011} cylindrical cavity. a) Side profile of magnetic field. b) Axial profile of magnetic field in the centre of cavity. c) Side profile of electric field. d) Axial profile of electric field in the centre of cavity (reproduced from ref. 8).

Typical EPR parameters were: time constant 5.12 ms; conversion time 10.24 ms; number of points 1024; sweep width 10 mT; microwave power 6.3 mW; microwave frequency 9.8 GHz; modulation amplitude 0.1 mT. To avoid distortion of the spectral lines, time constant was set to values lower than *ca.* 1/10 the time it takes to scan through the narrowest line of the spectrum.⁵ The data were acquired in incremental mode in order to obtain kinetic information concerning the radical species detected.

3.5.3.1 Phosphate buffer solution

The phosphate buffer (p.b.) 1 M concentrated solution was prepared mixing 72% of a solution of Na_2HPO_4 1 M with 28% of a solution of NaH_2PO_4 1 M. The pH of the resulting solution was measured with a pH meter and adjusted to pH 7.2 by adding either of the two solutions. The concentrated p.b. buffer was then diluted 1:20 in the sample solution.

3.5.3.2 Sample preparation

The spin trap solution of MNP was prepared solubilising the solid dimer in ACN at a concentration of either 0.8 M or 1.6 M and subsequently diluting 1:20 into the aqueous buffered solutions to give a final concentration of 40 or 80 mM.

The spin trap solution of DMPO was prepared in concentration of 0.2 M in water and then diluted 1:20 into the aqueous solutions to give a final concentration of 10 mM.

Samples were inserted into quartz EPR capillaries (Wilma-LabGlass 712-SQ-100M) using either a glass Pasteur pipette or a syringe with sterile stainless, chromium-nickel steel needle (Braun Sterican 4665643; 21G, 120mm).

Milli-Q water (18.2 M Ω ·cm) buffered at pH 7.2 with p.b. 50 mM was utilised for all the spin trapping experiments.

3.5.4 ENDOR

Electron Nuclear DOuble Resonance (ENDOR) is a technique that allows detection of the NMR intensities through simultaneous irradiation of the EPR lines, thus providing extremely valuable information towards the identification of the molecular structure of paramagnetic species.⁹

ENDOR spectra were recorded on a CW X-band *Bruker ESP 300E* spectrometer equipped with an ESP360 DICE ENDOR unit, operating at 100 kHz field modulation in an X-band *Bruker EN 801* ENDOR cavity. ENDOR spectra were recorded at 50 K and were obtained using 2 dB RF attenuation from an *ENI A-300 RF* amplifier, at 100 kHz RF modulation depth and 2 mW microwave power.

3.5.5 ¹H NMR

¹H NMR experiments were performed on a *Bruker Avance III* 600 MHz spectrometer at r.t. (ca. 298 K). Spectra were recorded with a standard ¹H NMR zg30 pulse program and acquired with 64 transients into 32 k data points with a spectral width of 20 ppm. Samples were prepared by dissolving either non-irradiated or irradiated powders in D₂O for a concentration of ca. 15 mg/ml. The solutions were centrifuged at 10K rpm to eliminate any undissolved particle. The samples were then transferred into 5 mm o.d. standard NMR tubes purchased from Wilma-LabGlass. Spectra were processed with an exponential line-broadening of 0.2 with *J* values quoted in Hz. The NMR spectra were internally calibrated to 1,4 dioxane (3.75 ppm in D₂O).

3.5.6 ESI-MS analysis

Electrospray ionization (ESI) mass spectrometry (MS) was performed on a *Shimadzu LC-MS 8030* triple quadrupole mass detector coupled to a *Shimadzu Nexera 2* UHPLC system. The samples were injected in the system in the absence of a separation column, and eluted into the MS system in 10% of acetonitrile in water, both containing 0.1% formic acid at a flow rate of 0.5 mL/min. Solutions of non-irradiated and γ -irradiated powder samples at different doses (25 and 250 kGy) were prepared at a concentration of 10 mM. Typically, 2 μ L of the sample was injected into the LC-MS system. Samples were run both in positive and negative mode in a mass range of 50–1000 m/z . The spectra of non-irradiated and irradiated samples were then compared in order to determine the presence of new signals ascribable to degradation products generated from the irradiation process.

3.5.7 XRF

X-ray fluorescence (XRF) analysis was conducted using an Energy Dispersive (ED)-XRF system (*NEX CG, Rigaku, Japan*) operating an X-ray tube with Pd anode at 50 kV with a 1 mA current and utilising an Cu secondary target ($K\alpha = 8.046$). All spectra were measured under moderate vacuum (12 Pa) for a sampling time of 150 s, and background subtracted. The interrogation area of the X-Ray source on the sample is elliptical and ca. 1.2 cm in diameter, thus in order to make the measurements, 3 of the 12 cm needles were cut into smaller (1.2 cm) segments and placed into the centre of a sample holder to ensure they came into contact with the X-ray beam.

3.6 Quantitative EPR

In the absence of microwave power saturation, the EPR signal intensity is proportional to the number of spins in the system, which is in turn proportional to the radical concentration of the sample under study. Although absolute quantification of the EPR signal through a calibrated spectrometer is possible,¹⁰ it is however challenging and difficult to pursue. Thus, in most cases quantification of the spectrum of an unknown paramagnetic sample is achieved by comparison with the spectrum of a sample of known spin concentration.⁵ To determine the unknown spin concentration of a sample (s) from a known reference (Ref), the conditions under which the spectra were acquired must be taken into account:

$$\frac{[S]}{[Ref]} = \frac{I_s}{I_{Ref}} \frac{g_{Ref}^2}{g_s^2} \frac{\eta_{Ref}}{\eta_s} \frac{Q_{Ref}}{Q_s} \frac{T_{Ref}}{T_s} \frac{S_{Ref}(S_{Ref} + 1)}{S_s(S_s + 1)} \frac{B_{m,Ref}}{B_{m,s}} \frac{P_{Ref}^{1/2}}{P_s^{1/2}} \frac{G_{Ref}}{G_s} \frac{t_{Ref}}{t_s} \frac{N_{Ref}}{N_s}$$

Where:

- I : the double integrated intensity of the EPR spectrum;
- g : the g -value of the paramagnetic species;
- η : the filling factor;
- Q : the loaded quality factor of the resonator;
- T : the temperature;
- S : the spin of the system;
- B_m : the modulation amplitude;
- P : the microwave power (where $\sqrt{P} \propto B_1$, assuming no microwave power saturation);
- G : the receiver gain;
- t : the conversion time;
- N : the number of scans.

As previously discussed, the Q of the resonator is an important parameter to consider, as the EPR signal intensity is proportional to Q . When a lossy sample is inserted in an EPR cavity, part of the microwave power is not stored in the cavity but dissipated, hence decreasing the value of Q . Since the Q value provided by Bruker WinEPR spectrometer software is not always very accurate, in this work references were selected in such a way to possess a Q comparable to the one of the samples under analysis.

3.6.1.1 Quantification of persistent radicals in the solid state

For the quantification of the persistent radicals formed in the powders upon γ -irradiation, solutions of the free radical 2,2,6,6-tetramethyl-piperidine-1-oxyl (TEMPO) in toluene were used. TEMPO's main EPR spectral feature is a triplet, which is due to the coupling with the nitroxide nitrogen (^{14}N , $I = 1$). Toluene was selected for being a non-lossy solvent, and as such the Q of the resonator remained approximately unvaried when measuring solid samples and references. Solutions of TEMPO in toluene were prepared in concentrations of 0.01, 0.1, 1, 10 and 50 mM. Both samples and references were inserted into 4 mm o.d. tubes (Wilmad-LabGlass 707-SQ-250M) and placed in the EPR cavity. In order to account for the same η , the tubes of both samples and references were filled and positioned in the spectrometer in such a way to cross the entire length of the cavity. The EPR spectrum of each samples was recorded. The

spectra were baseline corrected and double integration was performed. The resulting calibration curve is shown in Figure 3.7.

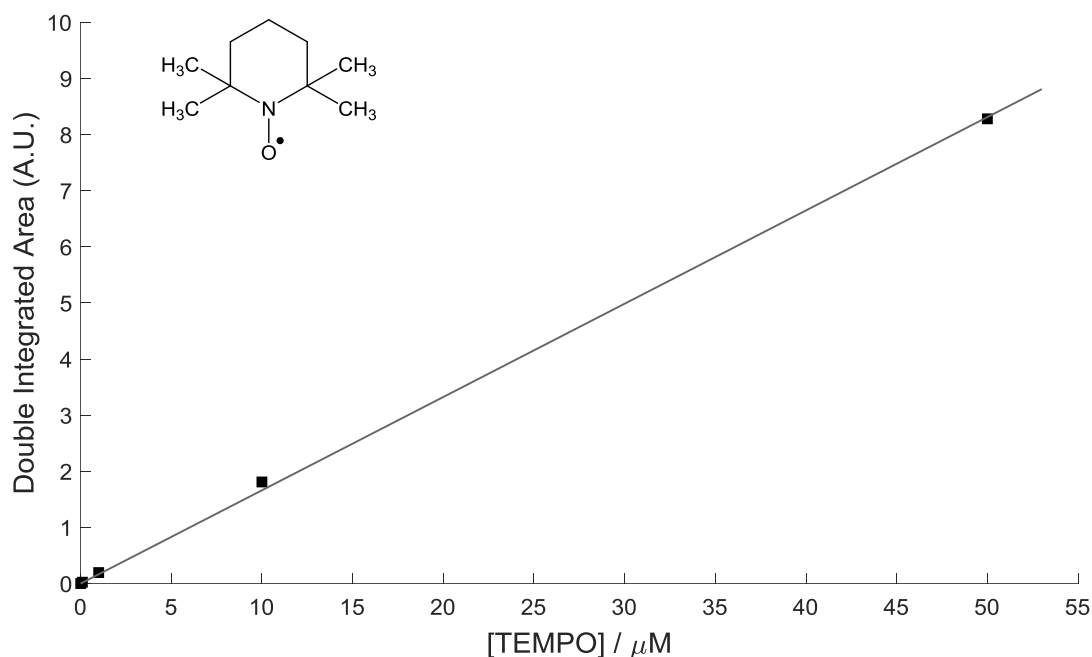


Figure 3.7 Calibration curve for the double integrated intensity of TEMPO in toluene at r.t. Inset: molecular structure of TEMPO.

3.6.1.2 Quantification of spin adducts

In this work, aqueous solutions containing the free radical 4-hydroxyl-2,2,6,6-tetramethylpiperidine-1-oxyl (TEMPOL) were used to quantify the formed spin adducts, as previously reported.¹¹ The choice of TEMPOL over TEMPO for quantifying spin adducts in aqueous solutions is due to the poor solubility of the latter in water. TEMPOL's main EPR spectral feature is a triplet, which is due to the coupling with the nitroxide nitrogen (^{14}N , $I = 1$).

For quantitative measurements, it is crucial that the standard sample is analysed in experimental conditions as close as possible to the system under study.⁵ Thus, the same experimental conditions were replicated including solvent, temperature, sample tubes, and tube position in the EPR cavity.

TEMPOL solutions in either i) water, ii) p.b. or iii) 20% of ethanol in p.b. were prepared in concentrations of 0.1, 0.5, 1, 5, 12.5, 25, 50, 75, 100, 200 and 300 μM . The EPR spectrum of each solution was recorded. The spectra were baseline corrected and simulated with EasySpin.¹²

Double integration was then performed on the simulated spectra. The resulting calibration curve is shown in Figure 3.8.

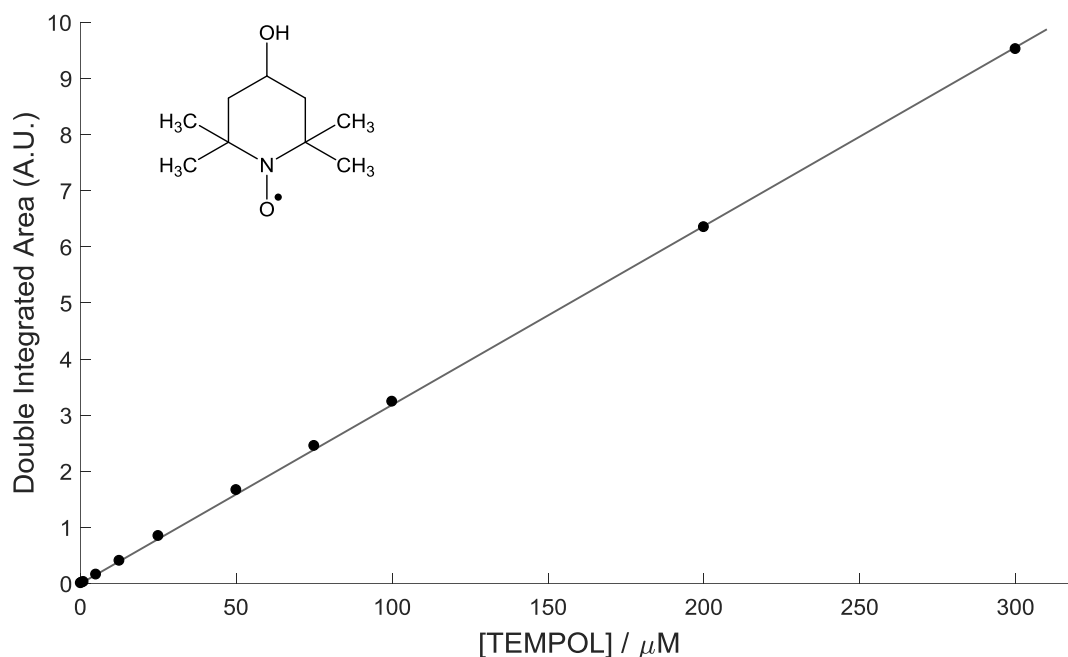


Figure 3.8 Calibration curve for the double integrated intensity of TEMPOL in p.b. 50 mM at pH 7.2 at r.t. Inset: molecular structure of TEMPOL.

3.7 EPR simulations

Simulations of the experimentally acquired EPR spectra were performed for identifying and quantifying the detected paramagnetic species.

The analysis of the extracted spectral parameters allows the characterisation of a paramagnetic species and, where possible, its identification by comparison with previously published parameters for the said species.

In order to quantify the signal of an EPR active species it is necessary to perform a double integration of the spectrum and compare it with a known standard. Quantification of EPR spectra by direct double integration of the data can be challenging and requires some precautions. For instance, if the S/N ratio is relatively low, the double integrated spectrum will include the signal deriving from the noise, therefore distorting the quantification. Additionally, direct double integration of the spectrum will not allow separation of the contributions of multiple species present in the spectrum or of a background signal. In order to overcome these limitations, in this work the paramagnetic species of interest were simulated and double

integrated. All the simulations of the EPR spectra were performed with the MATLAB package EasySpin.¹² EasySpin enables the simulation of EPR spectra by defining the spin Hamiltonian parameters of the system under study. The least-squares fitting technique can be then used to fit the line shape on the EPR spectrum from the starting parameters. Additional details regarding the EPR simulations performed are reported in the specific chapters.

3.8 References

1. Kertesz, A. Z. I. & Parsons, G. F. Ozone Formation in Air Exposed to Cobalt-60 Gamma Radiation. *Science* (80-.). **142**, 1289–1290 (1963).
2. Bochirol, L., Doulat, J. & Weil, L. C. A Cryogenic Device for Irradiation in Liquid Nitrogen. *Cryogenics (Guildf)*. **1**, 44–46 (1960).
3. Eaton, G. R. *et al.* A signal-to-noise standard for pulsed EPR. *J. Magn. Reson.* **205**, 109–113 (2010).
4. Montanari, L. *et al.* Gamma irradiation effects on stability of poly(lactide-co-glycolide) microspheres containing clonazepam. *J. Control. Release* **75**, 317–330 (2001).
5. Eaton, G. R., Eaton, S. S., Barr, D. P. & Weber, R. T. *Quantitative EPR*. (Springer Science & Business Media, 2010).
6. Eaton, S. & Eaton, G. Signal area measurements in EPR. *Bull. Magn. Reson* **1**, 130–138 (1980).
7. Dalal, D. P., Eaton, S. S. & Eaton, G. R. The effects of lossy solvents on quantitative EPR studies. *J. Magn. Reson.* **44**, 415–428 (1981).
8. Weber, R. T. EPR resonators. *Bruker Biospin User Serv. Train. Course* 1–26 (2009).
9. Murphy, D. M. & Farley, R. D. Principles and applications of ENDOR spectroscopy for structure determination in solution and disordered matrices. *Chem. Soc. Rev.* **35**, 249–268 (2006).
10. Yordanov, N. D. Quantitative EPR spectrometry - ‘State of the art’. *Appl. Magn. Reson.* **6**, 241–257 (1994).
11. Barr, D., Jiang, J. & Weber, R. T. How to quantitate nitroxide spin adduct using TEMPOL. *Bruker Biospin Tech. Note* (1996).

12. Stoll, S. & Schweiger, A. EasySpin, a comprehensive software package for spectral simulation and analysis in EPR. *J. Magn. Reson.* **178**, 42–55 (2006).

Chapter 4

Irradiation of L-histidine Free Base

The following publication is based on the present Chapter:

Vallotto, C., Williams, H.E., Murphy, D.M., Ayres, Z.J., Edge, R., Newton, M.E. & Wedge, C.J. An Electron Paramagnetic Resonance (EPR) spectroscopy study on the γ -irradiation sterilization of the pharmaceutical excipient L-histidine: regeneration of the radicals in solution. *Int. J. Pharm.* **533**, 315-319 (2017).

This Chapter investigates the effects of γ -radiation sterilization on the parenteral excipient L-histidine free base. The irradiation process induces the formation of a deamination radical which is persistent in the solid state. The reactivity of the radical species in solution was evaluated with spin trapping experiments. The radicals were found to regenerate in solution in the presence of trace metals through a Fenton-type reaction.

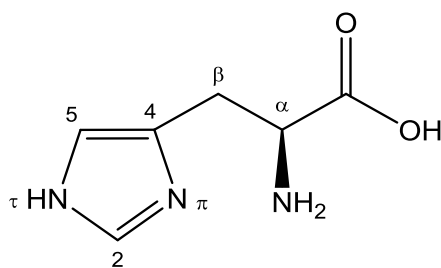


Figure 4.1 Chemical structure of L-histidine.

4.1 Introduction

4.1.1 Use of L-histidine in parenteral formulations

The amino acid L-histidine (L-his) is an excipient typically used in parenteral formulations as a buffering agent and a stabilizer for subcutaneous, intramuscular and peritoneal injections.^{1,2} In protein formulations, antibodies in particular, it is preferred over other buffers such as citrate

buffer, which can cause a painful reaction when injected subcutaneously and sodium succinate, which lacks a good buffer capacity at low strength, hence requiring the other excipients of the formulation to be decreased in order to maintain the osmolarity in a desired range (1 mM histidine = 1 mOsm; 1 mM sodium succinate = 3 mOsm).¹ Additionally, histidine has been shown to provide stabilizing non-covalent interactions with antibodies in the solid state, reducing the alterations of the antibodies' secondary structure upon freeze-drying.³

4.1.2 Scavenging properties of histidine

Histidine has also shown antioxidant properties, being a scavenger of the hydroxyl radical ($\cdot\text{OH}$) and singlet oxygen ($^1\text{O}_2$).^{4,5} The scavenging characteristics of histidine towards hydroxyl radical were found to rely on its ability to interfere with metal ions involved in redox reactions and responsible for the production of this highly reactive oxygen species (ROS). Studies involving *L*-his effects on lipid peroxidation reported the ability of the amino acid to coordinate with iron, suggesting this to be the reason for its physiologic antioxidant effects.^{6,7} Histidine is also generally recognized as the most active singlet oxygen scavengers amongst the amino acids,⁸ through a mechanism that involves direct interaction of the imidazole ring with singlet oxygen.⁴

Histidine residues have also been found to participate in the radical mediated degradation of proteins. In fact, protein bound histidine residues have been shown to mediate free radical cleavage of the peptide bond backbone in monoclonal antibodies.⁹

4.1.3 Solid state radicals

It has previously been shown that irradiation of *L*-his induces the formation of stable radical species in the solid state.^{10–12} X-irradiated single crystals of *L*-his free base had been investigated by EPR spectroscopy in the range of 77–300 K.¹² Nitrogen temperature irradiation was found to induce the formation of a carboxyl anion by addition of a proton to the carboxylic carbon. By annealing to room temperature (r.t.), the anion radical was then fully converted into the deamination radical, as typically occurs for many amino acids.^{13–17} The counter ion of the histidine salt was found to have a clear influence on the formation of the radical species, as the main radical at r.t. for irradiated histidine hydrochloride samples was proved to be the result of H addition at carbon C2 (see Figure 4.1) of the imidazole ring.^{10,11}

4.1.4 Spin trapped *L*-histidine radicals

Studies involving the spin trapping of radicals formed in the solid state have been previously reported for several organic compounds, including amino acids.^{18–21} Previous studies report γ -radiolysis experiments on solutions of *L*-his, where the amino acid was dissolved in a solution

of MNP and subsequently irradiated. EPR analysis of the irradiated solution showed that the deaminated L-his radical was trapped with MNP.²²

4.2 Experimental

Below are the experimental sample preparation and instrumentation set up specific to this Chapter. More details regarding instrumentation and the irradiation setup are described in **Chapter 3**.

4.2.1 Instrumentation

All EPR spectra were recorded on a X-band *Bruker EMX CW* EPR spectrometer at ambient temperature (*ca.* 295 K) unless otherwise stated. X-ray fluorescence (XRF) analysis was performed on a *Rigaku NEX CG Energy Dispersive(ED)-XRF*, using a Cu secondary target.

More specific details regarding the EPR acquisition and spin quantification are described in **Chapter 3**.

4.2.2 Sample preparation

4.2.2.1 Growth and analysis of L-histidine single crystals

Single crystals of L-his free base were grown from a saturated aqueous solution by slow evaporation at room temperature, as described in **Chapter 3**. Their structure was determined by single crystal X-ray diffraction on a *Rigaku Oxford Diffraction Gemini R* and was found to be orthorhombic with space group $P2_12_12_1$ ($a = 5.1480(3)$ Å, $b = 7.2330(4)$ Å, $c = 18.8122(11)$ Å), in agreement with previously published structures (Figure 4.2).^{12,23}

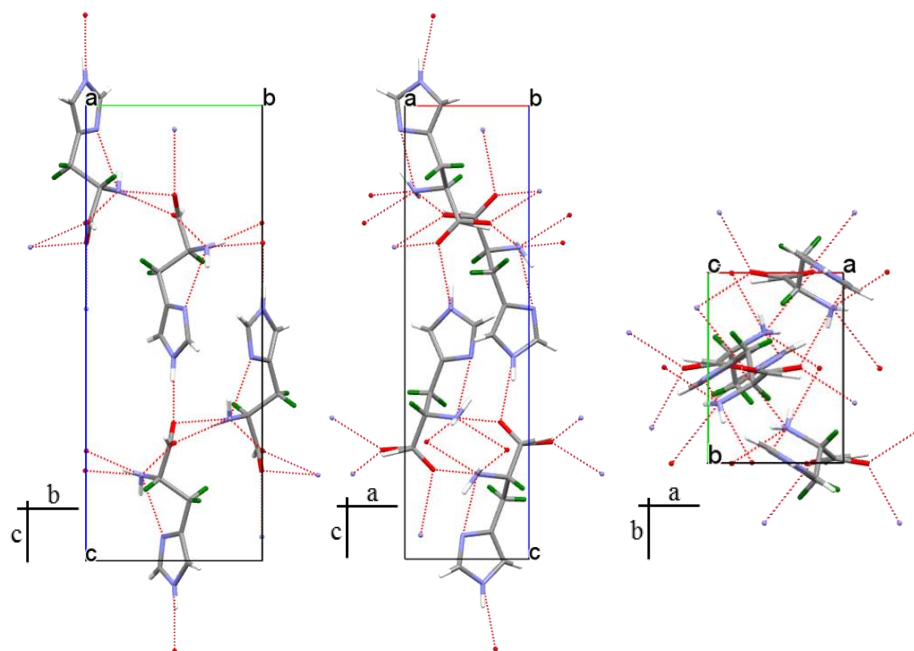


Figure 4.2 Crystallographic structure of the single crystal of *L*-his viewed along *a*, *b* and *c* crystallographic axes.

4.2.2.2 Spin trapping experiments

Spin trapping experiments were performed dissolving γ -irradiated powders either in i) an aqueous solution of the spin trapping agent; ii) water, adding the spin trap later (after 3 mins unless otherwise stated); iii) an aqueous solution of EDTA 1 mM, adding the spin trap after 3 mins. In order to obtain the maximum concentration of *L*-his in solution in the case of i), an excess of powder was added to a solution of MNP. The solution was then vortexed for 1 min, the supernatant was separated from the undissolved powder by centrifugation and analysed. The concentration of *L*-his in solution was therefore considered to be close to saturation (≈ 0.27 M).²⁴ When testing the regeneration of the radical in ii) and iii), the excess of powder was added to a solution lacking the spin trapping agent, and the supernatant was separated from the undissolved powder before the addition of the 0.8 M stock solution of MNP, diluted 1:20 into the aqueous buffered solution.

More specific details regarding EPR acquisition and spin adduct quantification are described in **Chapter 3**.

4.2.3 EPR Simulations

EPR spectral simulations were performed in Matlab using the EasySpin package.²⁵ The routine *pepper* was used for the solid state simulation, while the *garlic* routine (appropriate for the fast-motional regime) was used for all the solution experiments.

Simulation of the MNP-histidine spin adduct was performed considering axial hyperfine couplings and g-tensor, using the minimum number of parameters necessary to allow dynamic effects to be included in the simulation. The phenomenological lineshape used contained Lorentzian (0.029 mT) and Gaussian (0.017 mT) components and dynamics were considered in the fast motional regime, $\tau_c \approx 5.4$ ns; the said parameters were optimized from fitting.

EPR parameters of the MNP di-adduct di-*tert*-butyl nitroxide (DTBN) were obtained by fitting a spectrum acquired from a solution of MNP which had been illuminated overnight with a 465 nm LED (7.1 mW cm⁻²), in order to promote the formation of DTBN. Hyperfine couplings arising from both the nitroxidic nitrogen and statistical abundance of nearest neighbour ¹³C nuclei were included and considered to be fully isotropic. An isotropic g-tensor was used; dynamic effects were found not to affect the spectrum and were therefore neglected.

4.3 Results

4.3.1 Non-irradiated L-histidine powder control

Photodegradation and oxidation can induce the formation of EPR active radical species in pharmaceuticals products.^{26,27} To investigate the presence of background EPR signal in the purchased high purity ($\geq 99\%$) L-his free base powder, a spectrum of the non-irradiated powder was acquired at r.t. No EPR signal was detected, indicating the absence of persistent radical degradation products above the detection limit (\sim nM concentration).

4.3.2 γ -irradiated L-histidine powder EPR spectra

Next, the effects of r.t. γ -irradiation on L-his powder were evaluated. The irradiation of the powder was performed as described in **Chapter 3**.

The EPR analysis of the irradiated powder samples revealed the formation of persistent radical species, as shown in Figure 4.3. The EPR spectrum consisted of multiple overlapping lines, whose hyperfine couplings were suggestive of the presence of carbon-centred radical species. However, the complexity of the EPR spectrum did not allow a direct identification of the radicals formed upon irradiation.

Figure 4.3 also shows that the same radical species are observed irrespective of the radiation dose employed. Quantification of the EPR spectra was performed as described in **Chapter 3** and indicated a radical concentration of 2.46(2), 10.00(2) and 13.72(1) mM respectively for the samples receiving a total dose of 25, 125 and 250 kGy ($\pm 5\%$). This non-linear correlation between the radical concentration and the radiation dose was previously reported for other excipients²⁸ and suggests that above certain irradiation doses other processes are involved, limiting the radical formation.

The saturation behaviour of the powder sample was also investigated by varying the operating microwave power in the range 0.006–200 mW (Figure 4.4). As the microwave power was increased, the spectral features started to saturate at different rates, which is suggestive of the presence of more than one radical species.

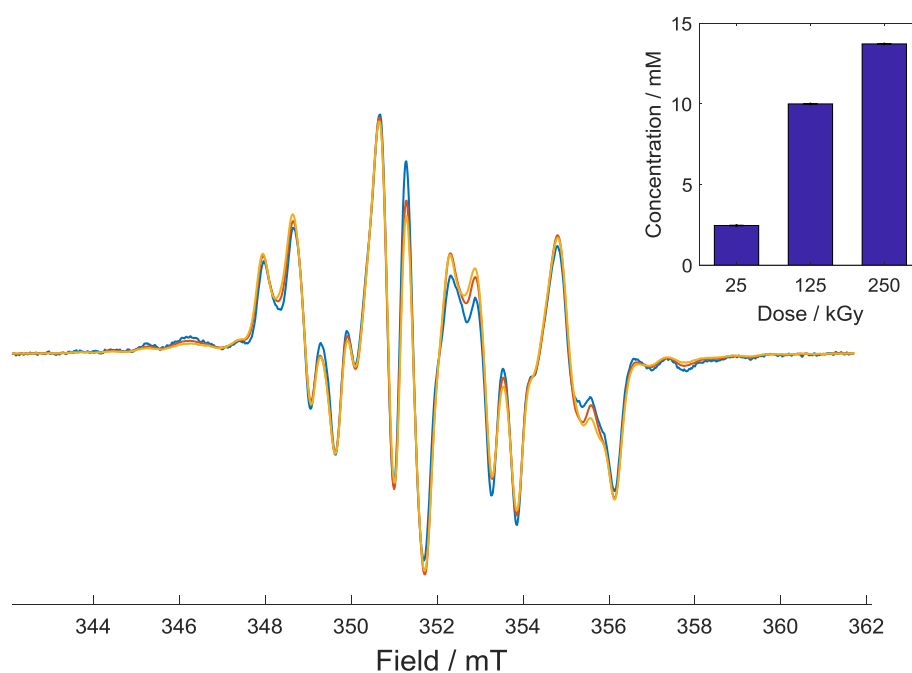


Figure 4.3 Radiation dose dependence of r.t. γ -irradiated L-his powder. Total irradiation dose of 25 kGy (blue), 125 kGy (red) and 250 kGy (yellow). CW EPR spectra were normalised to the intensity of the most intense peak to show that the same radical species are formed. Inset: concentration of radical species detected for each irradiated sample.

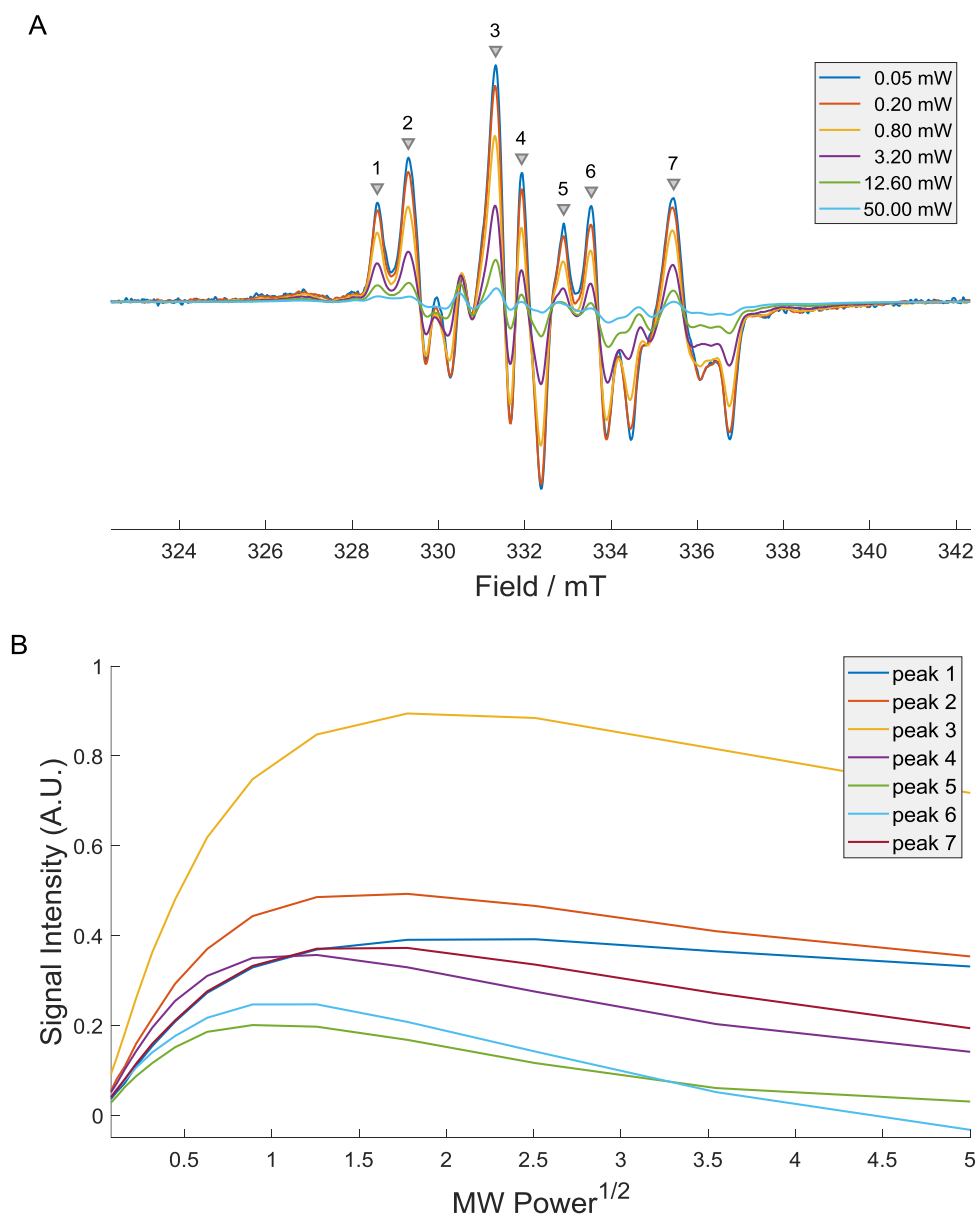


Figure 4.4 (A) CW EPR microwave power saturation spectra of r.t. γ -irradiated L-his powder. Each spectrum was scaled by the square root of the microwave power such that in a non-saturating regime the intensity of each spectrum would be equal. (B) EPR power saturation curves for the main peaks of the γ -irradiated L-his powder spectrum.

4.3.3 X-ray vs γ -ray irradiation

To investigate the influence of the radiation source on the radical formation, a sample of L-his powder was X-irradiated and compared to the γ -irradiated samples. Verifying that the same radical species can be formed from an X-ray source is of particular interest considering that X-ray irradiation facilities are generally more commonly available than γ -irradiation sources,

the latter being subjected to more safety restrictions. Any X-ray diffractometer for the analysis of powder and polycrystalline materials with a sufficient radiation dose rate can be conveniently utilized for a quick irradiation experiment. Figure 4.5 shows that very little difference can be observed between γ - and X-irradiated powder samples, which could be ascribed to a slightly different relative concentration of the multiple radical species formed upon irradiation in each sample.

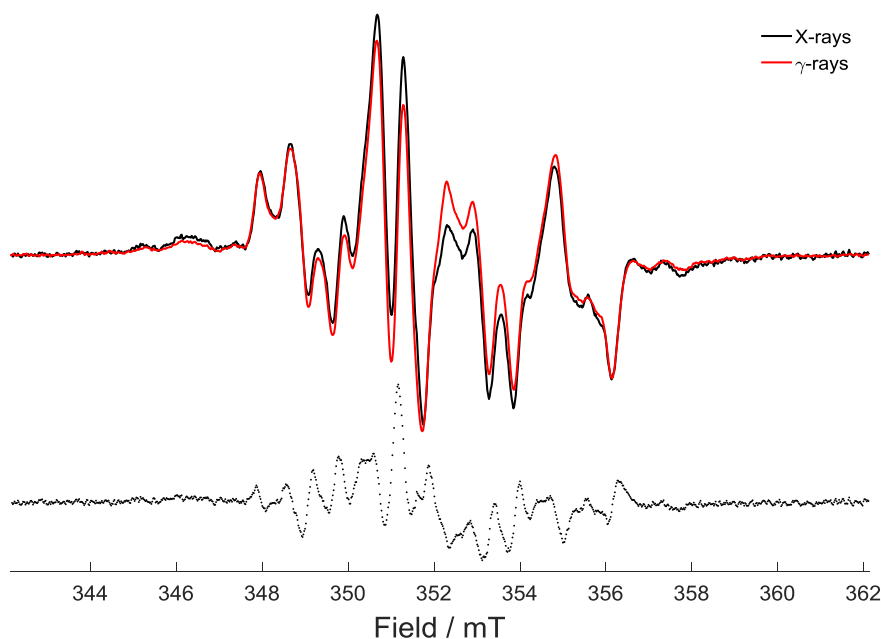


Figure 4.5 Effect of the radiation source on the EPR spectrum. *L*-his powder was irradiated at r.t. using X-rays (black) and γ -rays (red); the difference between the spectra is shown below (black dotted). Irradiation dose 10 kGy (X-rays), 25 kGy (γ -rays). The spectra were acquired in the same conditions and manually scaled to overlap.

4.3.4 Single crystal analysis

In order to identify the radical species produced upon irradiation, single crystal analysis was considered. The analysis of a single crystal over a powder sample is generally eased by the fact that a single orientation is selected so that, when dealing with anisotropic hyperfine couplings or *g*-tensors, the multiple resonance lines which are due to anisotropy are not present altogether in the spectrum as for a powder spectrum. Therefore, by orienting the crystal towards one of the main crystallographic axes, the resulting EPR spectrum is generally much simpler and easier to interpret.

Figure 4.6 shows the EPR spectrum of an X-irradiated *L*-his single crystal oriented along the *c* axis. The main features of the spectrum are eight lines which can be readily attributed to the

couplings with an α -proton and two inequivalent β -protons. This is consistent with the main radical species being the product of deamination (Figure 4.7), as previously reported.¹² Additional lines can also be observed in the spectrum suggesting the presence of a second, as yet unidentified, radical species, as also suggested by the microwave power saturation spectrum of the powder. Whilst these features are similar in appearance to the satellite lines known to arise from ^{13}C ($I = 1/2$), their intensity is inconsistent with the natural abundance of this isotope. The spectrum of the irradiated crystal was simulated with EasySpin²⁵ (Figure 4.6). However, an acceptable simulation of the irradiated powder was not obtained due to presence of other radical species.

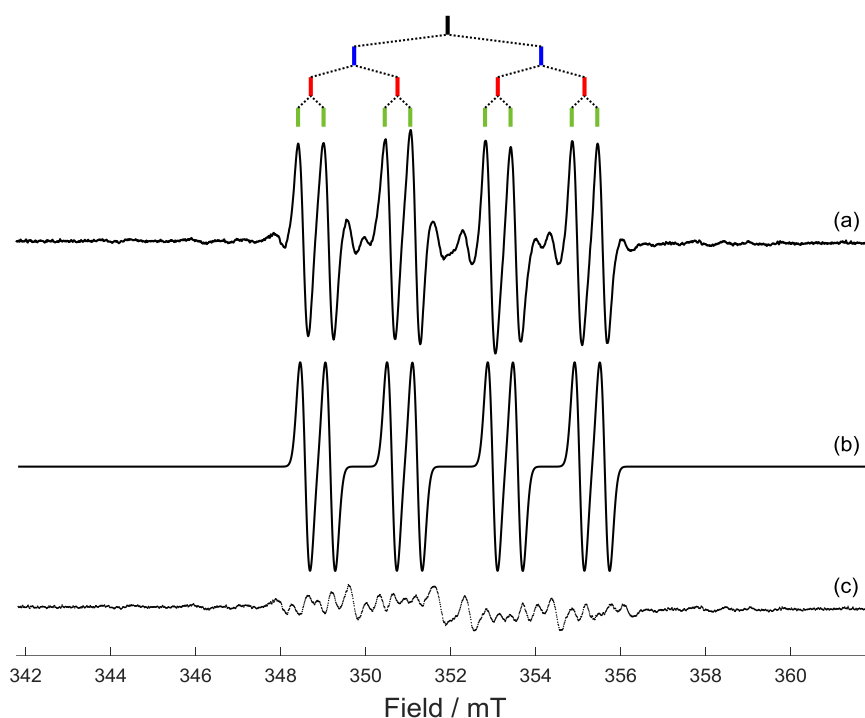


Figure 4.6 (a) X-band EPR spectrum of *L*-his single crystal with magnetic field parallel to the *c* axis after X-irradiation at r.t. with line diagram of the deaminated radical species; (b) EasySpin²⁵ simulation (Table 4.1); (c) difference between (a) and (b).

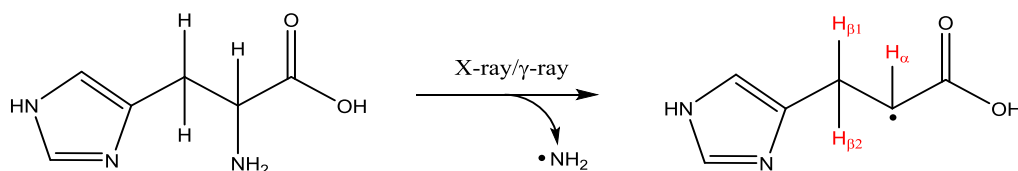


Figure 4.7 Radiolytic deamination of *L*-his.

To verify that the radical species formed upon irradiation are the same for the crystal and the powder, a single crystal of *L*-his was X-irradiated and subsequently crushed. An EPR spectrum of the crushed crystal was then acquired (Figure 4.8). The comparison between the spectrum of the crushed crystal and the one of the irradiated powder confirmed that in both cases the deamination radical was the main species produced, although minor differences between the spectra can be observed, which can be attributed to the formation of other species from the crushing or to the different irradiation dose. The complexity of the powder spectra did not allow separation of the contribution of this additional species from the main radical.

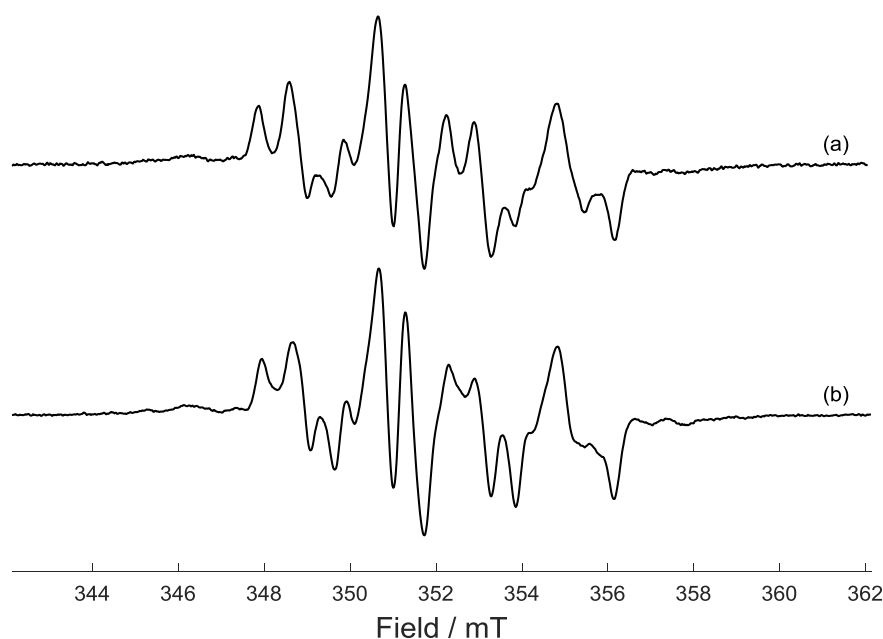


Figure 4.8 (a) EPR spectrum from crushed X-irradiated (13 kGy) *L*-his single crystal and (b) *L*-his γ -irradiated (25 kGy) directly in powder form. Spectra were scaled to the same intensity.

4.3.5 Single crystal roadmaps

In the presence of anisotropic spin-Hamiltonian tensors, the EPR spectrum of a single crystal will depend on the orientation of the crystal in the magnetic field B_0 . Roadmaps are spectra where the magnetic field is plotted in the x -axis against the angle between B_0 and a reference direction, plotted in the y -axis. If the Hamiltonian parameters of the said species are known, any possible orientation of the crystal in the magnetic field can be simulated. Understanding the symmetry of an unknown paramagnetic species can provide useful information for the identification of the same.

Roadmaps for the γ -irradiated single crystal of L-his rotating about the three main crystallographic directions are shown in Figure 4.9, Figure 4.10 and Figure 4.11. The spectra were fitted using the parameters previously published by Westhof.¹² The g-tensors were not reported in literature and have therefore been obtained by fitting the powder spectra, using as g-frame the frame given for the α -proton (see Table 4.1). The resulting simulation is in reasonably good agreement with the experimental data.

Table 4.1 Hyperfine parameters (mT) reported from Ref 12 and g-values determined experimentally for the deaminated L-his radical.

	Principal values	Direction cosines		
		a	b	c
a_{α}^H	-0.85	0.7675	0.2889	0.5723
	-1.86	-0.3941	0.9167	0.0657
	-3.02	-0.5056	-0.2760	0.8174
$a_{\beta 1}^H$	0.91	0.9463	0.2048	0.2383
	0.52	-0.3138	0.6569	0.6856
	0.65	-0.3138	-0.7256	0.6879
$a_{\beta 2}^H$	4.14	0.8936	-0.4457	-0.0534
	4.37	0.3693	0.7975	-0.4772
	3.95	0.2553	0.4067	0.8772
g-value	2.0049(2) ^a	0.7675	0.2889	0.5723
	2.0031(2) ^a	-0.3941	0.9167	0.0657
	2.0042(2) ^a	-0.5056	-0.2760	0.8174

^a determined by comparison with a DPPH standard

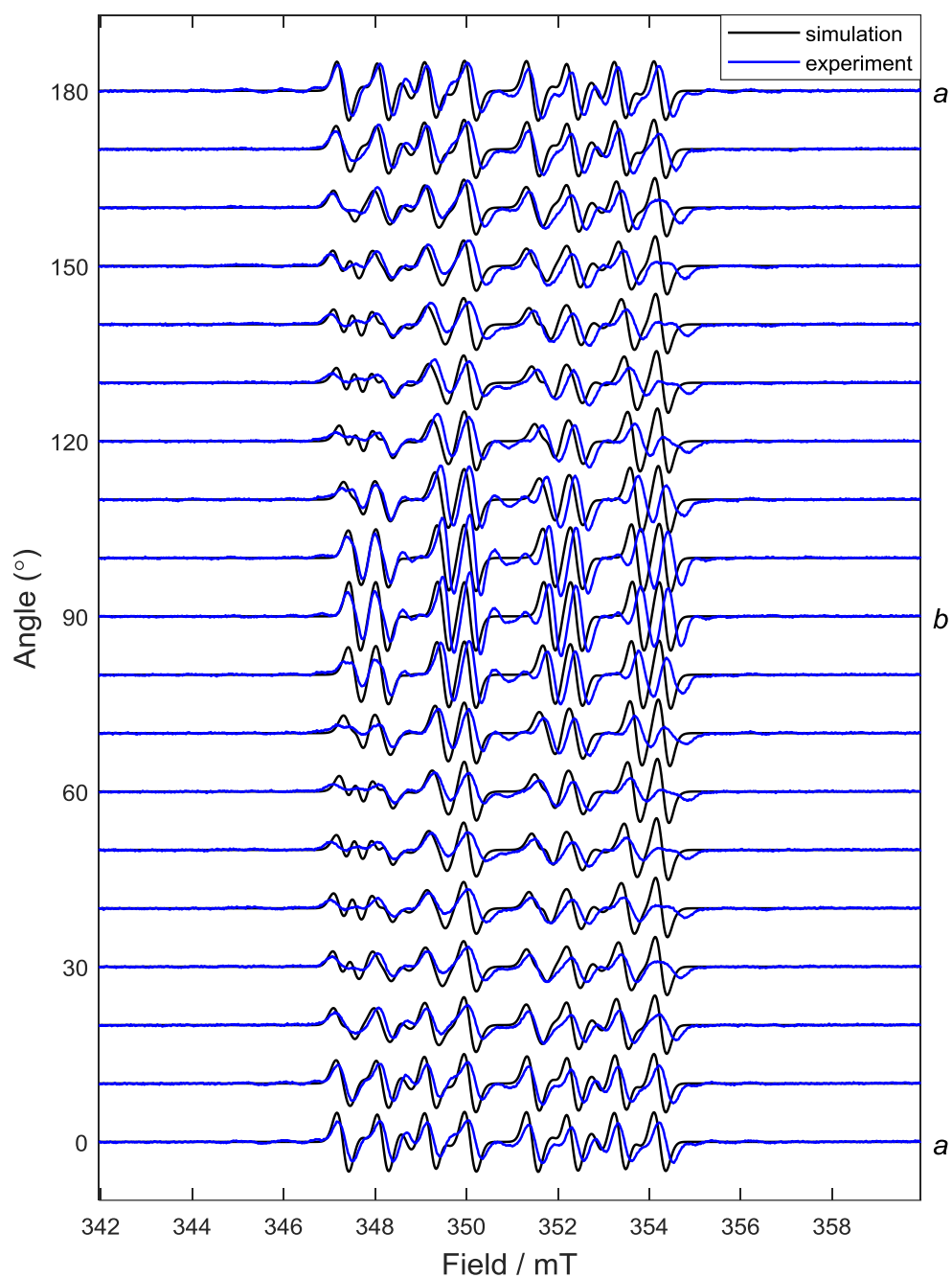


Figure 4.9 Roadmap spectra of the r.t. γ -irradiated single crystal of *L*-his with the crystallographic *c* axis perpendicular to B_0 and rotating in the *ab* plane. Each spectrum was shifted by its MW frequency of acquisition.

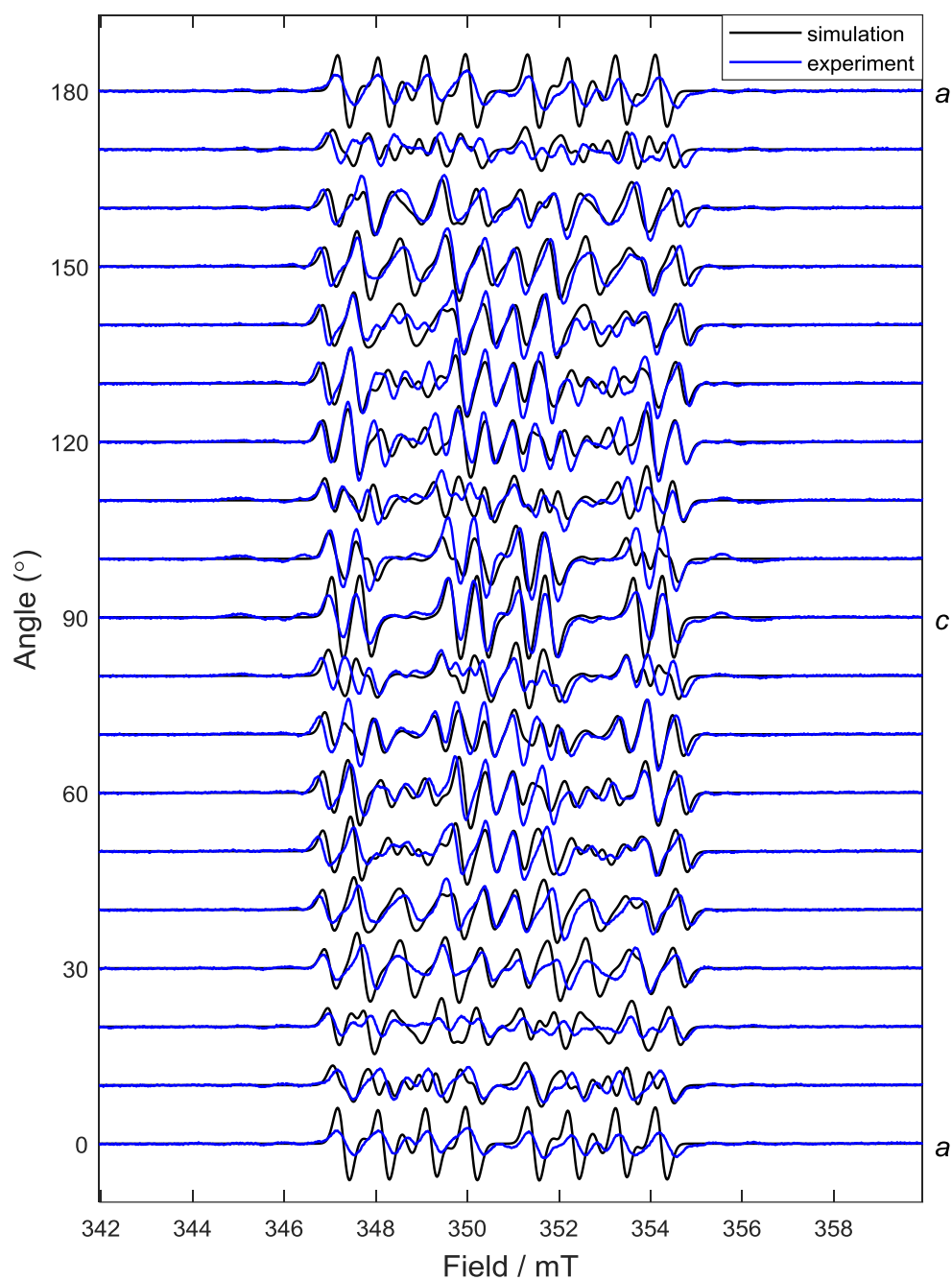


Figure 4.10 Roadmap spectra of the r.t. γ -irradiated single crystal of *L*-his with the crystallographic *b* axis perpendicular to B_0 and rotating in the *ac* plane. Each spectrum was shifted by its MW frequency of acquisition.

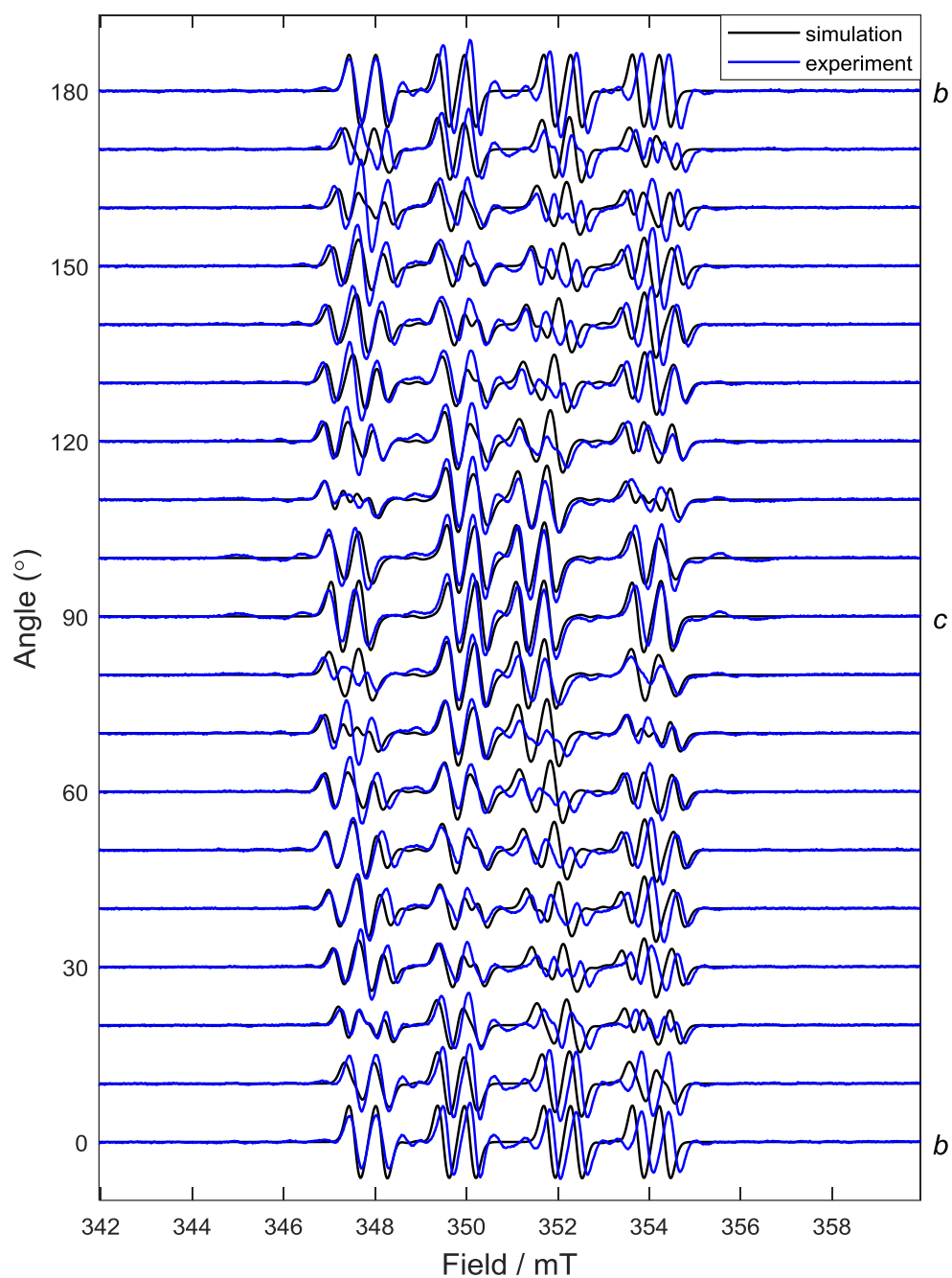


Figure 4.11 Roadmap spectra of the r.t. γ -irradiated single crystal of *L*-his with the crystallographic *a* axis perpendicular to B_0 and rotating in the *bc* plane. Each spectrum was shifted by its MW frequency of acquisition.

4.3.6 Multi-frequency EPR

Multi-frequency EPR can be used to identify and characterise unknown species as described in **Chapter 1**. Irradiated *L*-his powder was analysed at X-band (9.8 GHz), W-band (94 GHz) and 263 GHz (Figure 4.12) in order to extract the Hamiltonian parameters of the spectra. As can be inferred from the powder and crystal spectra, the paramagnetic species produced upon irradiation of *L*-his possess a near isotropic g -factor. The analysis of the W-band spectrum of X-irradiated *L*-his powder confirmed the presence of a rather small g -anisotropy. In fact, a ~ 10 -fold increase of the microwave frequency (and therefore of the magnetic field) at W-band produced only relatively minor change in the EPR spectrum (Figure 4.12b), with most of the spectral lines still overlapping. With an additional ~ 3 -fold increase of the microwave frequency (263 GHz), it is almost possible to distinguish the three anisotropic components x , y and z , the high-field component in particular (Figure 4.12c).

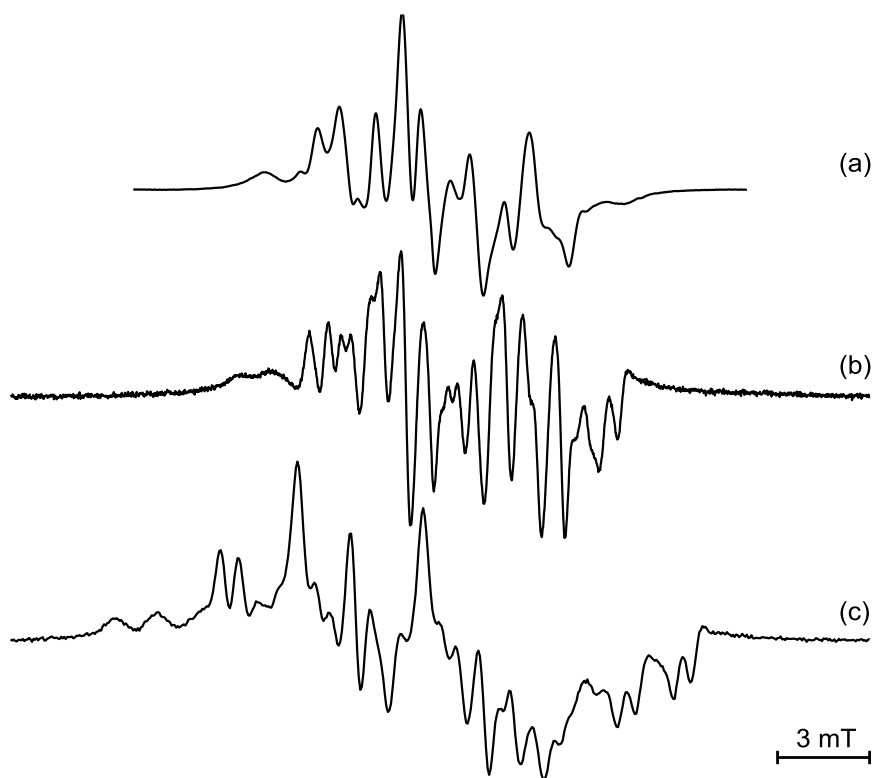


Figure 4.12 Multi-frequency EPR analysis of X-irradiated (40 kGy) *L*-his powder. (a) X-band, 9.8 GHz. (b) W-band, 95 GHz. (c) mm-wave, 263 GHz.

A simultaneous simulation of two of the three spectra (X- and W-band, or X-band and 263 GHz) was attempted, but no successful outputs were obtained for two main reasons. Firstly, a satisfactory determination of the magnetic field at high frequency using a field reference proved to be challenging and not possible to obtain, as some offset will always be present due to the instrumental setup. Secondly, it was not possible to discern the contribution of the other unknown paramagnetic species from that of the main deamination radical, which was believed to detrimentally influence the fit. Additionally, obtaining a correct phase during data acquisition on the 263 GHz spectrometer was challenging and not always successful, a factor which was also believed to negatively condition the simulations. The best simulation obtained is reported in Figure 4.13, where X-band and 263 GHz spectra have been simultaneously simulated. The starting parameters for the simulations are the parameters reported in Table 4.1. Both the g -factor and hyperfine couplings were varied, maintaining g - and hyperfine coupling directions unchanged. The parameters extracted from simulation are reported in Table 4.2.

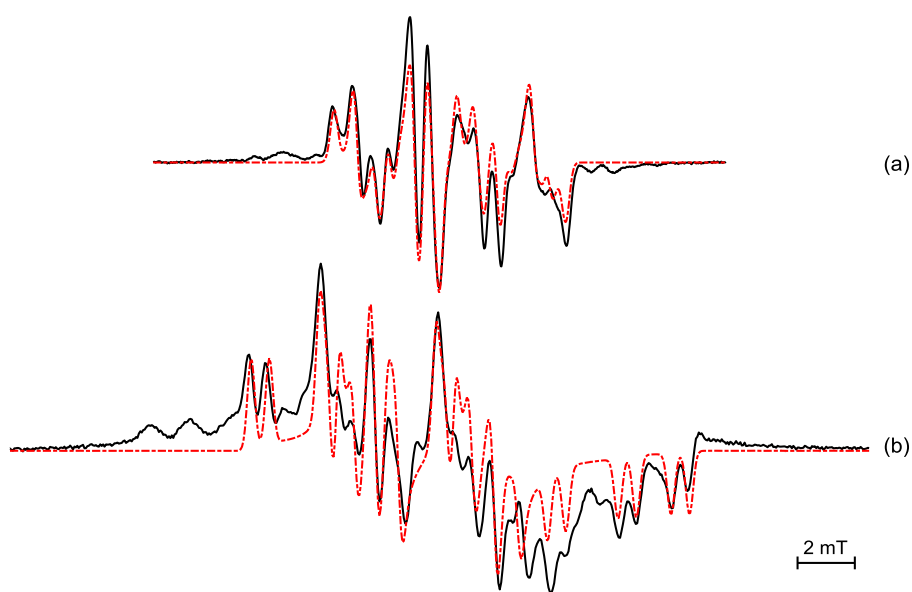


Figure 4.13 Multi-frequency EPR analysis of X-irradiated (40 kGy) *L*-his powder with simulated spectra (red dashed dotted line) overlapped to the experimental data (black solid line). (a) X-band, 9.8 GHz. (b) mm-wave, 263 GHz.

Table 4.2 Hyperfine parameters (mT) and *g*-values extracted from simultaneous simulation of X-band and 263 GHz data for the deaminated L-his radical.

Principal values			
a_{α}^H	-0.96(3)	-1.88(3)	-2.98(3)
$a_{\beta 1}^H$	0.87(3)	0.50(3)	0.75(3)
$a_{\beta 2}^H$	4.10(3)	4.46(3)	3.97(3)
<i>g</i> -value	2.0048(2) ^a	2.0030(2) ^a	2.0043(2) ^a

^a determined by comparison with a DPPH standard

4.3.7 Cold irradiation

Irradiation of L-his single crystals and powders was performed in liquid nitrogen as described in **Chapter 3**. The aim of the experiment was to analyse the primary radicals formed upon irradiation and follow their evolution into the room temperature stable species. It is worth noticing that at “liquid nitrogen temperature” some chemical reactions of active species and local physical processes cannot be stopped, and would require a “helium temperature” range to be studied.²⁹⁻³⁴ In the absence of information on the processes undergoing at temperatures below 77 K, in this study the species detected at liquid nitrogen temperature, which are described in the current and the following Chapters, will be referred to as the “primary species”. Characterizing these alleged “primary species” and their behaviour in this temperature range is an essential first step towards the consideration of multi-component systems.

Details concerning irradiation in liquid nitrogen are described in **Chapter 3**.

4.3.7.1 Carboxyl radical

The CW EPR spectrum obtained from irradiation of a single crystal of L-his in liquid nitrogen and measured at *ca.* 80 K is shown in Figure 4.14A. When the crystal was oriented along the *c* axis, the main features of the spectrum consisted of a broad 3-line signal. Smaller satellite peaks were also visible. As the crystal was rotated in the *yz* plane, the 3 lines get closer until collapsing into a broad single line, suggesting anisotropy of the hyperfine coupling and/or *g*-value (Figure 4.15). The microwave power saturation spectra in Figure 4.17 shows that, as the microwave

power is increased, the 3 lines characteristic of the spectrum are lost together with the satellite peaks, being replaced by a single, broad line. The 3-line spectrum had been previously ascribed to the radical formed from the addition of a hydrogen atom to the carboxylic group (Figure 4.16), which occurs for both histidine free base, used in this study,¹² and histidine HCl.¹¹ The unpaired electron is considered to be mainly located on the carboxylic carbon, and the main 3-line signal would therefore arise from the coupling to this proton and to the proton directly bound to the carboxylic carbon, producing a doublet of doublets with the 2 central lines partial overlaid. Nevertheless, it was not possible to perform a reasonable simulation with the parameters described in the literature.

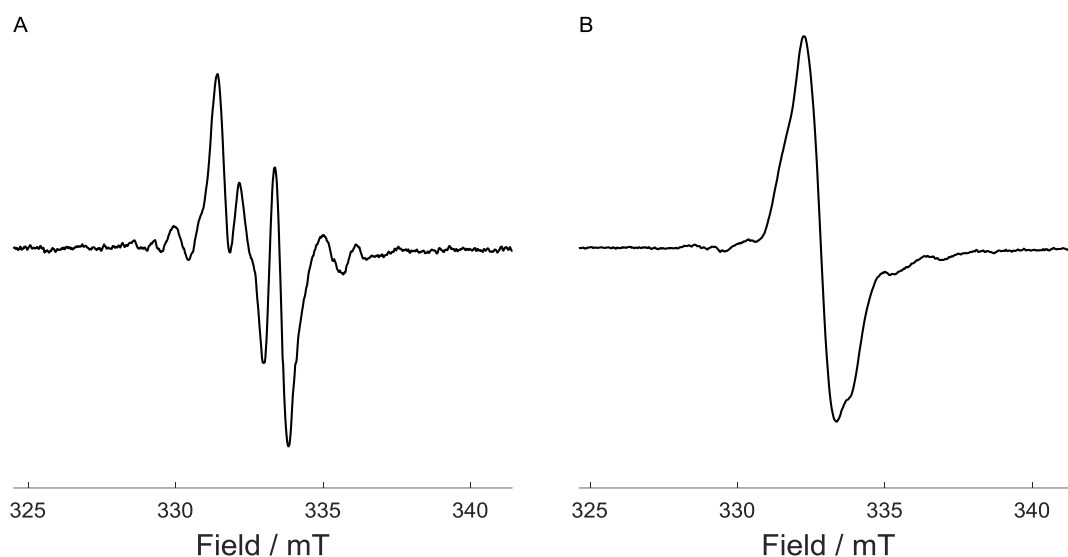


Figure 4.14 X-band EPR spectrum of (A) single crystal of *L*-his and (B) *L*-his powder γ -irradiated in liquid nitrogen and acquired at 80 K. The crystal is oriented along the *c* axis.

The powder spectrum of *L*-his irradiated in liquid nitrogen and measured at 85 K is shown in Figure 4.14B. The main features of the spectrum consisted of a single, broad line, with a shoulder emerging on top of it. Other less intense, broad side peaks can also be observed as for the single crystal spectrum. These minor features disappeared as the microwave power was increased (Figure 4.18).

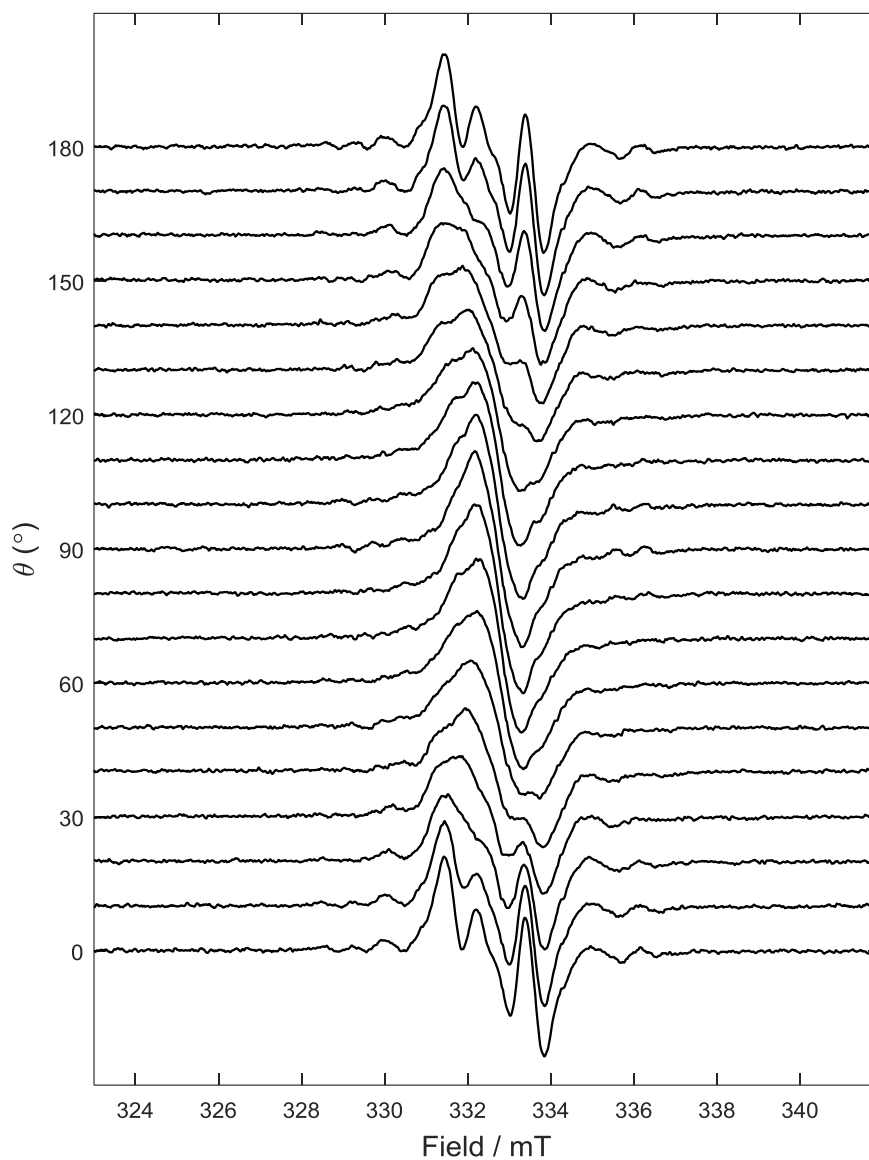


Figure 4.15 Roadmap spectrum of the γ -irradiated single crystal of L-his at 80 K with the crystallographic c axis perpendicular to B_0 and rotating on the ab plane.

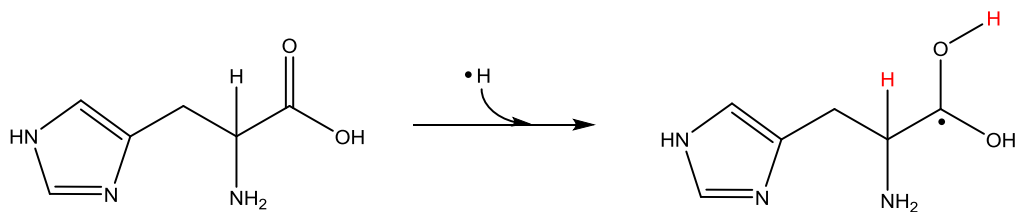


Figure 4.16 Formation of the carboxylic anion.

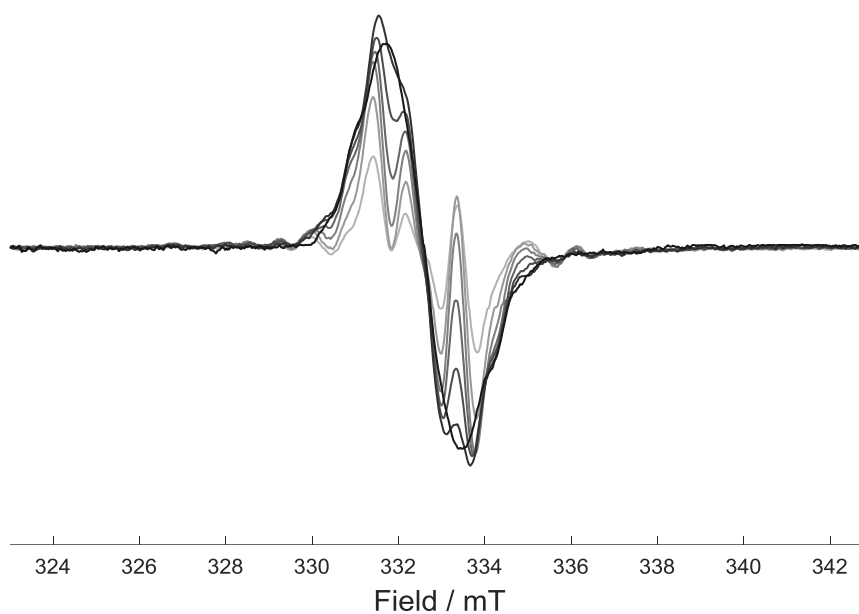


Figure 4.17 Microwave power saturation spectra of L-his single crystal at 80 K. The crystal is oriented along the *c* axis. Microwave power progressively increasing from 3.2 μ W (light gray) to 12.6 mW (black).

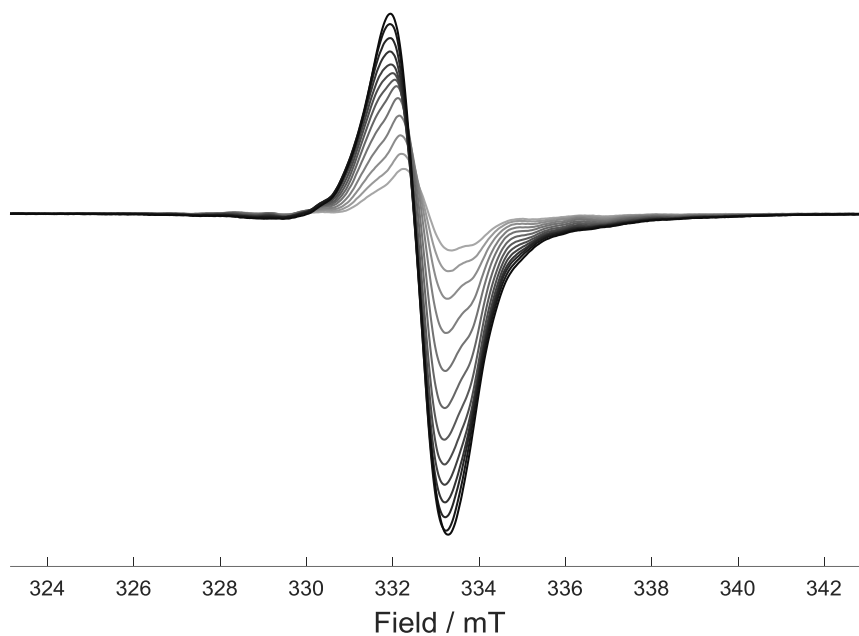


Figure 4.18 Microwave power saturation spectra of L-his powder, acquired at 80 K. Microwave power progressively increasing from 3.2 μ W (light gray) to 12.6 mW (black).

4.3.7.2 Formation of the deamination radical – 120 K

No changes in the spectrum were observed when the samples were annealed up to 110 K. Further annealing to 120 K resulted in the irreversible loss of the carboxyl radical and the production of the deamination radical, as observed for both crystal (Figure 4.19) and powder spectra (Figure 4.20) upon r.t. irradiation. The crystal spectrum in particular showed how the satellite peaks (∇) appeared not to be involved in the spectral evolution, supporting the hypothesis of a second distinct species that does not undergo any rearrangement in this temperature range.

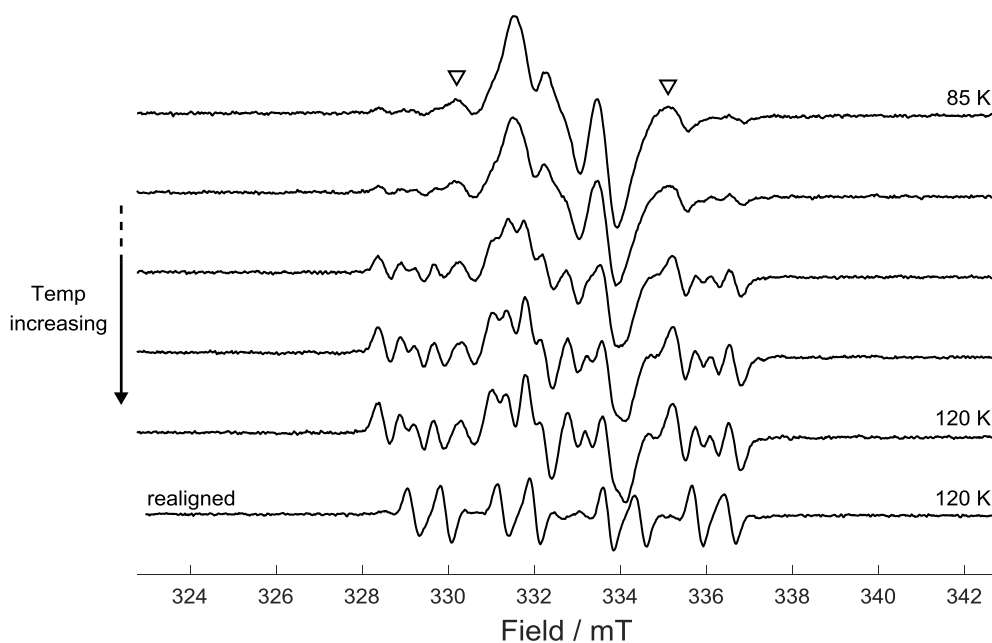


Figure 4.19 Annealing of γ -irradiated *L*-his single crystal to 120 K. The crystal was found not to be perfectly aligned along one of the main crystallographic directions during the annealing and was realigned afterwards. ∇ show satellite peaks which appear not to be involved in the spectral evolution

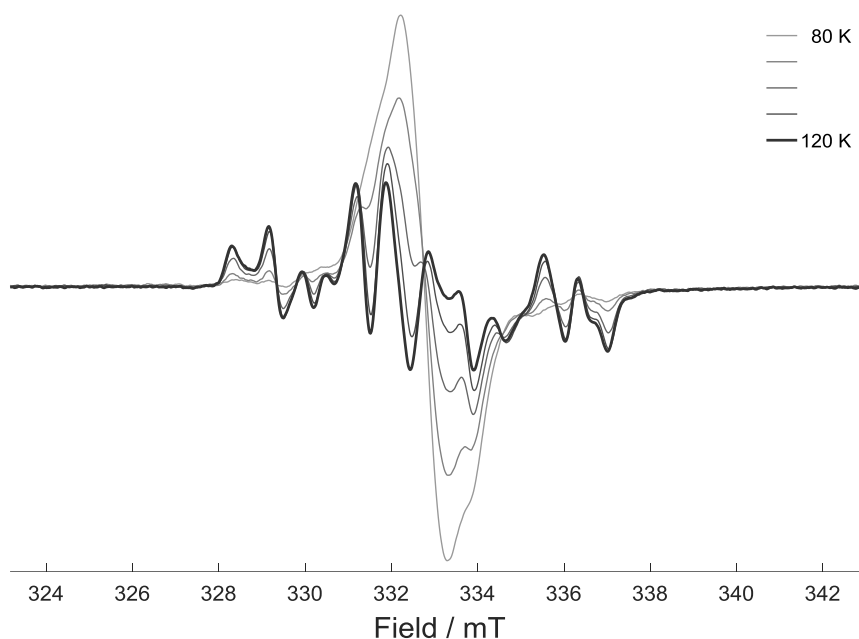


Figure 4.20 Annealing of γ -irradiated L-his powder from 80 K (light gray) to 120 K (black).

4.3.7.3 Rearrangement of the deamination radical – 120 K to r.t.

The annealing of the sample further proceeded in steps to reach the temperature of 170 K. In this range the deamination radical is known to undergo a conformational change due to the change of hybridization of the α -carbon from sp^3 to sp^2 , as a result of the elimination of the amino group that occurred at 120 K.¹² The resulting EPR spectrum is the same as that obtained by irradiating the sample at r.t. The above mentioned change is most clearly exhibited by the powder spectrum as shown in Figure 4.21.

Further annealing to r.t. did not result in other spectral changes of the main radical species (Figure 4.22), other than a decrease of the signal intensity due to the change of the Boltzmann population with temperature. Interestingly, at 200 K two broad, low intensity peaks can be observed at the side of the main spectrum, which quickly disappear by further annealing. The said peaks were therefore ascribed to a different, unidentified transient species. This can be seen more clearly from Figure 4.23. The figure shows how, not only satellite peaks formed, but also other peaks of the main deaminated histidine spectrum are affected by the presence of this transient species.

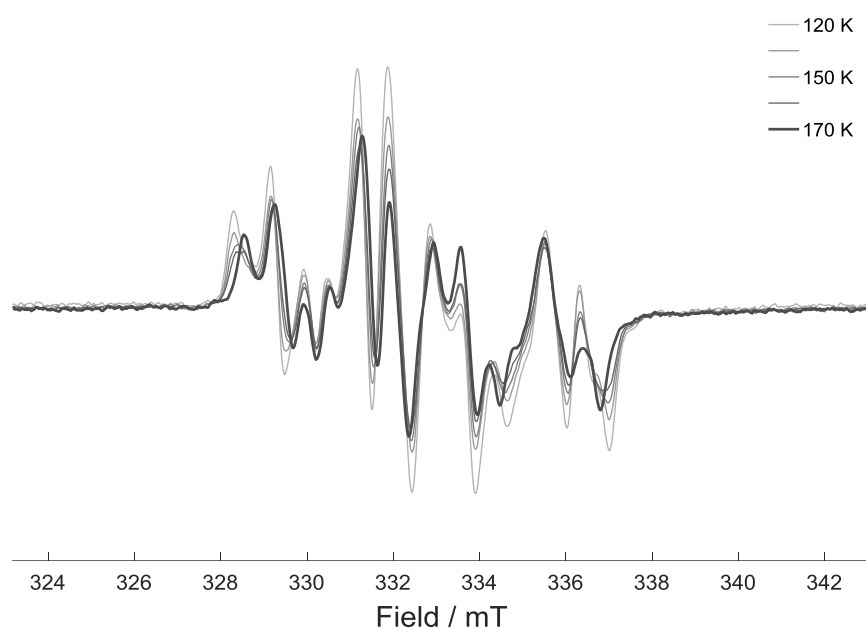


Figure 4.21 Annealing of γ -irradiated *L*-his powder from 120 K (light gray) to 170 K (black).

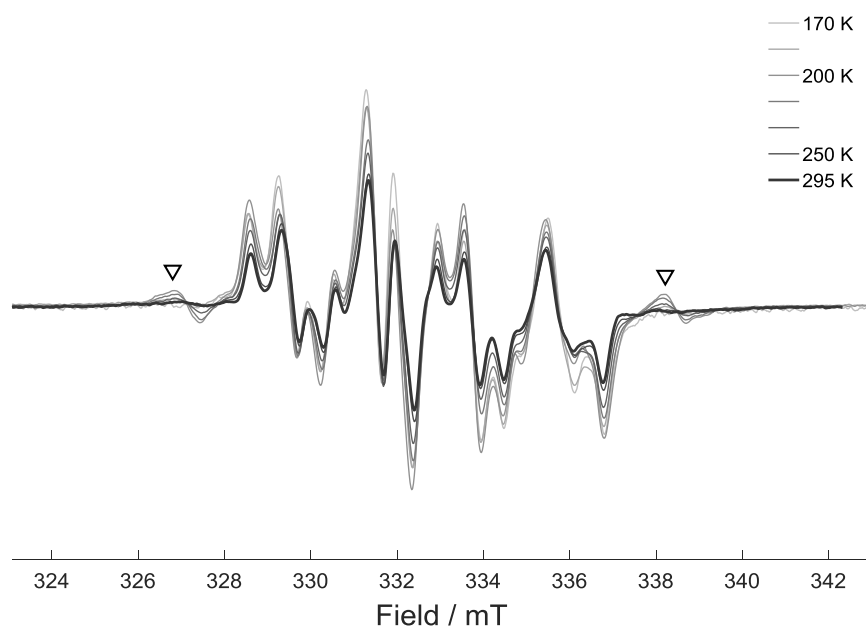


Figure 4.22 Annealing of γ -irradiated *L*-his powder from 170 K (light gray) to r.t. (black). ∇ show side peaks appearing at 200 K and subsequently disappearing upon further annealing.

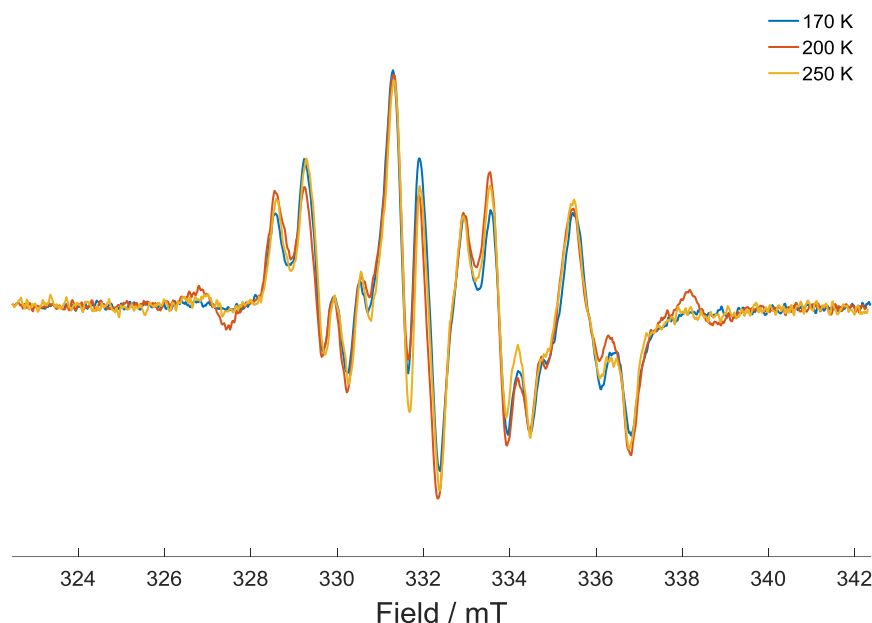


Figure 4.23 Irradiated L-his powder spectra at 170 K (blue), 200 K (red), and 250 K (yellow) showing the formation of a transient species at 200 K.

4.3.8 Dissolution experiments

Dissolution of the irradiated L-his powder was undertaken to study the reactivity of the radical species in solution, thereby mirroring the treatment of excipients in parenteral formulations reconstituted before injection. Knowing the behaviour of the radicals in solution is necessary to assess the safety of the irradiated drugs and the stability of the pharmaceutical products.

4.3.8.1 Spin trapping with MNP

Following dissolution of the irradiated powder in water, no EPR signal was detected (Figure 4.24), as expected for a short-lived carbon centred radical. However, when the irradiated powder was dissolved in a spin-trap solution of MNP (80 mM), a persistent spin-adduct signal was detected with a concentration of *ca.* 0.25 μM (Figure 4.25). The observed 18-line spectrum was assigned to the coupling of the unpaired electron with the nitroxidic nitrogen of the spin trapping agent, along with one α -proton and two almost equivalent β -protons of the trapped radical species. The hyperfine couplings extracted by simulation of the spectra are in good agreement with previous work in which the deaminated L-his radical was either formed from γ -irradiation of histidine in the solid²¹ or solution state²² followed by spin trapping in solution with MNP (Table 4.3). This 18-line signal was not obtained by dissolving non-irradiated L-his powder in a solution containing the spin trapping agent MNP (Figure 4.24b), indicating that the

trapped adduct species was indeed formed as a result of the irradiation process. The low-intensity 3-line background signal evident in Figure 4.24b was assigned to the formation of an MNP di-adduct, labelled di-*tert*-butyl nitroxide (DTBN), which commonly occurs in low concentration with this particular spin trapping agent.²²

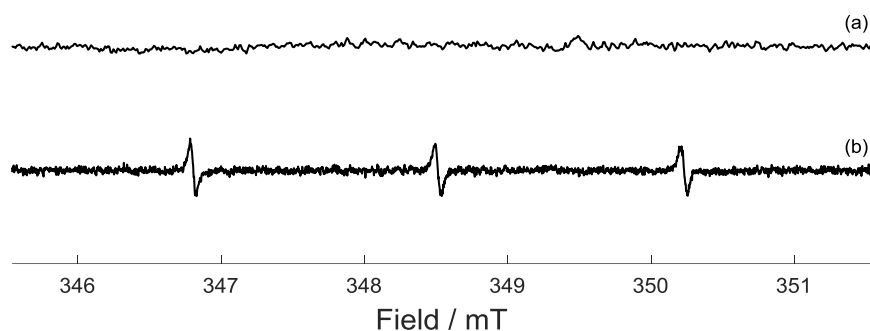


Figure 4.24 Control X-band EPR spectra. (a) 250 kGy γ -irradiated L-his powder dissolved in water buffered with p.b. 50 mM at pH 7.2; (b) non-irradiated L-his powder dissolved in a spin trap solution of MNP 80 mM buffered with p.b. 50 mM at pH 7.2.

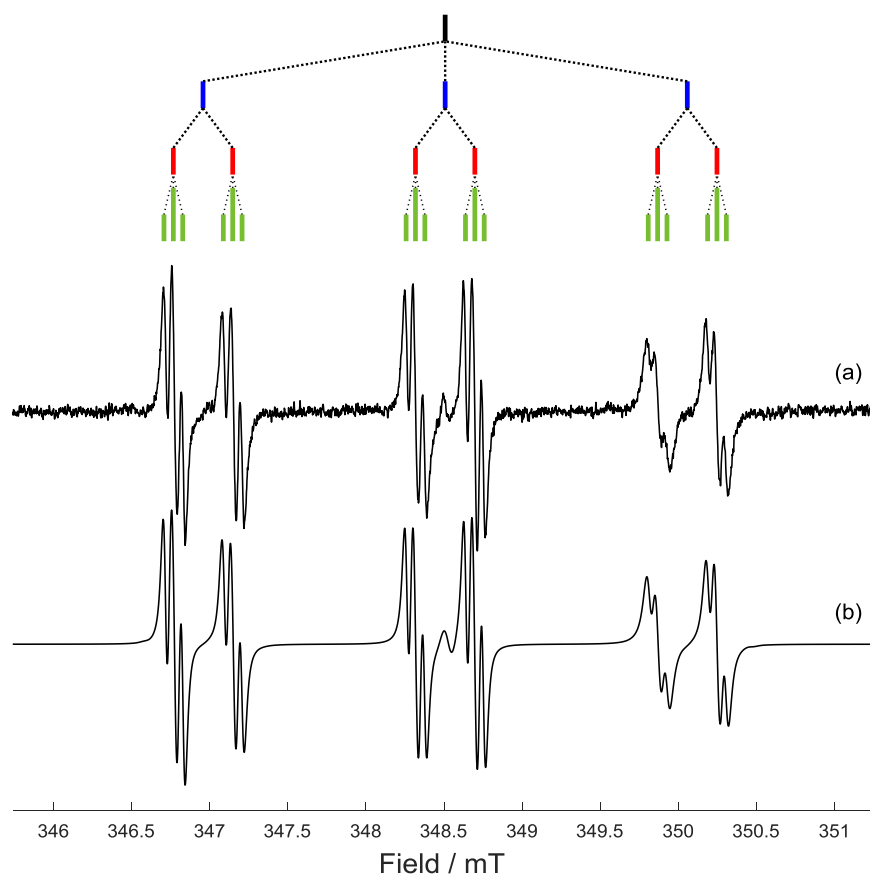


Figure 4.25 X-band CW EPR spectrum of (a) 250 kGy γ -irradiated L-his powder dissolved in a spin trap solution of MNP (80 mM) and (b) simulated EPR spectrum (obtained using EasySpin²⁵) and line diagram of the MNP-his spin adduct.

Table 4.3 Hyperfine parameters (mT) and g-values for spin trapped deaminated L-his radical.

		a_{NO}^{N}	a_{α}^{H}	$a_{\beta 1}^{\text{H}}$	$a_{\beta 2}^{\text{H}}$	g_{\perp}	g_{\parallel}
This study	a_{\perp}	1.771(5)	0.400(5)	0.079(5)	0.048(5)	2.0057(2) ^a	2.0052(2) ^a
	a_{\parallel}	1.442(5)	0.333(5)	0.057(5)	0.046(5)		
Previous work ²¹	a_{iso}	1.54	0.41	0.06	0.06	- ^b	- ^b
Previous work ²²	a_{iso}	1.545	0.392	0.05	0.05	- ^b	- ^b

^a determined by comparison with a DPPH standard; ^b not determined.

4.3.8.2 Radical regeneration

If the irradiated powder is firstly dissolved in water and the spin trap MNP added subsequently (i.e., only after the dissolution of the powder), then the spin-adduct signal of the trapped radical is still detectable (Figure 4.26a); due to lower intensity the modulation depth was increased, hence the β -proton coupling is not resolved. The concentration of the spin adduct was estimated to be *ca.* 0.1 μM , although in this experiment MNP was used at a concentration of 40 mM instead of 80 mM to minimize the formation of DTBN background signal. A second, though less intense, 4-line signal with a 1:2:2:1 pattern can also be observed in the spectrum.

The MNP-histidine spin-adduct has been detected following addition of MNP one hour after dissolution of the irradiated powder in water (Figure 4.27). Such a long persistence time of the radical in solution is inconsistent with the expected reactivity of carbon centred radicals, and is in contrast with the inability to directly detect the radical in the absence of a spin trapping agent which implies a short radical lifetime. It is therefore proposed that, rather than invoking long radical lifetimes in solution to account for the observed spin adduct signals, the deaminated histidine radical must be regenerated in solution. If for example iron is present in solution, together with a strong oxidant, Fenton-type reactions may take place leading to the formation of ROS.³⁵ Such ROS species could facilitate the continuous regeneration of the deaminated histidine radical which is readily and subsequently trapped by MNP at some prolonged time-interval following dissolution.

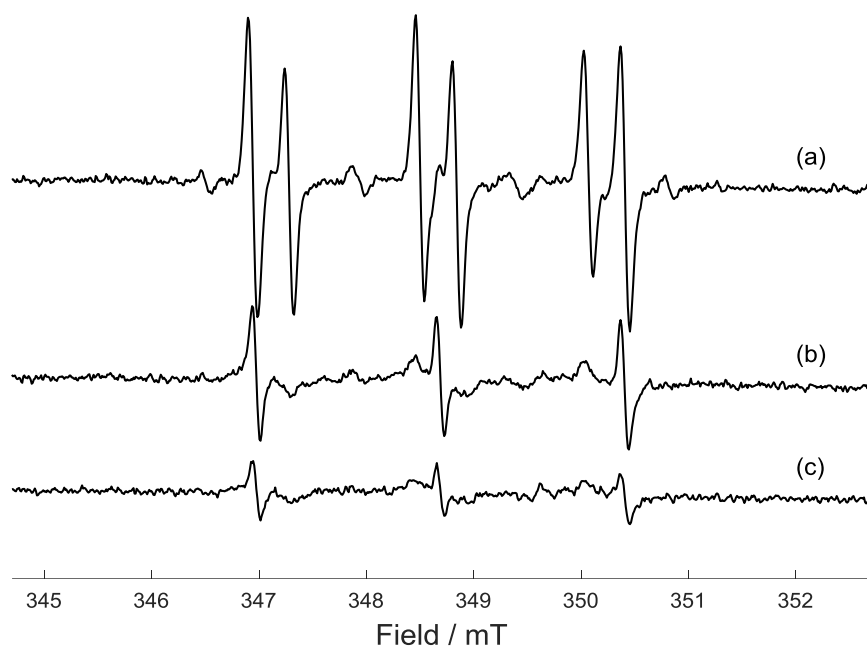


Figure 4.26 X-band EPR spectra of *L*-his powder dissolved (a) in water with MNP 40 mM added 3 mins after dissolution and transferred by using a syringe with metal needle; (b) in water containing EDTA (1 mM) followed by processing as (a); (c) same as (a) but transferred by using a glass Pasteur pipette.

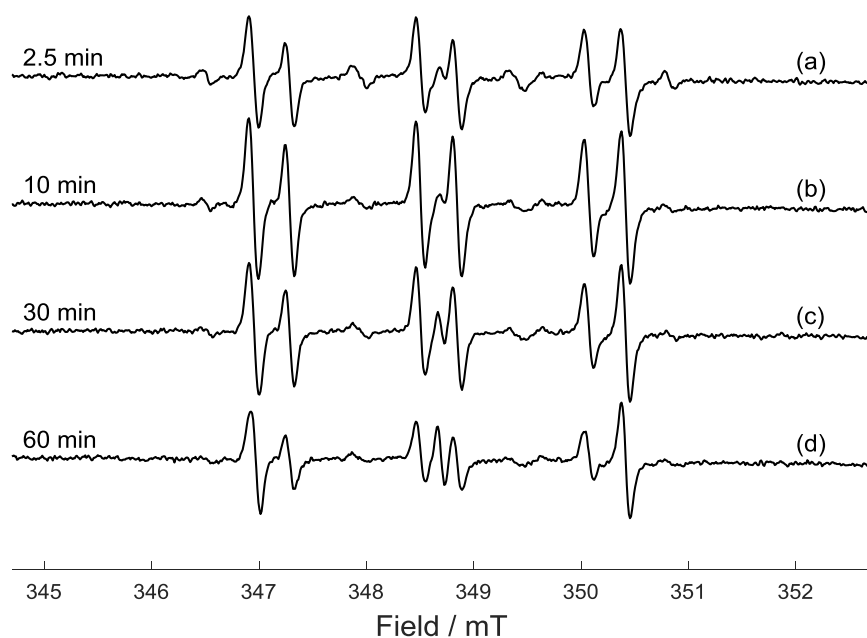


Figure 4.27 Regeneration of the deamination radical when γ -irradiated *L*-his powder is dissolved in water with later addition of the spin trapping agent. MNP (40 mM) added (a) 2.5 mins, (b) 10 mins, (c) 30 mins and (d) 60 mins after dissolution and transferred by using a syringe with metal needle.

To test this hypothesis irradiated L-his powder was dissolved in an aqueous solution containing the chelating agent EDTA (1 mM), and MNP was subsequently added to this solution 3 mins after dissolution of L-his. As shown in Figure 4.26b, the EPR signal from the L-his radical-adduct could not be detected when the chelating agent was present in the solution. In our initial experiments a syringe with a sterile metal needle was used to transfer the solution to the quartz capillary for EPR measurement. However, when a glass pipette was used instead of a syringe containing a metal needle to transfer the sampled solution into the EPR quartz capillary tube, only DTBN background was detected (Figure 4.26c). Additionally, the amount of spin-adduct formed by direct dissolution of the powder in the spin trap solution was found to be four times higher (*ca.* 1 μ M) if the glass pipette was used instead of the syringe and needle to transfer the sample solution in the EPR tube. An X-ray fluorescence analysis of the metal needles showed the presence of large amounts of iron, together with chromium, manganese, nickel and trace level of other metals (Figure 4.31). It therefore appears that the deaminated radical trapped after dissolution in water and later addition of MNP is a result of a Fenton-type reaction catalysed by trace metals contained in the syringe needle. Furthermore, such behaviour appears to be characteristic of L-his, as other excipients like D-mannitol did not show any radical regeneration properties (see **Chapter 5**).

According to these considerations, the 4-line spectrum of the previously unidentified radical species can be attributed to the formation of MNP-OH spin adduct (Figure 4.30), further supporting the assertion that Fenton-type reactions are operative. These Fenton-type reactions would also explain why the concentration of the MNP-histidine spin-adduct was found to be significantly lower when using the syringe and needle for sample transfer rather than the glass pipette, as the ROS produced might have quenched the formation of the spin-adduct.

The kinetics of formation of the MNP-his spin adduct when using a glass pipette or a syringe with metal needle are shown respectively in Figure 4.28 and Figure 4.29. The observation of the kinetics shows how the regeneration of the deamination radical reached an equilibrium in the initial part of the experiment, to then start decaying after *ca.* 40 min (Figure 4.28). Such equilibrium was related to the presence of strong oxidant species, which keep the Fenton-type chemistry running until depletion.

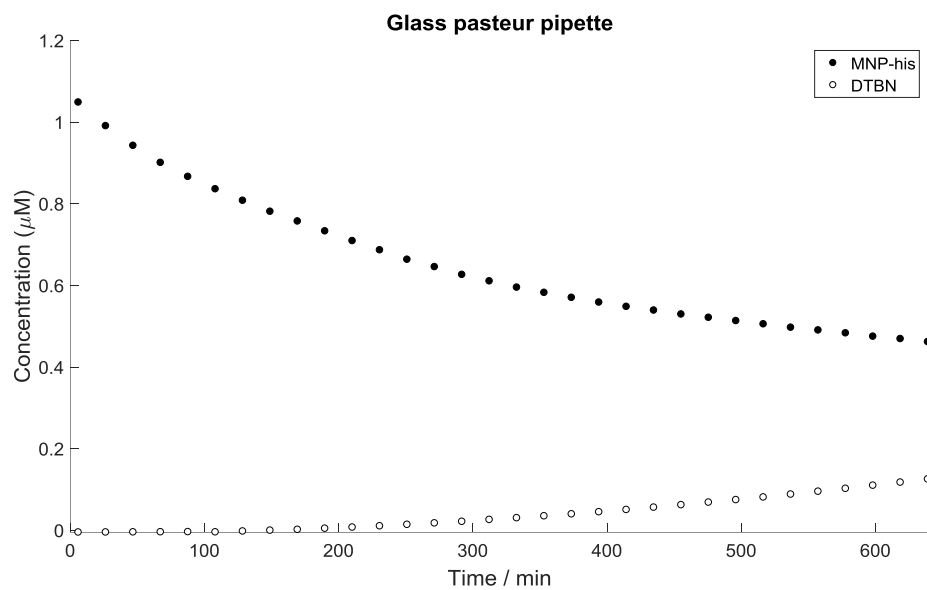


Figure 4.28 EPR quantification of the MNP-his spin adduct (●) and DTBN (○), generated from dissolution of γ -irradiated L-histidine powder in a solution of MNP (40 mM) prepared in p.b. 50 mM at pH 7.2 and with the sample solution being transferred with a glass pipette.

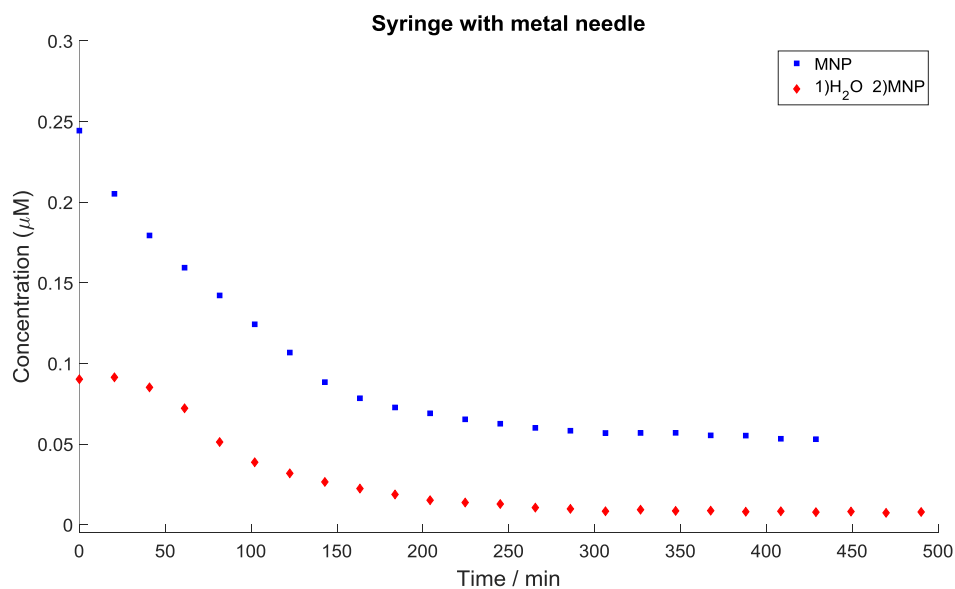


Figure 4.29 EPR quantification of the MNP-his spin adduct with the sample solution being transferred with a syringe with metal needle, directly dissolving γ -irradiated L-histidine powder in a solution of MNP (40 mM) (■); first dissolving the powder in an aqueous solution and adding the spin trap after 2 minutes (♦) .

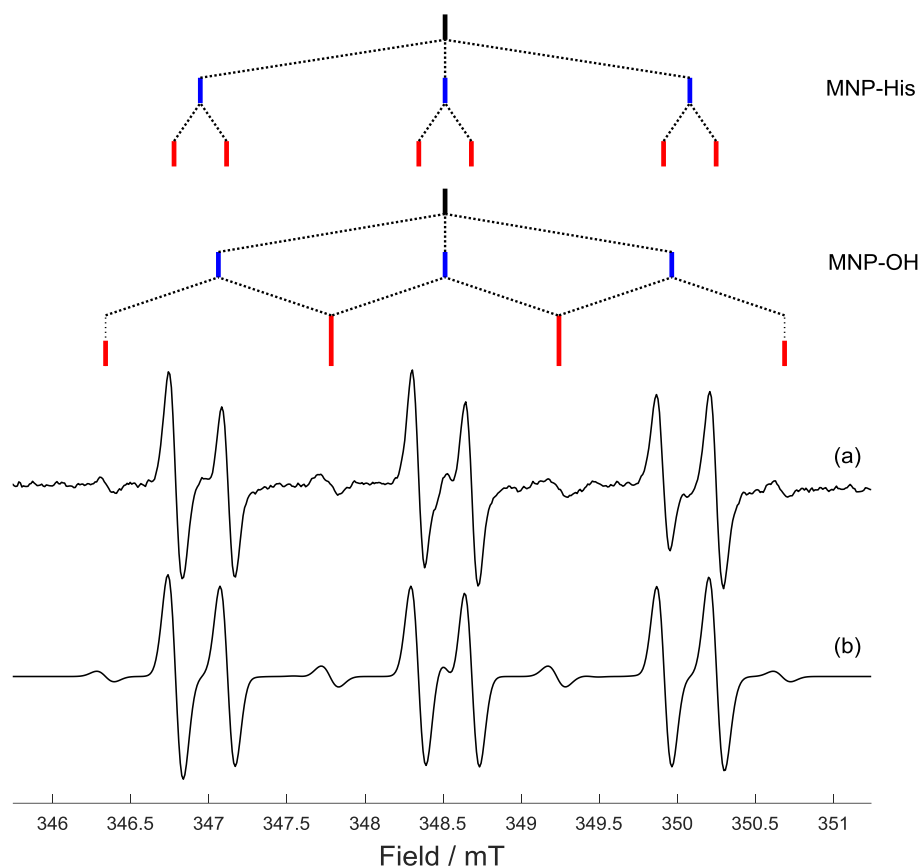


Figure 4.30 X-band EPR spectra of (a) 250 kGy γ -irradiated L-his powder dissolved in water with MNP (40 mM) added 2.5 mins after dissolution and transferred by using a syringe with metal needle and (b) EasySpin²⁵ simulation with line diagrams for the deamination radical (upper) and the hydroxyl radical (lower) spin adducts.

Table 4.4 EPR hyperfine couplings (mT) and g values for the trapped deaminated L-his radical (MNP-his), hydroxyl radical (MNP-OH) and the MNP di-adduct di-*tert*-butyl nitroxide (DTBN), comparing the parameters determined in this study with previously published ones.

Radical		a_{NO}^{N}	a_{α}^{H}	$a^{13\text{C}}$	g -value
MNP-his	This study	1.57(1)	0.34(1)	-	2.0055(2) ^a
	Ref. ²²	1.55	0.39	-	- ^b
MNP-OH	This study	1.45(1)	1.44(1)	-	2.0054(2) ^a
	Ref. ³⁶	1.44	1.44	-	- ^b
DTBN	This study	1.75(1)	-	0.48(1)	2.0056(2) ^a
	Ref. ²²	1.72	-	- ^b	- ^b

^a determined by comparison with a DPPH standard; ^b not determined.

4.3.8.3 XRF analysis on the metal needles

XRF analysis on the metal needles was performed as described in **Chapter 3**. Six key metals were identified: Fe-K α (6.405 KeV); Cr-K α (5.415 KeV); Co-K α (6.931 KeV); Ni-K α (7.480 KeV); Zr-K α (15.775 KeV) and Mn-K α (5.900 KeV). Qualitatively, the data suggest that there is significantly higher Fe in the needles than the other metals. The presence of these metals is consistent with the manufacturer information describing the needles as stainless, chromium-nickel steel.

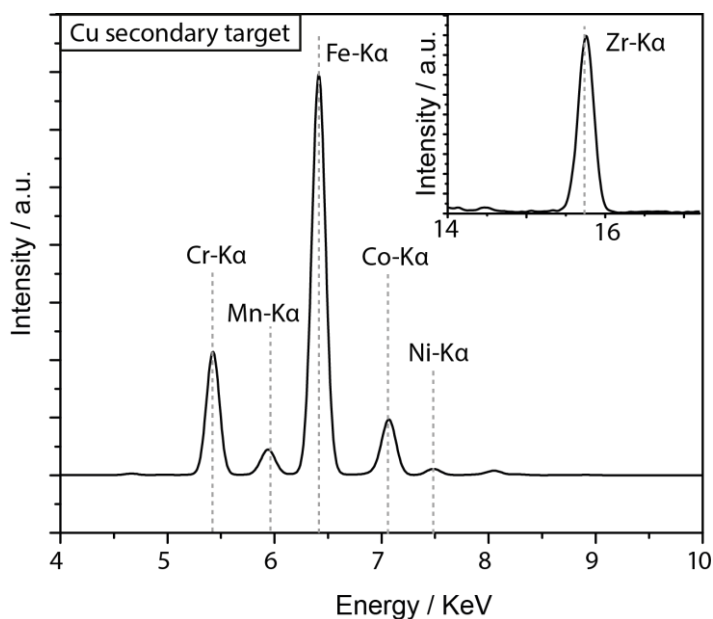


Figure 4.31 Background subtracted XRF spectra for the metal needles.

4.3.9 MS analysis

Mass spectrometry (MS) analysis was performed on irradiated and non-irradiated samples aiming to detect signals from the species originating from the irradiation process. Samples of non-irradiated, 25 kGy and 250 kGy γ -irradiated L-his were prepared and analysed as described in **Chapter 3**. The spectra obtained in positive and negative mode analysis are shown respectively in Figure 4.32 and Figure 4.33.

Table 4.5 reports the assignment of the main peaks. However, in neither spectrum was it possible to identify an m/z which could be directly attributed to the deaminated L-his fragment or a molecule deriving from it.

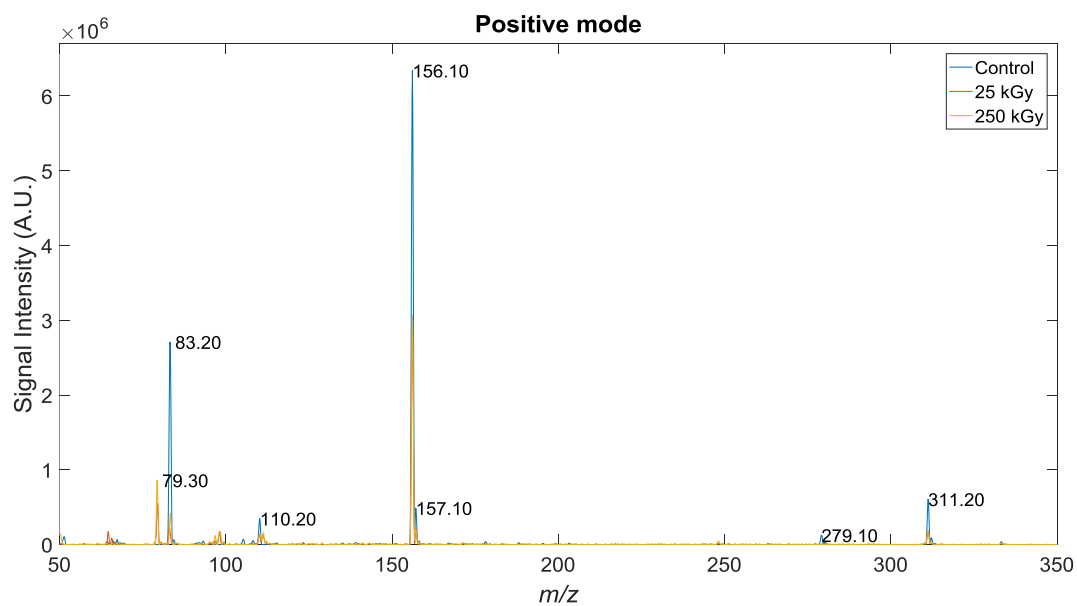


Figure 4.32 Positive mode MS analysis of non-irradiated, 25 kGy and 250 kGy γ -irradiated L-his.

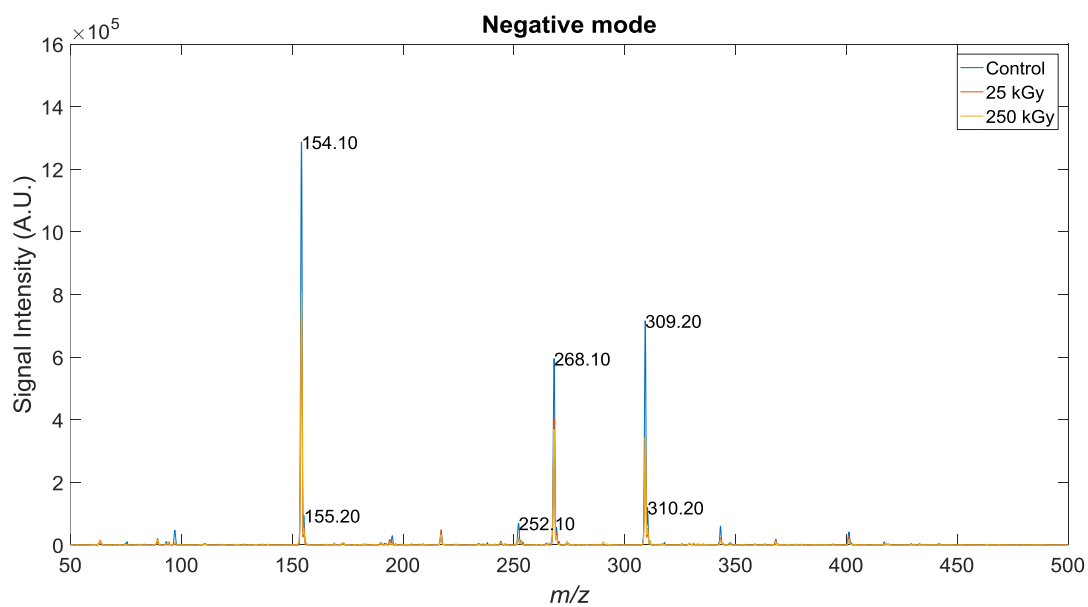


Figure 4.33 Negative mode MS analysis of non-irradiated, 25 kGy and 250 kGy γ -irradiated L-his.

Table 4.5 Main assignments of the peaks detected from the MS analysis.

Observed m/z	Proposed assignment
POSITIVE MODE	
79.30	Background
83.20	Background
156.10	$[\text{His} + \text{H}]^+$
311.20	$[2 \times \text{His} + \text{H}]^+$
NEGATIVE MODE	
154.10	$[\text{His} - \text{H}]^-$
268.10	Not assigned
309.20	$[2 \times \text{His} - \text{H}]^-$

4.3.10 Liquid NMR analysis

Liquid NMR analysis was performed on both a non-irradiated and a 250 kGy γ -irradiated samples of *L*-his. The sample preparation and analysis details are described in **Chapter 3**. As can be seen from Figure 4.34 and Figure 4.35, no major differences were found between the spectra.

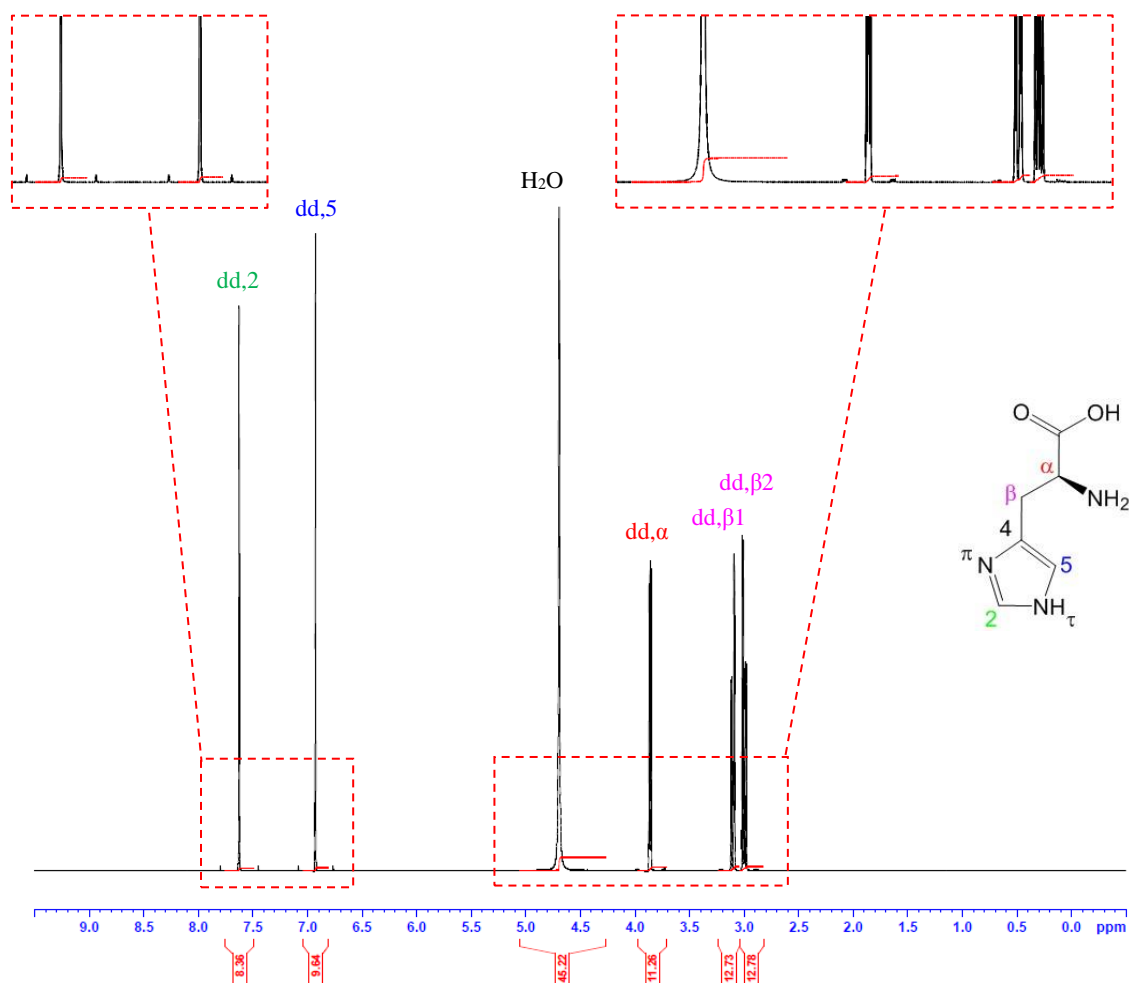


Figure 4.34 ^1H -NMR analysis of non-irradiated *L*-his.

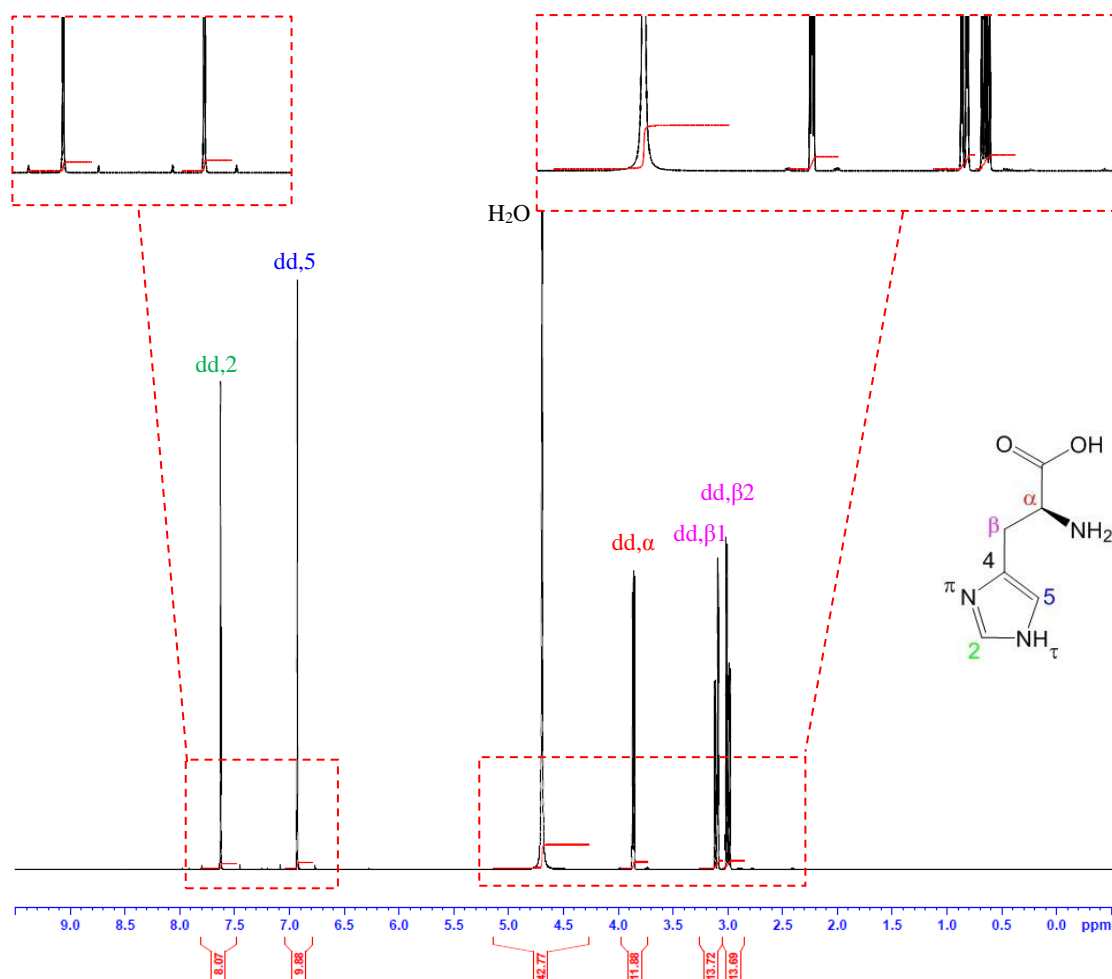


Figure 4.35 ^1H -NMR analysis of 250 kGy γ -irradiated L-his.

4.4 Discussion

4.4.1 Solid state persistent radicals at r.t.

The analysis of γ -irradiated L-his powder and crystals showed the formation of persistent radical species, being stable for several months. Powder samples were γ -irradiated delivering a dose in the range of 25–250 kGy, showing that the same radical species were observed at all doses, with the intensity of the EPR spectra increasing when the doses increase (Figure 4.3). Twenty-five kGy is typically considered the minimum dose necessary to achieve the desired sterility assurance level (SAL), but can be adapted depending on the system to sterilize.³⁷ Higher irradiation doses such as 125 and 250 kGy are generally considered too extreme to be applied to pharmaceuticals, but can be particularly useful for analytical purposes, on the condition that the degradation products formed at these doses and at lower, industrially relevant

doses are the same. Quantification of the radicals produced upon irradiation was performed with a TEMPO standard, showing that in this range the total radical yield is not proportional to the radiation dose delivered.

The influence of the type of ionising radiation source on the radical formation was also studied. X-irradiation was found to produce the same radical species as γ -irradiation. The comparison between the X- and γ -irradiated powder samples highlighted minor differences, which were attributed to additional, minor paramagnetic species also formed upon irradiation. The relative concentration between the main deamination radical and the said species could be influenced by the conditions at which the irradiation was conducted, such as by the presence/absence of O₂, humidity, light. As an example, it has been shown that the presence of O₂ can influence the radical formation and decay to a great extent.³⁸ Indeed, X-irradiation was performed in open air, while the samples that received γ -rays were inserted in glass vial and evacuated, as described in **Chapter 3**.

Single crystal analysis allowed the main radical species formed to be unequivocally ascribed to the product of deamination of *L*-his. Deamination is indeed a typical decomposition pathway for many amino acids.^{13–17} Roadmap simulations were performed combining previously published hyperfine coupling tensors and g-tensors extracted from the powder spectra. The simulations were found to be in reasonably good agreement with the experimental data. The differences between simulation and experimental data were attributed to small errors on the previously published hyperfine tensors.

The presence of additional unknown radical species has been suggested from different experiments. Most clearly, the single crystal spectra showed the presence of satellite peaks which were ascribed to a different paramagnetic species. Microwave power saturation spectra of the irradiated powder also suggested the presence of a second radical in the spectrum. Similarly, the difference in the CW EPR spectra between X- and γ -irradiated powder can be ascribed to a different concentration of the radical species formed upon irradiation due to different irradiation conditions. The presence of these additional radical species also prevented the extraction of more precise Hamiltonian parameters through multi-frequency fitting of the powder spectra.

4.4.2 Low temperature stable species

Irradiation in liquid nitrogen was performed in order to obtain valuable information on the primary radicals formed upon irradiation and their evolution into the r.t. stable species. Identifying the primary species formed and their behaviour in this temperature range is a necessary first step towards the study of multi-component systems, where transient radical

species can potentially interact with and degrade other components. This is of particular interest in pharmaceutical formulations that generally contain a number of different excipients, typically representing the major components of the pharmaceutical product, and one or more APIs. Therefore, for APIs in particular, not only direct degradation caused by irradiation, but also indirect degradation due to interaction with radical species formed from other drug components must be taken into account. In order to do that, the nature and behaviour of transient radical species of all the drug components in a formulation must be considered.

L-his powders and crystals were therefore irradiated in liquid nitrogen and analysed from 80 K to r.t. At 80 K, the crystal showed the presence of a 3-line signal, which was assigned to the carboxyl anion formed from addition of a H^\bullet to the carboxylic group, as previously reported.^{11,12} The unpaired electron is believed to be preferentially located on the carboxylic carbon, hence the EPR spectrum of the single spectra was interpreted as a doublet of a doublet with the two central lines overlapping, originating from a coupling with the hydrogen bound to the α -carbon and the hydrogen added to the carboxylic group.

The carboxylic anion was found to be stable up to 120 K, at which temperature it evolves into the deamination radical, as was observed in both crystal and powder analysis. Further annealing to 170 K induced a conformational change which was previously reported to be due to the change in hybridization of the α -carbon from sp^3 to sp^2 as a consequence of the deamination occurred at 120 K.¹² The powder spectrum observed at 170 K corresponds to the spectrum detected at r.t. Nevertheless, when the temperature was increased in steps from 170 K to r.t., the presence of an unreported, transient radical species was detected at 200 K which disappeared on further annealing.

No significant differences were found between the CW EPR spectra obtained from r.t. irradiation of the sample and irradiation in liquid nitrogen followed by annealing to r.t. Lowering the temperature at which the irradiation is performed was reported to decrease the radical formation as a result of lowering the activity of the free radicals, and was therefore suggested as a method to reduce the degradation that occurs in sterilized pharmaceuticals,³⁷ but this was not subject of the present study.

4.4.3 Dissolution experiments

After characterizing the radical species persistent in the solid state and studying the evolution of the primary species from 77 K to r.t., the dissolution process of the irradiated powder samples was investigated. Assessing the behaviour of the radiation-formed degradants in solution is key for excipients such *L*-his that are largely used in parenteral formulation, whose administration

often involves the dissolution of a lyophilised product and its injection into the patient. Injection of free radical containing solutions can in fact have direct toxicological consequences.^{39,40}

The radical species produced upon irradiation were found to have a short lifetime in solution, as expected for this type of carbon centred radicals. By the use of the spin-trapping agent MNP, the L-his deamination radical was trapped and characterized. The radical was demonstrated to be formed as a result of the irradiation process, since no radicals were trapped from dissolution of non-irradiated L-his powder in a solution containing the spin-trapping agent MNP.

Unexpectedly, the same radical species could still be trapped when the spin-trap was added after dissolution of the powder, and could be detected up to one hour after dissolution process. This finding was in contrast with the short lifetime of the radical species previously assessed. It was therefore proposed that a Fenton-type reaction was occurring, leading to the continuous regeneration of the radical. Fenton-type reactions may take place in the presence of trace metals and strong oxidants (Figure 4.36), leading to the formation of ROS which could then facilitate the regeneration of the histidine radical, readily trapped by the spin trapping agent.

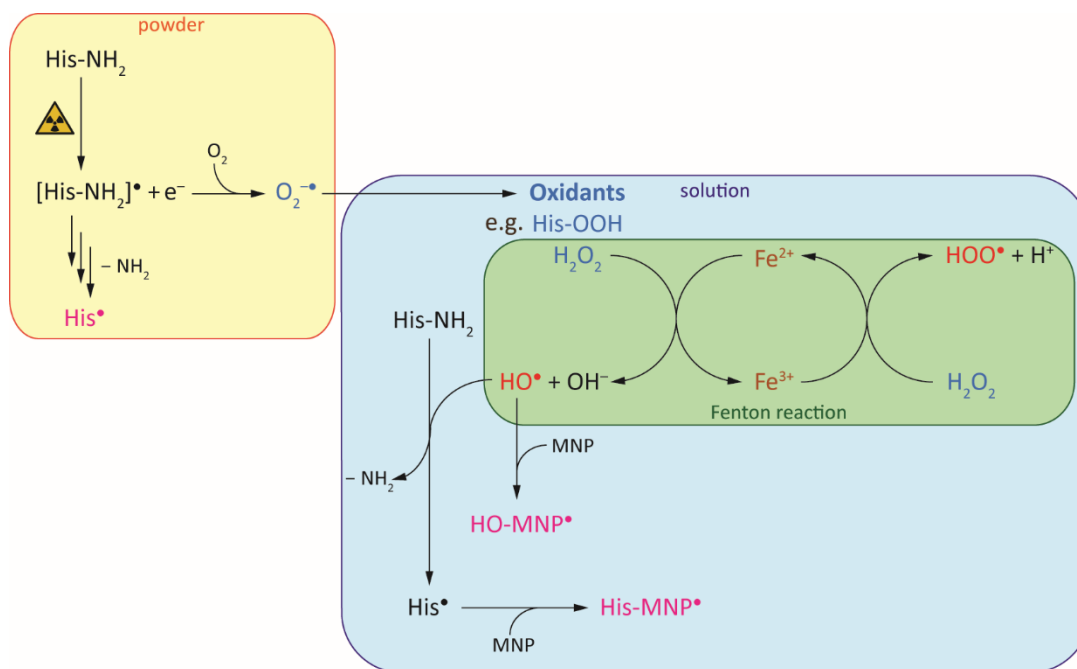


Figure 4.36 Irradiation of L-his powder with formation of strong oxidants (labelled in blue) involved in the regeneration of L-his radicals in solution. The ROS produced from the Fenton reaction (in red) are scavenged by L-his, with the consequent formation of L-his radicals readily trapped by MNP to form species detected by EPR (magenta).

This hypothesis was verified when, by adding a chelating agent to the reaction mixture, the regeneration of the radical was suppressed. The source of trace metals was found to be the medical needle which was used with a syringe to transfer the sample solution into the EPR quartz capillary tube, as showed by an XRF analysis on the needles. In fact, using a glass Pasteur pipette in place of the syringe for transferring the sample, the radical regeneration was suppressed. Strong oxidant species such as $\cdot\text{OH}$ and H_2O_2 that could be involved in the Fenton-type reaction can easily originate from the irradiation process from radiolysis of water.⁴¹ The fact that the same regeneration properties were not observed for other excipients such as D-mannitol (see **Chapter 5**) was attributed to the antioxidant characteristics of the histidine molecule, as previously described,⁴⁻⁸ that make it more susceptible to the oxidative attack of ROS.

As mentioned earlier, the presence of strong oxidants is required for the Fenton chemistry to occur. Such oxidants can easily form as a result of the irradiation process. In fact, the primary effect of exposing L-his to ionising radiations is the ejection of an electron from the molecule itself.⁴² Thus, in addition to the formation of a histidine radical, in the presence of air, the ejected electron can also combine with molecular oxygen leading to the formation of a superoxide radical. This reactive oxygen species can in turn lead to the generation of other ROS such as hydrogen peroxide and histidine hydroperoxides. All these species can be responsible for initiating the observed Fenton chemistry in solution and the consequent production of additional ROS. The well-known scavenging properties of L-his towards ROS^{4,5,43} suggest that these reactive species are quenched by histidine in solution, hence further generating deamination radicals which are readily trapped by MNP.

This results are of great significance in the use of irradiated sterilization of excipients in parenteral formulations, for which the reconstitution process or drug delivery might involve use of similar medical needles providing sufficient trace metals for radical regeneration. Special attention should therefore be taken when dealing with drug components, either excipients or APIs, with known antioxidant properties, as the same regeneration mechanism can potentially take place.

4.4.4 Recombination of radicals in solution

EPR techniques can indeed provide extremely valuable information on the effects of radiation sterilization on pharmaceutically relevant substances, allowing the characterization of radical species formed upon irradiation and investigating the behaviour of these degradants in solution. Such organic radicals are known to have a very limited life time in solution, and would therefore

recombine quickly after dissolution. Figure 4.37 shows possible decomposition pathways for histidine when it is directly irradiated in solution. As can be seen from the scheme, multiple reactions can occur, leading to the formation of a number of different molecules. In particular, imidazolelactic acid is reported to form after deamination of the molecule induced by irradiation. Such compound could then undergo several molecular rearrangements, producing either urocanic acid or imidazoleacetaldehyde which could then be further oxidized to imidazoleacetic acid.

MS and NMR analysis were performed in the attempt to obtain information regarding the fate of histidine radicals after dissolution. Neither analyses revealed the presence of newly formed degradants. This can be attributed to the limited sensitivity of such techniques, which did not allow signals of species other than the main compound to be discerned.

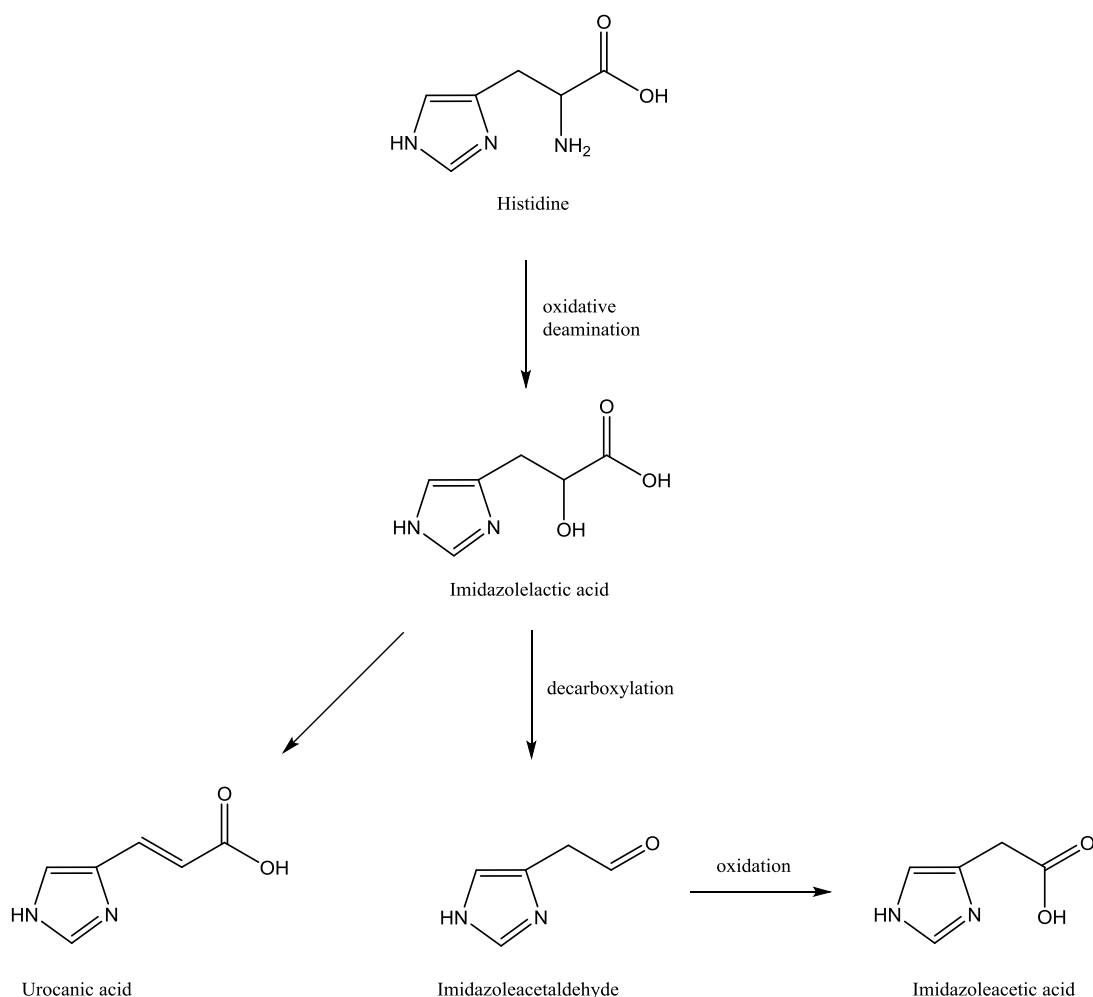


Figure 4.37 Suggested decomposition scheme for histidine from irradiation in solution, revised from ref. 44.

4.5 Conclusions

The effects of irradiation sterilization on the parenteral excipient L-his have been analysed by CW EPR spectroscopy and the spin-trapping methodology. Although studies on X-irradiated histidine crystals have been previously reported,¹⁰⁻¹² the experiments presented in this study are, to the best of our knowledge, the first report on the effects of γ -irradiation on solid L-his. Whilst the identity of the irradiation induced deamination radical formed has been confirmed previously through both direct analysis of the X-irradiated solid¹² and through spin-trapping experiments,^{21,22} in this work the fate of the irradiation products in solution has been further explored. As expected upon dissolution of the irradiated powder in a physiological solution, the radical species were found to have a short lifetime; however, spin-trapping experiments show not only the formation of C-centred radical adducts, but also the regeneration of radical species long after the initial dissolution of the irradiated material. Fenton-type chemistry, catalysed by trace metals from a standard sterile syringe needle, was implicated in this process. This appears to be the first report on a Fenton reaction driving radical regeneration in a medical context.

Knowing the behaviour of the reactive degradation products in solution is essential when dealing with excipients intended for parenteral formulations. Avoiding the regeneration of the radicals in solution is necessary in order to eliminate the potential for radical-induced degradation of other drug components, APIs in particular, in a complete pharmaceutical formulation. Unintentional injection of free radical containing solutions into patients could also have direct toxicological issues. Whilst a thorough analysis of each irradiation sterilized product remains necessary, assessing the effects of γ -irradiation on single drug ingredients is an essential first step towards the analysis of multi-component systems. In this Chapter it has been shown that not only the degradants formed directly by the irradiation procedure, but also the subsequent products of potentially complex solution mechanisms, must be taken into account.

4.6 References

1. Kaisheva, E. A., Flores-Nate, A. & Gupta, S. Stable lyophilized pharmaceutical formulation of IgG antibodies. (2003).
2. Kamerzell, T. J., Esfandiary, R., Joshi, S. B., Middaugh, C. R. & Volkin, D. B. Protein – excipient interactions : Mechanisms and biophysical characterization applied to protein formulation development. *Adv. Drug Deliv. Rev.* **63**, 1118–1159 (2011).

3. Tian, F. *et al.* Spectroscopic evaluation of the stabilization of humanized monoclonal antibodies in amino acid formulations. *Int. J. Pharm.* **335**, 20–31 (2007).
4. Foote, C. S. & Clennan, E. L. in *Active oxygen in chemistry* 105–140 (Springer, 1995).
5. Wade, A. M. & Tucker, H. N. Antioxidant characteristics of L-histidine. *J. Nutr. Biochem.* **9**, 308–315 (1998).
6. Erickson, M. C. & Hultin, H. O. A unique role of histidine in Fe-catalyzed lipid oxidation by fish sarcoplasmic reticulum. *Basic Life Sci.* **49**, 307–312 (1987).
7. Erickson, M. C. & Hultin, H. O. Influence of histidine on lipid peroxidation in sarcoplasmic reticulum. *Arch. Biochem. Biophys.* **292**, 427–432 (1992).
8. Matheson, I. B. C. & Lee, J. Chemical Reaction Rates of Amino Acids. *Photochem. Photobiol.* **29**, 879–881 (1979).
9. Yates, Z. *et al.* Histidine residue mediates radical-induced hinge cleavage of human IgG1. *J. Biol. Chem.* **285**, 18662–18671 (2010).
10. Box, H. C. ENDOR Study of Irradiated Histidine HCl. *J. Chem. Phys.* **46**, 2130 (1967).
11. Ngo, F. Q. Free radical formation in x-irradiated histidine HCl. *J. Chem. Phys.* **60**, 3373 (1974).
12. Westhof, E., Flossmann, W., Ludemann, H.-D. & Muller, A. ESR and INDO study of radical conformations in irradiated single crystals of L-histidine free base. *J. Chem. Phys.* **61**, 3376–3381 (1974).
13. Box, H. C., Freund, H. G. & Budzinski, E. E. Paramagnetic Absorption of Irradiated Glycine. *J. Am. Chem. Soc.* **88**, 658–661 (1966).
14. Sinclair, J. W. & Hanna, M. W. Electron paramagnetic resonance study of L-alanine irradiated at low temperatures. *J. Phys. Chem.* **71**, 84–88 (1967).
15. Ayscough, P. B. & Roy, A. K. Electron spin resonance studies of fundamental processes in radiation- and photo-chemistry. Part 5.—Dissociative electron capture in amino acids at low temperatures. *Trans. Faraday Soc.* **64**, 582–595 (1968).
16. Sinclair, J. W. & Hanna, M. W. ESR Study of L-Alanine-1-¹³C Irradiated at Low Temperatures. *J. Chem. Phys.* **50**, 2125–2129 (1969).

17. Castleman, B. W. & Moulton, G. C. Electron Spin Resonance and Electron Nuclear Double Resonance Studies of DL- Serine. II. Identification of Free Radicals Produced in the Range 153–340 °K. *J. Chem. Phys.* **57**, 2762–2768 (1972).
18. Kuwabara, M., Lion, Y. & Riesz, P. E.S.R. of Spin-trapped Radicals from Sugars. Reactions of Hydroxyl Radicals in Aqueous Solutions and γ -radiolysis in the Polycrystalline State. *Int. J. Radiat. Biol. Relat. Stud. Physics, Chem. Med.* **39**, 451–455 (1981).
19. Lagercrantz, C. & Forschult, S. Trapping of Free Radicals formed by γ -Irradiation of Organic Compounds. *Nature* **218**, 1247–1248 (1968).
20. Makino, K. & Riesz, P. E.S.R. of spin-trapped radicals in γ -irradiated polycrystalline amino acids. Chromatographic separation of radicals. *Int.J.Radiat.Biol.* **41**, 615–624 (1982).
21. Minegishi, A., Bergene, R. & Riesz, P. E.s.r. of spin-trapped radicals in γ -irradiated polycrystalline amino acids, N-acetyl amino acids and dipeptides. *Int. J. Radiat. Biol.* **38**, 627–650 (1980).
22. Rustgi, S., Joshi, A., Riesz, P. & Friedberg, F. E.s.r. of spin-trapped radicals in aqueous solutions of amino acids. Reactions of the hydrated electron. *Int. J. Radiat. Biol.* **32**, 533–552 (1977).
23. Lehmann, M. S., Koetzle, T. F. & Hamilton, W. C. Precision neutron diffraction structure determination of protein and nucleic acid components. IV. The crystal and molecular structure of the Amino Acid L-Histidine. *Chem. Biol. Drug Des.* **4**, 229–239 (1972).
24. Brown, T. A. *Molecular Biology LabFax*. (BIOS Scientific Publishers Ltd., 1991).
25. Stoll, S. & Schweiger, A. EasySpin, a comprehensive software package for spectral simulation and analysis in EPR. *J. Magn. Reson.* **178**, 42–55 (2006).
26. Baker, M. T., Gregerson, M. S., Martin, S. M. & Buettner, G. R. Free radical and drug oxidation products in an intensive care unit sedative: propofol with sulfite. *Crit. Care Med.* **31**, 787–792 (2003).
27. Williams, H. E., Loades, V. C., Claybourn, M. & Murphy, D. M. Electron paramagnetic resonance spectroscopy studies of oxidative degradation of an active pharmaceutical ingredient and quantitative analysis of the organic radical

- intermediates using partial least-squares regression. *Anal. Chem.* **78**, 604–608 (2006).
28. Karakirova, Y. & Yordanov, N. Mannitol as a radiation sensitive material for electron paramagnetic resonance dosimetry. *Bulg. Chem. Commun.* **47**, 144–148 (2015).
 29. Toriyama, K., Muto, H., Nunome, K. & Fukaya, M. Radiation damages of organic materials at 4 K: An ESR study of polyethylene and related hydrocarbons. *Radiat. Phys. Chem.* **18**, 1041–1052 (1981).
 30. Iwasaki, M., Toriyama, K., Fukaya, M., Muto, H. & Nunome, K. 4 K Radiolysis of Linear Alkanes as Studied by Electron Spin Resonance Spectroscopy: Selective Formation of Terminal Alkyl Radicals in the Primary Process. *J. Phys. Chem.* **89**, 5278–5284 (1985).
 31. Iwasaki, M., Toriyama, K., Muto, H. & Nunome, K. Pairwise trapping of radicals in single crystals of n-decane irradiated at 1.5 and 4.2 K. *J. Chem. Phys.* **65**, 596–606 (1976).
 32. Nunome, K., Muto, H., Toriyama, K. & Iwasaki, M. ESR Studies of Local Concentrations of Radicals in Polyethylene Irradiated at 1.5, 4.2 and 77 K. *Chem. Phys. Lett.* **39**, 542–546 (1976).
 33. Gillbro, T. & Lund, A. High yield of radical pairs in deuterated n-alkane single crystals γ -irradiated at 4.2 K. *Chem. Phys. Lett.* **34**, 375–377 (1975).
 34. Toriyama, K. & Iwasaki, M. Electron Spin Resonance Studies on Radiolysis of Crystalline Methanol at 4.2 K. *J. Am. Chem. Soc.* **101**, 2516–2523 (1979).
 35. Neyens, E. & Baeyens, J. A review of classic Fenton's peroxidation as an advanced oxidation technique. *J. Hazard. Mater.* **98**, 33–50 (2003).
 36. Lai, C-S; Piette, H. Further evidence for OH radical production in Fenton's reagent. *Tetrahedron Lett.* **20**, 775–778 (1997).
 37. Hasanain, F., Guenther, K., Mullett, W. M. & Craven, E. Gamma sterilization of pharmaceuticals - A review of the irradiation of excipients, active pharmaceutical ingredients, and final drug product formulations. *PDA J. Pharm. Sci. Technol.* **68**, 113–137 (2014).
 38. Zhao, Y., Wang, M., Tang, Z. & Wu, G. ESR study of free radicals in UHMW-PE fiber irradiated by gamma rays. *Radiat. Phys. Chem.* **79**, 429–433 (2010).

39. Przyklenk, K., Whittaker, P. & Kloner, R. A. In vivo infusion of oxygen free radical substrates causes myocardial systolic, but not diastolic dysfunction. *Am. Heart J.* **119**, 807–815 (1990).
40. Saray, A., Apan, A. & Kisa, U. Free radical-induced damage in experimental peripheral nerve injection injury. *J. Reconstr. Microsurg.* **19**, 401–406 (2003).
41. Gopal, N. G. S. Radiation sterilization of pharmaceuticals and polymers. *Radiat. Phys. Chem.* **12**, 35–50 (1978).
42. Symons, M. C. R. Electron spin resonance studies of radiation damage to DNA and to proteins. *Rad. Phys. Chem.* **45**, 837–845 (1995).
43. Zs.-Nagy, I. & Floyd, R. A. Hydroxyl free radical reactions with amino acids and proteins studied by electron spin resonance spectroscopy and spin-trapping. *Biochim. Biophys. Acta* **790**, 238–250 (1984).
44. Augenstein, L. G., Mason, R. & Quastler, H. *Advances in Radiation Biology.* **1**, (Academic Press, 1964).

Chapter 5

Irradiation of D-mannitol

This Chapter investigates the effects of γ -radiation sterilization on the parenteral excipient D-mannitol. Room temperature irradiation was found to induce the formation of at least two persistent radical species. The primary radical species formed by irradiation in liquid nitrogen were characterized and their evolution into the room temperature species was studied. The reactivity of the radical species in solution was evaluated with spin trapping experiments. MS and NMR analysis were performed in order to gather further information on the degradants formed upon irradiation.

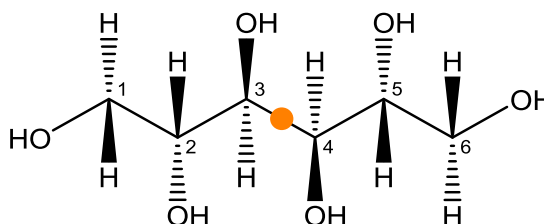


Figure 5.1 Chemical structure of D-mannitol, highlighting the axis of C_2 symmetry (orange).

5.1 Introduction

5.1.1 Industrial use of D-mannitol

D-mannitol ($C_6H_{14}O_6$, MW 182.17) is a naturally occurring sugar alcohol found in animals and plants, largely used in the pharmaceutical and food industries. It is also known simply as mannitol, manna sugar, mannite, mannitolum and, being approved as a food additive, it corresponds to the E number E421.¹ Chemically, it is a hexahydric alcohol, isomer of sorbitol to which it differs only for the planar orientation of the hydroxyl group on carbon 2 (Figure 5.2). This structural difference confers to the two sugars substantially different properties, the most important being the response to moisture that makes mannitol non-hygroscopic in contrast to sorbitol, which is instead hygroscopic.² The molecule of mannitol presents a C_2 symmetry, with the C_2 two-fold symmetry axis at a right angle to the aliphatic chain (Figure 5.1).

In food applications, mannitol is mainly used as a bulking agent. In pharmaceuticals preparations, it is primarily used as a diluent in tablet formulations (10–90% w/w) thanks to its non-hygroscopicity, a property that makes it suitable to be used with moisture-sensitive active ingredients. In lyophilized preparations, mannitol (20–90% w/w) is included to produce a homogeneous cake, improving the appearance of the lyophilized plug in a vial.²

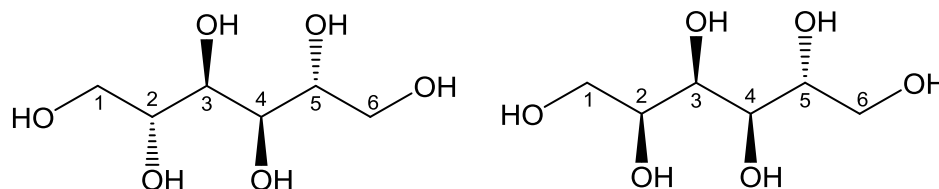


Figure 5.2 Structures of D-mannitol (left) and sorbitol (right).

5.1.2 Mannitol in lyophilized formulations

Mannitol is considered the most widely used bulking agent in lyophilized formulations. Its large use depends on its many positive properties such as promoting crystallinity, thus stabilizing the final product, and also for its high eutectic point and matrix properties.³ In protein containing formulations, mannitol also displayed significant protection of the protein against aggregation when used in small enough quantity not to promote excessive crystallization.⁴ It is also preferred to reducing sugars in protein formulation as a cryo- or lyoprotectant for its characteristic of not reacting with proteins via the Maillard reaction.³

5.1.3 Therapeutic properties of D-mannitol

Administered parenterally, mannitol exerts multiple therapeutic effects by elevating blood plasma osmolarity and consequently elevating the flow of water from tissues. As such it is used as an osmotic diuretic, a diagnostic agent for kidney function, an adjunct in the treatment of acute renal failure, an agent to reduce intracranial pressure, in the treatment of cerebral edema and to reduce intraocular pressure. Orally, it is not significantly absorbed from the gastrointestinal tract, but can cause osmotic diarrhoea if consumed in large doses.²

5.1.4 EPR studies on D-mannitol

The irradiation of mannitol leads to the formation of persistent paramagnetic species which have not yet been identified. The same radicals produced by γ -irradiation were also found to be produced by grinding.^{5,6} The complex unresolved EPR spectrum of irradiated mannitol was found to change in the first days after the irradiation due to the presence of unstable short-lived radical species,⁶ which is characteristic of different saccharides.^{7–9} Microwave (MW) saturation

studies of the stable EPR spectra suggested the presence of at least two different paramagnetic species. Mannitol had recently been proposed for dosimetric purposes, showing a linear dose response in the range of 1 Gy to up to 10 kGy and an EPR spectrum stable for several months, characteristics which make it suitable as a dosimetric material.⁶

The following work aims to characterize the radical species formed upon irradiation of D-mannitol, studying the evolution of the primary species formed into the r.t. stable species. The spin trapping methodology was applied to study the dissolution of the irradiated powder and MS and NMR analysis were used to investigate the recombination of the radical in solution.

5.2 Experimental

Below are the experimental sample preparation and instrumentation set up specific to this Chapter. More details regarding instrumentation and the irradiation setup are described in **Chapter 3**.

5.2.1 Sample preparation

5.2.1.1 Growth and analysis of D-mannitol single crystal

D-mannitol single crystals were grown from a saturated aqueous solution by slow evaporation at room temperature, as described in **Chapter 3**. Their structure was determined by single crystal X-ray diffraction on a *Rigaku Oxford Diffraction Gemini R* and was found to be orthorhombic with space group $P2_12_12_1$ ($a = 5.5376(1)$ Å, $b = 8.5976(2)$ Å, $c = 16.8069(4)$ Å), in agreement with previously published structures (Figure 5.3).^{10,11}

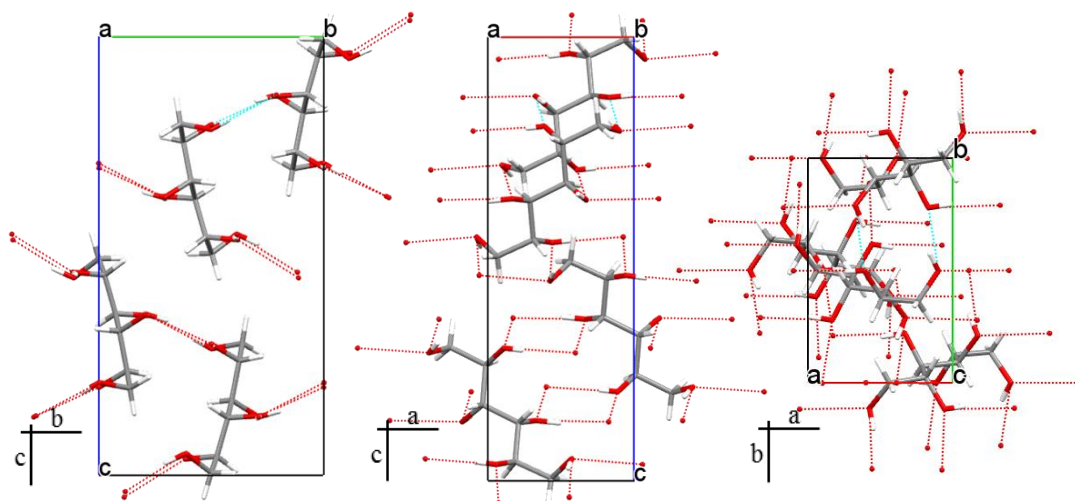


Figure 5.3 Crystallographic structure of the single crystal of D-mannitol viewed along *a*, *b* and *c* crystallographic axes.

5.2.1.2 Spin trapping experiments

Spin trapping experiments were performed dissolving γ -irradiated powders in an aqueous solution containing the spin trapping agent MNP. The concentration of D-mannitol in solution was approximately 0.27 M (unless otherwise stated), to match the concentration used for L-histidine in **Chapter 4**. The solution was vortexed for 1 min and the powder readily dissolved. The solution was then centrifuged and inserted in a 1 mm i.d. EPR quartz tube for the analysis. The regeneration of the radical in solution was also tested, solubilizing the powder in water first and adding the spin trapping agent after *ca.* 3 mins.

Samples were analysed on a *Bruker EMX* spectrometer with a cylindrical cavity (ER 4122 SHQE), starting the acquisition *ca.* 6 mins after the addition of the spin trapping agent. More specific details regarding EPR acquisition and spin adduct quantification are described in **Chapter 3**.

5.2.2 EPR simulations

Simulation of the MNP-mannitol spin adduct was performed by including the only hyperfine coupling arising from the nitroxidic nitrogen, which was considered to be fully isotropic. An isotropic *g*-tensor was used; dynamic effects were found not to affect the spectrum and were therefore neglected.

Further details regarding EPR simulations are reported in **Chapter 4**.

5.3 Results

5.3.1 Non-irradiated D-mannitol powder control

As previously mentioned, EPR active species can be formed in mannitol not only from irradiation, but also from other industrial processes.^{5,6} To investigate the presence of a background EPR signal on the purchased high purity (99%) D-mannitol powder, a spectrum of the non-irradiated powder was acquired at r.t. No EPR signal was detected, indicating the absence of persistent radicalic degradation products above the detection limit (\sim nM concentration).

5.3.2 γ -irradiated D-mannitol powder EPR spectra

The effects of r.t. γ -irradiation on D-mannitol powder were then evaluated. The irradiation of the powder was performed as described in **Chapter 3**.

The EPR analysis of the irradiated powder samples revealed the formation of persistent radical species, as shown in Figure 5.4. Four main features could be observed in the spectrum, suggesting a coupling with multiple protons. The microwave (MW) power saturation spectra in Figure 5.5 shows how, as the MW power is increased, the four main features disappear and another species consisting on a broad singlet emerges from the spectrum.

Figure 5.4 also shows that the same radical species are observed irrespective of the radiation dose delivered. Quantification of the paramagnetic species was performed as described in **Chapter 3** and indicated a radical concentration of 6.05(2), 11.46(2), 13.88(2) mM for the samples receiving respectively a total dose of 25, 125 and 250 kGy ($\pm 5\%$), suggesting a non-linear correlation between the radical concentration and the radiation dose in this range. This finds correspondence with a previous work where the linearity between the irradiation dose received and the EPR signal of D-mannitol was found to be maintained only up to 10 kGy.

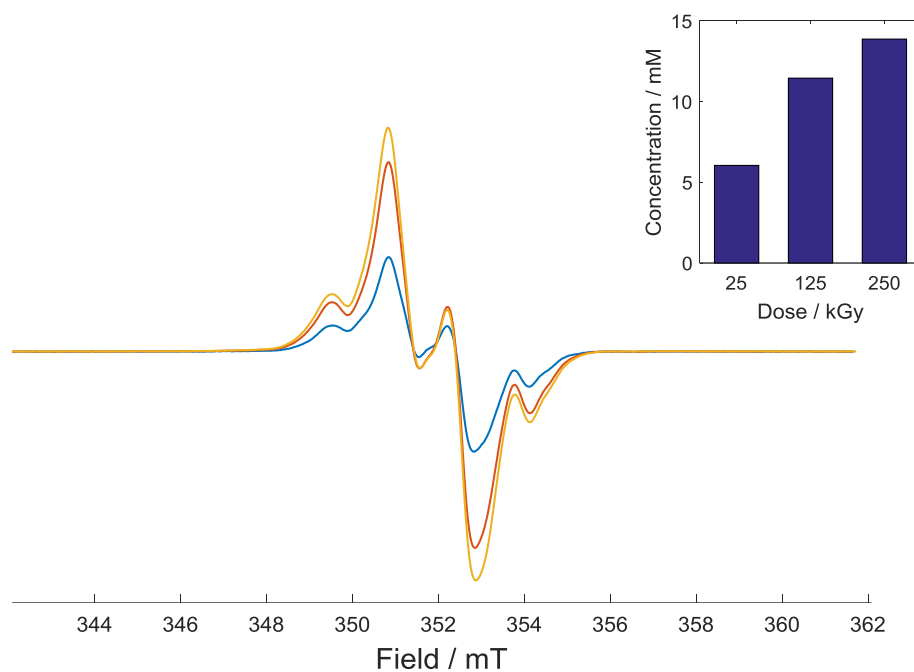


Figure 5.4 Radiation dose dependence of γ -irradiated D-mannitol powder. Total irradiation dose of 25 kGy (blue), 125 kGy (red) and 250 kGy (yellow). Inset: concentration of radical species detected for each irradiated sample.

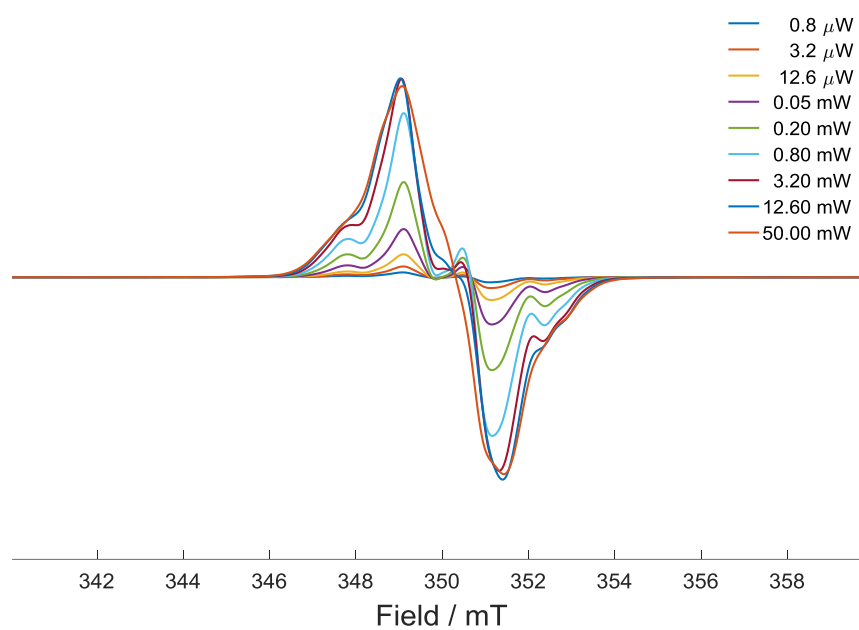


Figure 5.5 Microwave power saturation spectra of γ -irradiated (250 kGy) D-mannitol powder.

5.3.3 Multi-frequency EPR

Multi-frequency EPR analysis was undertaken to obtain information on the r.t. persistent species formed upon irradiation of D-mannitol. X-irradiated D-mannitol powder was analysed at X-band (9.8 GHz), W-band (94 GHz) and 263 GHz (Figure 5.6). All the spectra are dominated by a broad line on top of which additional signals can be observed. The 263 GHz spectrum in particular, allows the presence of multiple spectral components to be appreciated, which can be attributed to multiple radical species. The assignment of the said species cannot be easily done since, although the lines are much more differentiated compared to the X-band spectrum, some of them are still partially overlapping, impeding a direct attribution of the spectral features to a specific radical. The distribution of the lines over a wide magnetic field range could be an indication of species characterised by rather different g -values, but could also reflect the presence of anisotropic g -factors for some of them.

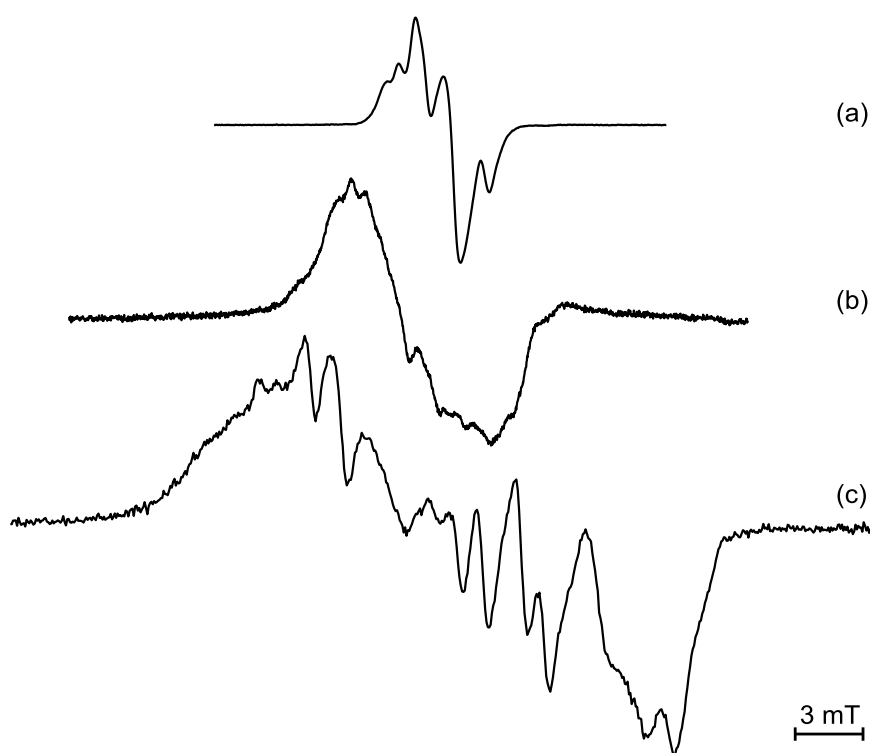


Figure 5.6 Multi-frequency EPR analysis of X-irradiated D-mannitol powder, receiving a dose of *ca.* 29 kGy. (a) X-band, 9.8 GHz. (b) W-band, 95 GHz. (c) mm-wave, 263 GHz.

5.3.4 Cold irradiation

5.3.4.1 Radical I – 80 K

The EPR spectra of γ -irradiated D-mannitol protonated and partially deuterated (see **Chapter 3** for details on deuteration) crystals at 80 K are shown in Figure 5.7A. At this temperature, when the crystals were oriented along one of the main crystallographic directions, a broad doublet was detected for both samples. Such paramagnetic species, hereafter labelled as *radical I*, exhibited a relatively small hyperfine anisotropy in the yz plane, as can be observed from the roadmap obtained from rotation of the crystal around the x axis (Figure 5.8). Furthermore, the overall anisotropy of the hyperfine coupling appeared to be small, as can be inferred from the spectra of protonated and partially deuterated powders (Figure 5.7B). The isotropic hyperfine coupling and g -factor parameters for the crystals were extracted by simulations with Easyspin¹² and are reported in Table 5.1.

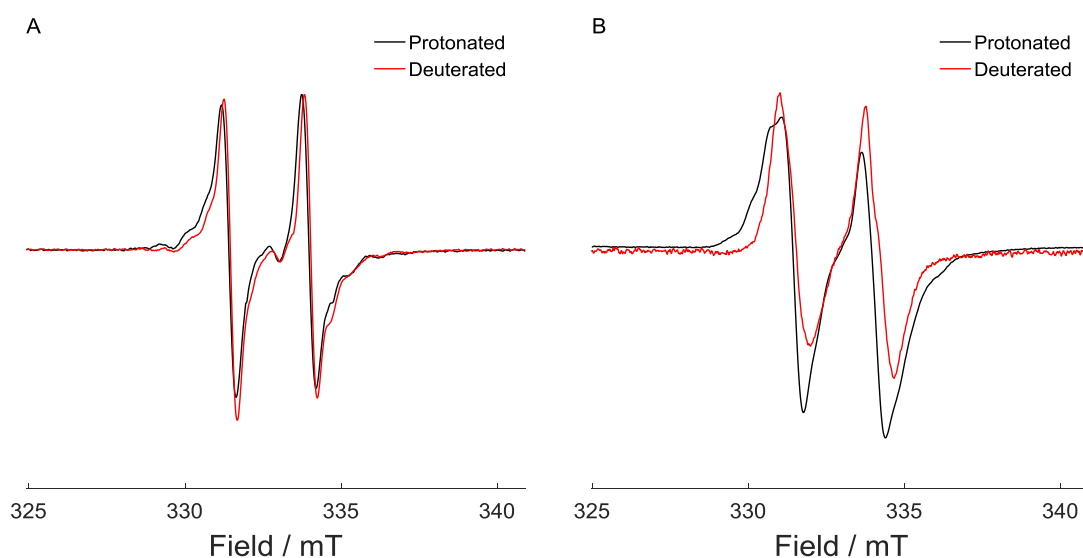


Figure 5.7 CW EPR spectra of D-mannitol protonated and partially deuterated single crystals (A) and powders (B) at 80 K after γ -irradiation in liquid nitrogen. The crystals are oriented along one of the main crystallographic axes.

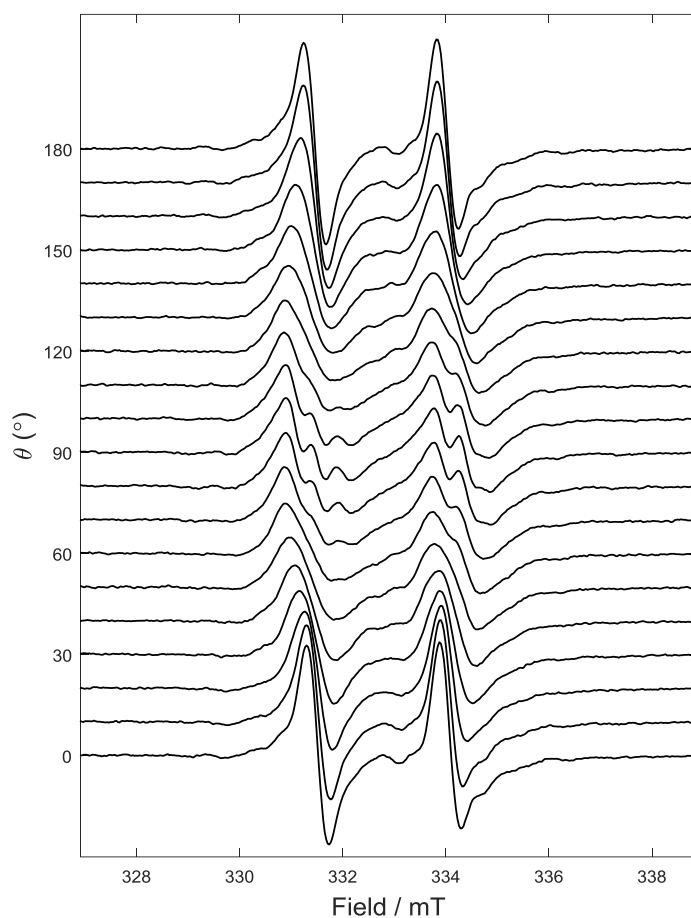


Figure 5.8 Roadmap of partially deuterated D-mannitol single crystal at 80 K, oriented along one of the main crystallographic axes and rotating in the yz plane.

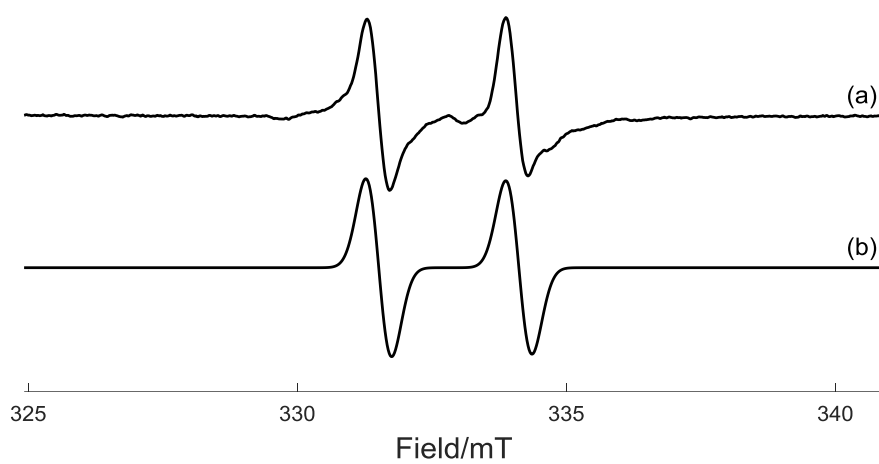


Figure 5.9 (a) CW EPR spectrum of partially deuterated D-mannitol single crystal at 80 K oriented along one of the main crystallographic axes. (b) Easyspin¹² simulation using the parameters reported in Table 5.1.

Table 5.1 EPR isotropic hyperfine couplings (MHz), g -values and peak-to-peak line width (mT) for *radical I* extracted from EasySpin¹² simulation of protonated and partially deuterated single crystals at 80 K.

		a_{β}^{H}	g -value	lw_{pp}
Radical I	Protonated	73.0(5)	2.0039(2) ^a	0.63(2)
	Deuterated	72.7(5)	2.0032(2) ^a	0.48(2)

^a determined by comparison with a DPPH standard.

5.3.4.2 Radical II – 120 K

As the temperature was raised from 80 K to 120 K, the EPR spectrum underwent significant changes. In particular, two additional peaks clearly emerged in the single crystal spectrum at higher g -values, as indicated in Figure 5.10 (∇). The formation of these peaks was found to be irreversible, as no changes were detected by decreasing the temperature back to 80 K. The same peaks were detected for both the protonated and partially deuterated crystals (Figure 5.12).

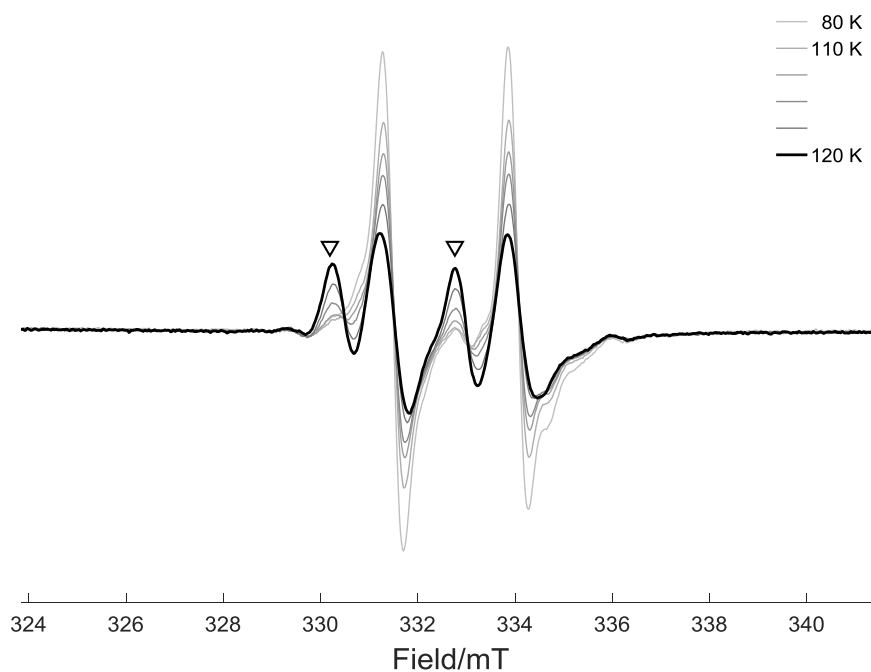


Figure 5.10 Annealing of γ -irradiated D-mannitol partially deuterated single crystal from 80 K (light gray) to 120 K (black). ∇ show additional peaks emerging upon annealing. The crystal is oriented along one of the main crystallographic axes.

A comparison between the spectra observed at 80 K and 120 K (Figure 5.11), highlighted how a small fraction of this species seemed to be already present before the annealing. It is also worth noticing that the lines of *radical I* are broadening when the new peaks emerge from the spectrum, as can be seen in particular on the high field line (Figure 5.10). Such broadening was interpreted as the presence of additional peaks almost overlapping to the lines of *radical I*. This interpretation is supported by the observation of the crystal roadmap at 120 K (Figure 5.13).

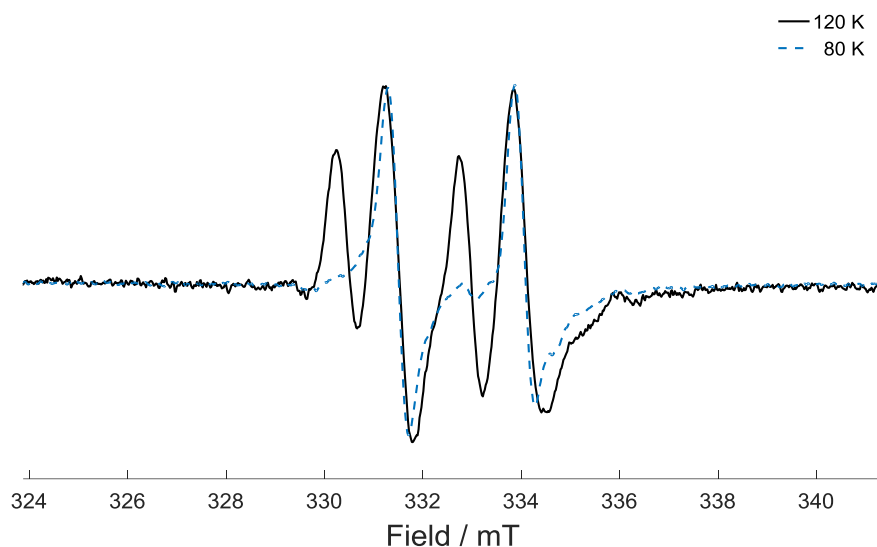


Figure 5.11 Comparison between the EPR spectra of the partially deuterated single crystal at 80 K and 120 K, oriented along one of the main crystallographic axes.

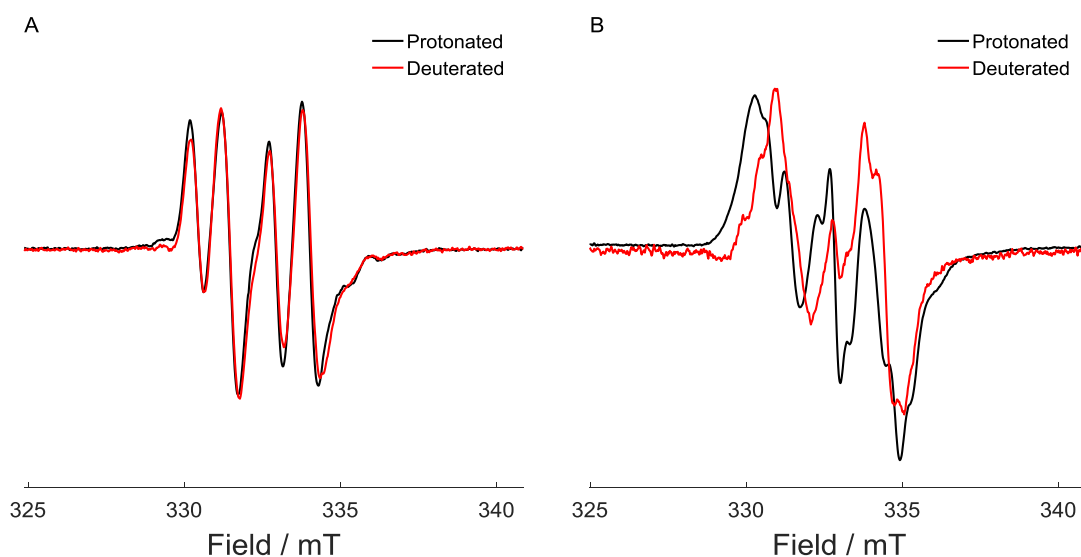


Figure 5.12 CW EPR spectra of D-mannitol protonated and partially deuterated single crystals (A) and powders (B) after γ -irradiation in liquid nitrogen and annealing to 120 K. The crystals are oriented along one of the main crystallographic axes.

When the crystal rotates in the yz plane, additional lines are emerging from the peaks of *radical I* as can be seen by comparison with the roadmap acquired at 80 K, which was characterized by a rather small anisotropy. The new paramagnetic species detected at 120 K, hereafter labelled as *radical II*, was therefore interpreted as a doublet of doublets, originating from the coupling of an unpaired electron with two non-equivalent protons. Along with these considerations, the crystal spectrum was fitted to extract the EPR parameters which are reported in Table 5.2. Minimization of the spectral parameters of *radical I* was performed in order to obtain a better fit. The simulation obtained in Figure 5.14 resulted in good agreement with the experimental data.

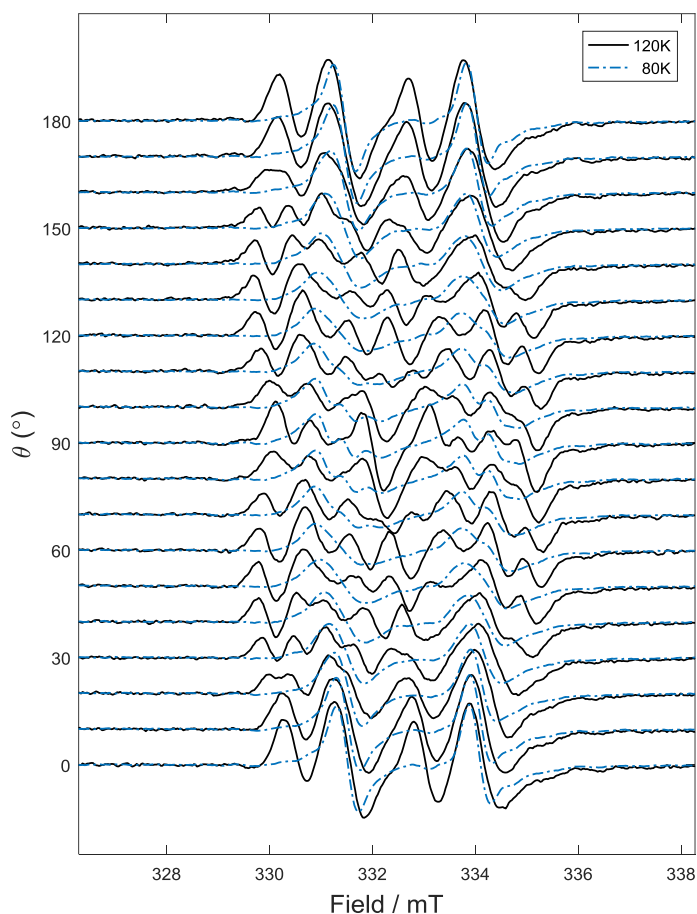


Figure 5.13 Roadmap of partially deuterated D-mannitol single crystal at 120 K (black) and 80 K (dashed dotted blue), oriented along one of the main crystallographic axes and rotating in the yz plane.

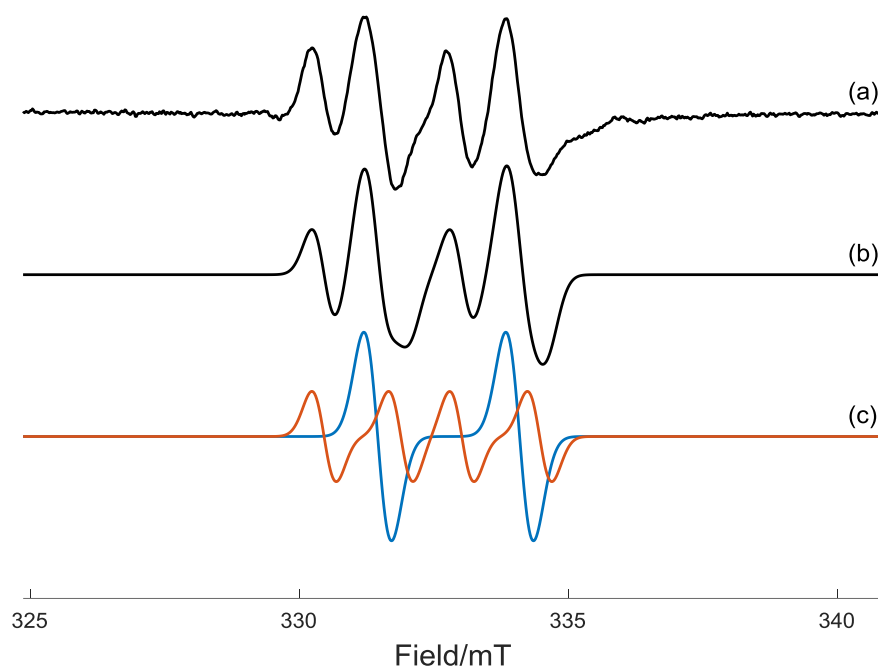


Figure 5.14 (a) CW EPR spectrum of partially deuterated D-mannitol single crystal spectrum at 120 K oriented along one of the main crystallographic axes. (b) Easyspin¹² simulation. (c) simulated contribution of *radical I* (blue) and *radical II* (red) using the parameters reported in **Table 5.2**. The relative weights of *radical I* and *radical II* are respectively *ca.* 60% and 40%.

Table 5.2 EPR isotropic hyperfine couplings (MHz), *g*-values and peak-to-peak line width (mT) for *radical I* and *radical II* extracted from EasySpin¹² simulation of protonated and partially deuterated single crystals at 120 K.

		a_{α}^H	a_{β}^H	<i>g</i> -value	lw_{pp}
Radical I	Protonated	73.9(3)	-	2.0040(2) ^a	0.45(2)
	Deuterated	73.8(3)	-	2.0034(2) ^a	0.51(2)
Radical II	Protonated	36.8(3)	71.9(3)	2.0061(2) ^a	0.45(2)
	Deuterated	40.1(3)	71.9(3)	2.0053(2) ^a	0.45(2)

^a determined by comparison with a DPPH standard.

5.3.4.3 Radical III – 170 K

When the temperature was further raised, no appreciable changes were registered until 170 K. At this temperature, significant alterations were detected in the EPR spectrum, as is shown in Figure 5.15. In particular, two new peaks emerge at ~332 mT and ~334 mT (indicated by ∇). Additionally, a broadening of the low field line is observed (\blacktriangledown), while the intensity of the peak at 333 mT appears to decrease much less than the other peaks (\triangledown). The presence of a new species is also highlighted by comparison of the roadmap spectra of the deuterated crystal at 120 and 170 K (Figure 5.16). Once again, no major differences were detected between protonated and partially deuterated crystal samples, implying that the main protons involved in the interaction do not belong to a hydroxylic group (Figure 5.17). The EPR spectrum was fitted including an additional 4-line species, hereafter labelled as *radical III* (Figure 5.18). Minimization of the spectral parameters of *radical I* and *radical II* was allowed in order to obtain a better fit. The resulting simulation of *radical III* returned isotropic hyperfine values of *ca.* 62 and 47 MHz, and a *g*-value of 2.0043 (Table 5.3).

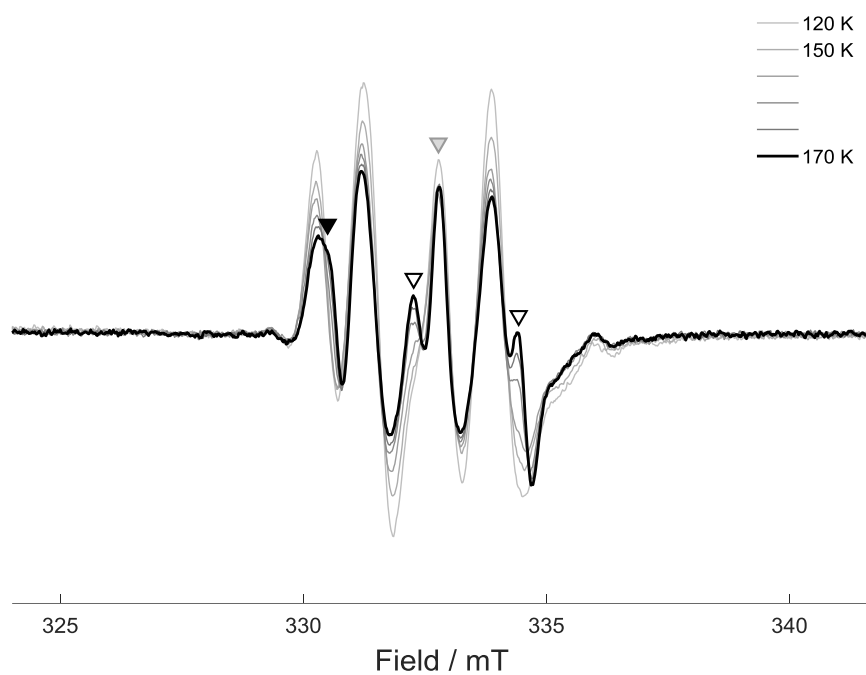


Figure 5.15 Further annealing of γ -irradiated D-mannitol partially deuterated single crystal from 120 K (light gray) to 170 K (black). Triangles highlight spectral changes taking place upon annealing. The crystal is oriented along one of the main crystallographic axes.

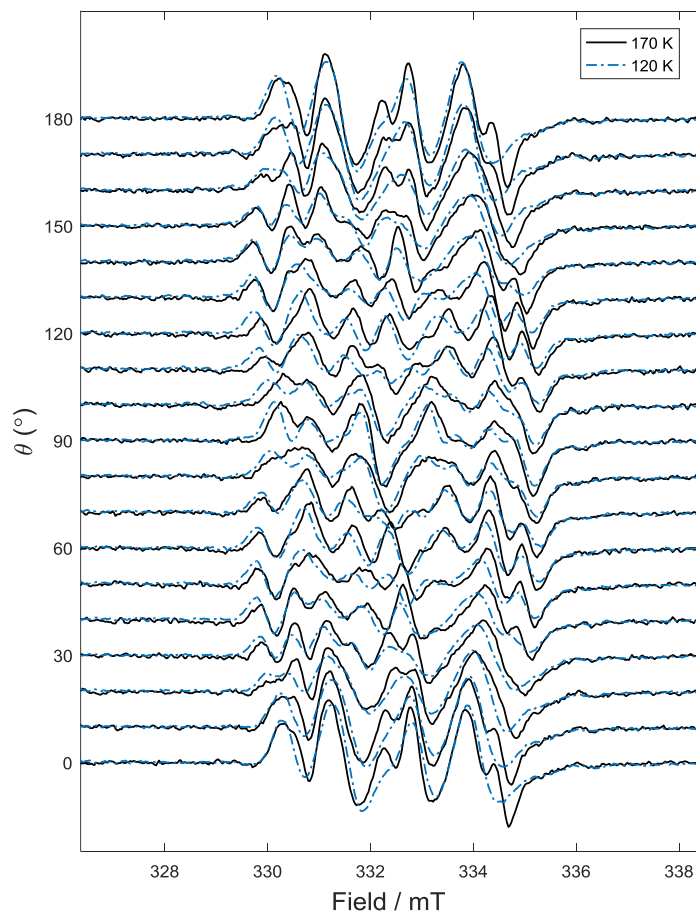


Figure 5.16 Roadmap of partially deuterated D-mannitol crystal at 170 K (black) and 120 K (dashed dotted blue) oriented along one of the main crystallographic axes and rotating in the yz plane.

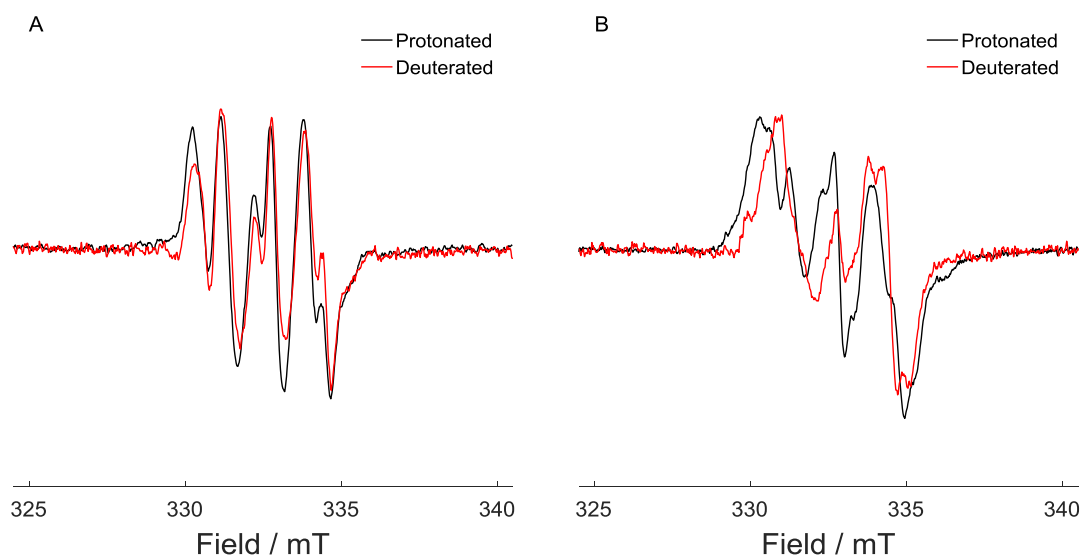


Figure 5.17 CW EPR spectra of D-mannitol protonated and partially deuterated crystals (A) and powders (B) after γ -irradiation in liquid nitrogen and annealing to 170 K. The crystals are oriented along one of the main crystallographic axes.

Table 5.3 EPR isotropic hyperfine couplings (MHz), g -values and peak-to-peak line width (mT) for *radical I*, *radical II* and *radical III* extracted from EasySpin¹² simulation of protonated and partially deuterated single crystals at 170 K.

		a_{α}^{H}	a_{β}^{H}	g -value	lw_{pp}
Radical I	Protonated	74.3(3)	-	2.0040(2) ^a	0.49(2)
	Deuterated	74.7(3)	-	2.0036(2) ^a	0.53(2)
Radical II	Protonated	39.0(3)	73.0(3)	2.0058(2) ^a	0.42(2)
	Deuterated	40.3(3)	74.9(3)	2.0052(2) ^a	0.49(2)
Radical III	Protonated	47.5(3)	61.7(3)	2.0043(2) ^a	0.42(2)
	Deuterated	47.0(3)	62.0(3)	2.0042(2) ^a	0.36(2)

^a determined by comparison with a DPPH standard.

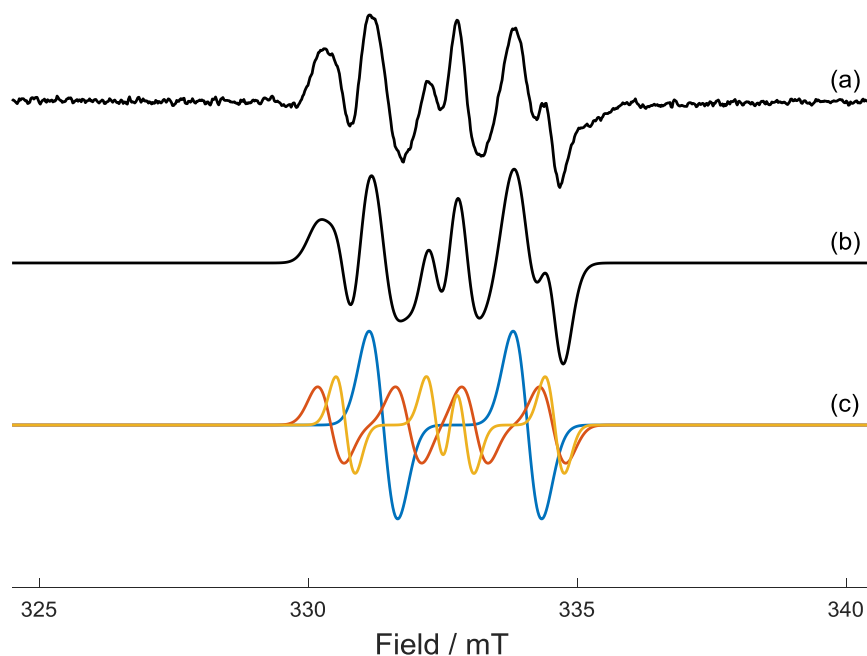


Figure 5.18 (a) CW EPR spectrum of partially deuterated D-mannitol single crystal at 170 K oriented along one of the main crystallographic axes. (b) EasySpin¹² simulation. (c) simulated contribution of *radical I* (blue), *radical II* (red) and *radical III* (yellow) using the parameters reported in **Table 5.3**. The relative weights of *radical I*, *radical II* and *radical III* are respectively *ca.* 46%, 32% and 22%.

5.3.4.4 170 – 200 K

Further annealing of the samples to 200 K resulted in small change in the EPR spectrum, shown in Figure 5.19. The changes include a new peak emerging at ~ 331 mT and a broadening of the peak at ~ 335 mT (∇). Though only minor differences were observed between the EPR spectra of protonated and partially deuterated crystals, appreciable differences can be seen between the powder spectra (Figure 5.20).

Although a thorough interpretation of the spectrum was found to be challenging, the minor differences registered at 200 K in respect to 170 K were tentatively attributed to changes in the concentration of the main components of the EPR spectrum, *radical I*, *radical II* and *radical III*. In particular, the simulation of the spectrum of the deuterated mannitol crystal suggested that, while all the species are decreasing as the temperature is raised, *radical II* and *radical III* are decreasing considerably more than the large doublet associated to *radical I*. The resulting simulation was found to be in good agreement with the experimental data (Figure 5.21). Instead, a satisfactory simulation of the protonated mannitol crystal was not obtained.

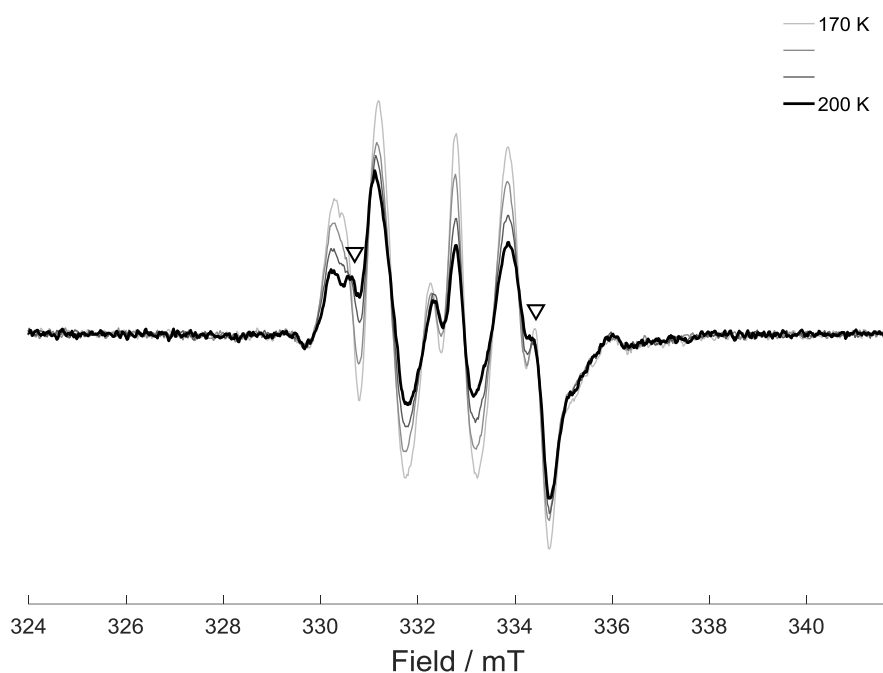


Figure 5.19 Annealing of γ -irradiated D-mannitol partially deuterated single crystal from 170 K (light gray) to 200 K (black). ∇ highlight new peaks emerging upon annealing. The crystal is oriented along one of the main crystallographic axes.

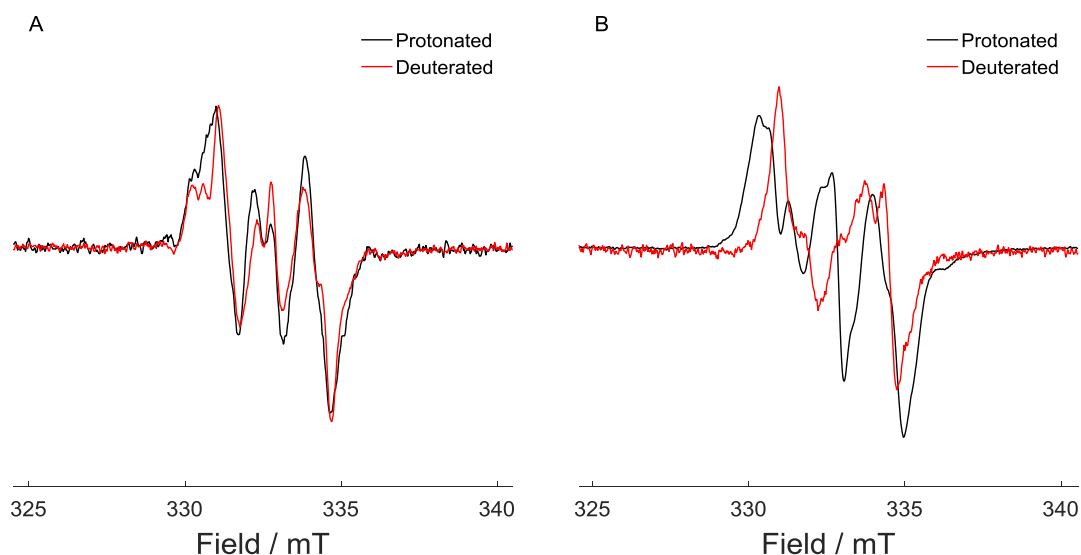


Figure 5.20 CW EPR spectra of D-mannitol protonated and partially deuterated crystals (A) and powders (B) after γ -irradiation in liquid nitrogen and annealing to 200 K. The crystals are oriented along one of the main crystallographic axes.

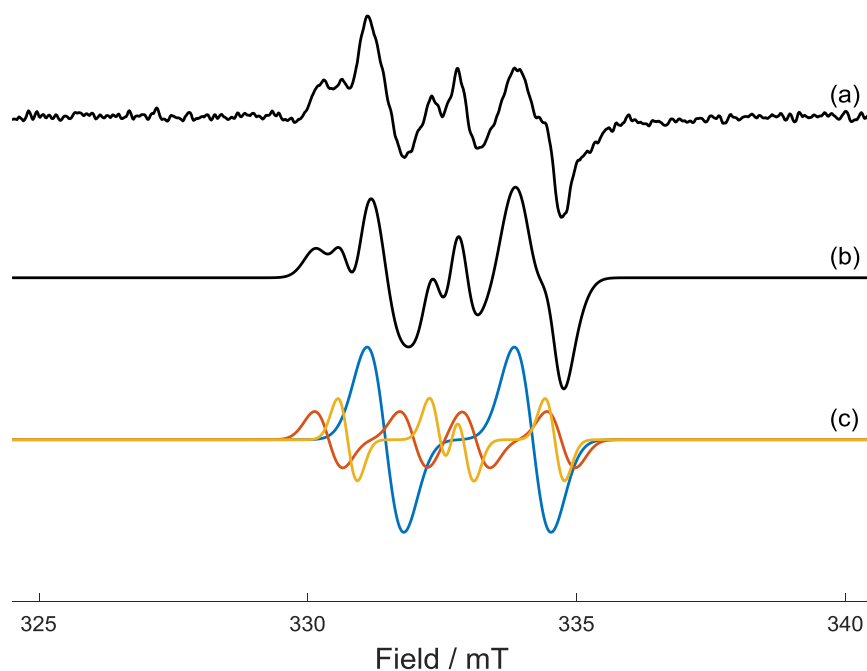


Figure 5.21 (a) CW EPR spectrum of partially deuterated D-mannitol single crystal at 200 K oriented along one of the main crystallographic axes. (b) Simulation obtained with EasySpin.¹² (c) Single components of the simulated spectrum: *radical I* (blue), *radical II* (red) and *radical III* (yellow). The relative weights of *radical I*, *radical II* and *radical III* are respectively *ca.* 62%, 22% and 16%.

Table 5.4 EPR isotropic hyperfine couplings (MHz), g -values and peak-to-peak line width (mT) for *radical I*, *radical II* and *radical III* extracted from EasySpin¹² simulation of partially deuterated single crystals at 200 K.

	a_{α}^H	a_{β}^H	g -value	lw_{pp}
<i>Radical I</i>	76.3(3)	-	2.0033(2) ^a	0.68(2)
<i>Radical II</i>	44.4(3)	76.7(3)	2.0048(2) ^a	0.52(2)
<i>Radical III</i>	47.2(3)	60.7(3)	2.0040(2) ^a	0.36(2)

^a determined by comparison with a DPPH standard.

5.3.4.5 200 – 240 K

As the annealing of the samples proceeded in steps, changes in the EPR spectrum were registered when reaching 240 K. The spectrum of the partially deuterated crystal at 240 K is dominated by a broad doublet progressively emerging as the temperature increase, which displayed similar features to those of *radical I* (Figure 5.22). This was supported by the analysis of the roadmap, which clearly showed a highly isotropic interaction dominating the spectrum (Figure 5.23). The same roadmap acquired at a higher MW power in partially saturated conditions showed how other minor species, also visible in the central part of the spectrum, are mostly hidden by the main radical doublet (∇). Since the contribution of such species was low, it was not possible to obtain a reasonable simulation of all the species involved.

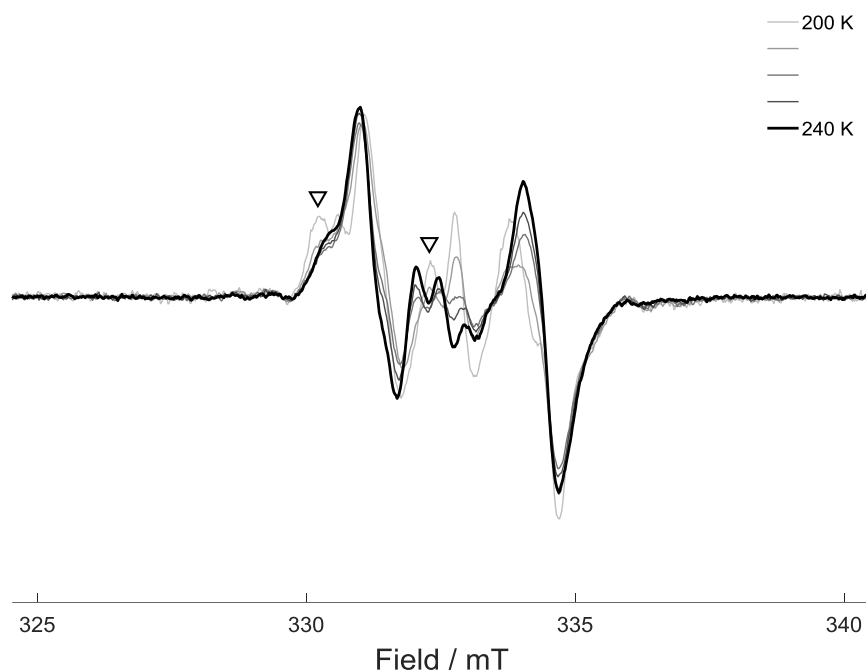


Figure 5.22 Annealing of γ -irradiated D-mannitol partially deuterated single crystal from 200 K (light gray) to 240 K (black). ∇ highlight spectral features of a minor species hidden by the main doublet. The crystal is oriented along one of the main crystallographic axes.

The comparison of the partially deuterated and protonated powder spectra highlighted again some differences between the two (Figure 5.24). In particular, both powder spectra seem to be dominated by a broad doublet, though the broadening of the protonated sample is clearly larger than the partially deuterated one. Such difference can be once again associated to a coupling to an hydroxylic proton. The protonated and partially deuterated crystals displayed instead a more pronounced difference. This was partially attributed to a different orientation of the two crystals in respect to the magnetic field. Nevertheless, it is also worth noticing that, as shown in the roadmap spectra, the partially deuterated crystal spectrum never resembles the protonated one, irrespective of the orientation of the former. As for the powder spectra, this is suggestive of the presence of hydroxylic proton couplings in the additional radical species contributing to the EPR spectrum.

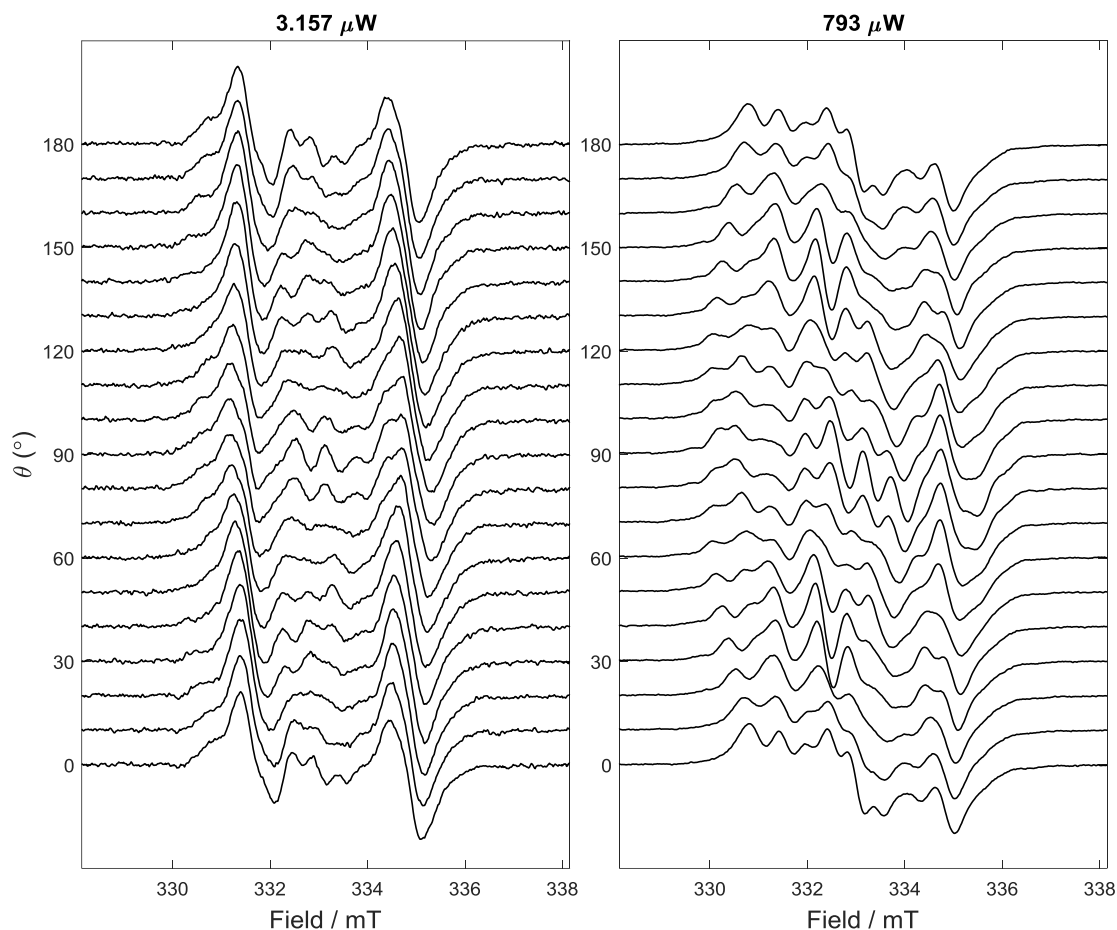


Figure 5.23 Roadmap of partially deuterated D-mannitol crystal at 240 K (left) and partially saturated spectrum (right), oriented along one of the main crystallographic axes and rotating in the yz plane.

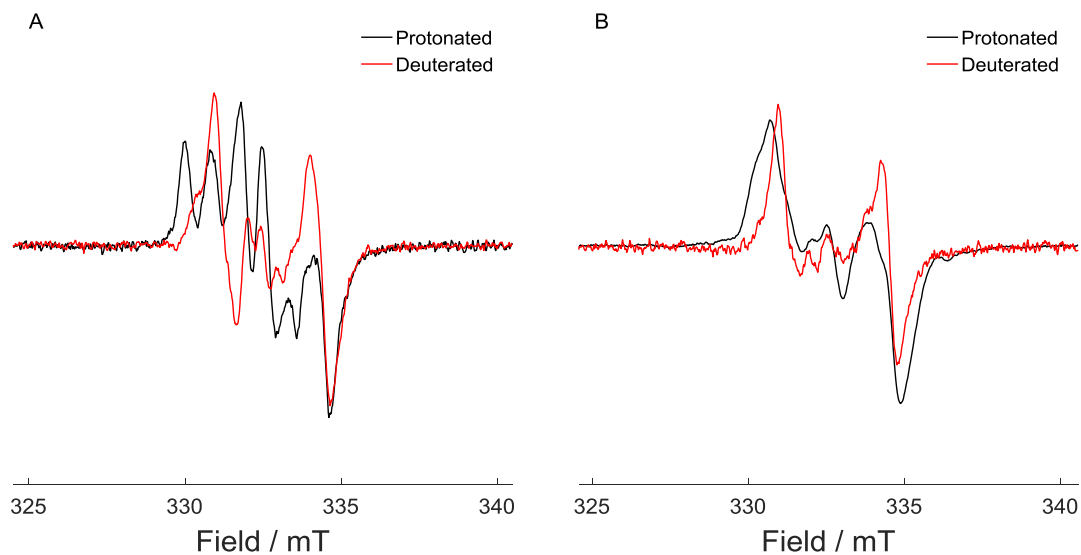


Figure 5.24 D-mannitol protonated and partially deuterated crystals (A) and powders (B) after γ -irradiation in liquid nitrogen and annealing to 240 K. The crystals are oriented along one of the main crystallographic axes.

5.3.4.6 240 – 260 K

Proceeding with the annealing of D-mannitol, at 260 K it was possible to observe additional changes in the spectrum (Figure 5.25). The broad β -proton coupling that dominated the spectrum at 240 K seemed to contribute less as the temperature was raised to 260 K. The central features of the spectrum were found to be more dominant at this temperature, with the three low intensity peaks detected at 240 K broadening and eventually becoming almost indistinguishable. This can be clearly seen by comparing the partially deuterated powder spectra at 240 and 260 K, with the latter displaying a pronounced central feature previously almost invisible. An additional feature emerged in the partially deuterated crystal spectrum at low field, while the presence of another one can be inferred from the asymmetrical broadening of the high field line (∇). Again, protonated and partially deuterated crystal spectra appeared rather different (Figure 5.26), most likely because of the different orientation of the two in respect to the magnetic field.

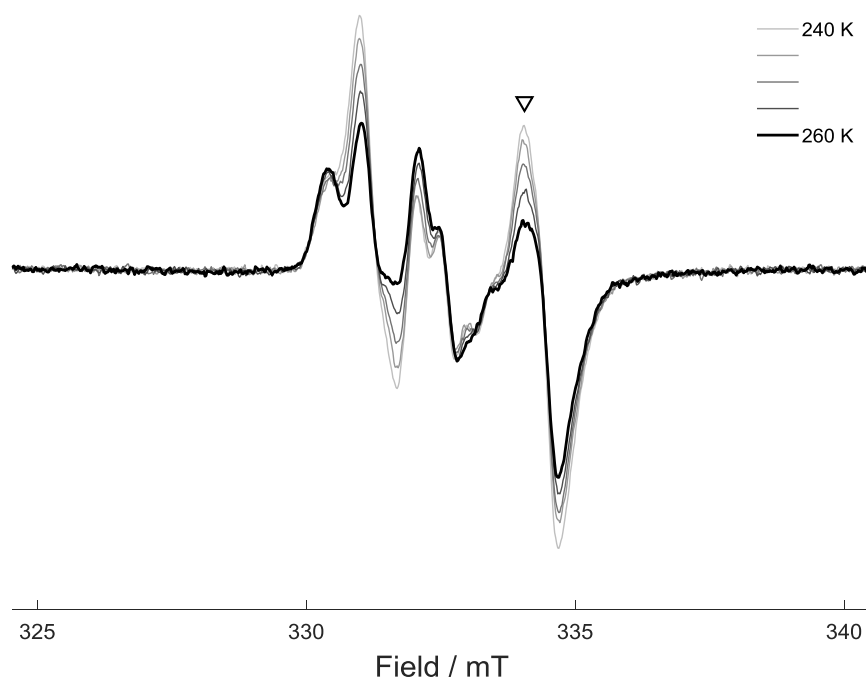


Figure 5.25 Annealing of γ -irradiated D-mannitol partially deuterated single crystal from 240 K (light gray) to 260 K (black). ∇ highlight asymmetrical broadening of the high field line. The crystal is oriented along one of the main crystallographic axes.

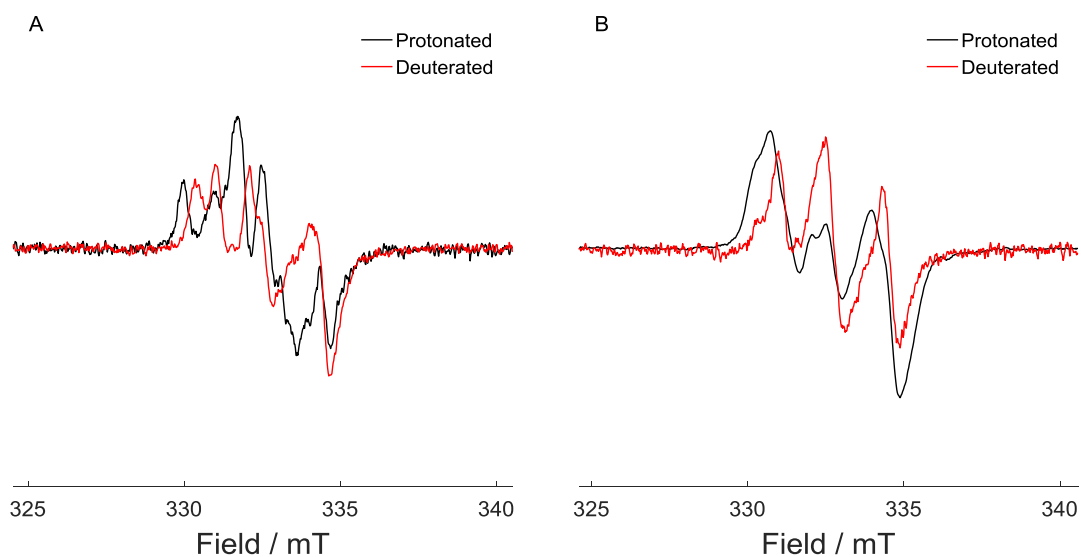


Figure 5.26 CW EPR spectra of D-mannitol protonated and partially deuterated crystals (A) and powders (B) after γ -irradiation in liquid nitrogen and annealing to 260 K. The crystals are oriented along one of the main crystallographic axes.

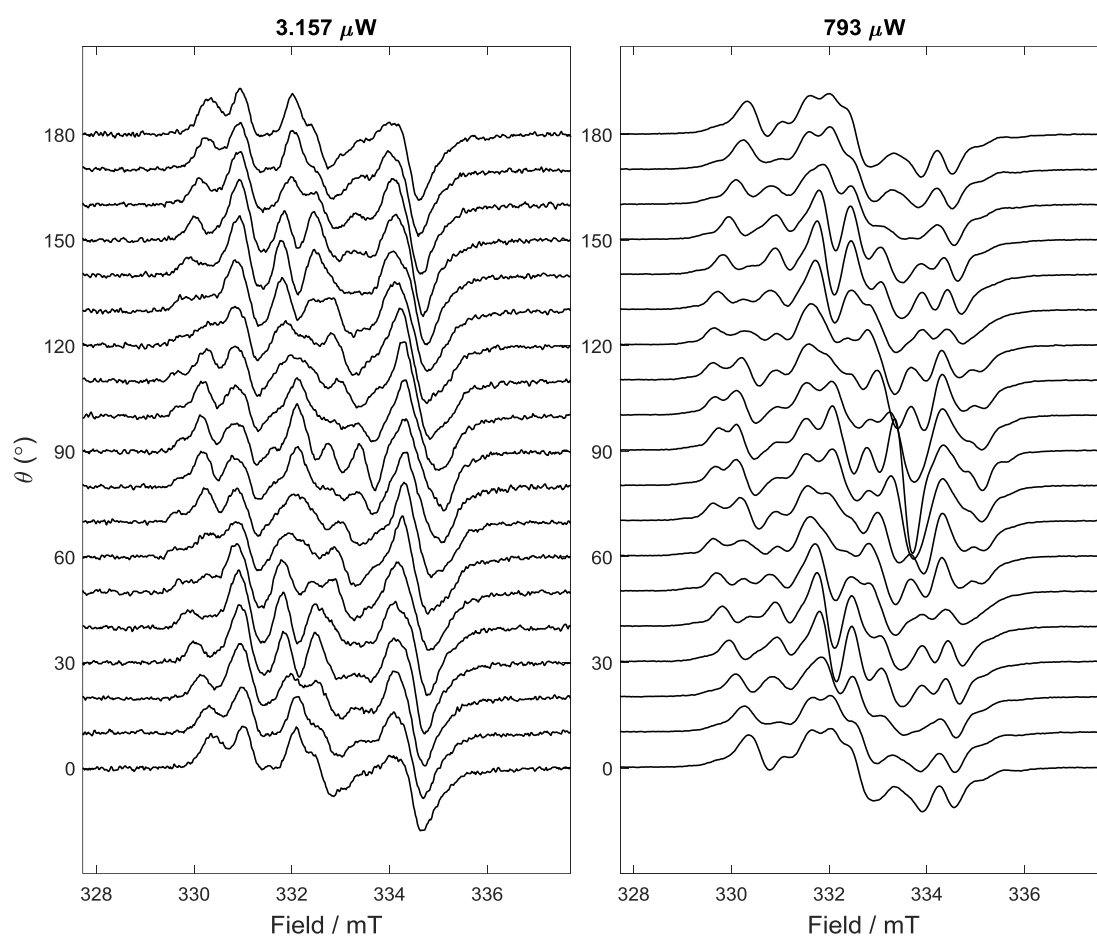


Figure 5.27 Roadmap of partially deuterated D-mannitol crystal at 260 K (left) and partially saturated spectrum (right) oriented along one of the main crystallographic axes and rotating in the yz plane.

5.3.4.7 260 – 295 K

Finally, the samples were annealed to r.t., *ca.* 295 K. Clear changes were detected in this temperature range as new peaks emerged from the spectrum. A comparison between the irradiated crystals, which were carefully reoriented along one of the main crystallographic directions, showed very little differences between the two (Figure 5.29A and Figure 5.30), implying that no exchangeable protons are involved. The spectrum is dominated by what seems to be a 4-line pattern, with additional peaks that can be distinguished on top of each feature. The MW power saturation spectra of the crystals (Figure 5.31) also highlighted the presence of a 1:2:1 three-line feature which clearly emerges at high microwave power.

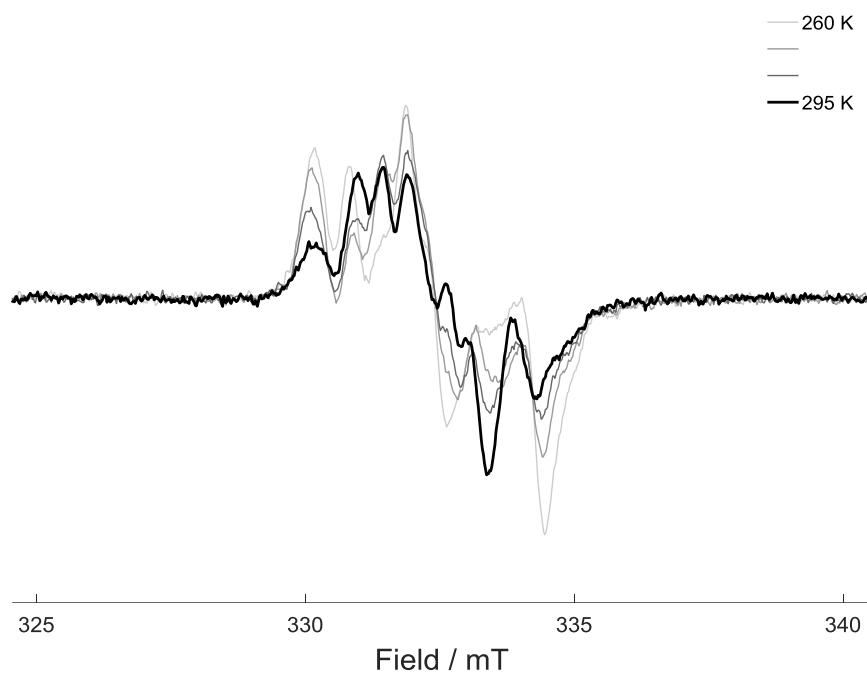


Figure 5.28 Annealing of γ -irradiated *D*-mannitol partially deuterated single crystal from 260 K (light gray) to 295 K (black). The crystal is oriented along one of the main crystallographic axes.

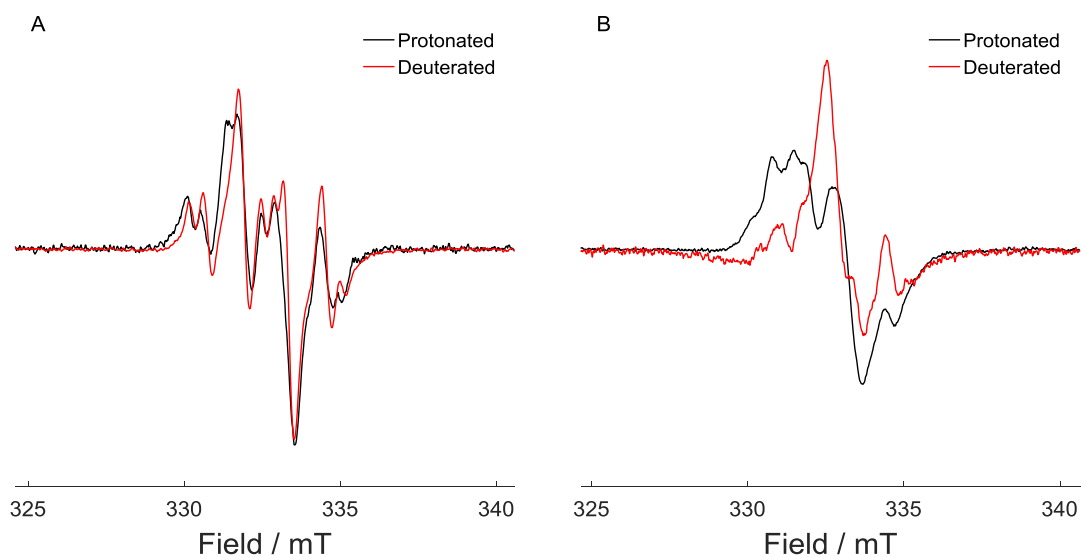


Figure 5.29 CW EPR spectra of D-mannitol protonated and partially deuterated crystals after reorientation along one of the main crystallographic orientations (A) and powders (B) after γ -irradiation in liquid nitrogen and annealing to 295 K. The crystals are oriented along one of the main crystallographic axes.

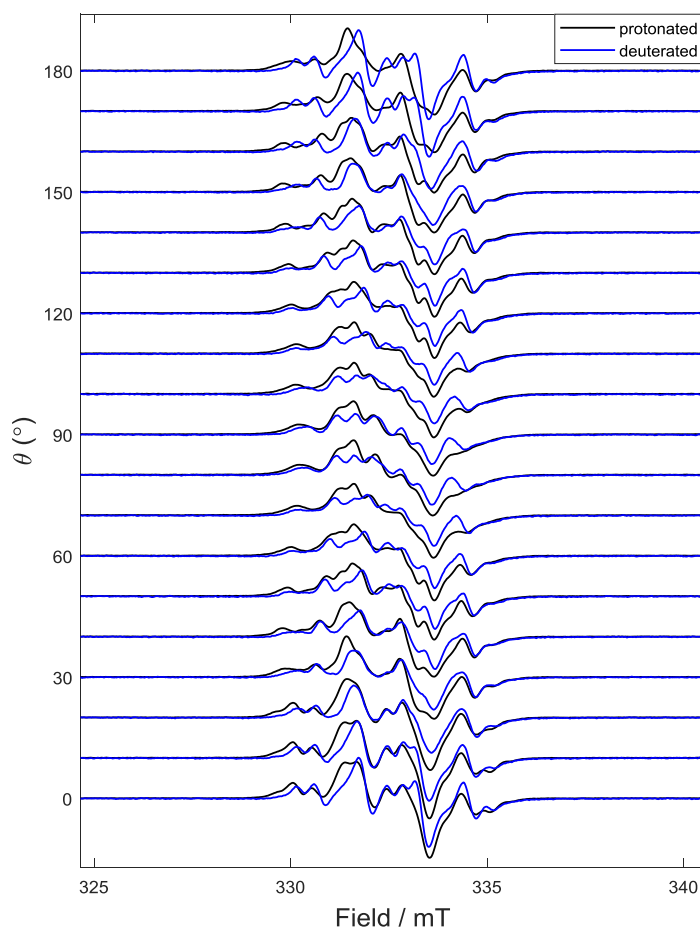


Figure 5.30 Roadmap of protonated (black) and partially deuterated (blue) D-mannitol crystal at 295 K, oriented along one of the main crystallographic axes and rotating in the yz plane.

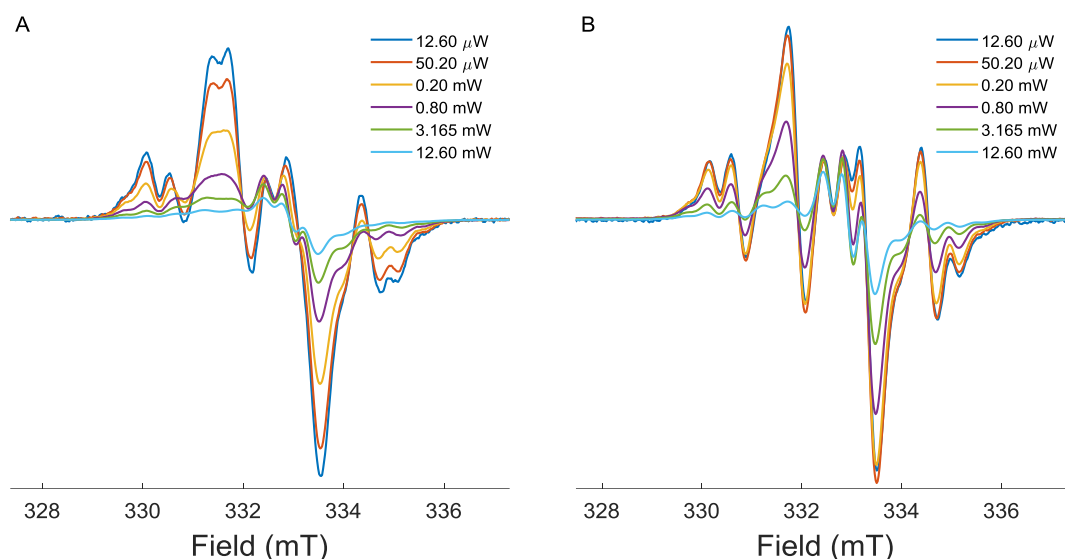


Figure 5.31 Microwave power saturation spectra of γ -irradiated D-mannitol protonated (A) and partially deuterated (B) crystals. Each spectrum was scaled by the square root of the microwave power. The crystals are oriented along one of the main crystallographic axes.

5.3.5 CW ENDOR

CW ENDOR experiments were performed on the low temperature irradiated crystal and powder samples in order to obtain information on the molecular structure of the radical species in the temperature range 77–295 K. Despite many attempts at different temperatures and experimental conditions, only signals related to small couplings (< 2 MHz) were observed, which were not useful towards the determination of the structure of the paramagnetic species under investigation. The absence of signals from large couplings was ascribed to the spin concentration of the samples that was insufficient for the CW ENDOR analysis.

5.3.6 Dissolution experiments

Dissolution experiments were performed to mimic the reconstitution of parenteral formulations before injection, thus obtaining valuable information on the reactivity of the radical species in solutions. The radical regeneration phenomenon observed for L-histidine and described in **Chapter 4** was also investigated in the case of D-mannitol.

5.3.6.1 Spin trapping with MNP

Firstly, irradiated D-mannitol powder was dissolved in pure water buffered with phosphate buffer (p.b.) 50 mM at pH 7.2. The solution was transferred to a 1 mm i.d. EPR quartz tube and

was then inserted into the spectrometer to start the acquisition. As for the case of L-histidine (**Chapter 4**), no EPR signal was detected (Figure 5.32a), meaning that the lifetime of the radical species formed after irradiation is too short to be detected directly, as can be expected from this type of organic radical.

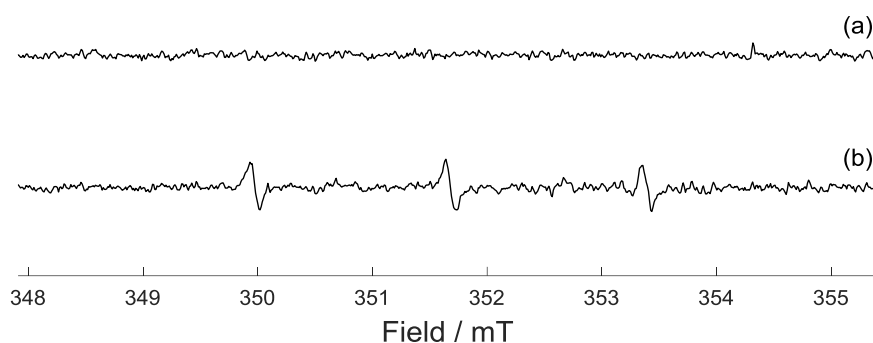


Figure 5.32 Control X-band EPR spectra. (a) 250 kGy γ -irradiated D-mannitol powder dissolved in water buffered with p.b. 50 mM at pH 7.2; (b) non-irradiated D-mannitol powder dissolved in a spin trap solution of MNP (80 mM).

Next, the dissolution of the powder in a spin trap solution was investigated. When non-irradiated powder was dissolved in a solution of MNP, only background signal was detected (Figure 5.32b). The 3-line signal that can be observed in Figure 5.32b was again assigned to the formation of di-*tert*-butyl nitroxide (DTBN), as can occur using this spin trapping agent.¹³ When irradiated powder was used instead, a persistent spin-adduct was detected at a concentration of *ca.* 1 μ M (Figure 5.33a). The detected signal consisted of a broad triplet, almost overlapping the DTBN background signal, which arises from coupling to the nitroxidic nitrogen. No further splittings were observed, even by lowering the modulation amplitude by a factor of 10 (from 0.1 mT to 0.01 mT, Figure 5.34), suggesting the absence of α -protons where the radical binds to MNP. The nitrogen hyperfine coupling and g-factor of the trapped species were extracted by simulations with EasySpin¹² (Figure 5.33). The fact that such spin adduct could not be detected by dissolving non-irradiated powder in a solution of MNP (Figure 5.32b) indicates that the trapped species is a product of the irradiation process.

Table 5.5 EPR hyperfine couplings (mT) and g -values for the trapped mannitol radical and the MNP di-adduct DTBN, comparing the parameters determined in this study with previously published ones.

Radical		a_{NO}^{N}	$a^{13\text{C}}$	g -value
MNP-mannitol	This study	1.55(1)	-	2.0055(2) ^a
	Ref. ¹³	1.71(1)	0.46(1)	2.0053(2) ^a
DTBN	This study	1.71(1)	0.46(1)	2.0053(2) ^a
	Ref. ¹³	1.72	- ^b	- ^b

^a determined by comparison with a DPPH standard; ^b not determined.

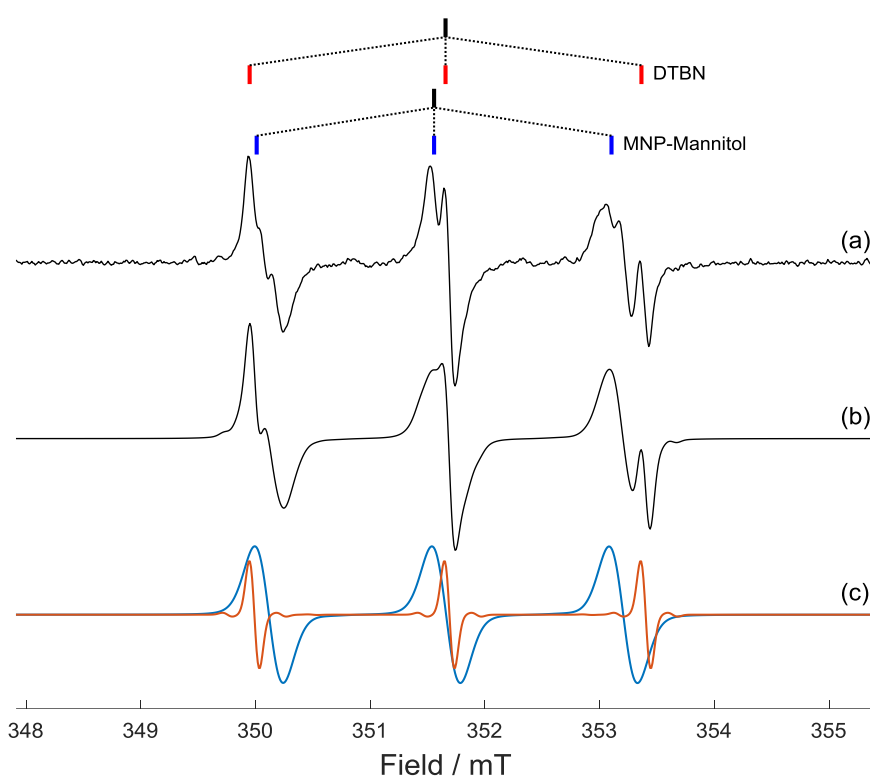


Figure 5.33 X-band CW EPR spectrum of (a) 250 kGy γ -irradiated D-mannitol powder dissolved in a spin trap solution of MNP (80 mM). (b) simulated EPR spectrum (obtained using Easyspin¹²). (c) single components of the simulated spectrum, consisting of the MNP-mannitol adduct (blue) and DTBN (red). The line diagrams of DTBN (upper) and of the MNP-mannitol spin adducts (lower) are also represented.

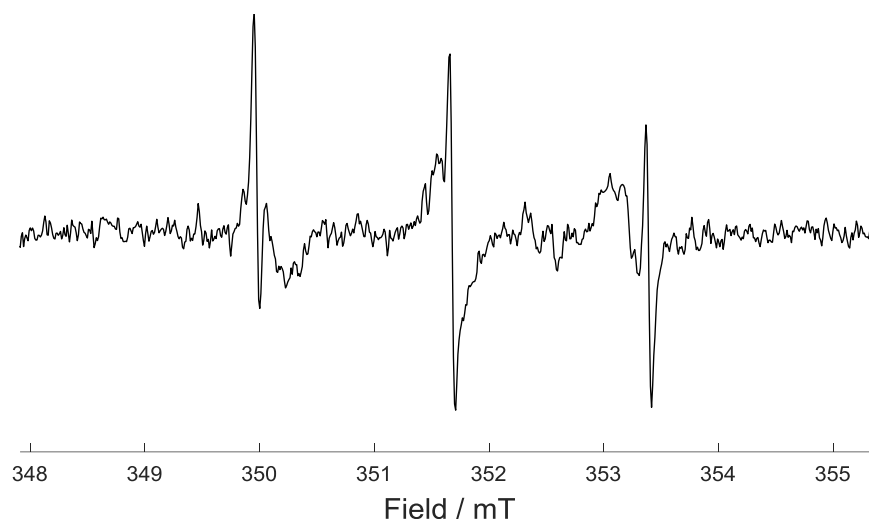


Figure 5.34 Spin trapping of irradiated D-mannitol powder in MNP (80 mM), detected by decreasing the modulation amplitude to 0.01 mT.

5.3.6.2 Testing radical regeneration for D-mannitol

Next, the regeneration process that was observed for L-histidine in **Chapter 4** was tested also for D-mannitol. The irradiated powder was therefore dissolved in water and the spin trap MNP was added after a time lag of 3 minutes. The sample was transferred to the EPR tube with a syringe with sterile steel needle.

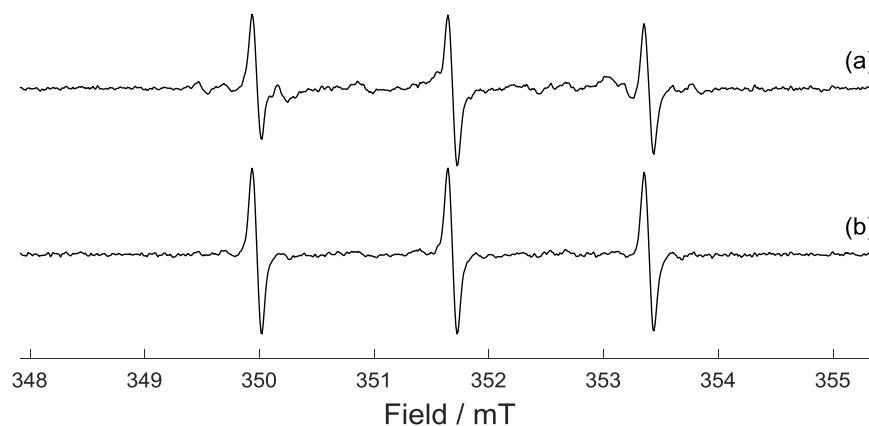


Figure 5.35 Dissolution of irradiated (a) and non-irradiated (b) mannitol powder in water with later (3 mins) addition of the spin trapping agent MNP.

As can be seen in Figure 5.35a, no major signals were detected for D-mannitol other than the DTBN background signal. The same process was repeated with non-irradiated powder (Figure

5.35b). The comparison between the two spectra highlighted that other rather weak signals ($\ll 0.1 \mu\text{M}$) can be observed in the case of irradiated D-mannitol, which might suggest that some species have been trapped. However, the intensity of the signals detected are negligible if compared to the amount of regenerated radicals trapped in the case of L-histidine.

5.3.6.3 Spin trapping with DMPO

Spin trapping with the nitron spin trapping agent DMPO was also tested in order to obtain complementary information on the reactivity of the radical species in solution. Despite the use of a high purity ($\geq 98\%$) recent DMPO batch, the control spectra exhibited a complex EPR spectrum ascribable to the presence of multiple paramagnetic species (Figure 5.36a). The presence of such background signal interfered with the analysis, preventing the identification of spin-trap adducts formed from D-mannitol radical species.

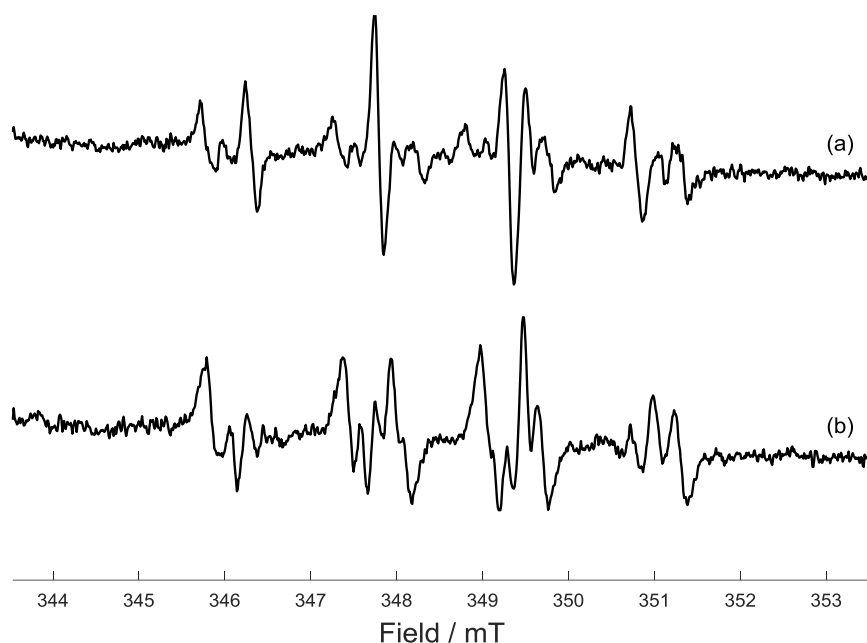


Figure 5.36 X-band CW EPR spectra of solutions of (a) DMPO (0.2 M) and (b) 250 kGy γ -irradiated D-mannitol powder dissolved in a spin trap solution of DMPO (0.2 M), both prepared in p.b. 50 mM at pH7.2.

5.3.7 MS analysis

Mass spectrometry (MS) analysis was undertaken in an attempt to obtain information regarding the mass of the degradation product originating from the irradiation process. In order to do that, samples of non-irradiated, 25 kGy and 250 kGy γ -irradiated D-mannitol were prepared and

analysed as described in **Chapter 3**. The spectra obtained in positive and negative mode analysis are shown respectively in Figure 5.37 and Figure 5.38. Table 5.6 reports the assignment of the main peaks. Whilst positive mode analysis did not highlight any new signal originating as a result of the irradiation process, in negative mode both peaks at 179.1 m/z and 361.2 m/z were exclusively detected for the irradiated samples. The 179.1 m/z signal was attributed to a molecule of D-mannitol where one of the hydrogen atoms bound to the aliphatic chain had been extracted upon irradiation, which when subsequently dissolved recombined in solution by eliminating an adjacent proton to form a double bond. The molecular mass of the said radical would therefore be 2 units lower than a non-degraded mannitol molecule, 180.2 instead of 182.2 m/z . The 179.1 m/z detected in negative mode would therefore correspond to a negatively charged mannitol ion that loses an additional hydrogen from one of the hydroxyl groups. The mass of the non-degraded negatively charged mannitol ion corresponding to 181.2 m/z was also detected in the spectrum. The higher m/z signals at 361.2 and 363.2 can be associated to the same species detected at 179.2 and 181.2 which have formed a non-covalent bond with another molecule of D-mannitol. This can indeed happen at high sample solution concentrations, when in a droplet of the nebulized sample two molecules are binding non-covalently and are detected as such. The same effect is observed in positive mode, where both a sodiated single molecule of D-mannitol and two non-covalently bonded molecules, one of which is sodiated, are detected respectively at 205.10 m/z and 387.20 m/z .

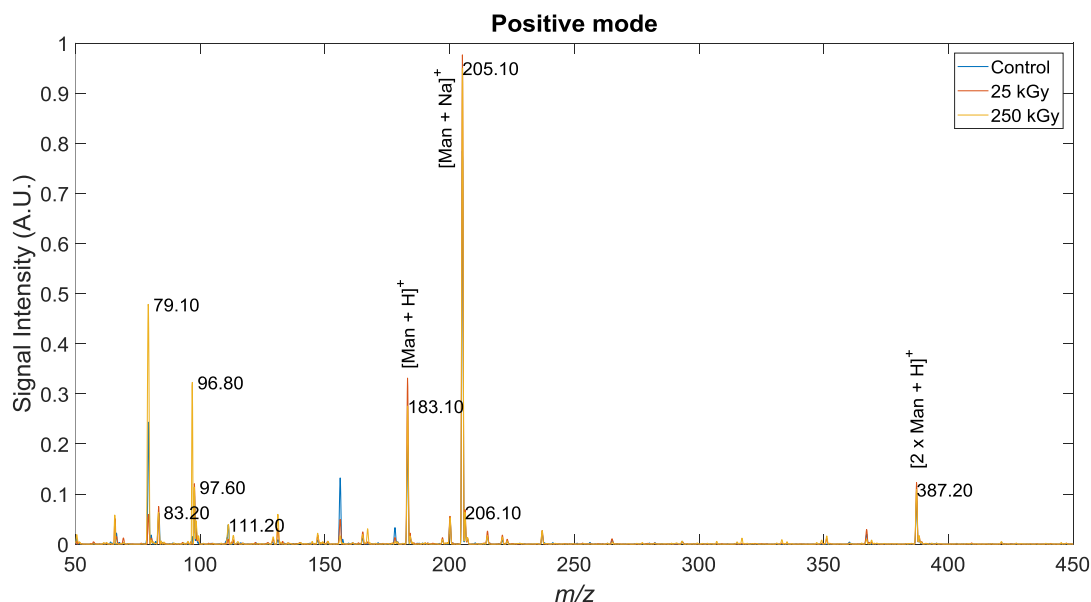


Figure 5.37 Positive mode MS analysis of non-irradiated (blue), 25 kGy (red) and 250 kGy (yellow) γ -irradiated D-mannitol.

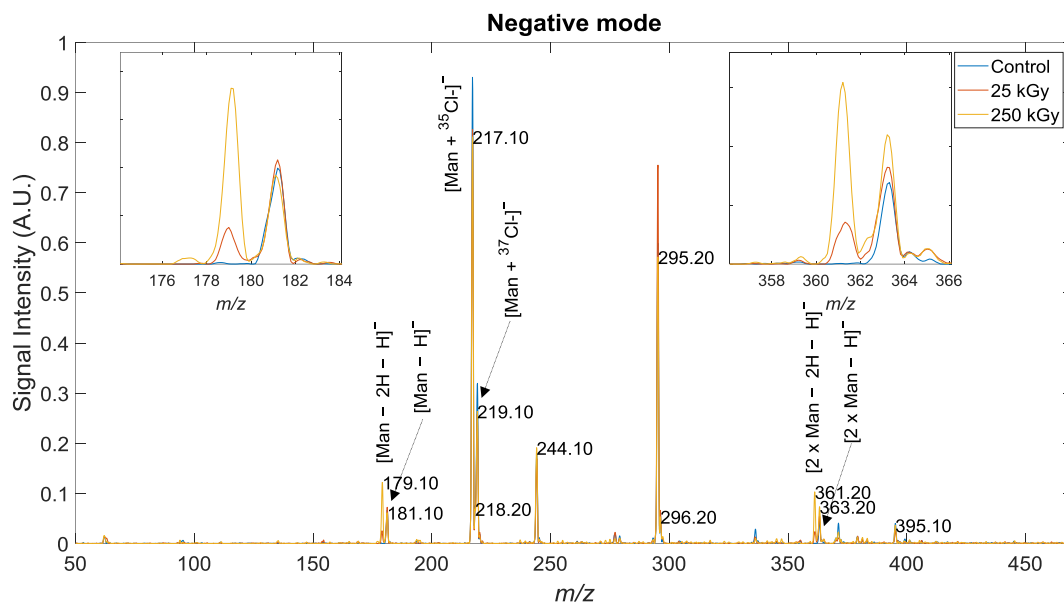


Figure 5.38 Negative mode MS analysis of non-irradiated (blue), 25 kGy (red) and 250 kGy (yellow) γ -irradiated D-mannitol.

Table 5.6 Main assignments of the peaks detected from the MS analysis.

Observed m/z	Proposed assignment
POSITIVE MODE	
79.10	Background
83.20	Background
183.10	$[\text{Man} + \text{H}]^+$
205.10	$[\text{Man} + \text{Na}]^+$
387.20	$[2 \times \text{Man} + \text{Na}]^+$
NEGATIVE MODE	
179.2	$[\text{Man} - 2\text{H} - \text{H}]^-$
181.2	$[\text{Man} - \text{H}]^-$
217.2	$[\text{Man} + {}^{35}\text{Cl}]^-$
219.1	$[\text{Man} + {}^{37}\text{Cl}]^-$
361.4	$[2 \times \text{Man} - 2\text{H} - \text{H}]^-$
363.4	$[2 \times \text{Man} - \text{H}]^-$

5.3.8 ^1H NMR analysis

^1H NMR analysis was performed on both a non-irradiated sample and a 250 kGy γ -irradiated sample of D-mannitol in an attempt to detect signals ascribable to the degradation products formed upon irradiation. The sample preparation and analysis details of the NMR experiment are described in **Chapter 3**. The comparison between Figure 5.39 and Figure 5.40 shows how the main features of the spectra are the same despite the irradiation process. All the main peaks were observed between 3.4 and 3.9 ppm and have previously been assigned.¹⁴ These values are characteristic for aliphatic protons located close to hydroxyl groups, which is the case of all the protons in the molecule. The hydroxyl group exerts a deshielding effect that shifts the chemical shift to higher ppm values than the ones typically detected for standard aliphatic protons. Nevertheless, a closer look at the spectra allowed the identification of new, low intensity peaks emerging from the irradiated D-mannitol spectrum. In particular, a spectral doublet and a singlet appeared respectively at *ca.* 1.2 and 1.4 ppm, while other signals can be observed at 3.3 and 3.9 ppm.

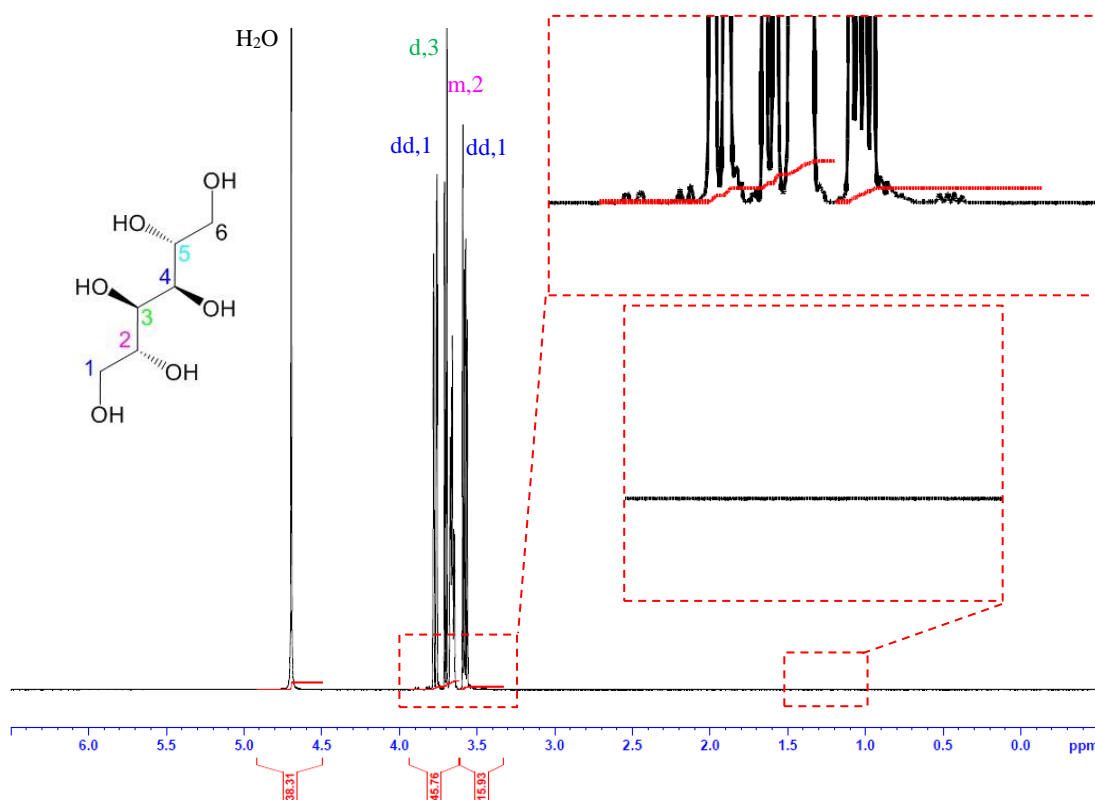


Figure 5.39 ^1H -NMR analysis of non-irradiated D-mannitol.

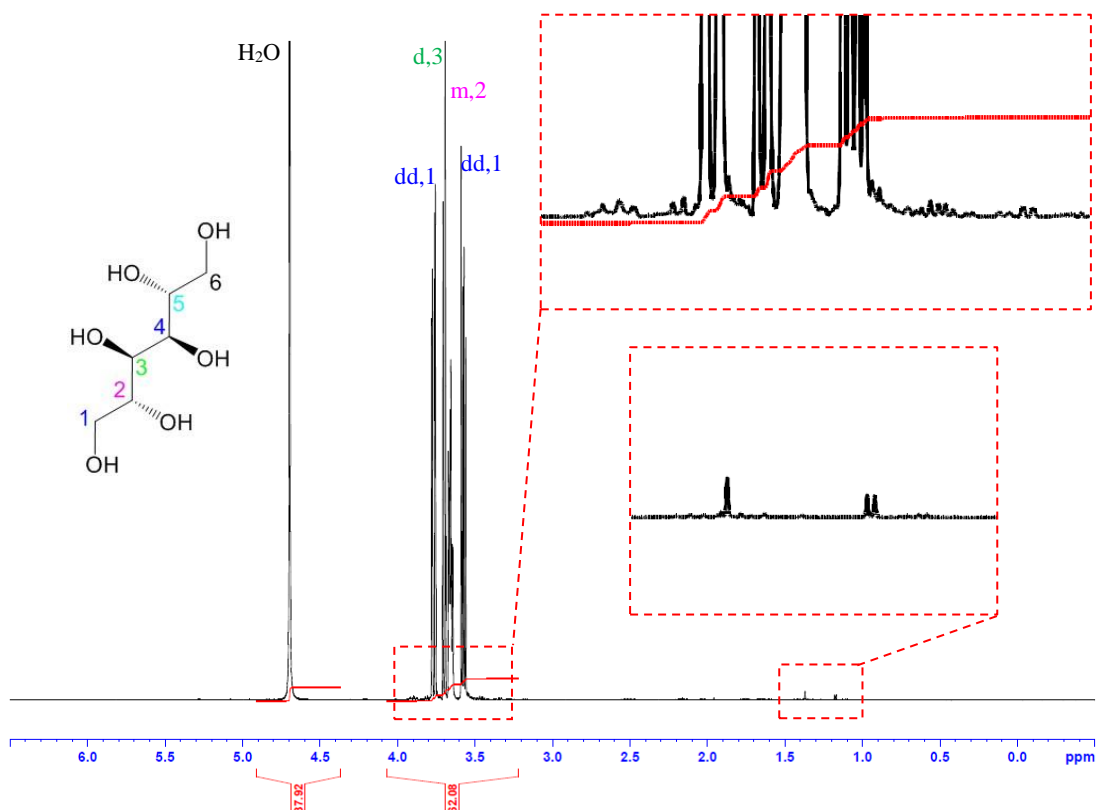


Figure 5.40 ^1H -NMR analysis of 250 kGy γ -irradiated D-mannitol.

5.4 Discussion

5.4.1 Evolution of the radicals from nitrogen temperature to r.t.

5.4.1.1 Detection of *radical I* at 77 K

The analysis of the CW EPR spectra of cold irradiated D-mannitol samples (Figure 5.7) showed the formation of a broad doublet which was labelled as *radical I*. The EPR parameters of the paramagnetic species were extracted by simulation with EasySpin¹² and are reported in Table 5.1.

The analysis of the extracted parameters provides valuable information regarding the structure of the paramagnetic species. To begin, the g -values of the detected radicals can be used to determine whether the paramagnetic species is carbon-centred or oxygen-centred. It is generally accepted that the closer the unpaired electron is to an oxygen atom, the greater the g -value of the radical will be.¹⁵ For g -values < 2.003 , a C-centred radical is expected. Values in the range

of 2.003-2.004 typically indicate the unpaired electron to be located on a carbon atom adjacent to an oxygen. Finally, for *g*-values greater than 2.004 oxygen-centred radicals are expected. In the case of *radical I*, the calculated *g*-factor of 2.0033 falls in the range of values typical for carbon-centred radicals adjacent to an oxygen atom, which is the case of each of the carbon atoms in the molecule.

Furthermore, some considerations on the magnitude of both the isotropic and anisotropic components of the hyperfine coupling can help to distinguish the type of proton coupled to the paramagnetic centre. In the case of *radical I*, although the anisotropic component of the hyperfine coupling was not calculated nor extracted by simulation, from the observation of the roadmap (Figure 5.8) and powder spectra (Figure 5.7B), it is possible to attribute the coupling to a rather small anisotropic contribution. The small anisotropic feature of the hyperfine coupling is indicative of a coupling with a β -proton, for which the anisotropy rarely exceeds 10% of the isotropic hyperfine interaction.¹⁶ The isotropic part of the hyperfine coupling of a β -proton is described in Equation 5.1:

$$a_{\beta}^H = b_0 + b_2 \cos^2 \varphi \quad \text{Eq. 5.1}$$

where: φ is the dihedral angle between the plane through the C–C bond and the p_z orbital where the unpaired electron is located, and the plane through the C–C bond and the C–H $_{\beta}$ bond; $b_2 \gg b_0$, with b_0 being 0 to +10 MHz.¹⁶ Typical values for b_0 and b_2 are 9 and 122 MHz.¹⁷ The dependence of the isotropic hyperfine couplings on the dihedral angle described in Equation 5.1 is well depicted in Figure 5.41.

As previously mentioned in Section 2.2.3, predicting the effects of ionising radiations on organic molecules is a rather complicated matter. As the energy of the radiation is absorbed and quickly spreads out over the entire molecule, one would expect it to cause the rupture of the weakest bond in the molecule, provided that the energy of the radiation exceeds the energy of the molecular bond. Nevertheless, C–H bond rupture generally dominates in respect to C–C rupture,¹⁸ despite the former (4.3-4.6 eV) being a stronger bond than the latter (3.8-3.9 eV)¹⁹ and both being at an inferior energy than the average energy of γ -rays emitted from a ^{60}Co source (1.25 MeV).²⁰ Additionally, the C–H bond rupture is not necessarily localised to the weakest bond.¹⁸

Thus, starting from the assumption that radicals trapped in irradiated aliphatic compounds are usually the result of C–H bond rupture, followed by the formation of a π -orbital consisting mainly of the carbon atom 2p-orbital,¹⁶ two possible structures of *radical I* are proposed, with the paramagnetic species originating from abstraction of an α -proton from either C3 or C4. Indeed, if the unpaired electron were to be located on either C2 or C5, a total of three β -proton

couplings should have been detected, while one only can be inferred by the spectrum; in the case of C1 and C6 instead, one α -proton and one β -proton coupling would have been detected, but the data allow us to exclude involvement of any α -proton coupling. In the case of C3 and C4, only two β -proton couplings should be detected. Here, we discuss the magnitude of the β -proton coupling that should be detected for the unpaired electron located on C3 (or C4) and coupling to the proton bound in α position in C4 (or C3).

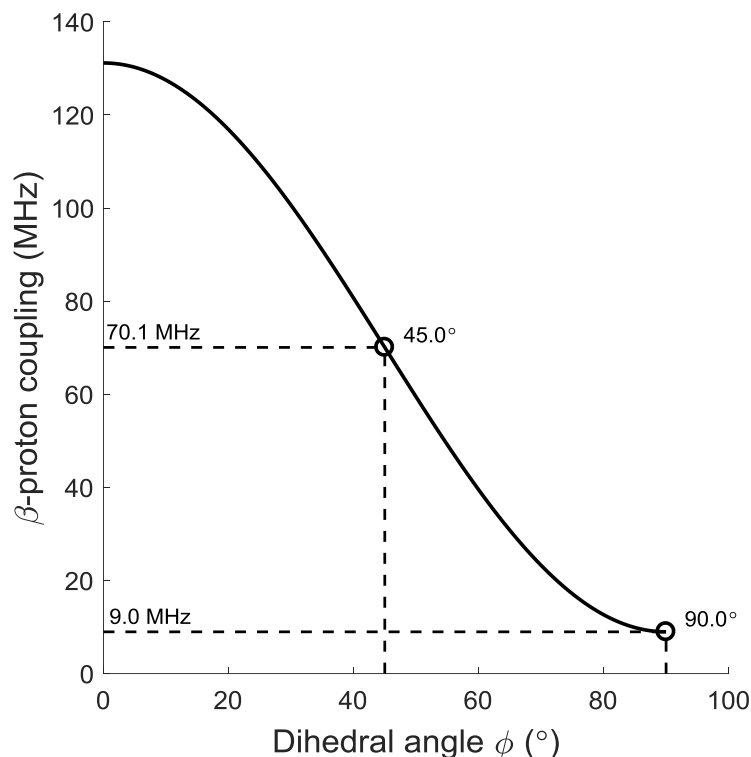


Figure 5.41 Influence of the dihedral angle ϕ on the β -proton coupling, as described in Equation 5.1.

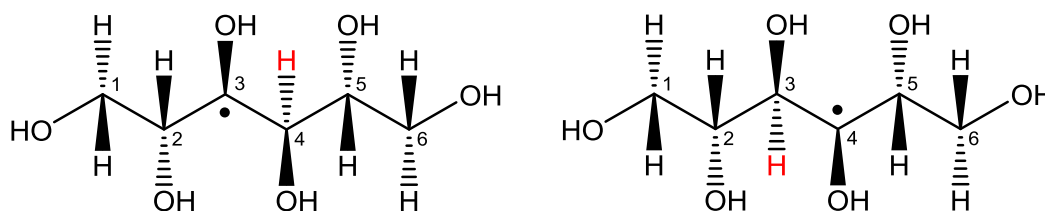


Figure 5.42 Proposed chemical structures for *radical I*.

Figure 5.43 shows the Newman projections of the D-mannitol molecule considering both the cases where the unpaired electron is localized on C3 (A) or C4 (B). The X-ray crystallographic analysis of the non-irradiated crystal indicates the dihedral angle between the α -protons in C3

and C4 to be 61.81° . After irradiation and rupture of the C–H $_\alpha$ bond, the change of hybridization from sp^3 to sp^2 would trigger a structural rearrangement, involving the rotation of the OH group in α position (blue) about the C3–C4 bond to be planar with HOH $_2$ CHOHC. Consequently, the p_z orbital (green) where the unpaired electron is located would also rotate. As a result of the rotation, the angle between the p_z orbital and the β -proton would measure *ca.* 45° , yielding an isotropic hyperfine coupling of approximately 70.1 MHz. This value is in very good agreement with the observed coupling of *ca.* 73 MHz obtained from the fitting of the crystal spectra in Figure 5.7A. Nevertheless, only one dominating β -proton coupling is detected while two β -protons should be coupled to the unpaired electron. It is therefore assumed that the second β -proton lies close to a perpendicular plane to the p_z orbital where the unpaired electron is located so that, according to Equation 5.1, the resulting coupling is negligible and indistinguishable under the broad lines.

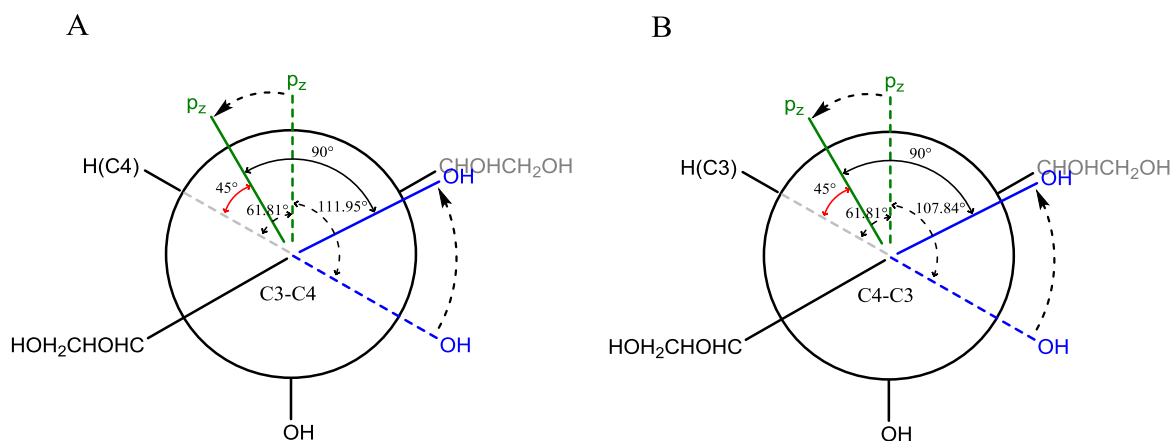


Figure 5.43 Newman projections along C3–C4 with the unpaired electron localised in C3 (A) and C4–C3 with the unpaired electron in C4 (B).

The coupling with the proton belonging to the α -OH group should also potentially be detected on the protonated samples. The dihedral angle between the plane through the C3–O bond and the p_z orbital and the plane through the same C–O bond and the hydroxylic proton is 39.16° on the non-irradiated crystal structure. If this angle were to be maintained after the change in hybridization, it would have produced a coupling of the order of 82 MHz. The fact that such coupling had not been observed, suggests that the O–H bond lies on the plane of the sp^2 hybridized orbitals, hence forming a 90° angle with the p_z orbital. In this situation, the contribution to the isotropic coupling component would solely derive from b_0 , therefore being too small to be detectable considering the broadening of the lines. This is also corroborated by the similarity between the protonated and partially deuterated spectra (Figure 5.7), thus

confirming that no hydroxylic protons (or deuterons) with large hyperfine couplings are coupled to the unpaired electron.

It has been previously mentioned that the molecule of D-mannitol presents a C_2 two-fold symmetry axis perpendicular to the C3–C4 bond, meaning that by a 180° rotation the same molecule is obtained. Additionally, an approximate C_2 molecular symmetry is maintained in the orthorhombic crystal structure as well.¹¹ It therefore appears that only minimal differences in terms of β -proton coupling can be expected from proton abstraction from either C3 and C4, implying that the proposed structures for *radical I* shown in Figure 5.42 essentially represent the same radical.

5.4.1.2 Formation of *radical II* at 120 K

The annealing of the samples to 120 K revealed a change of the EPR spectra, which was interpreted as the formation of a new paramagnetic species named *radical II* (Figure 5.10). The extracted parameters reported in Table 5.2 showed a g -value > 2.004 for *radical II*, which indicates that the unpaired electron for this species is located on an oxygen atom. The comparison between protonated and partially deuterated samples offered useful information toward the determination of the structure of *radical II*. No major differences were observed from the analysis of the spectra of both protonated and partially deuterated single crystals (Figure 5.12A), suggesting the absence of hydroxylic protons nearby the paramagnetic centre of the newly formed species. Nevertheless, the analysis of the irradiated powders highlighted some changes due to deuteration of the sample (Figure 5.12B), which can be ascribed to an interaction with a distant hydroxylic proton, that induces appreciable changes only on the EPR powder spectra.

The sum of these considerations suggests that *radical II* is formed after the abstraction of a proton from the hydroxylic group of either C1 or C6. These in fact represent the only positions in the molecule where the unpaired electron could be located to couple with two different protons. Indeed, for any other position in the molecule, only one proton would be available for coupling with the oxygen-centred unpaired electron. The geometry of the molecule does not allow unequivocal assignment of either of these structures to *radical II*, for which however only minor differences are expected according to the C_2 molecular symmetry.

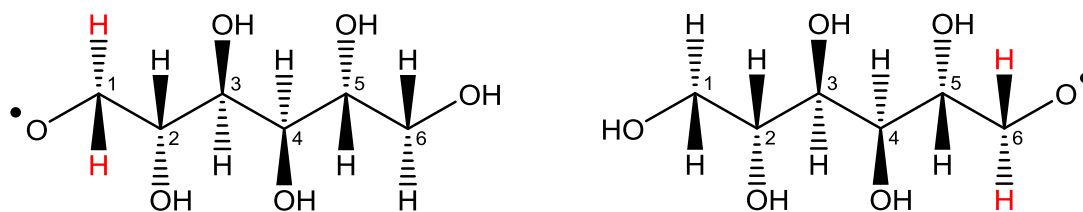


Figure 5.44 Proposed chemical structures for *radical II*.

The mechanism by which *radical II* is formed is unclear. Interestingly, the analysis of the mannitol molecule highlights the presence of numerous intramolecular short contact bonds, *i.e.* any contact shorter than the sum of the van der Waals Radii of the atoms involved. In particular, short contact bonds are observed respectively between the proton in C3 and the oxygen bonded to C1, and the proton in C4 and the oxygen in C6 (Figure 5.45). These observations suggest the possibility of intramolecular rearrangements, with the unpaired electron initially located on a carbon atom at the centre of the aliphatic chain (*radical I*) moving to an oxygen atom, thus leading to the formation of *radical II*.

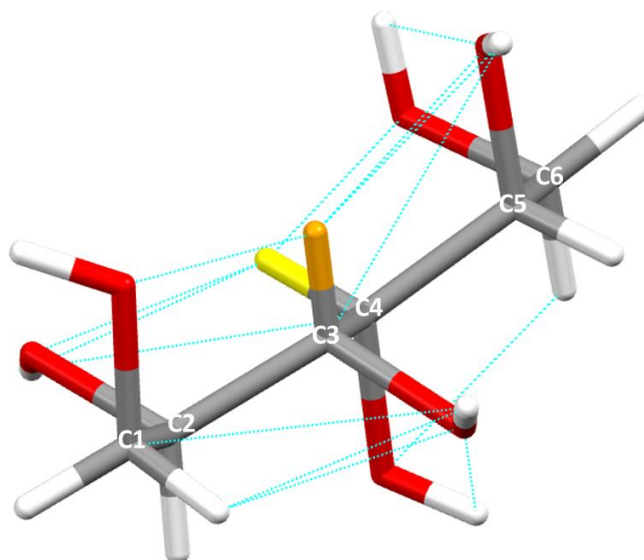


Figure 5.45 Molecule of D-mannitol highlighting intermolecular short contact bonds (cyan) and the protons in C3 (orange) and C4 (yellow).

5.4.1.3 Formation of *radical III* at 170 K

Further annealing of the samples proceeded in steps until reaching 170 K, at which temperature the EPR spectrum underwent an irreversible transformation (Figure 5.15). The analysis of the spectrum before and after this mutation suggested the presence of an additional paramagnetic

species with a 4-line feature, *radical III*. The g-factor extracted from an EasySpin¹² simulation was found to be of ~ 2.004 and was considered not high enough to belong to an oxygen-centred radical (Table 5.3). Additionally, no major differences were registered between protonated and partially deuterated samples (Figure 5.17). According to these considerations, *radical III* was interpreted as a carbon-centred paramagnetic species coupling to two protons bound to carbon atoms. Thus, the structure of *radical III* was assigned to the radical formed from abstraction of a proton from either C1 or C6, with the unpaired electron coupling to one α - and one β -proton (Figure 5.46).

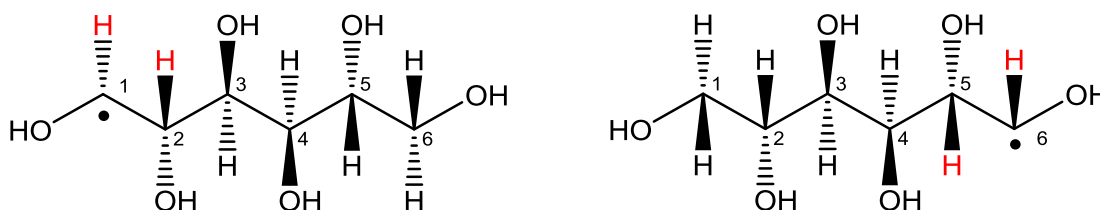


Figure 5.46 Proposed chemical structures for *radical III*.

5.4.1.4 Decrease of concentration of *radical II* and *III* at 200 K

When the temperature was raised to 200 K, the spectral features rapidly changed (Figure 5.19). The change in the spectrum registered at this temperature was tentatively associated with a change in the relative concentration of the paramagnetic species already present at 170 K. The EPR spectrum was therefore simulated considering only these three species (Figure 5.21). The good agreement between the experimental data and the resulting spectral simulation seemed to confirm this hypothesis, suggesting that, although the signal intensity of the overall spectrum decreased by annealing from 170 to 200 K, the concentration of both *radical II* and *radical III* decreased by approximately 25% and 20% respectively in comparison to the species associated with *radical I*.

5.4.1.5 Dominant β -proton coupling at 240 K

As the temperature was raised to 240 K, the EPR spectrum was dominated even more by the broad doublet with similar characteristics to *radical I*, namely a broad β -proton coupling and g-value ascribable to a C-centred radical (Figure 5.22). This was confirmed by the roadmap of the partially deuterated crystal that shows almost no anisotropic character of the hyperfine coupling, which is typical for β -protons (Figure 5.23). Although the spectral features of the dominant radical are similar to those of *radical I*, it is likely that the said species represent a different radical, formed upon annealing of the samples, rather than a kinetically unfavourable reformation of *radical I*. Other minor species can be also observed, especially in partially

saturated conditions (Figure 5.23). These species are likely to be *radical II* and *radical III*, whose concentration was further decreasing as the temperature was raised. Despite this, a satisfactory simulation of the spectrum including a lower contribution from such species could not be obtained, suggesting the presence of other radicals emerging at this temperature. The double integrated areas of the simulated radicals were corrected by the temperature according to the Curie law (Figure 5.47). The resulting plot showed *radical II* and *III* remaining at the same concentration from their first detection up to 200 K, with the simultaneous increasing of the large isotropic doublet radical. However, the total concentration of the radical species is not supposed to increase as the temperature increases, therefore this effect was attributed to a change in the performance of the spectrometer in the said temperature range. This can occur while the EPR cavities dries out during the annealing experiments, eliminating the water formed from icing of the setup. Thus, the data were replotted assuming the total radical concentration to be maintained constant in this temperature range (Figure 5.48).

The trend registered in the temperature range 80–200 K is in line with a further decrease in the concentration of *radical II* and *III* at 240 K, as proposed. Furthermore, the differences observed between protonated and partially deuterated powders and crystals suggested the coupling to hydroxylic protons, although it was not possible to judge more specifically which OH group was involved in the interaction.

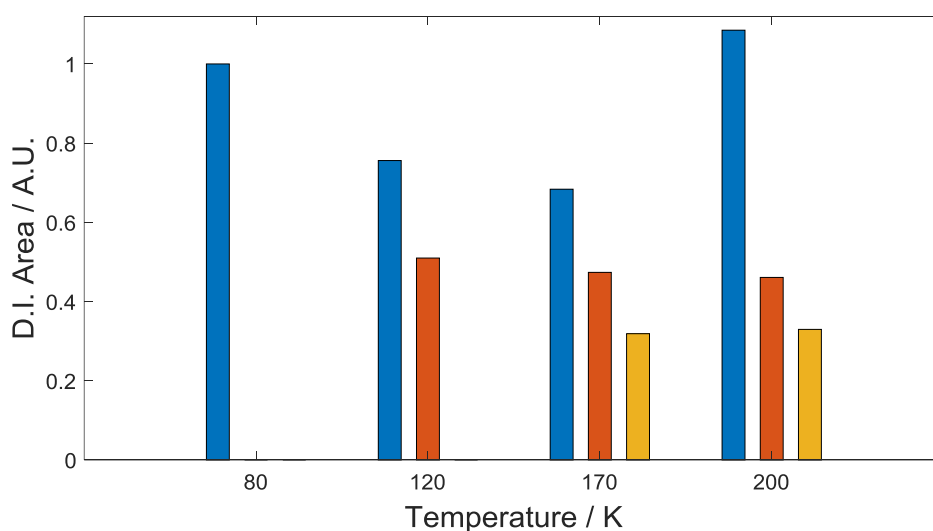


Figure 5.47 Double integrated area of the paramagnetic species detected in the range 80–200 K, *radical I* (blue), *radical II* (red) and *radical III* (yellow) corrected by the Curie law.

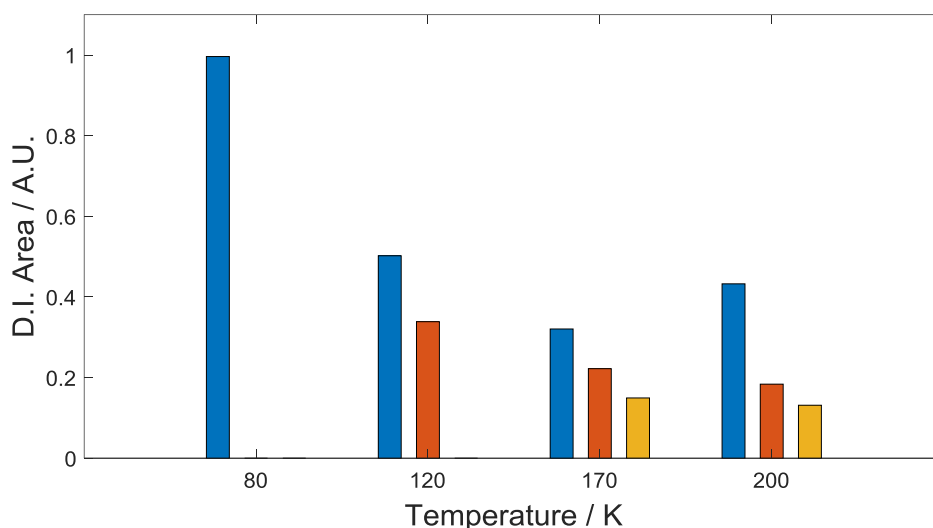


Figure 5.48 Fraction of the paramagnetic species detected in the range 80–200 K, *radical I* (blue), *radical II* (red) and *radical III* (yellow), assuming the total radical concentration to be constant.

5.4.1.6 Spectral evolution at 260 K

Further annealing to 260 K resulted in spectral changes that reflected the presence of additional radical species becoming more dominant at this temperature compared to 240 K (Figure 5.25). The isotropic doublet was still a major component of the spectrum at 260 K. The comparison between the roadmap spectrum of D-mannitol at 260 K showed similarities with the partially MW-saturated roadmap spectrum obtained at 240 K (Figure 5.27), suggesting the same species being present at lower temperature and becoming more dominant with further annealing. The complexity of the spectra did not allow simulation of the single species involved and therefore a complete characterization of the radicals contributing to the EPR spectrum at this temperature was not possible.

5.4.1.7 R.t. persistent species

Lastly, the samples were annealed to r.t., *ca.* 295 K (Figure 5.28). At this temperature, when the crystals were aligned to a main crystallographic orientation, four main features were detected, with an additional splitting observable. The MW power saturation spectra of both crystals showed these species to quickly saturate as the MW power increases, and a 1:2:1 three-line pattern to appear. Simulation of the species was attempted considering various possibilities, but was not successful. The presence of an isotropic doublet can still be inferred from the spectra, although in lower concentration compared to previous temperatures. Most likely, at r.t. such species is still present together with another species which is shifted to a higher *g*-value and therefore likely to be oxygen-centred radical, plus the 3-line species detected

at high MW powers. The presence of multiple species characterised by different g -values was also inferred from the multifrequency analysis of the X-irradiated powder (Figure 5.6).

The quantification of radical species produced by direct irradiation at r.t. showed approximately a 3 times higher presence of persistent radical species for D-mannitol (Figure 5.4) compared to L-histidine for an irradiation dose of 25 kGy (see **Chapter 4**). The difference in the radical concentration diminished for higher doses, reaching a maximum difference of *ca.* 14 mM for 250 kGy. The high susceptibility of D-mannitol to γ -irradiation at industrially relevant irradiation doses is an important finding, especially considering its high usage in parenteral formulations.

5.4.2 Spin trapping experiments

The r.t. persistent radical species formed from irradiation of D-mannitol exhibited a short lifetime in aqueous solution, as proved by the fact that no EPR signal could be detected from the analysis of irradiated powder dissolved in physiological solutions (Figure 5.32a). Despite this, a spin-adduct was detected when dissolving the irradiated powder directly in a solution of MNP. The spin-adduct formed exhibited a broad 3-line signal; no further splittings were observed, even by decreasing the modulation amplitude by a factor of 10 (from 0.1 mT to 0.01 mT). This finding, together with the renowned specificity of MNP towards the trapping of carbon-centred species, suggested the spin-trapped radicals to be carbon-centred and lacking of protons to couple to in the α position. It is therefore proposed that the radical trapped by MNP corresponds to a newly formed species presenting similar features to those of *radical I*. Spin trapping was also tested with the nitron spin trap DMPO in an attempt to trap O-centred radical species for which this class of spin trapping agent is more specific, however the presence of impurities in the spin trap solution interfering with the analysis did not allow the identification of additional spin trap adducts.

In **Chapter 4** it has been shown that L-histidine radicals can regenerate in solution in the presence of trace metals through a Fenton-type reaction. This behaviour was associated with the antioxidant properties of L-histidine, which is a well-known scavenger for different reactive oxygen species (ROS).²¹⁻²⁵ Similarly, D-mannitol is known for being a scavenger of the hydroxyl radical,²⁶⁻²⁹ and could therefore be involved in a similar process. The regeneration of D-mannitol radicals in solution was therefore tested. Unlike the L-histidine case, D-mannitol radicals were not found to regenerate in solution under the same conditions (Figure 5.35a). This is a crucial finding for a broadly used excipient like D-mannitol, especially considering its use as a bulking agent, for which it can represent up to 90% w/w of lyophile formulations.

5.4.3 MS

MS experiments were undertaken to help identify the degradants produced upon irradiation and learn about the fate of the radicals after dissolution. In fact, there are multiple mechanisms by which radicals can recombine in aqueous solution. Non-irradiated and irradiated mannitol samples were therefore analysed and the spectra obtained were compared to identify signals from the degradation products formed upon irradiation (Figure 5.37 and Figure 5.38). The comparison between the negative mode spectra highlighted the presence of a species of m/z 179.20 which was detected only for the irradiated samples, whose signal was stronger for the sample that received the higher irradiation dose. This value corresponds to a negatively charged molecule of D-mannitol that has lost two protons. It was therefore proposed that the observed species was formed as a result of the irradiation process, which promoted the abstraction of a proton from the aliphatic chain of a molecule of D-mannitol and, either in the solid state or in solution, rearranged through a β -elimination mechanism.

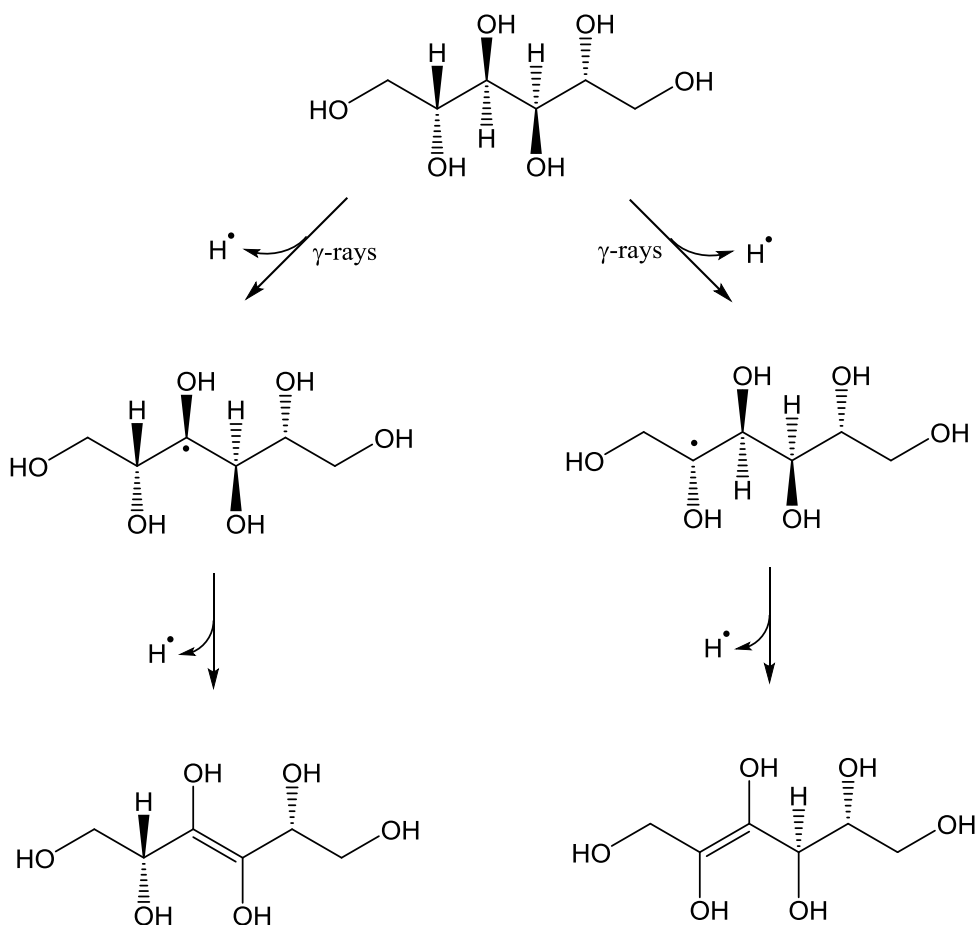


Figure 5.49 Proposed mechanism for the rearrangement of the radical leading to β -elimination.

5.4.4 NMR

^1H NMR experiments were carried out with the intent of obtaining useful information on the structure of the degradants formed from irradiation. The comparison between non-irradiated and irradiated ^1H NMR spectra (Figure 5.39 and Figure 5.40) showed the presence of additional signals which can be correlated to the irradiation process. Although the low intensity of the signal and the low resolution of the spectrum limited an exhaustive analysis, some conclusions can be drawn from the chemical shift of the peaks. The chemical shift of the doublet and singlet at 1.2 and 1.4 ppm is typical of protons belonging to aliphatic chains. For these lower values to be obtained the deshielding effect brought by the OH groups must no longer be in place, suggesting that the peaks belong to a mannitol molecule where one of the OH groups has been eliminated. The doublet could therefore originate from a coupling to a proton bound to the carbon atom from which the OH group has been extracted, or from a fragmentation of the parent molecule. More low intensity signals were found in the range of 3.4–3.9 ppm and can be associated to protons close to OH groups. The fact that this is also the range where the rest of the peaks of the parent molecule lie, makes the assignment of the peaks rather challenging. These could in fact potentially belong to *radical I*-like species or be associated to the peaks detected at 1.2 and 1.4 ppm. These findings suggest that NMR is unsuitable for the direct analysis of similar samples. Such limitations can potentially be overcome by applying a separation step prior to the NMR analysis, *e.g.* chromatographic techniques like HPLC, thus allowing to selectively analyse the small content of degradation products.

5.5 Conclusions

In this Chapter, the effects of γ -radiation sterilization on the pharmaceutical excipient D-mannitol have been studied. Mannitol is the most utilised excipient in parenteral formulations, where it is mostly used as a bulk agent and as such can represent up to 90% w/w of the drug. To the best of our knowledge, the degradation products formed upon irradiation of the said excipient have not been characterised before, nor studies on spin trapped mannitol radicals reported.

In this study, the evolution of the EPR active species formed after irradiation of the excipient in liquid nitrogen have been analysed in the range of 77–295 K by CW EPR spectroscopy. Our findings suggest that the primary effect of the ionising radiation on D-mannitol at this temperature is the abstraction of a proton from the aliphatic chain from either the carbon atom in position 3 or 4, leading to the formation of *radical I*. By first annealing to 120 K and subsequently to 170 K, a second and a third radical species are formed, *radical II* and *radical*

III, respectively by abstraction of a proton from the hydroxylic groups bound to either C1 or C6 and directly from the C-atom either in position 1 or 6. Univocal assignment of a structure to each of the newly formed paramagnetic species was not possible. Further annealing to 200 K and 240 K showed a progressive decrease of all the previously formed species, with a new radical characterised by a large isotropic doublet becoming the more dominant species. When the temperature was increased to 260 K and finally to r.t., other paramagnetic species were observed in the spectrum which were interpreted as the formation of new radicals. The complexity of the EPR spectrum in this temperature range did not allow the identification of the newly formed species. At least three r.t. persistent radical species are believed to be present, being a species with characteristics similar to *radical I*, a second species oxygen-centred and a third species which emerged from the spectrum at high MW power. The characterisation of the radicals' formation and evolution is essential for a thorough understanding of the radiation process in a multi-component system, particularly for a key excipient like mannitol, which exhibits rather complex EPR spectral features when irradiated. The quantification of the paramagnetic species at r.t. also showed, for industrially relevant radiation doses, a three times higher radical concentration compared to L-histidine. Spin trapping experiments offered important information about the reactivity of the radicals in solution. Not only a short lifetime of the species was assessed, but also the radical regeneration process that was witnessed for L-histidine was not observed for D-mannitol. Nevertheless, a spin trap adduct was detected by direct spin trapping with MNP. The use of other analytical techniques such as MS and NMR was tested in an attempt to obtain complementary information on the degradants formed upon irradiation. The MS analysis in particular highlighted the presence of a species 2 m/z units lower than the unaltered mannitol molecule, which was interpreted as the rearrangement of a C-centred radical formed by H abstraction, through elimination of a second proton with formation of a double bond. NMR also highlighted the presence of degradation products formed upon irradiation, but a full characterisation of such species was not possible due to intrinsic limitations of this magnetic resonance technique in this context.

5.6 References

1. European Parliament and Council of the European Union. *Directive 95/2/EC on food additives other than colours and sweeteners. Official Journal of the European Union* **60**, (1995).
2. Rowe, R., Sheskey, P. & Quinn, M. *Handbook of Pharmaceutical Excipients*. (The

- Pharmaceutical Press, London, UK, 2009).
3. Akers, M. J. Excipient-drug interactions in parenteral formulations. *J. Pharm. Sci.* **91**, 2283–2300 (2002).
 4. Pikal, M. J. & Costantino, H. R. *Lyophilization of Biopharmaceuticals. Biotechnology: Pharmaceutical Aspects* **2**, (AAPS Press, Arlington, VA, 2004).
 5. Raffi, J. *et al.* Electron paramagnetic resonance of radicals induced in drugs and excipients by radiation or mechanical treatments. *Spectrochim. Acta - Part A Mol. Biomol. Spectrosc.* **58**, 1313–1320 (2002).
 6. Karakirova, Y. & Yordanov, N. Mannitol as a radiation sensitive material for electron paramagnetic resonance dosimetry. *Bulg. Chem. Commun.* **47**, 144–148 (2015).
 7. Yordanov, N. D., Gancheva, V. & Georgieva, E. EPR and UV spectroscopic study of table sugar as a high-dose dosimeter. *Radiat. Phys. Chem.* **65**, 269–276 (2002).
 8. Yordanov, N. D. & Georgieva, E. EPR and UV spectral study of gamma-irradiated white and burned sugar, fructose and glucose. *Spectrochim. Acta Part A Mol. Biomol. Spectrosc.* **60**, 1307–1314 (2004).
 9. Karakirova, Y., Yordanov, N. D., De Cooman, H., Vrielinck, H. & Callens, F. Dosimetric characteristics of different types of saccharides: an EPR and UV spectrometric study. *Radiat. Phys. Chem.* **79**, 654–659 (2010).
 10. Kaminsky, W. & Glazer, A. M. Crystal optics of D-mannitol, C₆H₁₄O₆: crystal growth, structure, basic physical properties, birefringence, optical activity, Faraday effect, electro-optic effects and model calculations. *Zeitschrift für Krist.* **212**, 283–296 (1997).
 11. Fronczek, F. R. & Kamel, N. Three polymorphs (α , β , and δ) of D-mannitol at 100 K. *Acta Crystallogr. Sect. C Cryst. Struct. Commun.* **59**, 567–570 (2003).
 12. Stoll, S. & Schweiger, A. EasySpin, a comprehensive software package for spectral simulation and analysis in EPR. *J. Magn. Reson.* **178**, 42–55 (2006).
 13. Rustgi, S., Joshi, A., Riesz, P. & Friedberg, F. E.s.r. of spin-trapped radicals in aqueous solutions of amino acids. Reactions of the hydrated electron. *Int. J. Radiat. Biol.* **32**, 533–552 (1977).
 14. Wishart, D. S. *et al.* HMDB: A knowledgebase for the human metabolome. *Nucleic*

- Acids Res.* **37**, 603–610 (2009).
15. Dellinger, B. *et al.* Formation and stabilization of persistent free radicals. **31**, 521–528 (2007).
 16. Morton, J. R. Electron Spin Resonance Spectra of Oriented Radicals. *Chem. Rev.* **64**, 453–471 (1964).
 17. Carrington, A. & McLachlan, A. *Introduction to Magnetic Resonance*. (Harper and Row, New York, 1969).
 18. Choppin, G., Liljenzin, J.-O. & Rydberg, J. *Radiochemistry and Nuclear Chemistry*. (Butterworth-Heinemann Ltd, 1995).
 19. Alkorta, I. & Elguero, J. The carbon-carbon bond dissociation energy as a function of the chain length. *Chem. Phys. Lett.* **425**, 221–224 (2006).
 20. Thoraeus, R. Chapter III. Standard Measurements of the Cobalt 60 Gamma Radiation. *Acta radiol.* **51**, 63–78 (1959).
 21. Foote, C. S. & Clennan, E. L. in *Active oxygen in chemistry* 105–140 (Springer, Dordrecht, 1995).
 22. Wade, A. M. & Tucker, H. N. Antioxidant characteristics of L-histidine. *J. Nutr. Biochem.* **9**, 308–315 (1998).
 23. Erickson, M. C. & Hultin, H. O. A unique role of histidine in Fe-catalyzed lipid oxidation by fish sarcoplasmic reticulum. *Basic Life Sci.* **49**, 307–312 (1987).
 24. Erickson, M. C. & Hultin, H. O. Influence of histidine on lipid peroxidation in sarcoplasmic reticulum. *Arch. Biochem. Biophys.* **292**, 427–432 (1992).
 25. Matheson, I. B. C. & Lee, J. Chemical Reaction Rates of Amino Acids. *Photochem. Photobiol.* **29**, 879–881 (1979).
 26. Misra, H. P. & Fridovich, I. Superoxide dismutase and the oxygen enhancement of radiation lethality. *Arch. Biochem. Biophys.* **176**, 577–581 (1976).
 27. Gutteridge, J. M. C. & Halliwell, B. The role of superoxide and hydroxyl radicals in the degradation of DNA and deoxyribose induced by a copperphenanthroline complex. *Biochem. Pharmacol.* **31**, 2801–2805 (1982).
 28. Goldstein, S. & Czapski, G. Mannitol as an OH. scavenger in aqueous solutions and in

- biological systems. *Int. J. Radiat. Biol. Relat. Stud. Phys. Chem. Med.* **46**, 725–9 (1984).
29. Desesso, J. M., Scialli, A. R. & Goeringer, G. C. D-mannitol, a specific hydroxyl free radical scavenger, reduces the developmental toxicity of hydroxyurea in rabbits. *Teratology* **49**, 248–59 (1994).

Chapter 6

Photoactivation of a Platinum(IV) Anticancer Complex

The following publication in preparation is based on the present Chapter:

Vallotto, C., Shaili, S., Shi, S., Butler, J.S., Wedge, C.J., Newton, M.E. & Sadler P.J. Photoactivatable platinum anticancer complex generates tryptophan radicals. To be submitted to *Chem. Comm* (2018).

The octahedral platinum(IV) complex *trans,trans,trans*-[Pt(N₃)₂OH₂(pyridine)₂] is a potent cytotoxic anticancer compound when it is activated with blue or green light. The design and development of novel platinum anticancer agents is a priority considering that mechanisms of acquired or intrinsic resistance in cancer cells are undermining the potency of classic platinum anticancer compounds. This Chapter further investigates the mechanism of action of this novel compound and the biological target(s) of azidyl radicals in order to elucidate their *in vivo* reactivity.

6.1 Introduction

6.1.1 Cancer

Cancer is considered the second leading cause of death globally, accounting for 8.8 million deaths in 2015, meaning that nearly 1 in 6 deaths worldwide is due to cancer. According to the World Health Organization (WHO), the number of new cases is expected to rise by about 70% over the next 2 decades.¹ Cancer initiation is a multistep process, which has been correlated by numerous studies to free radicals and reactive species.²

Reactive oxygen species (ROS) and reactive nitrogen species (RNS) can originate in the organism respectively from reduction of molecular oxygen and oxidation of L-arginine. These

highly reactive species can induce damage to multiple biological structures, including DNA, lipids, membranes and proteins, with an average of 10^5 oxidative hits per day per cell in the human.³ The cell has therefore developed several resistance mechanisms, including nucleotide excision repair (NER), mismatch repair (MMR)⁴ and presence of antioxidants. The unbalance between prooxidant and antioxidant species in favour of the former is defined as oxidative stress.⁵ The possibility to take advantage of such reactive species to induce damage in tumour tissues has been previously explored. As discussed in the previous chapters, Electron Paramagnetic Resonance (EPR) is the technique of choice for the study of reactive radical species.⁶ In this Chapter the EPR spin trapping methodology is utilised to study the radical-based mechanism of action of novel platinum(IV) diazo anticancer complexes.

6.1.2 Metallo-organic compounds

The use of metals in medicines can be dated back to *ca.* 1910, when Ehrlich developed an arsenic-based antimicrobial agent, salvarsan, for the treatment of syphilis.^{7,8} Additionally, metals have been successfully used in the formulation of diagnostic agents for imaging of abnormal issues. The interest in metal complexes for both therapy and diagnosis is increasing, and approximately 50% of anticancer treatments nowadays involve the use of platinum-based compounds.⁹

Next, an overview on the development of Pt-based anticancer compounds is presented, from the early platinum(II) complexes to the potent photo-activable *trans,trans,trans*-[Pt(N₃)₂(OH)₂(pyridine)₂] complex. This promising photo-chemotherapy candidate that has been previously developed by the Sadler group¹⁰ is the subject of this work, which focuses in particular in investigating the mechanism of action of the said anticancer compound.

6.1.3 Pt-based chemotherapeutics

6.1.3.1 Pt^{II} complexes

Platinum is characterised by oxidation states that range from 0 to +6, with the two most common oxidation states being +2 and +4. Platinum(II) complexes exhibit a planar structural geometry, with the lower d orbitals completely filled and the upper most orbital ($d_{x^2-y^2}$) left empty (Figure 6.1). Amongst the various isotopes of Pt, ¹⁹⁵Pt is the most abundant (33.8%)¹¹ isotope and being the only nuclear magnetically active with a spin of ½. The square planar geometry allows both *cis* and *trans* isomers.

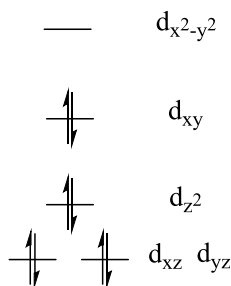


Figure 6.1 Splitting of the d-orbitals of a square-planar Pt^{II} (d^8) complex with strong donor ligands.

Cis-diamminedichloroplatinum(II), also referred to as *cis*-platin or CDDP (**1**, Figure 6.2), is the most famous and successful metallodrug, accidentally discovered by Rosenberg in 1965.¹² This platinum-based metallodrug is strongly active towards several types of cancer including ovarian, testicular and bladder cancer.¹³

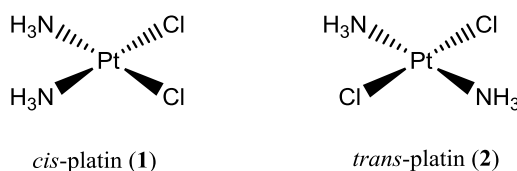


Figure 6.2 Structures of *cis*-platin (**1**) and *trans*-platin (**2**).

The mechanism of action of CDDP relies on the difference between plasma and intracellular concentrations of chlorine. After intravenous injection, the complex remains stable because of the high concentration of chloride in the blood plasma (*ca.* 100 mM).¹⁴ After CDDP enters the cell through passive diffusion¹⁵ or by active uptake,¹⁶ it is subject to hydrolysis consequently to the lower chloride concentration (4 – 20 mM)¹⁴ and the active chloroaqua species is formed (Figure 6.3).

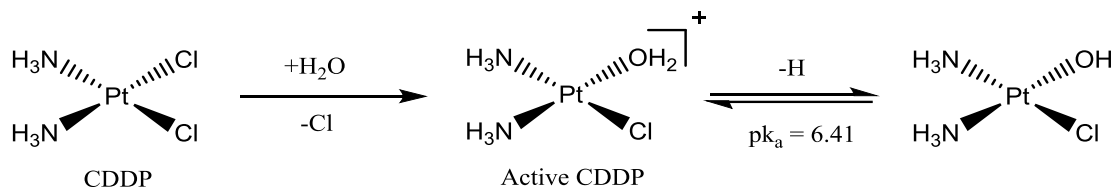


Figure 6.3 Hydrolysis of CDDP in the cytoplasm of the cell with formation of the active chloroaqua species and subsequent deprotonation of the complex.

Once the active CDDP chloroaqua species is formed, it reacts forming crosslinks with the DNA double strand, inducing unwinding and bending of the macromolecule which results in cell apoptosis.¹⁷ It has been reported that Pt^{II} preferentially binds to the N^7 atom of the purine nucleobase guanine (G). The majority of the crosslinks formed are reported to be intrastrand 1,2-d(GpG) crosslinks between two adjacent guanines (60-65 %) but also intrastrand crosslinks between guanine and adenine (A) occur (20-25 %), as well as interstrand crosslinks between opposite guanines.¹⁸ Although *cis*-platin is to date the most potent anticancer agent for the treatment of various cancers, important side-effects are associated to its administration. Such side-effects have been attributed to the formation of Pt^{II} -S species with physiological sulfur-based molecules, such as glutathione (GSH) and sulphur-containing amino acids like methionine and cysteine.¹⁹

Interestingly, *trans*-platin (**2**, Figure 6.2) did not show an anticancer activity as for the *cis* isomer, a finding that was associated to its inability to form 1,2-(GpG) intrastrand crosslinks which are the major product of *cis*-platin that induces cell apoptosis.²⁰

6.1.3.2 Second generation of Pt^{II} complexes

A second generation of Pt^{II} complexes was developed in order to overcome the unwanted side effects of CDDP. The new class of anticancer metallodrugs presented more stable ligands, replacing labile ligands which were easily substituted by water. The structure of carboplatin (**3**, Figure 6.4) presents a 1,1-cyclobutanedicarboxylate substituting the two chloride ligands in CDDP. This structural change resulted in an increased stability of the compound, but at the same time a reduced activity with consequent need of higher dosage. Carboplatin has been approved world-wide for the treatment of cancer, replacing CDDP as the treatment of choice for ovarian cancer.

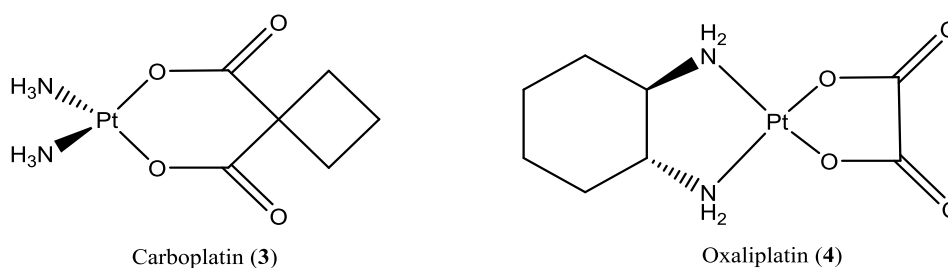


Figure 6.4 Structure of the second generation Pt^{II} complexes carboplatin (**3**) and oxaliplatin (**4**).

Another example of an approved second generation Pt^{II} complex is oxaliplatin (**4**, Figure 6.4). This compound was found to overcome *cis*-platin resistance by the presence of a bulky 1,2-diaminocyclohexane (DACH) group which prevents the binding of DNA repair proteins. Other

second generation complexes are nedaplatin, lobaplatin and heptaplatin, yet to be approved by the FDA but already in clinical use in Japan, China and South Korea.²¹

6.1.3.3 Pt^{IV} complexes

Pt^{IV} complexes present an octahedral, 5d⁶ geometry (Figure 6.5). Such compounds are considered “prodrugs”, being generally substitution inert and thermally stable in the +4 oxidation state, thus avoiding unwanted side reactions. The mechanism of activation of these compounds involves the intracellular reduction of the metal to generate reactive Pt^{II} species, which exhibit a pronounced cytotoxic activity.

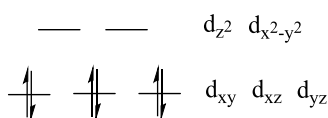


Figure 6.5 Splitting of the d-orbitals of an octahedral Pt^{IV} (d⁶) complex with strong donor ligands.

Several Pt^{IV} complexes were developed, including the promising satraplatin (**5**, Figure 6.6). This compound is reduced by intracellular metal-containing redox proteins to produce the active Pt^{II} form. Although satraplatin has not been approved by FDA yet, it has been involved in several clinical trials^{21,22} and it has been investigated both in the treatment of prostate cancer²³ and in combination therapy.²⁴

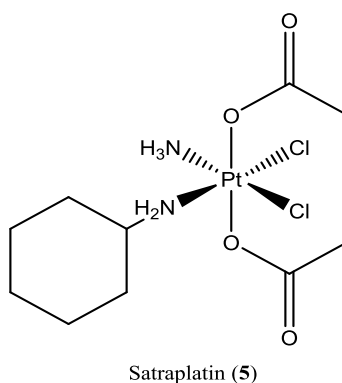


Figure 6.6 Structure of the Pt^{IV} octahedral complex satraplatin (**5**).

Despite the progresses made in limiting the unwanted reactions of these compounds, Pt^{II} species are still non-specifically generated throughout the body by reaction with reducing agents, hence inducing damages in non-cancer tissues. The need for more specific therapeutic agents led to the development of targeted delivery systems.

6.1.4 Targeted delivery

In order to increase the efficiency of the platinum compounds and limit the unwanted side effects, targeted delivery systems have been developed. These systems consist in incorporating the metallo-organic complex into a scaffold that protects the compound from premature hydrolysis and allows specific delivery to its biological target, typically the DNA of the cancer cell.

Targeted delivery can be distinguished in passive or active. With passive drug delivery, the chemotherapeutic agent is incorporated in scaffolds such as nanoparticles or liposomes, and reaches the tumour site by exploiting the enhanced permeability and retention effect.²⁵

Active drug delivery is mediated by receptor-binding molecules that are attached to the nano-scaffold to produce a specific uptake of the system into the tumour cell through receptor mediated internalisation. A number of receptors have been used for active delivery, including folate (FR), epidermal growth factor (EGF), androgen (AR) and transferrin (TfR) receptors, which are often overexpressed in certain tumour cells.

Although passive and active delivery represented an important advancement in the development of specific chemotherapeutic systems, the development of drug resistance mechanisms remains a major issue for platinum anticancer complexes. In order to overcome these resistance mechanisms, alternative therapeutic therapies such as phototherapy have been developed.

6.1.5 Phototherapy

The term phototherapy describes the exposure to specific wavelengths of light to treat specific medical disorders. More specifically, photodynamic therapy (PDT) is a form of phototherapy that involves the use of light in combination with a light-sensitive compound, also called photosensitiser (PS).^{26,27} The administration of the PS in the patient is followed by activation of the same by irradiation at a specific wavelength, so inducing the cytotoxic effect in the region of interest. Longer wavelengths (> 600 nm) are preferred in PDT for their ability to penetrate deeper into tissues (Figure 6.7).²⁸

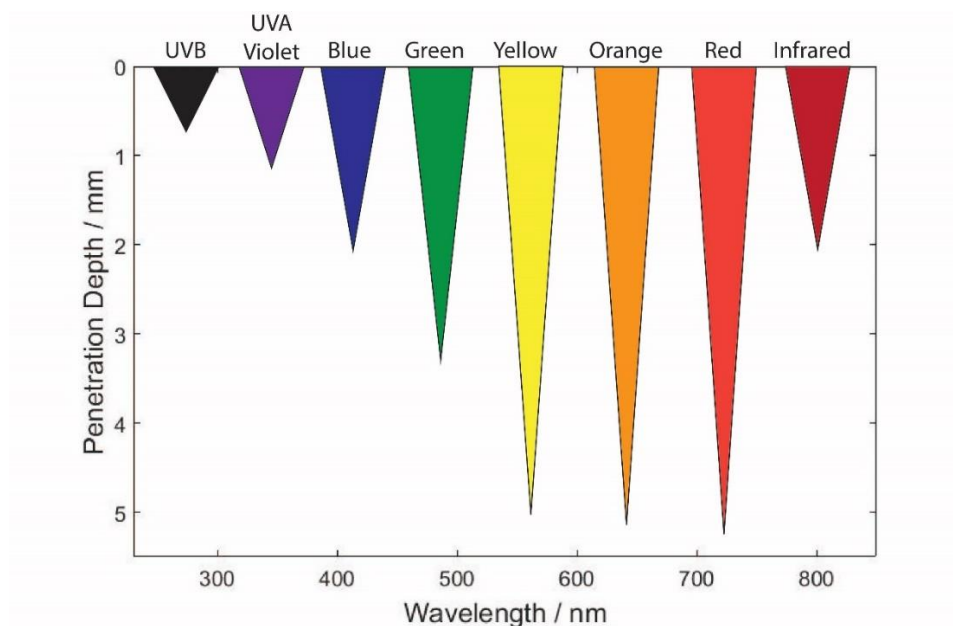


Figure 6.7 Depth of penetration of different wavelengths (figure adapted from ref. 28).

The mechanism by which PDT exerts its action involves i) a photo-sensitiser, often porphyrins which absorb in the 600-800 nm;²⁹ ii) light; iii) molecular oxygen ($^3\text{O}_2$) which is also required to induce the cytotoxic effect. The PS is photo-excited from a ground (S_0) state to a single excited (S_1) state, at which point can be dissipated through different pathways. Amongst them, a triplet excited (T_1) state is believed to be involved in the process. In particular, PDT has been reported to be induced by quenching of the T_1 state, which can happen through two different processes, type I and type II, both proceeding during PDT. Type I mechanism involves either an electron or hydrogen transfer between the T_1 state and a molecular substrate, leading to the formation of radical species which in turn reacts with $^3\text{O}_2$ to form ROS. Type II mechanism involves instead direct interaction of T_1 with $^3\text{O}_2$, which results in formation of the cytotoxic singlet oxygen ($^1\text{O}_2$).

Although PDT is still being used in cancer therapy for the advantage of being a non-invasive procedure, several disadvantages are limiting its application. Firstly, the fact that numerous cancer tissues are characterised by oxygen deficiency (hypoxia)³⁰ is a major drawback for PDT, which requires molecular oxygen to induce its cytotoxic effect. Secondly, some PS have a clearance time of several weeks, thus limiting the patient's exposure to daylight for months.²⁹ Finally, resistance mechanisms are associated with PDT, involving the inactivation of ROS mediated by antioxidant enzymes³¹ and the stabilisation of damaged proteins through the action of heat shock proteins (HSP).³²

6.1.6 Photo-chemotherapy

Differently from PDT, the photo-activation process of chemotherapeutics does not involve the presence of molecular oxygen to exert its action, being defined as a type III mechanism. This section describes the development of kinetically inert Pt^{IV} photo-activable complexes.

6.1.6.1 Pt^{IV} diiodo complexes

The first photo-activable Pt^{IV} diiodo complexes were developed by Bednarski.³³ These complexes presented an ethylene-diamine ligand as opposed to the ammine ligands in *cis*-platin, in order to stabilise the complex and avoid photo-isomerisation. The complex *cis,trans*- $[\text{Pt}(\text{en})(\text{Cl})_2(\text{I})_2]$ (**6**, Figure 6.8) was synthesised, where iodine was selected as opposed to more electronegative atoms (Cl, Br) for the ability to absorb longer wavelengths.³³

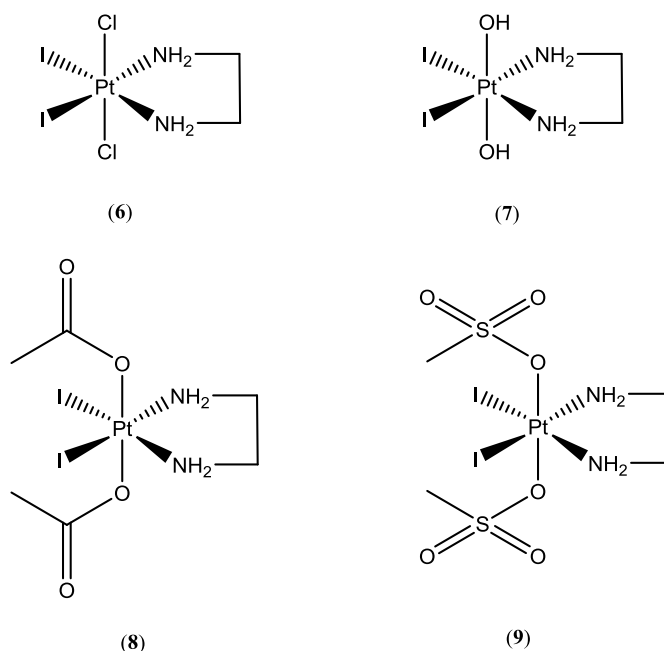
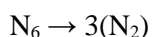


Figure 6.8 Structures of early photo-activable Pt^{IV} -diiodo complexes.

However, the complex was found to exhibit an equivalent dark and light cytotoxicity which was attributed to its high reduction potential (*ca.* 75 E/mV). The chlorido ligands were substituted with hydroxido-based ligands, resulting in a lower reduction potential and LMCT band at *ca.* 400 nm. Nevertheless, these complexes were found to undergo reduction from Pt^{IV} to Pt^{II} by biological reducing agents rendering them not specific to tumour cells,³³ so that alternative ligands to iodides were investigated.

6.1.6.2 Pt^{IV} diazo complexes

Transition metal complexes containing azido ligands have been reported to be light sensitive, independently from the transition metal centre utilised. Photo irradiation of the platinum diazido complex *trans*-[Pt(CN)₄(N₃)₂]²⁻ at 300 nm was reported to induce a simultaneous two one-electron reduction of the Pt^{IV} centre, producing azidyl radicals (•N₃), as confirmed by EPR.³⁴ Interestingly, the irradiation of *cis*-[Pt(PPh₃)₂(N₃)₂] led to the formation of hexaazabenzene (N₆) and [Pt(PPh₃)₂]. The observation of bubbles in the solution was attributed to the decomposition of N₆ into nitrogen gas:



A second generation of Pt^{IV} photo-activable diazo complexes was developed by the Sadler group (Figure 6.9). Both *cis* (**10**) and *trans* (**11**) exhibited dark stability in the presence of intracellular reducing agents,³⁵ and were found to produce bubbles upon photo-irradiation with 365 nm UVA.³⁶ In a later study, *trans* diamine diazido Pt^{IV} complexes were found to display a greater photo-cytotoxicity compared to their *cis*-isomers, an effect that was attributed to a different intra cellular target or a different mechanism of DNA attack.³⁷

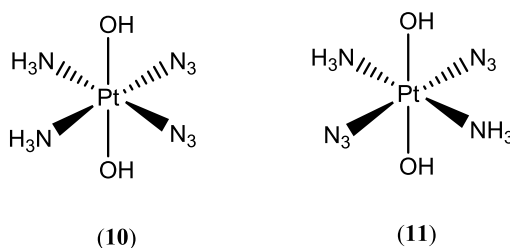


Figure 6.9 Structures of platinum(IV) diamine diazo complexes.

Despite the promising characteristics of these complexes, the photo-activation at 365 nm was a limit to the *in vivo* applications of the compounds. In order to lower the energy of the LMCT band of the Pt^{IV} diazo complexes involved, amine groups were substituted with π -acceptor pyridine ligands (Figure 6.10). Single substitution (complex **12**) did not lower the LMCT band energy, but contributed in decreasing the half maximal inhibitory concentration (IC₅₀) value from 99.2 μM to 1.9 μM in A2780 ovarian cancer cells, an effect that was attributed to the formation of alternative Pt^{II}-DNA adducts. Photo-irradiation of complex **12** in the presence of 5'-guanosine monophosphate (5'-GMP) showed formation of both mono and bis-adducts,³⁸ suggesting the presence of a novel mechanism of action which could overcome resistance mechanisms. *In vivo* irradiation also showed anti-cancer activity of the complex, which was reported to occur through an autophagic pathway instead of apoptosis.³⁹

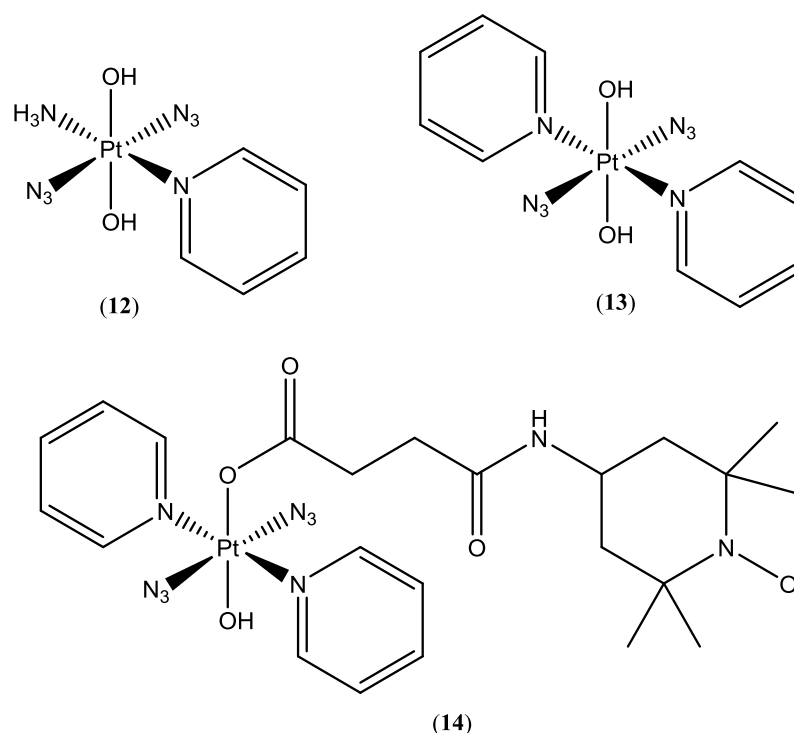


Figure 6.10 Structure of mono-pyridine **(12)**, bis-pyridine **(13)** and bis-pyridine-TEMPO platinum(IV) diazo complexes.

Replacement of the second ammine ligand with a pyridine led to the production of *trans,trans,trans*-[Pt(N₃)₂(OH)₂(pyridine)₂] (complex **13**, Figure 6.10), which is the subject of this work. Complex **13** was the first photo-activable Pt^{IV} diazo anticancer complex to be activated with UVA, blue and green light. The complex exhibited a LMCT band at 294 nm, which decreased upon irradiation and was attributed to the loss of azide ligands.⁴⁰

The photo-cytotoxicity of complex **13** was demonstrated in various cancer cell lines. Photo-irradiation of the complex in the presence of 5'-GMP showed the formation of bubbles, as well as a number of Pt^{II} adducts which were characterised by ¹⁹⁵Pt NMR spectroscopy.⁴⁰ To date, complex **13** is one of the most potent platinum(IV) diazo photo-activable anticancer complexes.

Conjugation of complex **13** with the nitroxide spin label 2,2,6,6-tetramethylpiperidine 1-oxyl (TEMPO) led to the production of *trans,trans,trans*-[Pt(N₃)₂(OH)(OCOCH₂CH₂CONH-TEMPO)(py)₂] (complex **14**, Figure 6.10). This complex exhibited a phototoxicity comparable to complex **13**, respectively displaying a IC₅₀ of 5.9 ± 0.2 and 7.1 ± 0.4 μM against A2780 human ovarian carcinoma cells. Both complexes were found much more cytotoxic than CDDP (IC₅₀ > 80 μM).⁴¹

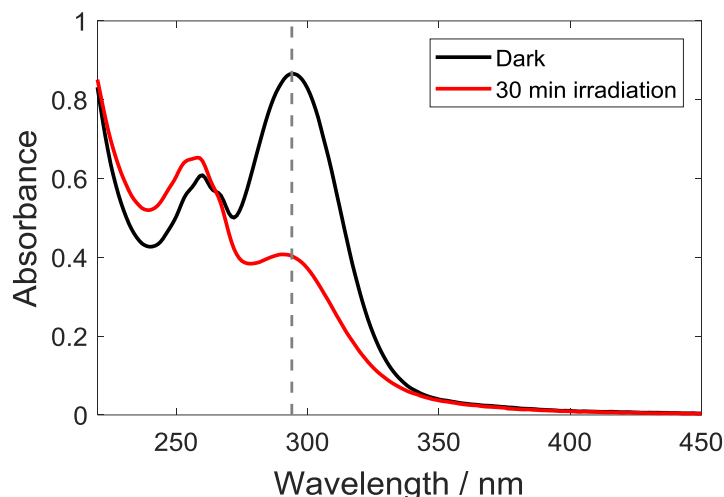


Figure 6.11 UV-visible spectra of complex **13** (62.5 μ M) prepared in phosphate buffer at pH 7.2 in the dark (black) and after 30 minutes of irradiation with 465 nm blue LED light (red). The dashed gray line indicates the LMCT band at 294 nm. Spectra were collected on a LAMBDA 1050 UV/Vis spectrophotometer in a 1 cm pathlength cuvette.

6.1.6.3 Photo-degradation pathways of complex **13**

The decrease of the LMCT band at 294 nm obtained upon photo-irradiation of complex **13** has been previously assigned to the loss of azide ligands.⁴⁰ This finding, together with the observation of bubbles formed upon irradiation of the platinum compound, suggested the release of azidyl radicals ($\bullet\text{N}_3$) with consequent dimerization of $\bullet\text{N}_3$ to form N_2 . The release of $\bullet\text{N}_3$ as a consequence of the photo-activation of complex **13** was proved by spin trapping experiments. The irradiation of complex **13** in the presence of the nitron spin trapping agent DMPO showed the formation of the DMPO- N_3 spin adducts, which was generated upon release of $\bullet\text{N}_3$ as confirmed by experiments with labelled ^{15}N azides.⁴² Additionally, previous photo-irradiation studies of complex **13** in the presence of 5'-GMP showed the formation of mono- and bi-functional Pt^{II} -GMP adducts, suggesting a stepwise loss of azide ligands.^{36,40,43} The irradiation of an analogue of complex **13**, *trans,trans,trans*-[Pt(N_3)₂(OH)₂(MA)(py)] (**14**, with MA = methylamine) has been reported to generate singlet oxygen ($^1\text{O}_2$) through $\bullet\text{OH}$ dimerization and formation of H_2O_2 , which upon disproportionation generated $^1\text{O}_2$ and H_2O .⁴⁴ It therefore appears that multiple degradation pathways of photo-activated complex **13** are possible (Figure 6.12).

A similar photo-degradation pathway was reported for complex **14**, where illumination of the compound with blue (420 nm) light led to the formation of multiple products involving the release of azidyl radicals and of the nitroxide radical, which was suggested to be partially responsible for the anticancer activity of the compound.

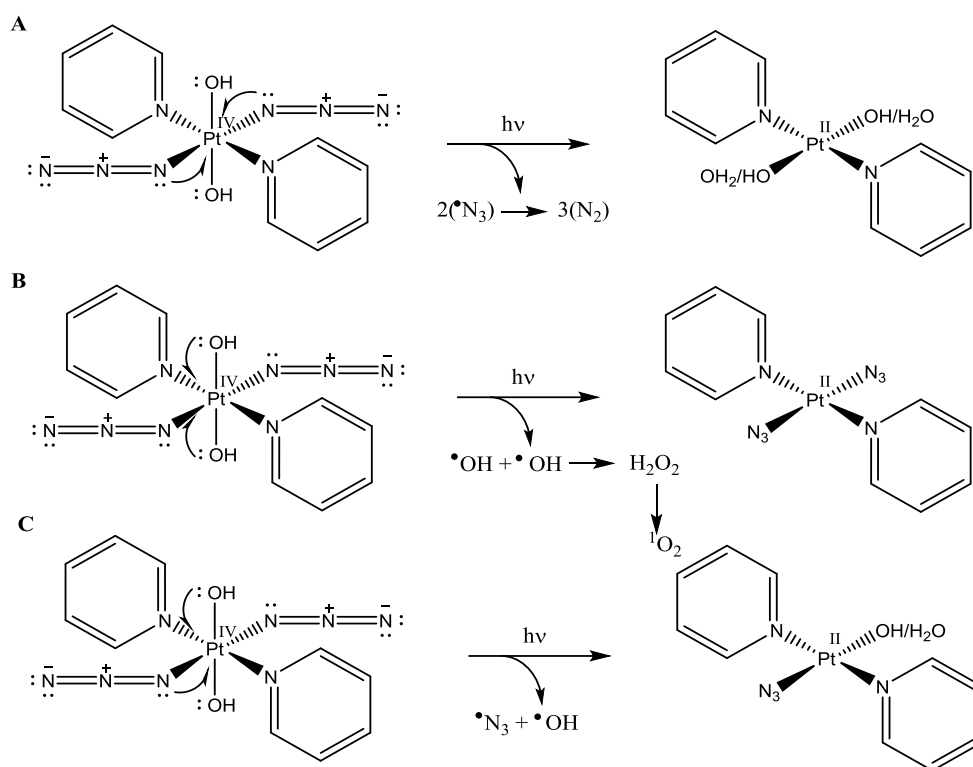


Figure 6.12 Photo-irradiation of complex 13 leading to the reduction of Pt^{IV} to Pt^{II} via two one-electron donations from (A) two azide; (B) two hydroxyl; (C) one azide and one hydroxyl ligands (figure adapted from ref. 10).

6.1.6.4 Reactivity of azidyl radicals towards amino acids

Like reactive oxygen species (ROS), reactive nitrogen species (RNS) are able to induce major damages in living organisms.^{45,46} The reactivity of azidyl radicals towards aromatic amino acids has been previously reported,⁴⁷ as opposed to their non-reactivity towards aliphatic amino acids and nucleic acid derivatives.⁴⁸

Amino acids are organic compounds which play a major role in a variety of biochemical pathways. L-tryptophan is an essential amino acid (*i.e.* cannot be synthesised *de novo* by the human organism) precursor of a number of biomolecules, including neurotransmitters such as serotonin and hormones like melatonin.⁴⁹ Pulse radiolysis studies reported $\bullet\text{N}_3$ to react with L-trp leading to the formation of free azide (N_3^-) and a neutral tryptophan radical (L-trp \bullet). The reaction was suggested to proceed through a one-electron transfer mechanism (Figure 6.13 B), as opposed to an hydrogen atom transfer mechanism (Figure 6.13 A) with formation of an intermediate tryptophan cation radical (L-trp \bullet^+) which, with a pK_a of 4.3, at physiological pH quickly deprotonates to form the L-trp neutral radical species.⁵⁰

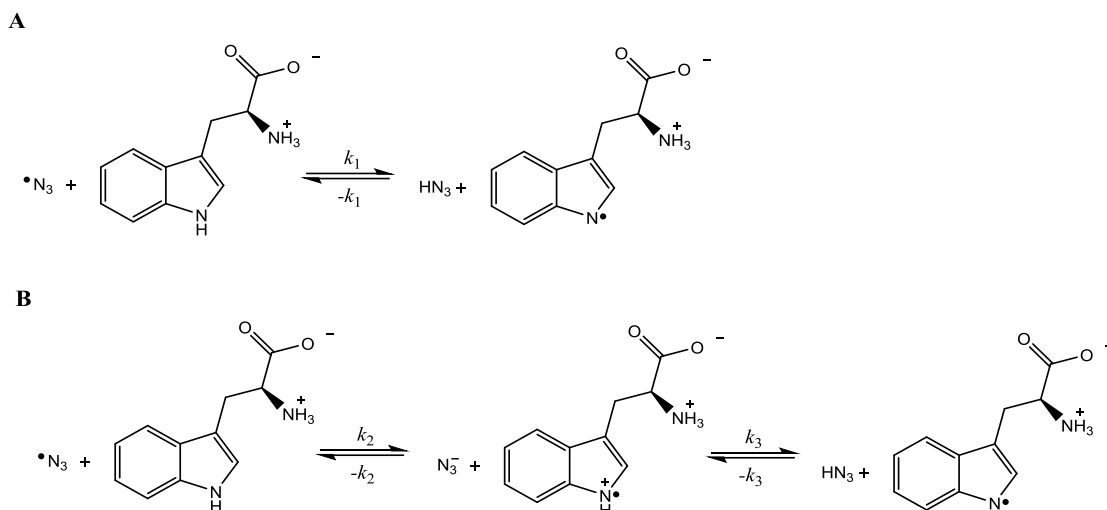


Figure 6.13 Reaction between the azidyl radical and L-trp proceeding through A) hydrogen atom abstraction and B) one-electron transfer pathways.

A previous spin trapping study conducted by Butler *et al.*, reported the ability of L-trp to partially and completely suppress the formation of the DMPO- N_3 spin adduct upon photoactivation of complex **13**.⁴² The lack of ^1H NMR resonances attributable to the non-radical species formed from decomposition of DMPO- N_3 further supported the quenching of the azidyl radicals.¹⁰ The detection of free azide (N_3^-) was in agreement with previous studies suggesting one-electron oxidation pathway.⁵⁰ The photoprotective effect of L-trp was also tested on A2780 human ovarian cancer cells, proving its ability to increase cell viability at low, physiologically relevant concentrations (μM).⁴² These findings suggested indoles and derivatives to be a favourable target for photo-released azidyl radicals when part of biological structures in the cell, inducing cell death through an additional pathway in alternative to DNA platination.

6.1.6.5 Photo-irradiation in the presence of melatonin

Melatonin (MLT), also known as N-acetyl-5-methoxytryptamine, is a hormone produced by the pineal gland in mammals that regulates the circadian rhythms in animals.

Approved by the FDA as a dietary supplement,⁵¹ melatonin is commonly used in the treatment of insomnia⁵² and jet lag.⁵³ The intracellular concentration of melatonin was reported to be tissue/organ dependent,⁵⁴ while the plasma concentration is in the nanomolar range.⁵⁵ Melatonin was reported to present antioxidant properties towards both ROS and RNS. The interaction of melatonin with the hydroxyl radical was reported to proceed through a one-electron oxidation, to produce a melatonin cation radical ($\text{MLT}^{\bullet+}$) which readily deprotonates at physiological pH

to give, similarly to L-trp, the melatonin neutral radical (MLT \bullet).⁵⁶ Moreover, the addition of the hydroxyl radical to the indole ring of melatonin has been reported.⁵⁷ Antioxidant properties towards singlet oxygen ($^1\text{O}_2$) were also exhibited,⁵⁸ but not towards the superoxide radical ($\text{O}_2\bullet^-$).⁵⁹ Regarding RNS, melatonin exhibited scavenging properties towards nitric oxide ($\text{NO}\bullet$), peroxynitrite anion (ONOO^-) and azidyl radical ($\bullet\text{N}_3$).

Anti-tumour activity of MLT towards various types of cancer has also been reported, including breast⁶⁰ and colon.⁶¹ Nevertheless, no serious side-effects deriving from administration of MLT in patients have been reported to date.^{62,63}

The quenching ability of MLT towards $\bullet\text{N}_3$ released upon photo-activation of complex **13** has been previously investigated with the spin trapping methodology.¹⁰ Butler reported the simultaneous detection of both the DMPO- N_3 spin adduct, partially quenched by MLT, and the DMPO-OH adduct, suggesting alternative activation pathways for complex **13** in the presence of MLT which involved the release of $\bullet\text{OH}$. High resolution mass spectrometry (HR-MS) experiments showed the formation of $[\text{Pt}(\text{OH})_2(\text{py})_2(\text{MLT})]^{2+}$ adducts, supporting the formation of a MLT \bullet which binds to the platinum centres.¹⁰ These findings are corroborated by previous studies, which reported the ability of MLT to bind to various metal ions.^{64,65} Additionally, the formation of MLT-OH adducts was reported, accounting for the photo-protective effect of MLT despite the induced release of hydroxyl radicals.

In this Chapter, photo-irradiation of *trans,trans,trans*- $[\text{Pt}(\text{N}_3)_2(\text{OH})_2(\text{pyridine})_2]$ (complex **13**) in the presence of indole derivatives was investigated with the spin trapping methodology. A deeper understanding of the dual mechanism of action by which platinum(IV) chemotherapeutic drugs perform their anticancer activity is essential in order to design more specific and therefore safe anticancer drugs. Additionally, experiments aimed to explore the cellular targets of this class of anticancer compounds were performed.

6.2 Experimental

Below are the experimental sample preparation and instrumentation set up specific to this Chapter. More details regarding instrumentation are described in **Chapter 3**.

6.2.1 Materials

Trans,trans,trans-[Pt(N₃)₂(OH)₂(py)₂] (complex **13**) was supplied by the Sadler group, having been synthesised as previously reported.¹⁰ L-tryptophan (L-trp), melatonin (MLT), L-histidine (L-his), pentagastrin (N-t-Boc-β-Ala-Trp-Met-Asp-Phe amide), acetonitrile (ACN), dimethylformamide (DMF), 5,5-dimethyl-1-pyrroline N-oxide (DMPO) and 2-methyl-2-nitrosopropane (MNP) dimer were all purchased from Sigma Aldrich. Melatonin, pentagastrin, DMPO and MNP dimer were stored at -20 °C. Absolute ethanol (AR grade) was purchased from Fischer Scientific.

6.2.2 Sample preparation

Solutions containing combinations of complex **13** (5 mM), MNP (80 mM), L-tryptophan (40 mM), L-histidine (100 mM) and melatonin (different concentrations) were prepared in phosphate buffer (p.b.) 50 mM at pH 7.2. MNP (1.6 M) was prepared by dissolution of the dimer in ACN and subsequent dilution 1:20 in water. Melatonin (200 mM) was either dissolved in ethanol (EtOH) and subsequently diluted 1:5 in water or dissolved directly in water. Samples *ca.* 100 µL were transferred using a plastic syringe with metal needle to a standard quality quartz tube with inner diameter of 1.0 mm and outer diameter of 2.0 mm (Wilmad LabGlass) and sealed with parafilm. Sample tubes were then positioned in the EPR cavity so that the sample solution was crossing the entire length of the cavity. Sample preparation was done under dim controlled lightning conditions and transfer to the EPR spectrometer was done in the dark in order to prevent the photo-activation of complex **13** prior to the beginning of the experiment.

6.2.3 Instrumentation

6.2.3.1 EPR spectroscopy

All EPR spectra were recorded on a X-band *Bruker EMX* CW EPR spectrometer at ambient temperature (*ca.* 295 K).

6.2.3.2 Irradiation

The LED bulb was inserted at the end of a Teflon tube which was clamped to a support. The TM₁₁₀ cavity is equipped with a grid on the front to allow optical access to the sample (*ca.* 80% transmission). The tube was therefore placed in contact with the grid of the EPR cavity in order

to convey all the light into it (Figure 6.14). In this work, the position of the LED was maintained throughout all the irradiation experiments. The LED bulb was connected to a current generator, which was switched on at the beginning of the irradiation. Either a 465 nm blue light (LED465E, Thorlabs) or a 528 nm green light (LED528E, Thorlabs) LED was used for irradiating the samples. The radiation power was measured with a power meter and was found to be 7.1 mW cm^{-2} for the 465 nm diode and 5.4 mW cm^{-2} for the 528 nm diode.

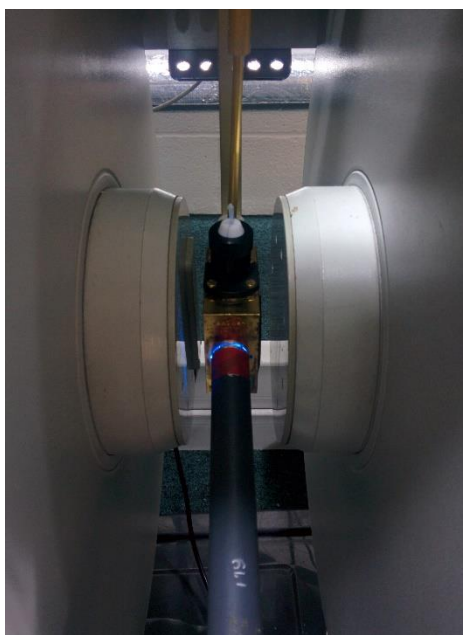


Figure 6.14 Setup of the X-band EPR cavity for the irradiation experiments, showing the LED light bulb inserted at the end of a Teflon tube, which is clamped on a support (not shown in the figure).

6.2.4 EPR simulations

EPR spectral simulations were performed in Matlab using the EasySpin package.⁶⁶ The *garlic* routine (appropriate for the fast-motional regime) was used for all the experiments.

Simulations of the MNP-tryptophan (MNP-Trp) and the MNP-melatonin (MNP-MLT) spin adducts were performed by including the only hyperfine coupling arising from the nitroxidic nitrogen, which was considered to be fully isotropic. Simulation of the MNP- α -hydroxy-ethyl adduct was performed including the hyperfine couplings of both the nitroxidic nitrogen and the α -proton. Simulation of the DMPO- N_3 nitrene spin adduct was performed considering couplings to the nitroxidic nitrogen, the β -proton of the spin trapping agent and the α -nitrogen of the trapped azidyl radical.

EPR parameters of the MNP di-adduct di-*tert*-butyl nitroxide (DTBN) were obtained by fitting a spectrum acquired from a solution of MNP which had been illuminated overnight with a

465 nm LED, in order to promote the formation of DTBN. Hyperfine couplings arising from both the nitroxidic nitrogen and statistical abundance of nearest neighbour ^{13}C nuclei were included and considered to be fully isotropic.

An isotropic \mathbf{g} -tensor was used for all the simulations and dynamic effects were neglected.

6.3 Results

6.3.1 L-tryptophan

The ability of L-trp to switch the cytotoxicity of complex **13** by quenching photo-generated azidyl radicals was previously reported by Butler *et al.*⁴² It was also suggested that the mechanism by which the process occurs involved one-electron oxidation of the amino acid. This assertion was supported by a previous pulse radiolysis study where transient tryptophan radical cation ($\text{L-trpH}^{\bullet+}$) was formed after reacting with azidyl radicals, subsequently deprotonating to give the neutral tryptophan radical (L-trp^{\bullet}).⁵⁰ Nevertheless, the formation of a tryptophan radical intermediate formed as a result of photo-activation of platinum(IV) complexes has not yet being directly observed. In this work, spin trapping of L-trp^{\bullet} was attempted with the nitroso spin trap MNP.

6.3.1.1 Spin trapping of complex 13 with MNP

First, the photo-activation of complex **13** was tested in the presence of the spin trapping agent 2-methyl-2-nitrosopropane (MNP). Nitroso spin trapping agents like MNP are known for their specificity towards the trapping of carbon-centred radicals, as described in **Chapter 1**.

A solution of complex **13** (5 mM) in the presence of an excess of MNP (80 mM) in p.b. 50 mM at pH 7.2 was irradiated with a 465 nm blue LED, with the setup described in Section 6.2.3.2. No other signal than di-tert-butyl nitroxide (DTBN) was observed in the dark. The formation of the DTBN background signal in spin trapping experiments with MNP has been discussed previously in **Chapter 4**. Photo-irradiation of the sample resulted in the progressive increase of the DTBN signal, the formation of which is known to be promoted by light⁶⁷ (Figure 6.15). Additionally, several low intensity lines could be observed (Figure 6.16). The multiplicity of the lines and the fact that only a small amount of such unknown species was detected, suggested this paramagnetic species to be a small fraction of azidyl radicals being trapped by MNP. Nevertheless, previously reported hyperfine couplings for the MNP-N_3 spin-adduct⁶⁸ did not match the observed signal (Figure 6.16).

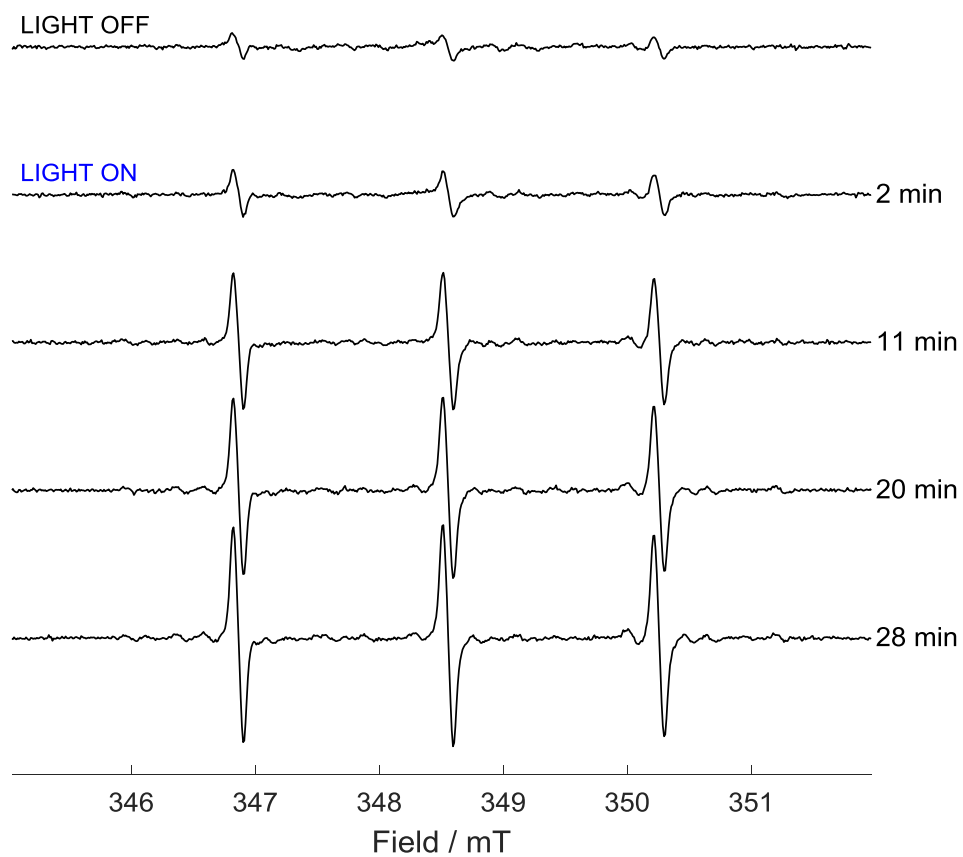


Figure 6.15 X-band CW EPR spectrum of a solution of complex **13** (5 mM) and MNP (80 mM) in p.b. 50 mM at pH 7.2, before and during continuous irradiation with a 465 nm blue LED. Each scan is the sum of 10 consecutive scans. Times reported refer to the time passed between the start of the irradiation and the end of the acquisition of the last scan included in the spectrum.

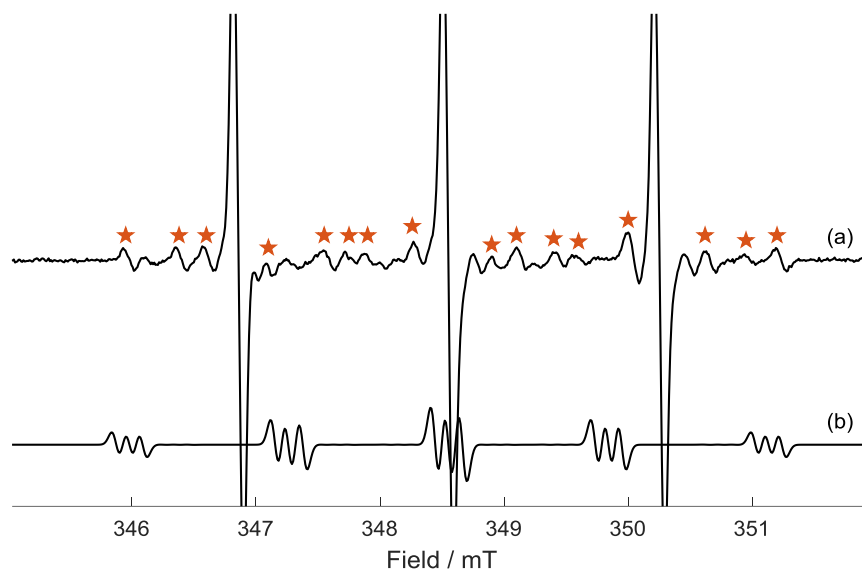


Figure 6.16 a) X-band CW EPR spectrum of a solution of complex **13** (5 mM) and MNP (80 mM) in p.b. 50 mM at pH 7.2, after 32 minutes of continuous irradiation with a 465 nm blue LED. The spectrum is the sum of 156 consecutive scans. ★ indicate additional paramagnetic species other than DTBN. b) simulation of the MNP- N_3 spin adduct obtained with previously reported hyperfine couplings ($a_{N1,N2} = 1.29$ mT; $a_{N3} = 0.11$ mT).⁶⁸

6.3.1.2 Spin trapping of L-trp radical with blue light

Next, the irradiation of complex **13** in the presence of L-trp and MNP was investigated. A solution of complex **13** (5 mM) and MNP (80 mM) was prepared in the dark adding an excess of L-trp (40 mM) to the sample mixture. No EPR signal other than a low intensity DTBN triplet was detected in the dark (Figure 6.17). When the sample was irradiated with blue light, an additional 3-line species was detected. The lines of the newly formed signal are almost overlapping the spectrum of DTBN, but can be easily distinguished from it for being broader and characterised by a slightly smaller hyperfine coupling. This signal was attributed to the spin-adduct MNP-Trp, with a neutral L-trp radical is being trapped by the nitroso spin trapping agent. The EPR spectrum was simulated with Easyspin⁶⁶ considering a combination of the MNP-Trp spin adduct and DTBN (Figure 6.18). The EPR parameters extracted by simulation (Table 6.1) were found to be in good agreement with previously published ones, where the tryptophan radical was formed from UV photolysis and subsequently trapped with MNP.⁶⁹ Previous EPR studies carried out at low temperatures suggested that photolysis of Trp induced the rupture of the N-H indole bond, following an electron rearrangement with the unpaired electron locating in position 3 of the indole ring (refer to Figure 6.39).⁷⁰ In fact, if the unpaired electron were to be located in any other position in the molecule, additional hyperfine splitting would have been detected from the spin-trap adduct.

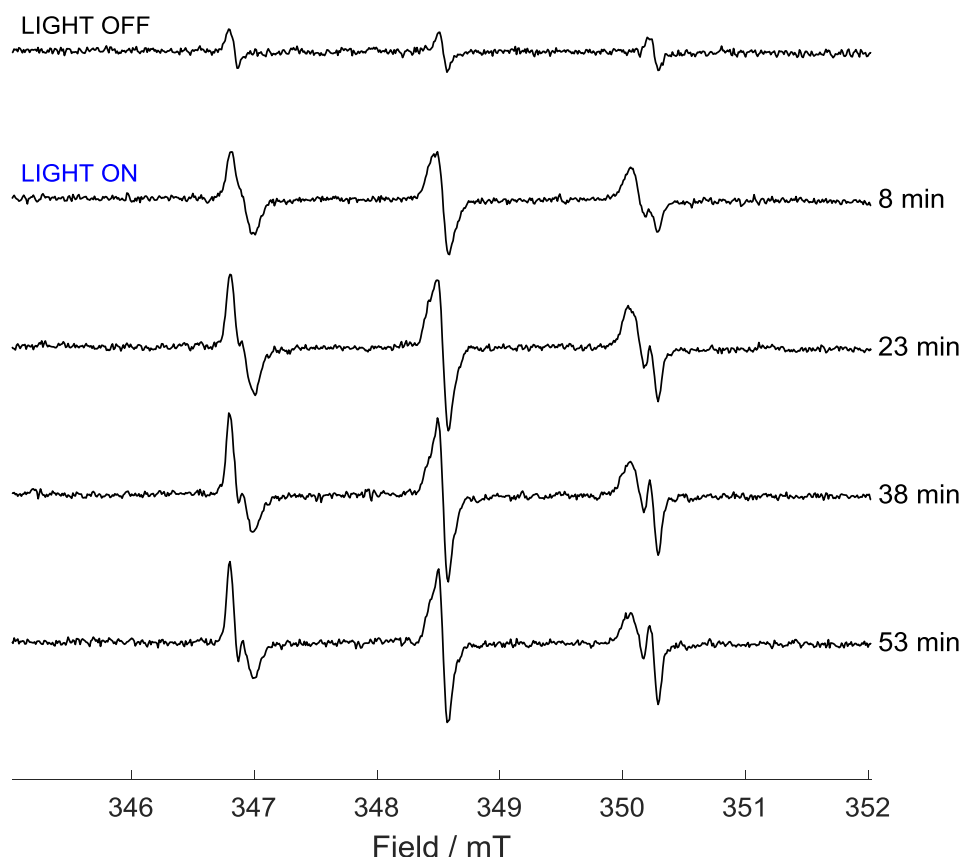


Figure 6.17 X-band CW EPR spectrum of a solution of complex **13** (5 mM), L-trp (40 mM) and MNP (80 mM) in p.b. 50 mM at pH 7.2, before and during continuous irradiation with a 465 nm blue LED. Each spectrum is the sum of 30 consecutive scans. Times reported refer to the time passed between the start of the irradiation and the end of the acquisition of the last scan included in the spectrum.

To determine the concentration of the radical species detected, the contribution of the MNP-Trp adduct and DTBN were separated by simulation and quantified by comparison with TEMPOL standard solutions as previously described in **Chapter 3**. The concentration of the spin adduct reached a maximum of 0.7 μM after *ca.* 16 minutes of irradiation and slowly decreased afterwards (Figure 6.19). Considering that the quantification of the spin trap adducts has been obtained against a reference solution measured on low precision tubes, an absolute error on this and the following kinetics data of *ca.* 10-20% can be indicatively estimated. When the irradiation stopped, a fraction of the spin-adduct could still be detected for over one hour.

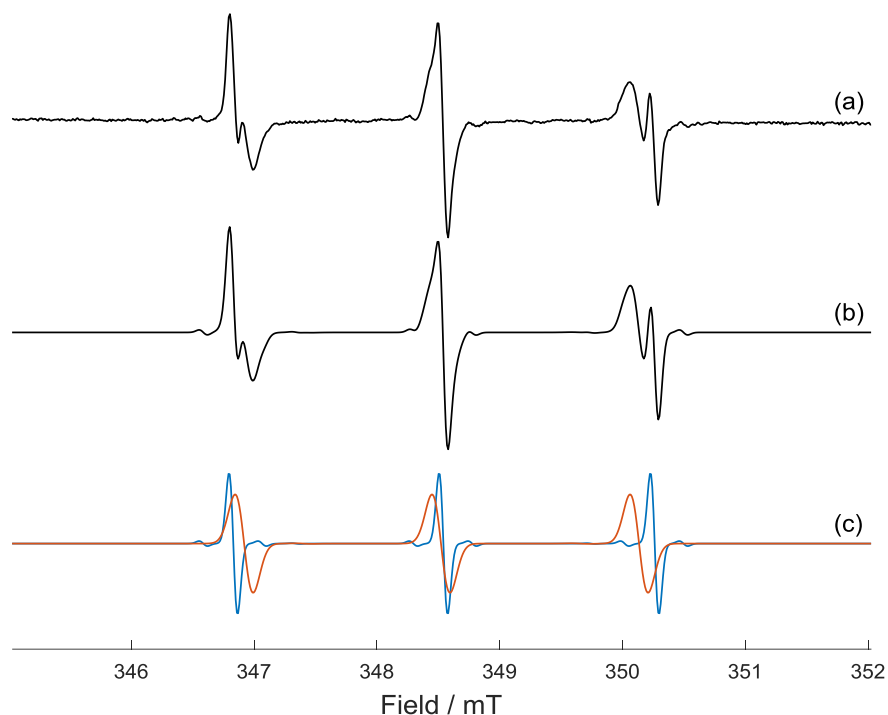


Figure 6.18 (a) X-band EPR spectrum of MNP-Trp spin adduct formed from photo-irradiation of complex **13** (5 mM), L-trp (40 mM) and MNP (80 mM) after 41 min of irradiation with 465 nm blue LED light; (b) EasySpin⁶⁶ simulation of the EPR spectrum for a combination of MNP-Trp spin adduct and DTBN; (c) simulation of the only MNP-Trp spin adduct (red) and of the only DTBN (blue). The relative weights of MNP-Trp and DTBN are respectively *ca.* 75% and 25%.

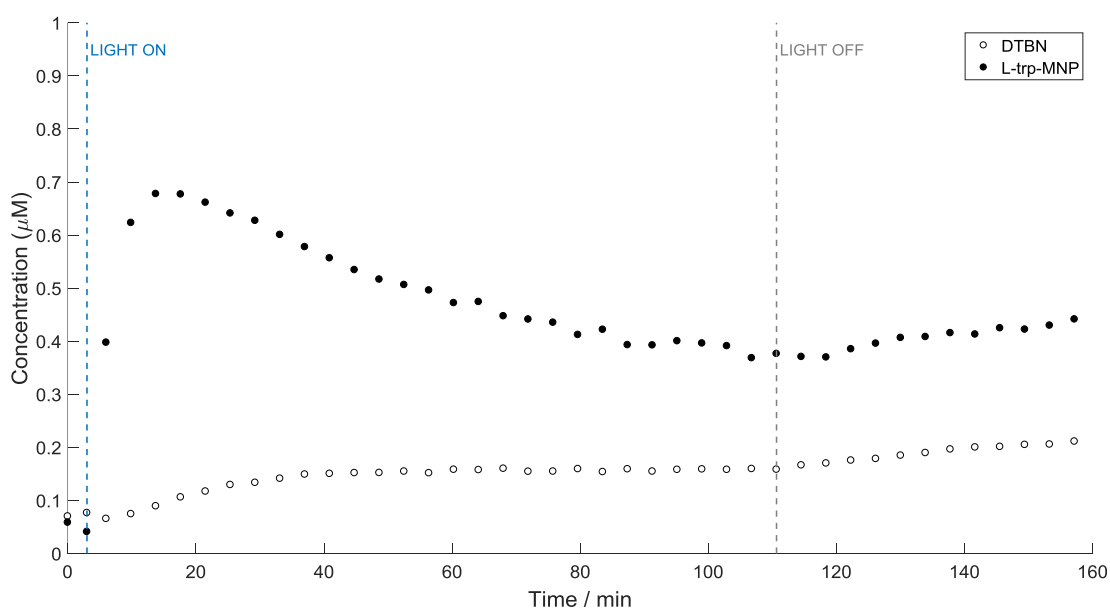


Figure 6.19 Quantification of the MNP-Trp spin adduct (●) and DTBN (○) generated from the photo-activation of complex **13** (5 mM) in the presence of L-trp (40 mM) and MNP (80 mM) with 465 nm LED light prepared in p.b. 50 mM at pH 7.2.

Table 6.1 EPR hyperfine couplings (mT) and *g*-values for the trapped L-trp radical (MNP-Trp) and the MNP di-adduct di-*tert*-butyl nitroxide (DTBN), comparing the parameters determined in this study with previously published ones.

Radical		a_{NO}^{N}	$a^{13\text{C}}$	Linewidth (I_{wpp})	<i>g</i> -value
MNP-Trp	This study (465 nm)	1.61(1)	-	0.15	2.0054(2) ^a
	This study (528 nm)	1.62(1)	-	0.16	2.0053(2) ^a
	Ref. ⁶⁹	1.58	-	0.16	- ^b
DTBN	This study (465 nm)	1.71(1)	0.43(1)	0.07	2.0053(2) ^a
	Ref. ⁶⁹	1.72	- ^b	- ^b	- ^b

^a determined by comparison with a DPPH standard; ^b not determined.

6.3.1.3 Spin trapping of L-trp radical with green light

The photo-irradiation of complex **13** at longer wavelengths had been previously investigated.¹⁰ Photo-activation of complex **13** and the consequent release of N_3 radicals, trapped by DMPO, was obtained with green light (517 nm) although to a much lower extent.

The photo-activation of complex **13** with 528 nm green LED light in the presence of L-trp was therefore investigated. A solution of complex **13** (5 mM) was prepared in p.b. 50 mM at pH 7.2 in the presence of L-trp (40 mM) and MNP (80 mM). The sample was kept in the dark and transferred into the EPR spectrometer. No signals other than the DTBN triplet were observed in the dark. The sample was then irradiated with 528 nm green light for several hours. As can be observed in Figure 6.20, a small weak 3-line signal was detected, and was attributed to the MNP-trp spin adduct.

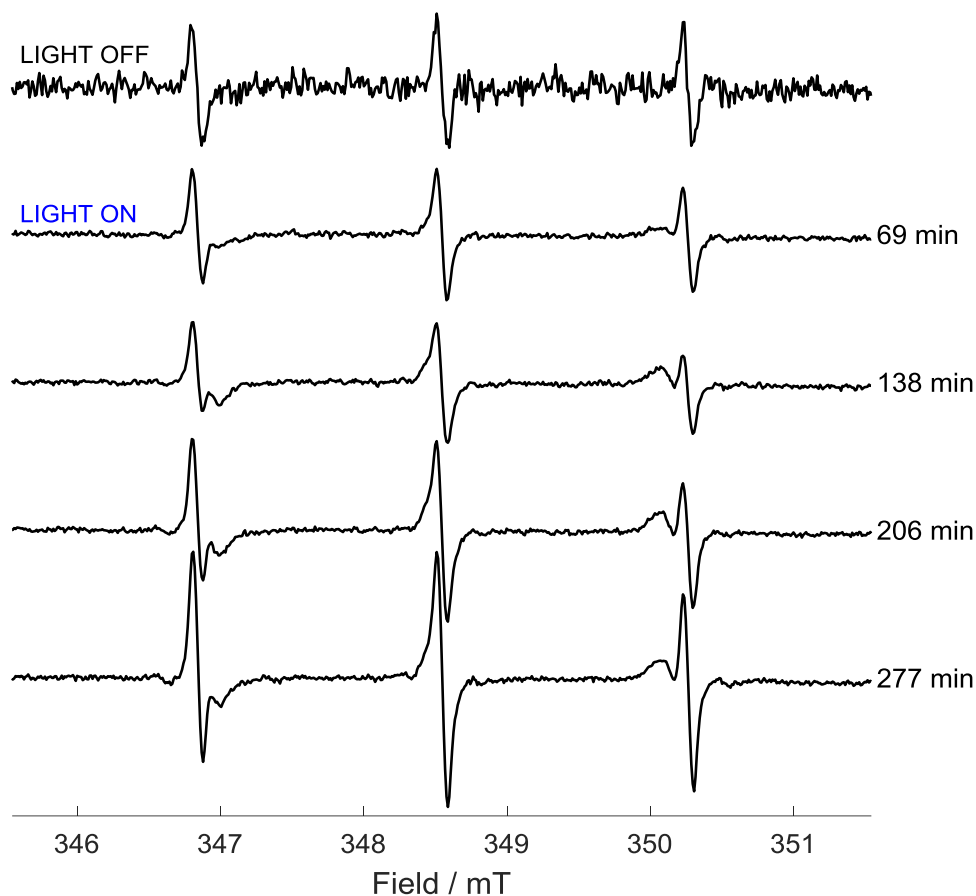


Figure 6.20 X-band CW EPR spectrum of a solution of complex **13** (5 mM), L-trp (40 mM) and MNP (80 mM) in p.b. 50 mM at pH 7.2, before and during continuous irradiation with a 528 nm green LED. Each of the spectra obtained during illumination is the sum of the previous 250 consecutive scans, while the spectrum obtained in the dark is the sum of 10 consecutive spectra and was multiplied by a factor of 25. Times reported refer to the time passed between the start of the irradiation and the end of the acquisition of the last scan included in the spectrum.

The reduced rate of activation of the complex is illustrated in Figure 6.21, which reports the double integrated (D.I.) area of the detected radical species against the acquisition time of the experiment. The activation of complex **13** appeared to slowly increase up to approximately 3 hours, after which the concentration of the MNP-trp spin adduct reached a plateau. The concentration of the said spin adduct was below the limit for a reliable quantification ($\ll 0.1 \mu\text{M}$), which was therefore not attempted. The low concentration of the MNP-trp spin adduct was attributed to a reduced photo-activation of complex **13** as previously reported,¹⁰

which could be partially ascribable to the lower irradiation power of 528 nm green LED light (5.4 mW cm^{-2}) in comparison to the 465 nm blue LED light (7.1 mW cm^{-2}).

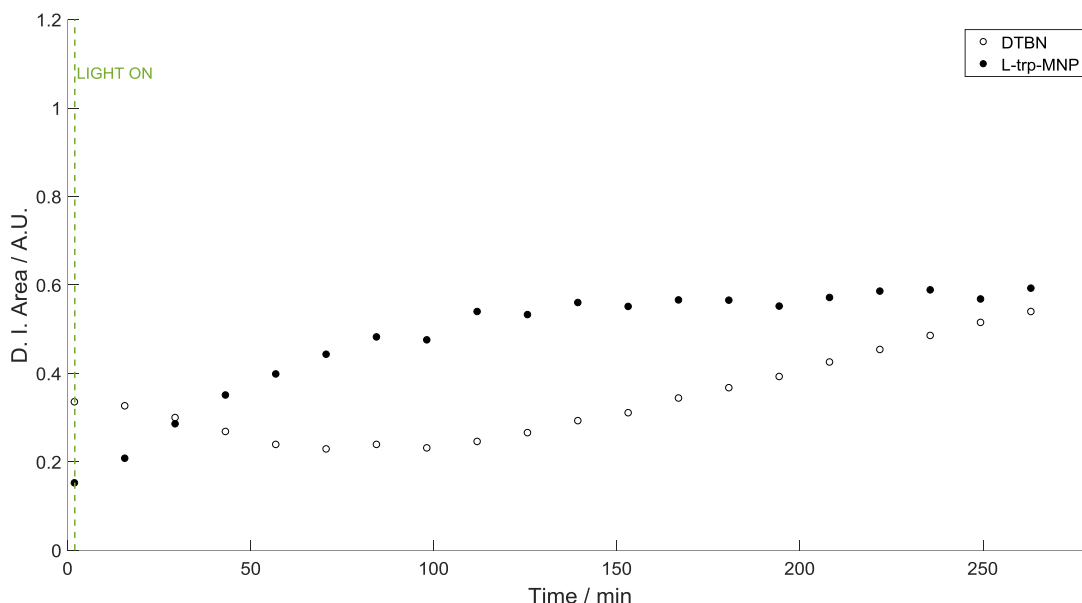


Figure 6.21 Detection the MNP-trp spin adduct (●) and DTBN (○) generated from the photo-activation of complex **13** (5 mM) in the presence of L-trp (40 mM) and MNP (80 mM) with 528 nm LED prepared in p.b. 50 mM at pH 7.2.

6.3.2 Melatonin

6.3.2.1 Spin trapping of melatonin radical (EtOH 20%) with blue light

Next, the effects of photo-activation of complex **13** in the presence of melatonin (MLT) were tested.

Solutions containing MLT (40 mM) in 20% EtOH with either MNP (80 mM) or complex **13** (5 mM) were prepared in p.b. at pH 7.2. The photo-stability of MLT upon irradiation with 463 nm light had been previously assessed by UV-Vis and ^1H NMR analysis.¹⁰ No EPR signals were detected in the dark, other than the 3-line DTBN background signal which could be observed in the solution containing the spin trapping agent. Photo-irradiation with 465 nm blue light did not generate new EPR signals in the solution containing only melatonin and complex **13**. Instead, when melatonin was irradiated in the presence of MNP, not only the DTBN signal enhanced as a result of the illumination, but also a new, less intense, signal was detected (Figure 6.22).

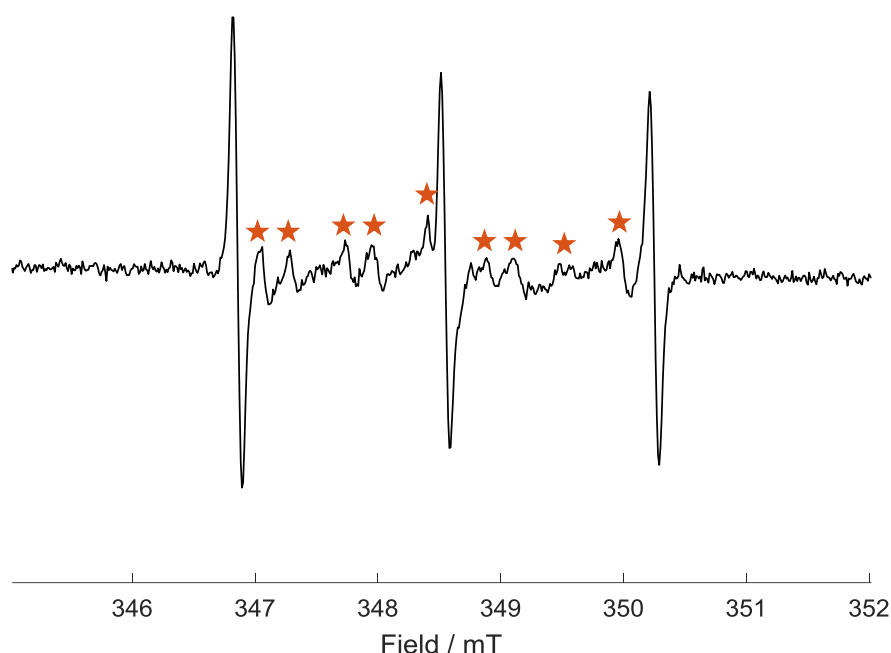


Figure 6.22 X-band CW EPR spectrum of a solution of MLT (40 mM) and MNP (80 mM) in p.b. 50 mM 20% EtOH at pH 7.2, after 26 minutes of continuous irradiation with a 465 nm blue LED. The spectrum is the sum of 118 consecutive scans. ★ indicate additional paramagnetic species other than DTBN.

A solution containing complex **13** (5 mM) was then prepared in the presence of both MLT (40 mM in 20% EtOH) and MNP (80 mM). No signals were detected in the dark also in this case. When the sample solution was irradiated with the 465 nm blue LED light a new, broad 3-line signal was observed (Figure 6.23). The experiment was repeated decreasing the modulation amplitude by one order of magnitude (from 0.1 to 0.01 mT) in an attempt to detect additional hyperfine structure covered by the broadening of the lines, but no further splittings were observed (Figure 6.24). The EPR parameters of the species were extracted by simulation (Figure 6.25) and were found to be in good agreement with the previously detected MNP-trp spin adduct (Table 6.2). The detected paramagnetic species was therefore assigned to the formation of the MNP-MLT spin adduct, with MLT binding to MNP in position 3 of the indole ring, as for L-trp.

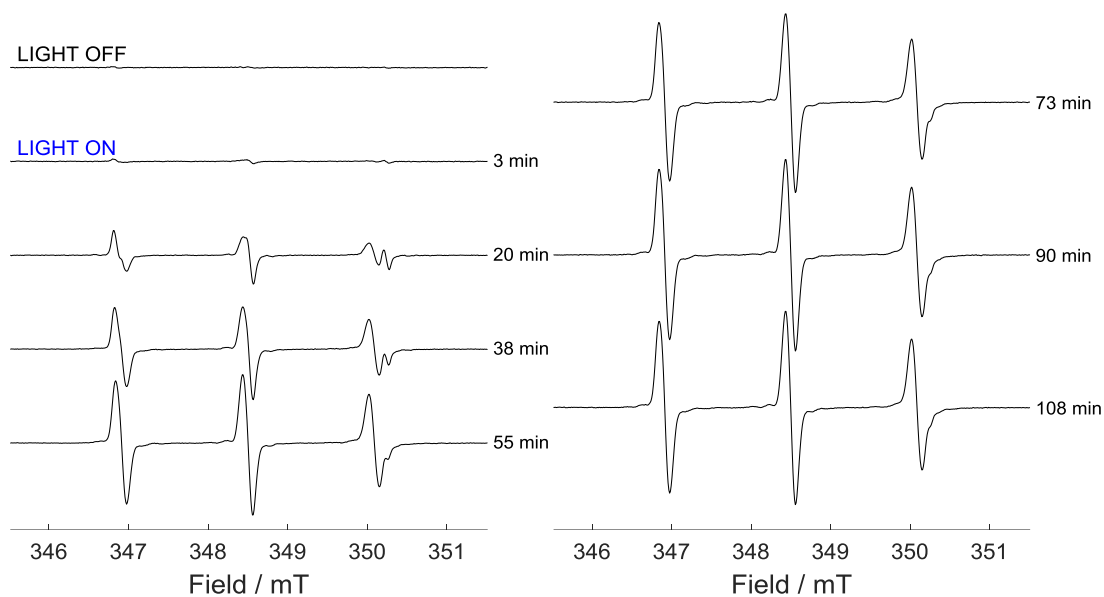


Figure 6.23 X-band CW EPR spectrum of a solution of complex **13** (5 mM), MLT (40 mM) and MNP (80 mM) in p.b. 50 mM 20% EtOH at pH 7.2, before and during continuous irradiation with a 465 nm blue LED. Each spectrum is the sum of 10 consecutive scans. Times reported refer to the time passed between the start of the irradiation and the end of the acquisition of the last scan included in the spectrum.

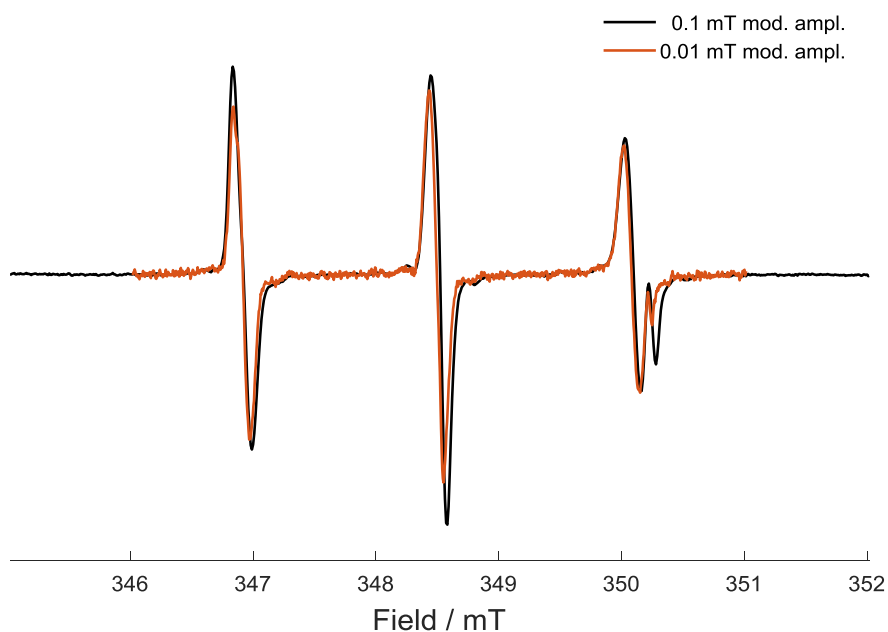


Figure 6.24 X-band CW EPR spectrum of a solution of complex **13** (5 mM), MLT (40 mM) and MNP (80 mM) in p.b. 50 mM 20% EtOH at pH 7.2 irradiated with a 465 nm blue LED, using either 0.1 mT (black) or 0.01 mT (red) modulation amplitude. Each spectrum is the sum of 30 consecutive scans. The spectra were manually scaled to the same intensity for comparison.

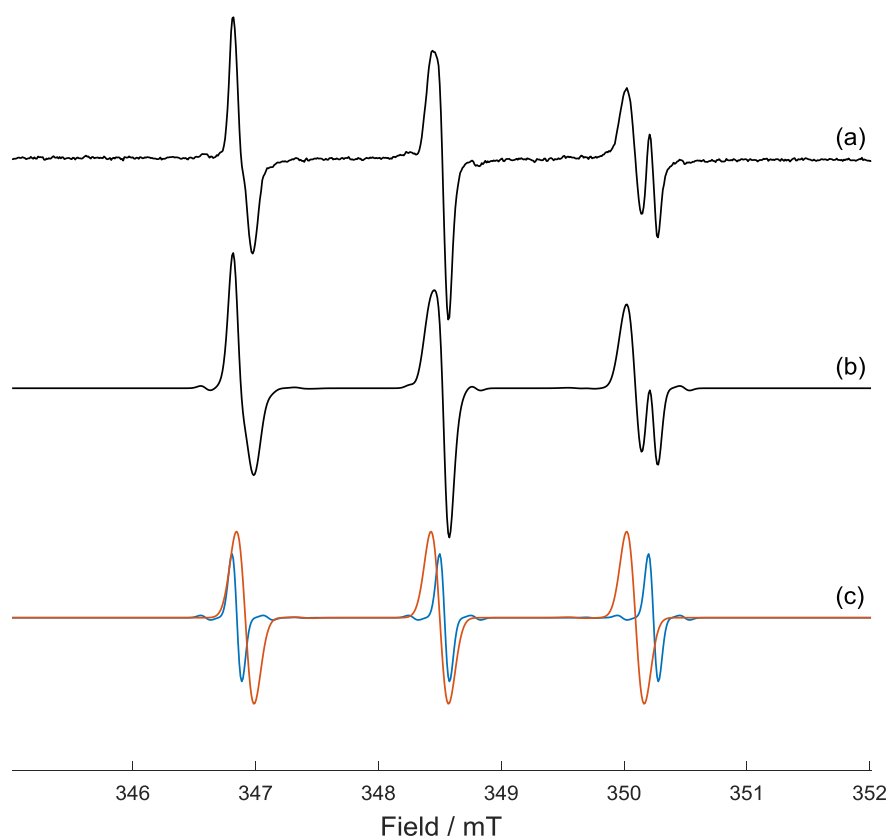


Figure 6.25 (a) X-band EPR spectrum of MNP-MLT spin adduct formed from photo-irradiation of complex **13** (5 mM), MLT (40 mM) and MNP (80 mM) in p.b. 50 mM 20% EtOH at pH 7.2 after 51 min of irradiation with 465 nm blue LED light; (b) EasySpin⁶⁶ simulation of the EPR spectrum for a combination of MNP-MLT spin adduct and DTBN; (c) simulation of the only MNP-MLT spin adduct (red) and of the only DTBN (blue). The relative weights of MNP-MLT and DTBN are respectively *ca.* 80% and 20%.

The concentration of the spin adduct was calculated by comparison with a TEMPOL standard, and the kinetics of the spin trap adduct were analysed (Figure 6.26). Interestingly, the kinetics of the MNP-MLT and MNP-trp appeared to substantially differ. Firstly, the concentration of the MNP-MLT adduct was found to be *ca.* 30 times higher compared to MNP-trp, with a maximum of 19.5 μM as opposed to the 0.7 μM obtained with L-trp. Secondly, the formation of the melatonin spin adduct appeared to be slower, with the maximum reached after 95 minutes of irradiation against the 16 minutes for L-trp. Additionally, a closer observation of the curve of formation of the MNP-MLT radical adduct showed a bump in the initial part of the experiment (*ca.* 15 min), which is suggestive of the co-participation of two distinct events, a feature that was not observed with L-trp.

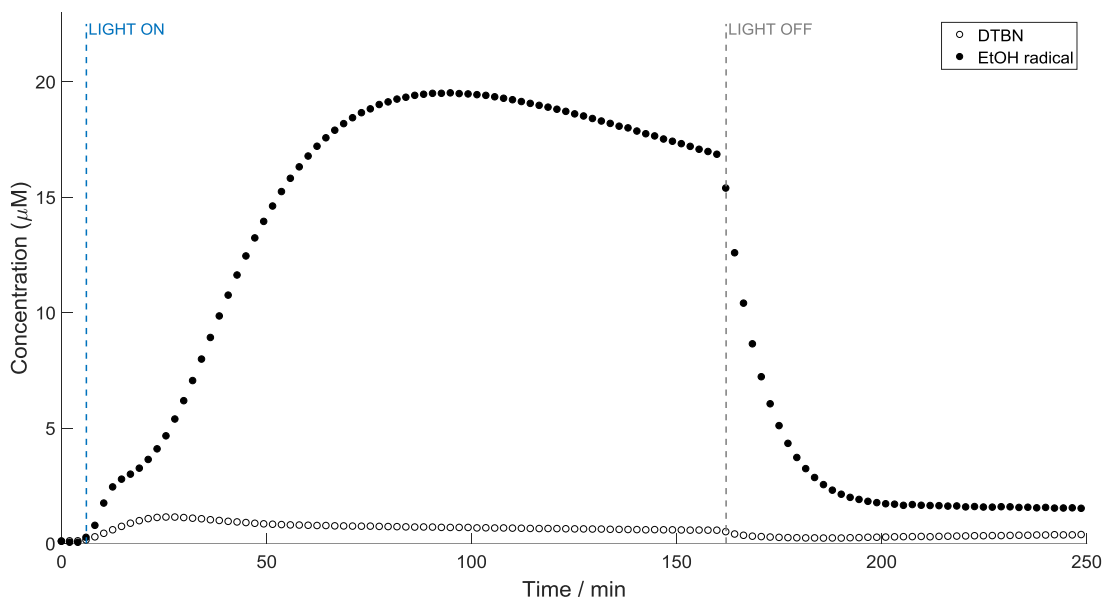


Figure 6.26 Quantification of the MNP-MLT spin adduct (●) and DTBN (○) generated from the photo-activation of complex **13** (5 mM) in the presence of MLT (40 mM) and MNP (80 mM) in p.b. 50 mM 20% EtOH at pH 7.2 with 465 nm LED light.

6.3.2.2 Spin trapping of melatonin radical (H₂O) with blue light

The experiments conducted with MLT in 20% EtOH were repeated avoiding the use of EtOH as a solvent to exclude its involvement in the kinetics of MLT, which showed the concurrence of two distinct kinetic processes. EtOH was used in the first place to allow a high concentration of MLT in the sample solution. MLT is in fact scarcely soluble in H₂O, consequently the concentration of MLT obtained in the absence of EtOH was *ca.* two orders of magnitude lower than what was obtained by solubilising the compound in EtOH (0.4 mM vs 40 mM).

A solution of complex **13** was thereby prepared in the presence of MLT (0.4 mM) and MNP (80 mM) in p.b. 50 mM at pH 7.2. No signals other than the DTBN three lines were detected in the dark. As the sample solution was irradiated with 465 nm blue LED light, an additional 3-line signal was detected and was found to progressively increase as the irradiation proceeded (Figure 6.27). As for the experiments performed with MLT in EtOH (20%), the signal was attributed to the formation of the MNP-MLT spin adduct, originated from the presence of an indole radical with the unpaired electron in position 3 of the indole ring.

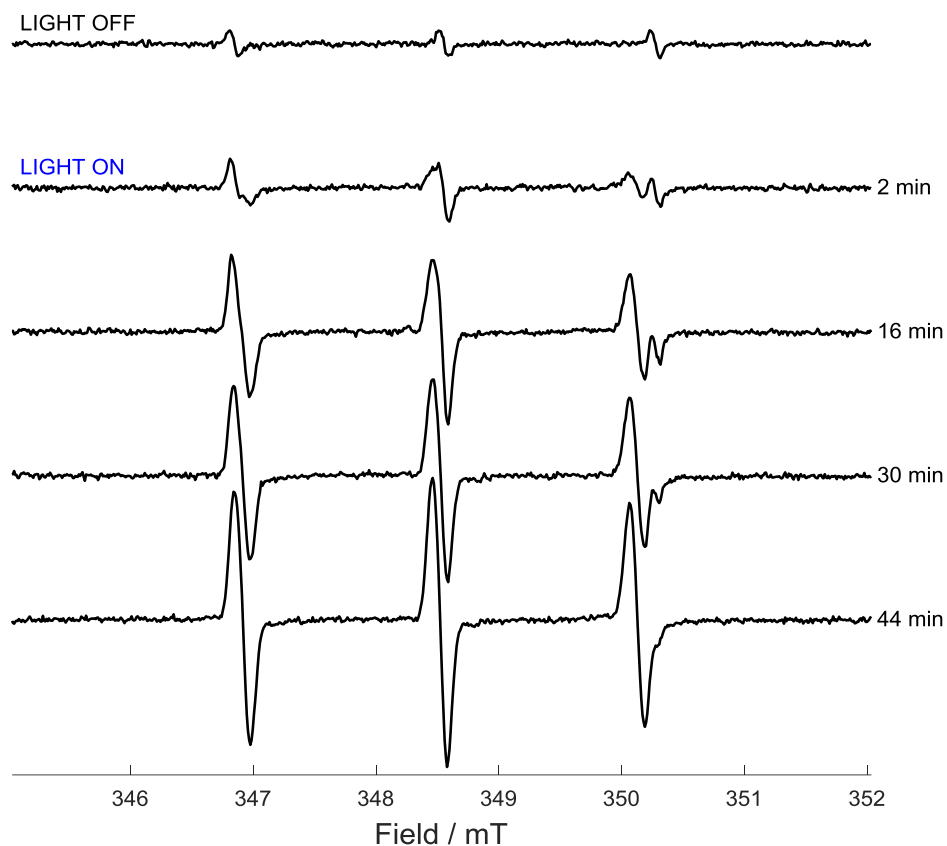


Figure 6.27 X-band CW EPR spectra of a solution of complex **13** (5 mM), MLT (0.4 mM) and MNP (80 mM) in p.b. 50 mM at pH 7.2, before and during continuous irradiation with a 465 nm blue LED. Each spectrum is the sum of 10 consecutive scans. Times reported refer to the time passed between the start of the irradiation and the end of the acquisition of the last scan included in the spectrum.

The parameters extracted by simulation were found to be in good agreement with the spin adducts detected from photo-activation of complex **13** in the presence of L-trp or MLT in 20% EtOH (Table 6.2). The analysis of the kinetics revealed the same profile detected for MLT in EtOH, with a faster adduct formation detected in the initial part of the irradiation experiment (Figure 6.28). The concentration of the spin adduct in this case was found to be 5-10 times lower than with the previous experiment performed in EtOH, which is to be expected as a consequence of the lower concentration of MLT in the sample solution.

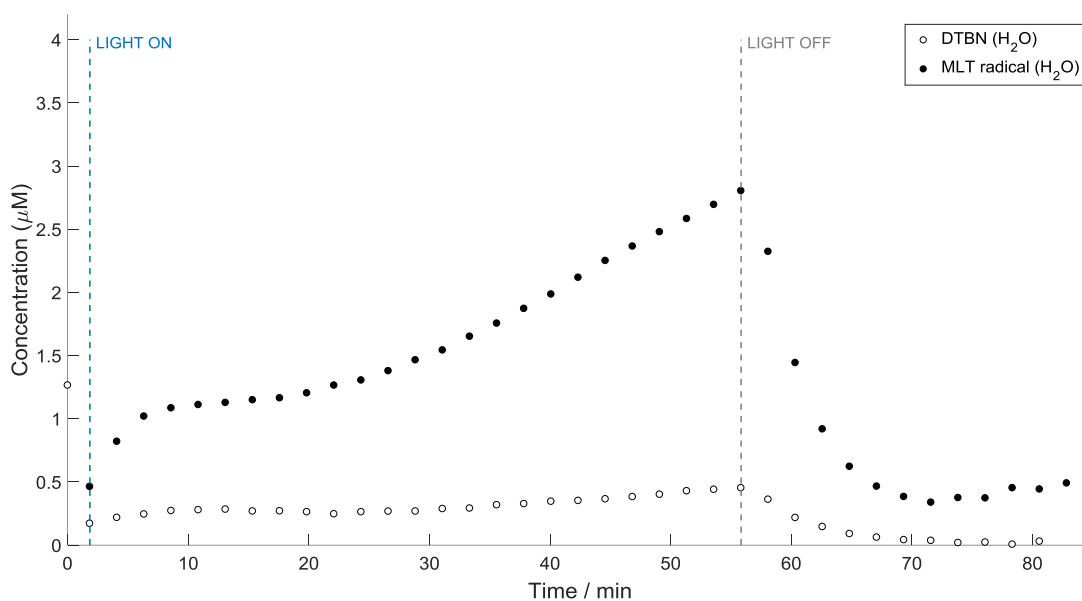


Figure 6.28 Quantification of the MNP-MLT spin adduct (●) and DTBN (○) generated from the photo-activation of complex **13** (5 mM) in the presence of MLT (0.4 mM) and MNP (80 mM) in p.b. 50 mM at pH 7.2 with 465 nm LED light.

Table 6.2 EPR hyperfine couplings (mT) and *g*-values for the trapped MLT radical (MNP-MLT) compared to the MNP-trp spin adduct and the MNP di-adduct di-*tert*-butyl nitroxide (DTBN).

Radical		a_{N}^{N}	$a^{13\text{C}}$	Linewidth	<i>g</i> -value
MNP-MLT (20% EtOH)	This study	1.59(1)	-	0.14(1)	2.0056(2) ^a
MNP-MLT (H ₂ O)	This study	1.61(1)	-	0.12(1)	2.0054(2) ^a
MNP-trp	This study	1.61(1)	-	0.15(1)	2.0054(2) ^a
	Ref. ⁶⁹	1.58	-	0.16(1)	- ^b
DTBN	This study ^c	1.70(1) ^c	0.51(1) ^c	0.08(1) ^c	2.0054(2) ^{a,c}
	Ref. ⁶⁹	1.72	- ^b	- ^b	- ^b

^a determined by comparison with a DPPH standard; ^b not determined; ^c determined for the experiment with MLT in EtOH (20%)

6.3.2.3 Photo-activation of complex **13** with MLT at longer wavelengths

As for L-trp, the photo-activation of complex **13** in the presence of MLT was investigated at longer wavelengths. A solution of complex **13** (5 mM) was irradiated with 528 nm green LED light in the presence of MLT (40 mM) and MNP (80 mM), prepared in p.b. 50 mM 20% EtOH at pH 7.2. Differently from what was obtained with L-trp, in the presence of MLT no signals were detected other than the DTBN signal, suggesting that the MLT indole radical is not produced under these conditions (Figure 6.29).

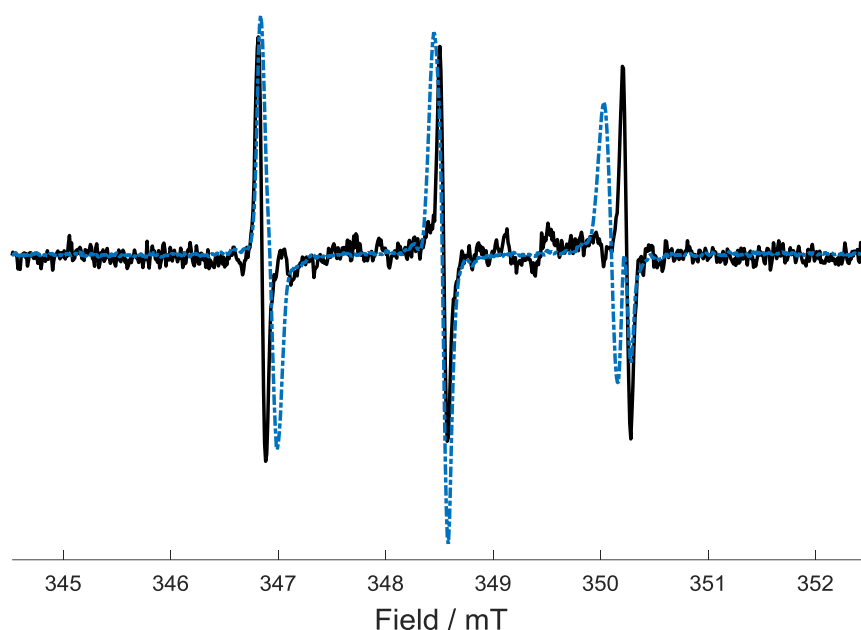


Figure 6.29 X-band CW EPR spectrum of a solution of complex **13** (5 mM), MLT (40 mM) and MNP (80 mM) in p.b. 50 mM 20% EtOH at pH 7.2 and irradiated with a 528 nm green LED (black) in comparison to irradiation with 465 nm blue LED (dashed dotted blue). The spectrum obtained with green light irradiation is the sum of 200 scans, while the spectrum obtained with blue light irradiation is the sum of 8 scans.

6.3.2.4 Detection of hydroxyl radicals

To further investigate the mechanism of photo-activation of complex **13**, the compound was analysed in the presence of EtOH (20%) but in the absence of MLT. EtOH is known to be a scavenger specific for the hydroxyl radical (OH^\bullet). The trapping of α -hydroxyl ethyl radical with DMPO, formed from reaction of OH^\bullet with EtOH was previously reported,¹⁰ and suggested a multi photo-decomposition pathway for complex **13** which also involves the formation of hydroxyl radicals.

A solution of complex **13** (5 mM) was therefore prepared in the presence of 20% EtOH (~ 34 M) and MNP (80 mM) in p.b. 50 mM at pH 7.2. The solution was therefore irradiated with a 465 nm blue LED, under continuous acquisition of the EPR spectrum. The photoactivation of the platinum complex was found to induce the formation of a 6 line signal, partially overlapping with the 3-line signal assigned to DTBN, which was attributed to the formation of the α -hydroxyl ethyl radical (Figure 6.30).

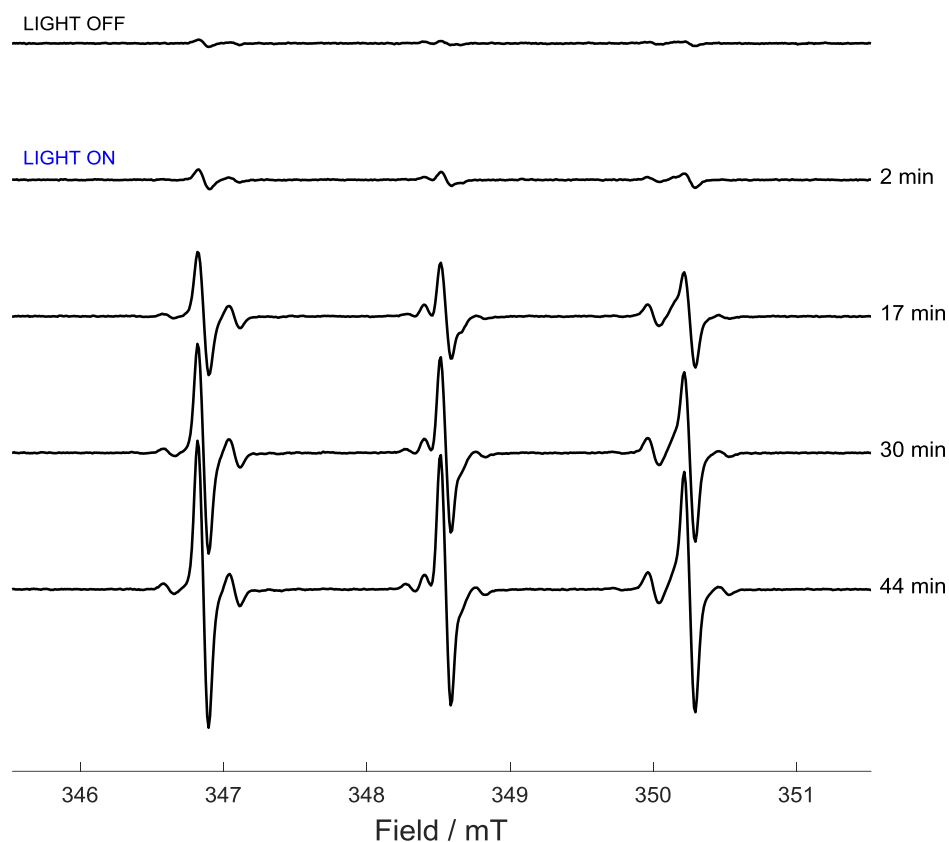


Figure 6.30 X-band CW EPR spectra of a solution of complex **13** (5 mM) in the presence of 20% EtOH and MNP (80 mM) in p.b. 50 mM at pH 7.2, before and during continuous irradiation with a 465 nm blue LED. Each spectrum is the sum of 10 consecutive scans. Times reported refer to the time passed between the start of the irradiation and the end of the acquisition of the last scan included in the spectrum.

The EPR spectral parameters of the paramagnetic species were extracted by simulation with EasySpin⁶⁶ (Figure 6.31) and are reported in Table 6.3. The extracted parameters were found to be in good agreement with previously reported parameters for the trapped α -hydroxyl ethyl radical,^{71,72} confirming the formation of the above mentioned radical following the photoactivation of complex **13**. The kinetics of formation and decay of the MNP-EtOH spin trap adduct are shown in Figure 6.32. The spin adduct concentration reached a maximum of *ca.* 1.9 μM after 25 minutes of continuous irradiation with 465 nm LED light, and then slowly decreased until the irradiation was stopped.

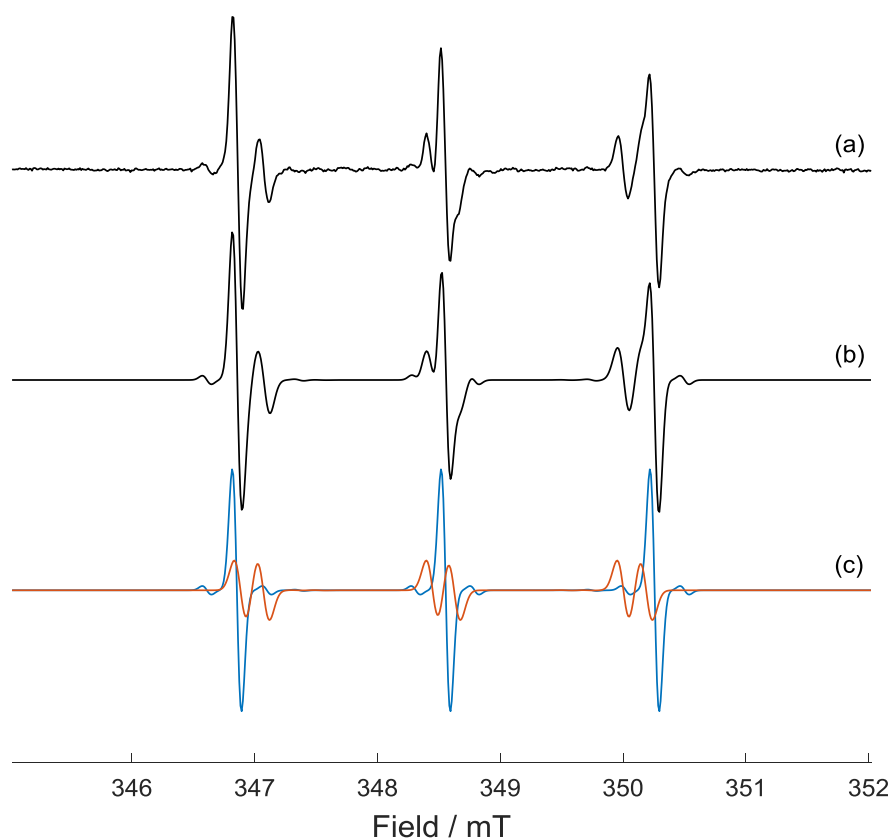
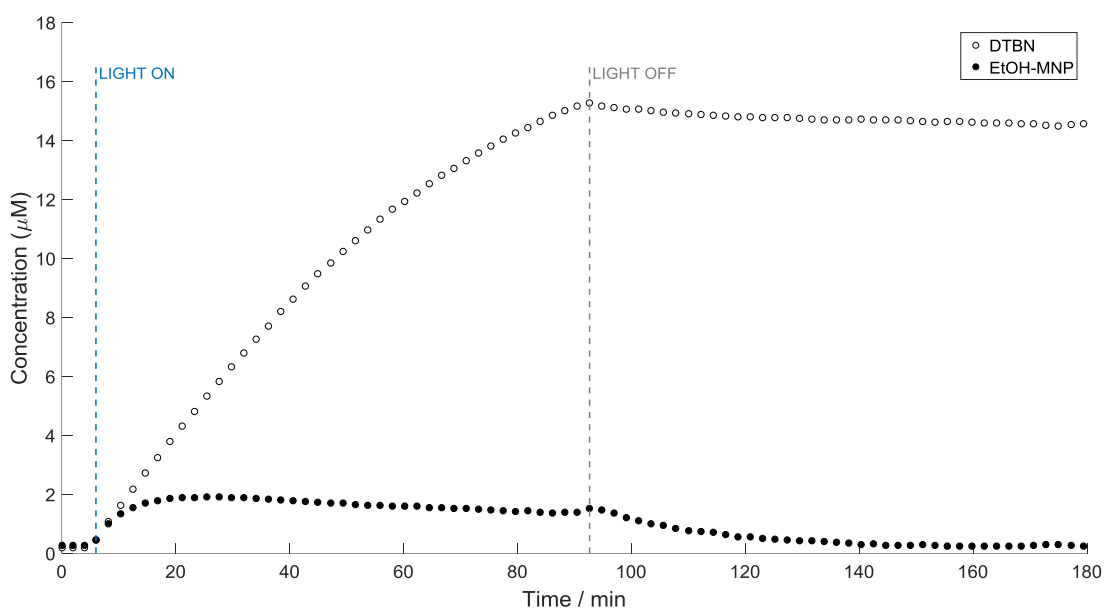


Figure 6.31 (a) X-band EPR spectrum obtained from photo-irradiation of complex **13** (5 mM), in the presence of EtOH 20% and MNP (80 mM) in p.b. 50 mM at pH 7.2 after 10 min of irradiation with 465 nm blue LED light; (b) EasySpin⁶⁶ simulation of the EPR spectrum for a combination of MNP-EtOH spin adduct and DTBN; (c) simulation of the only MNP-EtOH spin adduct (red) and of the only DTBN (blue). The relative weights of MNP-EtOH and DTBN are respectively *ca.* 46% and 54%.

Table 6.3 EPR hyperfine couplings (mT) and g -values for the trapped α -hydroxyl ethyl radical (MNP-EtOH) and the MNP di-adduct di-*tert*-butyl nitroxide (DTBN).

Radical		a_{NO}^{N}	$a^{13\text{C}}$	a_{α}^{H}	g -value
MNP-EtOH	This study	1.56(1)	-	0.18(1)	2.0054(2) ^a
	Ref. ^{71,72}	1.55	-	0.18	- ^b
DTBN	This study	1.71(1)	0.48(1)	-	2.0054(2) ^a
	Ref. ⁶⁹	1.72	- ^b	-	- ^b

^a determined by comparison with a DPPH standard; ^b not determined**Figure 6.32** Quantification of the MNP-EtOH spin adduct (●) and DTBN (○) generated from the photo-activation of complex **13** (5 mM) in the presence of EtOH (20%) and MNP (80 mM) in p.b. 50 mM at pH 7.2 with 465 nm LED light.

6.3.3 L-histidine

L-histidine is known for being, like the amino acid L-trp, an efficient mediator of electron transfer in proteins.⁷³ According to its reduction potential ($E^0 = 1.17$ V),⁷⁴ histidine is a slightly stronger oxidant than tryptophan ($E^0 = 1.015$ V),⁷⁵ but weaker than the azidyl radical ($E^0 = 1.33$ V).⁷⁶ The reduction potentials therefore suggest that an electron transfer from L-his to the azidyl radicals is still favourable. Thus, the possibility that L-his could modulate the cytotoxicity of complex **13** was investigated.

A solution of L-his (100 mM) with MNP (80 mM) and complex **13** (5 mM) was prepared in p.b. at pH 7.2 in the dark. The photo-activation of complex **13** led only to the formation of DTBN (Figure 6.33). It therefore appeared that, unlike L-trp and MLT, L-his does not interact with the azidyl radicals released upon photo-degradation of complex **13**.

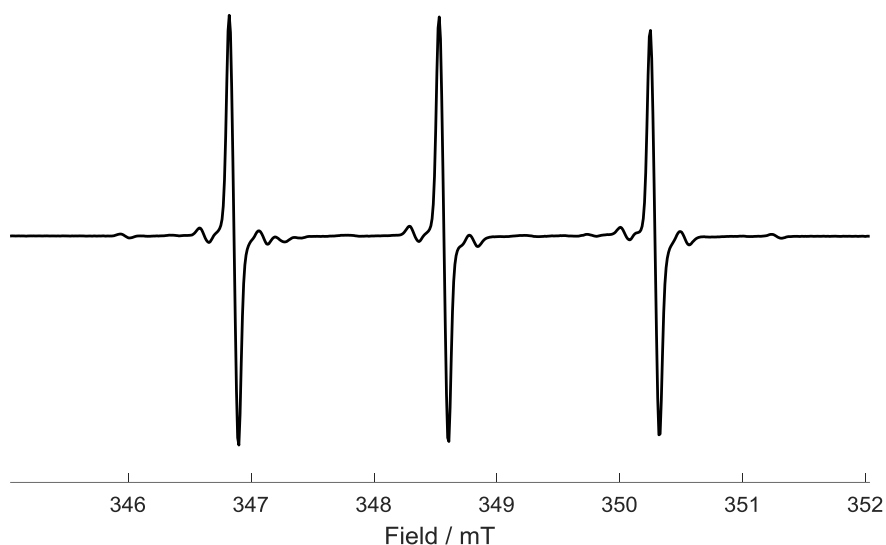


Figure 6.33 X-band EPR spectrum obtained from photo-irradiation of complex **13** (5 mM), in the presence of L-his (100 mM) and MNP (80 mM) in p.b. 50 mM at pH 7.2 after 65 min of irradiation with 465 nm blue LED light.

6.3.4 Pentagastrin

To further investigate the formation of L-trp[•] as a result of the photo-activation of complex **13**, the photo-activation of the Pt-compound was performed in the presence of a trp-containing peptide, pentagastrin.

6.3.4.1 Spin trapping with MNP in the presence of pentagastrin

A solution of complex **13** (5 mM) was irradiated in the presence of pentagastrin (18 mM in DMF 70%) and MNP (80 mM) in p.b. 50 mM at pH 7.2. No signals other than the DTBN triplet were detected in the dark. As the photo-irradiation was initiated, the DTBN signal was found to increase with time (Figure 6.34). A closer observation of the EPR spectrum showed the presence of additional, low intensity species. The multiplicity of the trapped radical suggested that it originates from the trapping of a N-centre radical.

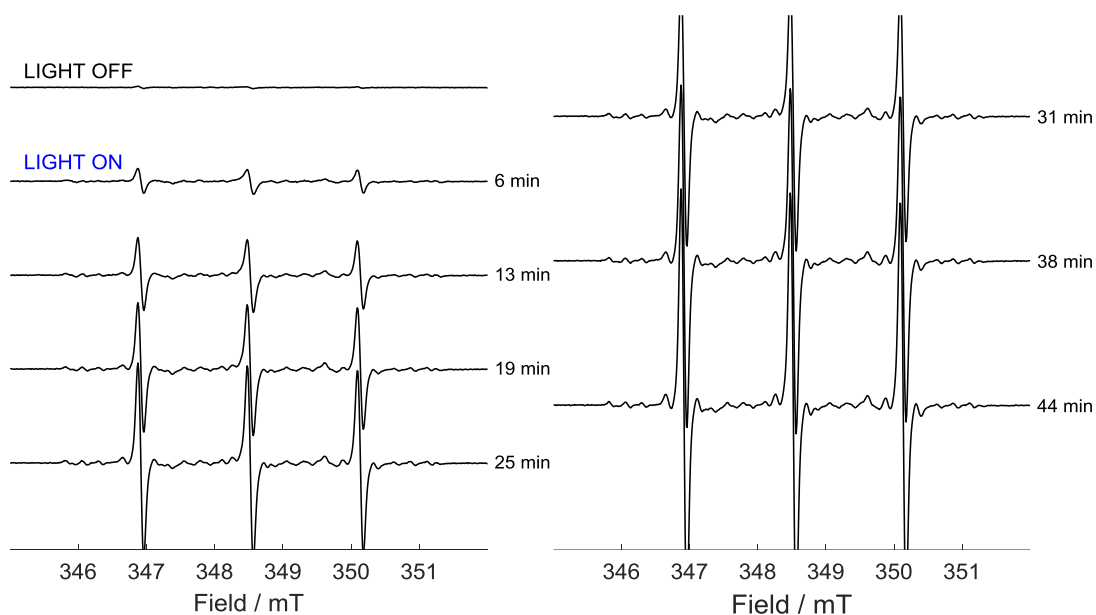


Figure 6.34 X-band CW EPR spectra of a solution of complex **13** (5 mM), pentagastrin (18 mM in DMF 70%) and MNP (80 mM) in p.b. 50 mM at pH 7.2, before and during continuous irradiation with a 465 nm blue LED. Each spectrum is the sum of 25 consecutive scans. Times reported refer to the time passed between the start of the irradiation and the end of the acquisition of the last scan included in the spectrum.

The experiment was repeated in the absence of pentagastrin (Figure 6.35). The same features were detected also in this case (★), although some lines were found to be more intense (▼). Both signals were therefore attributed to the solvent, implying that no radicals deriving from pentagastrin as a result of the photo-activation of complex **13** were trapped.

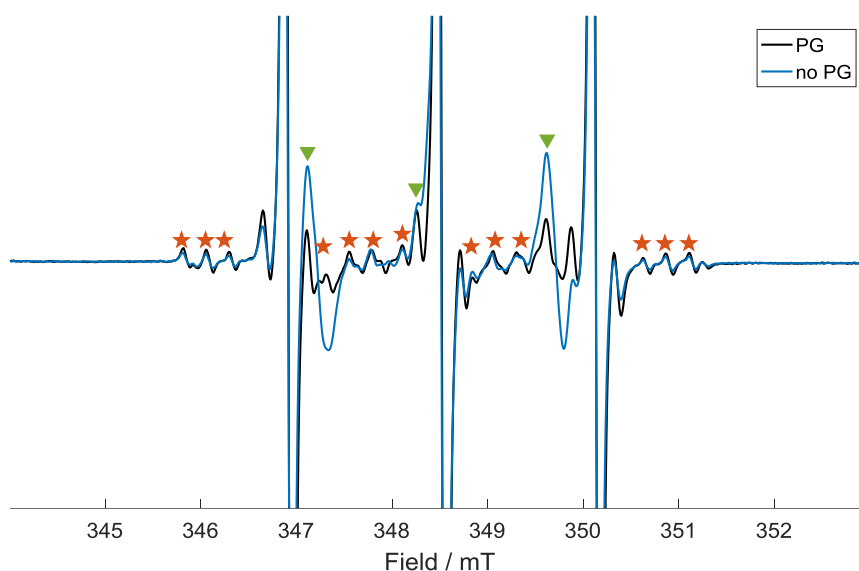


Figure 6.35 X-band CW EPR spectra of a solution of complex **13** (5 mM), and MNP (80 mM) in p.b. 50 mM 70% DMF at pH 7.2 in the presence (black) and absence (blue) of pentagastrin (18 mM) after 75 minutes of continuous irradiation with a 465 nm blue LED. Each spectrum is the sum of 300 consecutive scans. ★ and ▼ indicate additional paramagnetic species formed upon irradiation.

6.3.4.2 Spin trapping with DMPO

Following the inability to spin trap and thereby detect indole radicals generated from the photo-activation of complex **13** in the presence of pentagastrin, the same experiments were repeated using DMPO as a spin trapping agent in place of MNP. DMPO is known for its specificity towards the trapping of oxygen- and nitrogen-centred transient radicals, and it is therefore the spin trapping agent of choice for the detection of azidyl radicals. DMPO has been previously used to spin trap photo-released azidyl radicals in the presence and absence of L-trp, thereby to measure of the photo-protective effect of the said amino acid.⁴² The effects of the presence of pentagastrin on the trapping of azidyl radicals released upon photo-degradation of complex **13** were therefore examined.

A solution of complex **13** (5 mM) prepared with DMPO (10 mM) in p.b. 50 mM 70% DMF at pH 7.2 was irradiated with 465 nm blue LED light in the presence and absence of pentagastrin (20 mM). No signals were detected in the dark. In the absence of pentagastrin, the photoactivation of complex **13** was found to induce the formation of a 12-line signal of pattern 1:1:1:2:2:2:2:2:2:1:1:1, which was assigned to the DMPO- N_3 spin adduct as previously reported.⁴² The detected splitting arises from the coupling to the nitroxidic nitrogen, the β -proton of the spin trap structure and the α -nitrogen of the azidyl radical, giving 18 lines which partially overlap. The EPR parameters extracted by simulation (Table 6.4) were found to be in reasonably good agreement with previously reported works,^{42,77} despite differences of the magnitude of the couplings which can be attributed to the different solvents used to prepare the samples and will be discussed in Section 6.4.5.

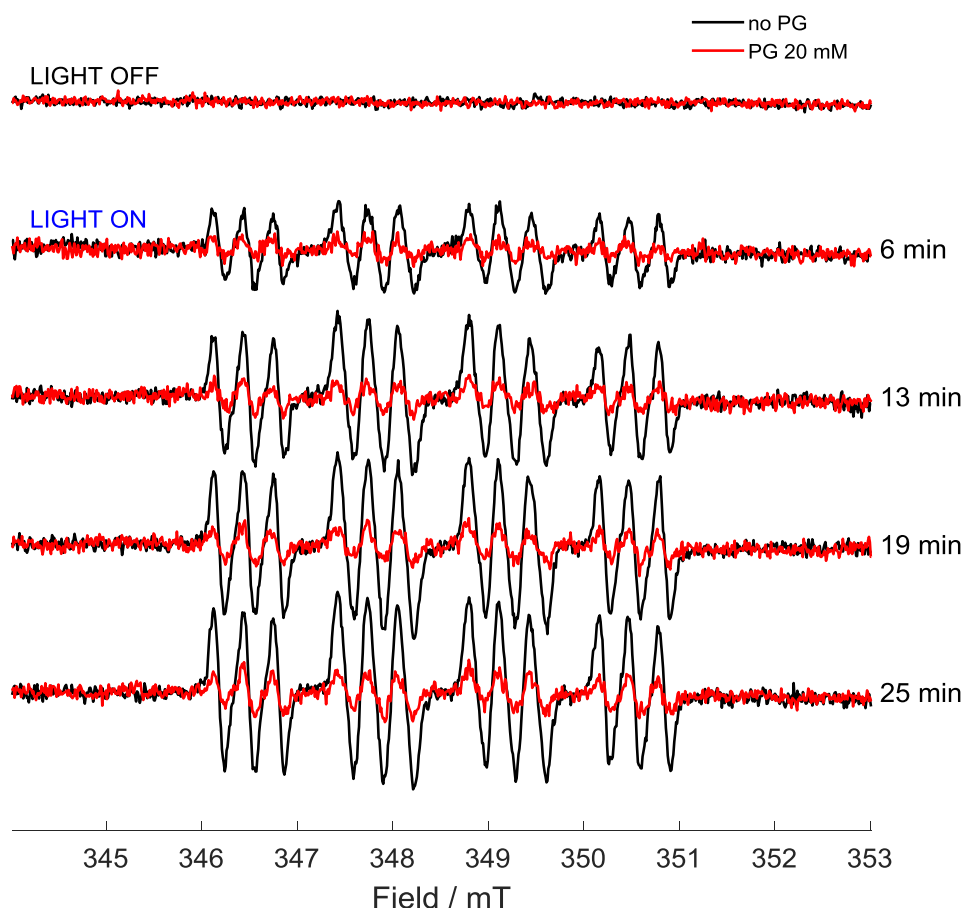


Figure 6.36 X-band CW EPR spectra of a solution of complex **13** (5 mM), pentagastrin (20 mM) and DMPO (10 mM) in p.b. 50 mM 70% DMF at pH 7.2, before and during continuous irradiation with a 465 nm blue LED. Each spectrum is the sum of 25 consecutive scans. Times reported refer to the time passed between the start of the irradiation and the end of the acquisition of the last scan included in the spectrum.

The same experiment was then repeated preparing a sample which also contained pentagastrin (20 mM). As shown in Figure 6.36, the presence of pentagastrin produced a pronounced decrease in the concentration of the DMPO- N_3 spin adduct, to *ca.* the 30% of what was detected in the absence of pentagastrin. The kinetics of formation and degradation of the spin adduct in the two cases (presence and absence of pentagastrin) are reported in Figure 6.38. In the presence of pentagastrin (20 mM), the concentration of the DMPO- N_3 formed as a consequence of the photo-degradation of complex **13** did not exceed 0.9 μ M. On the contrary, in the absence of pentagastrin, the concentration of the spin adduct progressively increased upon irradiation up to *ca.* 2.3 μ M. As the photo-irradiation was stopped, the signal rapidly decreased as the spin trap adduct decomposed. Such results represent a strong evidence that pentagastrin does interact with the azidyl radicals released upon photo-activation of complex **13**, similarly to L-trp and MLT.

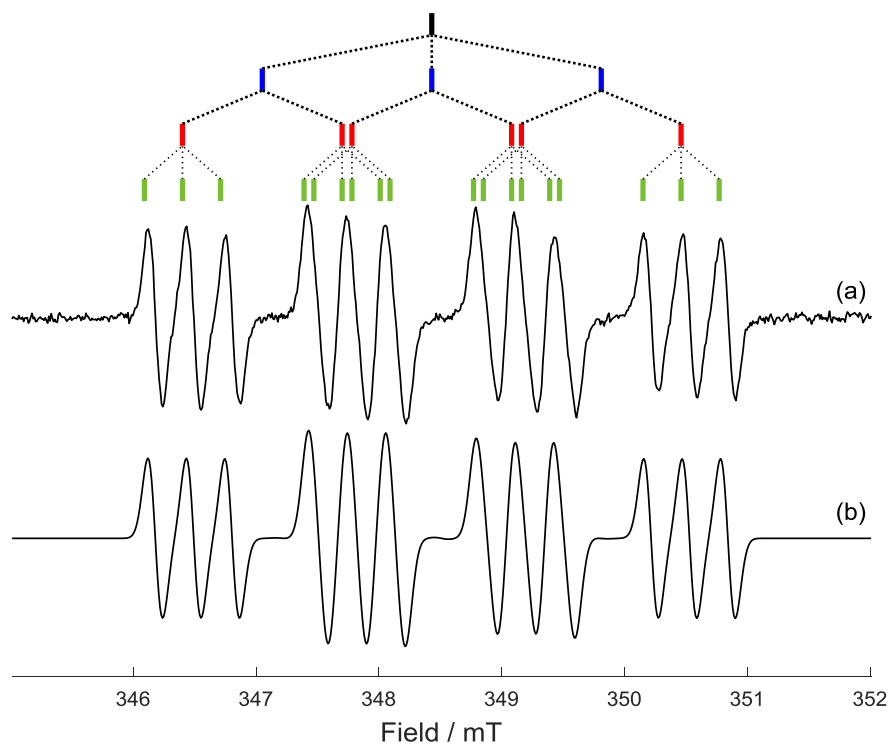


Figure 6.37 (a) X-band EPR spectrum obtained from photo-irradiation of complex **13** (5 mM) in the presence of DMPO (10 mM) prepared in p.b. 50 mM 70% DMF at pH 7.2, after 43 min of irradiation with 465 nm blue LED light; the spectrum is the sum of 70 slices; (b) EasySpin⁶⁶ simulation of the EPR spectrum with the parameters reported in Table 6.1. The line diagram for the DMPO- N_3 spin adduct is also shown.

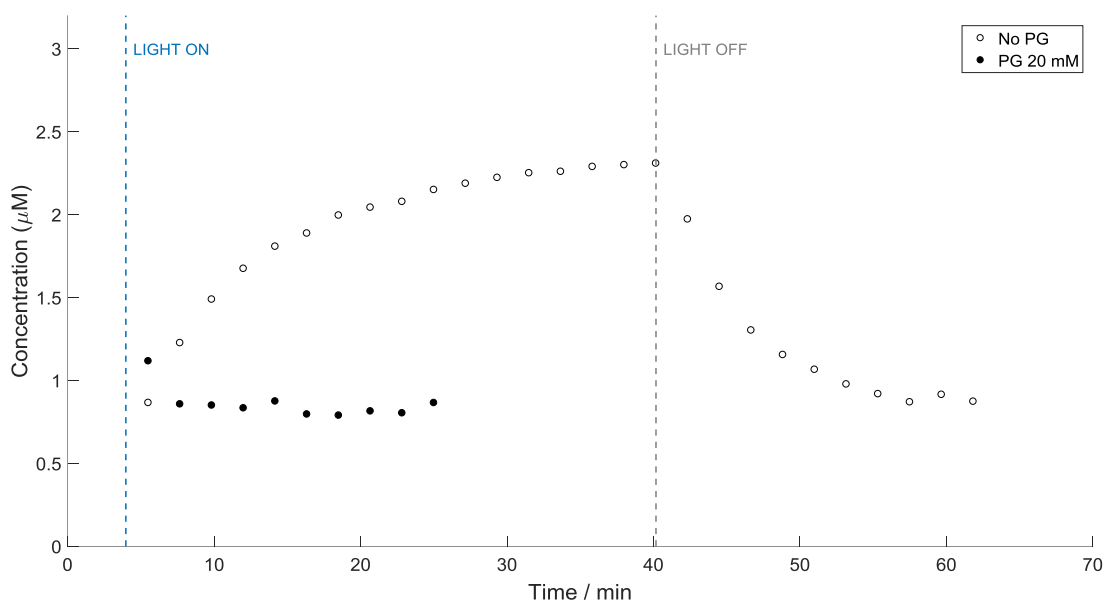


Figure 6.38 Quantification of the DMPO- N_3 spin adduct in the presence (●) and absence (○) of pentagastrin (20 mM) generated from the photo-activation of complex **13** (5 mM) in the presence of DMPO (10 mM) in p.b. 50 mM 70% DMF at pH 7.2 with 465 nm LED light.

Table 6.4 EPR hyperfine couplings (mT) and g -values for the azidyl radical nitron spin adduct (DMPO- N_3).

Radical		$a_{\text{N}\alpha}^{\text{N}}$	a_{β}^{H}	$a_{\text{N}\alpha}^{\text{N}}$	g -value
DMPO- N_3	This study (DMF 70%)	1.38(1)	1.30(1)	0.31(1)	2.0055(2) ^a
	Ref. ⁷⁷ (DMF 50%)	1.38	1.39	0.30	— ^b
	Ref. ⁴² (H ₂ O)	1.45	1.49	0.32	— ^b

^a determined by comparison with a DPPH standard; ^b not determined

6.4 Discussion

6.4.1 Detection of MNP-indole radicals

The formation of MNP-tryptophan radical adducts from flash photolysis in solution has been previously reported. The observed spin trap adducts were suggested to be originated from a carbon-centred tryptophan radical, with the unpaired electron located in position 3 of the indole ring.⁶⁹ Indeed, if the unpaired electron were to be located in any other position of the molecule, hyperfine couplings to nearby protons would have been expected. Additionally, the increased stability of a tertiary radical over primary and secondary radicals supports the suggested structure.

Previously published pulse radiolysis studies proved that the reaction between reactive radical species such as $\bullet\text{N}_3$ and tryptophan proceeds through a direct electron transfer between the amino acid and the RNS, as opposed to a hydrogen atom transfer.⁵⁰ Additionally, it was proposed that photolysis of the tryptophan initially takes place at the indole N-H bond with formation of a N-centred radical, followed by an electron rearrangement to leave the unpaired electron in position 3 of the indole ring.⁷⁰ The sum of these considerations is in Figure 6.39:

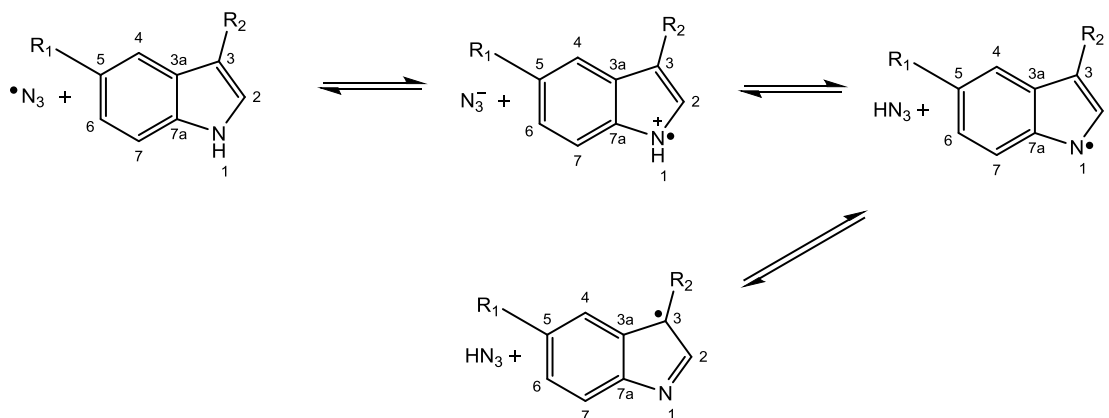


Figure 6.39 Reaction between the azidyl radical and indole derivatives proceeding through one-electron transfer pathway and successful rearrangement to produce the C3-centred indole radical. $\text{R}_1 = \text{H}$ (trp); OCH_3 (MLT). $\text{R}_2 = \text{CH}_2\text{CH}(\text{NH}_2)\text{COOH}$ (trp); $\text{CH}_2\text{CH}_2\text{NHCOCH}_3$ (MLT).

The ability of L-tryptophan (L-trp) to quench azidyl radicals formed from photo-activation of complex **13** has been previously reported. It has been suggested that the presence of the amino acid does not prevent the release of such RNS from photo-degradation of the metallo-organic compound, but quenches the formation of the DMPO- N_3 spin adduct at low, biologically

relevant concentrations.⁴² Although L-trp radical is a strong oxidant ($E^\circ = 1.015$ V at pH 7),⁷⁸ it is weaker than the azidyl radical ($E^\circ = 1.33$ V),⁷⁶ and therefore an electron transfer between the two species is favourable. The mechanism by which tryptophan destroys the azidyl radicals was suggested to proceed through a one-electron oxidation, with formation of an intermediate tryptophan radical.¹⁰ Nevertheless, previous studies failed in detecting such tryptophan intermediate.

In this work, photo-activation of complex **13** in the presence of L-trp was tested with the nitroso spin trap MNP, a spin trapping agent specific for the trapping of reactive C-centred radicals. The irradiation of complex **13** with 465 nm blue LED light with MNP and L-trp led to the detection of a 3-line signal (Figure 6.17), which was assigned to the radical spin adduct formed from the trapping of a L-tryptophan radical (L-trp \bullet), with the unpaired electron located in position 3 of the indole ring. The spectral parameters extracted by simulation are in good agreement with previously reported work where tryptophan radical was formed from flash photolysis in solution⁶⁹ (Table 6.1).

Photo-activation of complex **13** was also tested in the presence of melatonin (MLT). The ability of this indole derivative of L-trp to quench the formation of DMPO-N₃ during photo-irradiation of complex **13** was previously reported.¹⁰ Photo-activation of complex **13** in the presence of MLT and MNP was shown to produce a radical with the same features of the MNP-trp spin adduct (Figure 6.23). The similarity between the two spectra suggested that the nitroso spin trapping agent trapped the radical at the same position of the indole ring.

Interestingly, major differences were found in the kinetic profiles of formation of the MNP-trp and MNP-MLT spin adducts. To start, the concentration of the spin trapped MLT radical was found to be *ca.* 30 times higher than the concentration of the MNP-trp adduct. An explanation for this pronounced difference can be found from the comparison between the reduction potentials of L-trp ($E^\circ = 1.015$ V)⁷⁸ and MLT ($E^\circ = 0.73$ V).⁷⁹ In fact, despite both species possessing a reduction potential lower than azidyl radical ($E^\circ = 1.33$ V),⁷⁶ the much lower reduction potential of MLT suggests that an electron transfer from MLT to the azidyl radical is more favourable than from L-trp. Secondly, the formation of the MNP-MLT spin adduct appeared to be more sustained compared to the analogous trp adduct, with the maximum reached after 95 min compared to 16 min (Figure 6.19 and Figure 6.26), an effect that can be ascribed to an increased stability of the MNP-MLT spin adduct compared to the MNP-trp adduct. Additionally, a bump can be seen in the first part of the kinetic profile of formation of the MNP-MLT spin adduct, regardless the presence or absence of EtOH (Figure 6.26 and Figure 6.28). The data therefore suggest the co-participation of two distinct events that cause the formation of the MLT radical, readily trapped by MNP.

6.4.2 Formation of hydroxyl radical

Photo-activation of complex **13** in the presence of EtOH and MNP led to the detection of a nitroso spin adduct which was ascribed to the trapping of the α -hydroxyl ethyl radical. EtOH is a well known hydroxyl radical ($\bullet\text{OH}$) scavenger, and therefore the formation of an ethanol radical was attributed to the interaction of the alcohol with $\bullet\text{OH}$ released upon photo-degradation of the Pt-complex. These findings suggested the presence of multiple degradation pathways for complex **13**, involving not only the release of azidyl radicals, but hydroxyl radicals too. The complex kinetics of formation of the melatonin radical can therefore be interpreted as the interaction of this indole derivative with both $\bullet\text{N}_3$ and $\bullet\text{OH}$, both concurring to the formation of MLT radicals which are readily trapped by MNP.

6.4.3 Longer wavelength of activation

Photo-irradiation of complex **13** with 528 nm green light was tested. Activation at longer wavelengths is of interest because of their ability to penetrate deeper into tissues, thereby broadening the clinical range of applicability of this photo-activable anticancer compound.

The wavelength of activation used in previously reported EPR studies was 465 nm. Previous UV-Vis investigations found photo-activation of complex **13** still occurring at 517 nm green LED light, although to *ca.* 20 fold lower extent compared to activation with 465 nm blue light.⁴² In this work, complex **13** was irradiated using 528 nm green LED light in the presence of the nitroso spin trap MNP and either L-trp or MLT. In the presence of L-trp, the formation of the MNP-indole radical adduct was still observed, although to a much lower rate (Figure 6.21). The reduced photo-activation of the complex can partially be attributed to the lower irradiation power of the green light (5.4 mW cm^{-2} at 528 nm) compared to blue (7.1 mW cm^{-2} at 465 nm).

Interestingly, irradiation of complex **13** with green light in the presence of MLT did not lead to the detection of any radical spin adduct. This finding was unexpected considering that the amount of MNP-MLT adduct detected from irradiation with blue light was *ca.* 30 fold higher in comparison to the MNP-trp adduct.

6.4.4 Photo-protective effect of pentagastrin

The cytotoxicity of complex **13** was previously suggested to involve a dual attack on cancer cells carried out by the reactive platinum(II) and azidyl radicals, both produced upon photo-activation of the compound.⁴² Although Pt^{II} is known to perpetrate its cytotoxic effect through

platination of DNA, the unreactivity of N_3 radicals towards nucleic acids and derivatives was previously reported.⁴⁸ On the other hand, azidyl radicals were found to be reactive towards aromatic functionalised amino acids.⁴⁷

Pentagastrin was selected as a tryptophan-containing small peptide to test its effects on the photo-activation of complex **13**. In the presence of MNP, no spin trap adducts ascribable to the peptide were detected (Figure 6.35), suggesting either a non-susceptibility of azidyl radicals towards the peptide or the inability of the nitroso spin trap to bind to any pentagastrin radical product formed from interaction with the RNS.

Therefore, irradiation of complex **13** in the presence of pentagastrin was tested using the nitron spin trap DMPO. In the absence of pentagastrin, a 1:1:1:2:2:2:2:2:1:1:1 twelve-line spectrum was detected, and was readily attributed to the DMPO- N_3 adduct as previously reported.⁴² The differences between the spectral parameters of the detected spin adduct compared to previously reported ones will be discussed in Section 6.4.5. Instead, the presence of pentagastrin was found to quench the formation of the DMPO- N_3 spin adduct (Figure 6.36). It therefore appears that, even as part of a small peptidic chain, tryptophan still preserves its photoprotective effect towards azidyl radicals. The impossibility to detect a tryptophan radical intermediate through spin trapping with MNP was attributed to a decreased accessibility to the amino acid within the peptidic chain, which could still be available for the oxidative attack brought by N_3 radicals but not for trapping with the nitroso spin trap. These findings suggest that azidyl radicals may exert their cytotoxic activity by carrying out an oxidative attack on L-trp residues in proteins, with the consequent disruption of the cell homeostasis leading to cell death.

6.4.5 Hyperfine coupling constants

Differences between the spectral parameters of the spin trap adducts detected in this work and the parameters previously reported for the same species have been observed. The hyperfine splittings of a spin adduct are strongly influenced by the solvent used for the experiment. In general, an increase in the polarity of the solvent is related to an increased spin density in the nitroxidic nitrogen, with a consequent increase of the nitrogen hyperfine splitting.⁷¹ Accordingly, the β -hydrogen splitting is expected to decrease, although this is not always the case. It therefore appears that the best way to identify a spin adduct is still by comparison with previously identified adducts in the same solvent. Table 6.4 represents an exemplification of the variation of the hyperfine couplings for the DMPO- N_3 spin adduct obtained by changing the solvent. A decrease of both the $a^{N_{NO}}$ and a^{H_β} couplings are reported when the solvent changes from H_2O ⁴² to DMF 50%,⁷⁷ respectively of 0.07 and 0.1 mT. Thus, a further decrease

of the polarity of the solvent is expected to further decrease the hyperfine couplings. Therefore, the decrease of the a^{H_β} coupling of 0.09 mT observed in this work for a sample solution of 70% DMF is consistent with previously reported data.

6.4.6 Mechanism of photo-activation of complex **13**

As discussed at the beginning of this Chapter, complex **13** has the potential to release both ROS and RNS upon irradiation (Figure 6.12). This work provides further evidences on the formation of both N_3 and OH radicals upon photo-activation of the Pt^{IV} -compound. The detection of the α -hydroxyl ethyl radical, spin trapped with MNP, provided a direct evidence for the photo-release of the hydroxyl radical which is readily quenched by ethanol. Similarly, melatonin has been reported to possess the ability to quench not only RNS, but ROS too.^{80–82} The kinetics of formation of the MNP-MLT spin adduct also suggest that MLT radical is formed from interaction with both N_3 and OH radicals, through two kinetically distinct pathways.

6.4.7 Amino acid radicals

The detection of the L-trp radical intermediate formed from interaction with azidyl radicals verifies the theory of an oxidative attack brought by the RNS towards this aromatic amino acid. Consequently, two considerations can be made. Firstly, the cytotoxicity of this class of anticancer compounds will depend on the presence of target aromatic amino acids and derivatives. Therefore, it is important to consider the serum levels of metabolites such as tryptophan and melatonin in the patient, as they will influence the antitumoral action of the drug. The serum levels of melatonin are known to vary during the day, with the maximum production during sleep hours.⁸³ Therefore, the optimum time for the administration of similar drugs must be determined in order to achieve the maximum therapeutic effect. These considerations fall under the emerging field of Chronopharmacology.⁸⁴ Interestingly, the serum L-trp levels in some cancer patients have been found to be depleted in comparison with normal controls,^{85,86} a finding that suggests an increased efficacy of phototherapy with complex **13** in similar cases. It also appears that the potency of the anticancer compound may be fine-tuned by coordinated administration of L-trp, a strategy that can potentially help to prevent unwanted side effects of chemotherapy which is a major issue for the Pt complex class of anticancer drugs.

Secondly, this work shines a light in respect to the target of the RNS released from photo-activation of complex **13**. Whilst the targets for the reactive Pt^{II} are known to be nucleic acids and derivatives, azidyl radicals have previously been found to be unreactive towards DNA, but

reactive towards aromatic amino acids.⁴⁷ Amino acids like tryptophan and tyrosine are involved in important electron transfer pathways in proteins.^{87,88} A disruption of such pathways may strongly impair cellular homeostasis leading to cell death. This work showed how azidyl radicals can be quenched by both free L-trp and derivatives and tryptophan containing peptides, providing a further evidence towards the identification of the cellular target of such RNS.

6.5 Conclusions

In this Chapter, the mechanism of action and intracellular targets of the photo-activable platinum(IV) complex *trans,trans,trans*-[Pt(N₃)₂OH₂(pyridine)₂] (complex **13**) were investigated with the spin trapping methodology. The cytotoxic activity of complex **13** has been reported to rely on a dual mechanism of action, involving simultaneous DNA platination carried out by the photo-reduced Pt^{II} centre and an oxidative attack brought by azidyl radicals ([•]N₃) released upon photo-activation of the compound. The presence of indole derivatives such as L-trp and MLT has been previously reported to produce a photo-protective effect to be ascribed to the quenching of [•]N₃. The interaction between the indole derivatives and the RNS released upon photo-activation of complex **13** has been suggested to proceed through a one-electron oxidation mechanism, with formation of a transient indole radical, which has not been observed before.

In this work, transient L-trp and MLT radicals have been detected by performing EPR spin trapping experiments with the nitroso spin trapping agent MNP. Photo-activation of complex **13** in the presence of L-trp and MNP resulted in direct detection of the MNP-trp radical spin adduct. The formation of L-trp adducts was observed from both irradiation with blue (465 nm) and green (528 nm) LED light. On the contrary, the MNP-MLT spin adduct was observed only from activation of complex **13** with blue light, producing a *ca.* 30 fold higher EPR signal compared to MNP-trp. The kinetics of formation of the MNP-MLT adduct suggested the presence of two kinetically different processes. Irradiation of complex **13** in the presence of EtOH and MNP resulted in the trapping of the α -hydroxy-ethyl radical, which is known to be formed specifically from interaction of the alcohol with hydroxyl radicals ([•]OH). These findings confirmed the presence of multiple photo-degradation pathways for complex **13**, involving the release of both azidyl and hydroxyl radicals.

Photo-activation of complex **13** in the presence of the tryptophan-containing peptide pentagastrin was tested to determine the ability of L-trp to quench azidyl radicals as part of a small peptidic chain. It has been suggested that the cytotoxic effect of ROS/RNS relies on the interaction of the radicals with biological structures containing aromatic amino acids. Spin

trapping experiments with MNP failed to detect MNP-pentagastrin spin adducts, suggesting either the absence of a photo-protective effect or the inability of the nitroso spin trapping agent to trap peptide radicals generated from interaction with photo-released $\bullet\text{N}_3$. The nitron spin trap DMPO was therefore used to test the effect of pentagastrin on the formation of the DMPO- N_3 spin adduct upon irradiation of complex **13**. The presence of pentagastrin gave a decrease of *ca.* 70% in the amount of DMPO- N_3 detected, suggesting that the peptide is able to quench photo-released azidyl radicals.

6.6 References

1. World Health Organization (WHO). Fact sheet on cancer. (2017). at <http://www.who.int/mediacentre/factsheets/fs297/en/>
2. Reuter, S., Gupta, S. C., Chaturvedi, M. M. & Aggarwal, B. B. Oxidative stress, inflammation, and cancer: How are they linked? *Free Radic. Biol. Med.* **49**, 1603–1616 (2010).
3. Fraga, C. G. *et al.* Ascorbic acid protects against endogenous oxidative DNA damage in human sperm. *Proc. Natl. Acad. Sci.* **88**, 11003–11006 (1991).
4. Martin, L. P., Hamilton, T. C. & Schilder, R. J. Platinum resistance: The role of DNA repair pathways. *Clin. Cancer Res.* **14**, 1291–1295 (2008).
5. Sies, H. Biochemistry of Oxidative Stress. *Angew. Chemie Int. Ed. English* **25**, 1058–1071 (1986).
6. Banerjee, K. *et al.* ROS and RNS induced apoptosis through p53 and iNOS mediated pathway by a dibasic hydroxamic acid molecule in leukemia cells. *Eur. J. Pharm. Sci.* **52**, 146–164 (2014).
7. Fleming, A. & Colebrook, L. On the Use of Salvarsan for the Treatment of Syphilis. *Lancet* **177**, 1631–1634 (1911).
8. Lloyd, N. C., Morgan, H. W., Nicholson, B. K. & Ronimus, R. S. The composition of Ehrlich's Salvarsan: Resolution of a century-old debate. *Angew. Chemie - Int. Ed.* **44**, 941–944 (2005).
9. Johnstone, T. C., Park, G. Y. & Lippard, S. J. Understanding and Improving Platinum Anticancer Drugs - Phenanthriplatin. *Anticancer Res.* **34**, 471–6 (2014).

10. Butler, J. S. Photodecomposition Pathways for Photoactivatable Platinum (IV) Anticancer Complexes. (PhD Thesis, University of Warwick, 2014).
11. Arblaster, J. W. The Discoverers of the Platinum Isotopes. *Platin. Met. Rev.* **44**, 173–178 (2000).
12. Rosenberg, B., Van Camp, L. & Krigas, T. Inhibition of Cell Division in *Escherichia coli* by Electrolysis Products from a Platinum Electrode. *Nature* **205**, 698–699 (1965).
13. Barnard, C. F. J. Platinum Anti-Cancer Agents. *Platin. Met. Rev.* **33**, 162–167 (1989).
14. Alderden, R. A., Hall, M. D. & Hambley, T. W. The Discovery and Development of Cisplatin. *J. Chem. Educ.* **83**, 728 (2006).
15. Gately, D. P. & Howell, S. B. Cellular accumulation of the anticancer agent cisplatin: a review. *Br. J. Cancer* **67**, 1171–6 (1993).
16. Ishida, S., Lee, J., Thiele, D. J. & Herskowitz, I. Uptake of the anticancer drug cisplatin mediated by the copper transporter Ctr1 in yeast and mammals. *Proc. Natl. Acad. Sci.* **99**, 14298–14302 (2002).
17. Stoian, I., Oros, A. & Moldoveanu, E. Apoptosis and Free Radicals. *Biochem. Mol. Med.* **59**, 93–97 (1996).
18. Fichtinger-Schepman, A. & Veer, J. Van der. Adducts of the antitumor drug cis-diamminedichloroplatinum (II) with DNA: formation, identification, and quantitation. *Biochemistry* **24**, 707–713 (1985).
19. Hall, M. D., Okabe, M., Shen, D.-W., Liang, X.-J. & Gottesman, M. M. The Role of Cellular Accumulation in Determining Sensitivity to Platinum-Based Chemotherapy. *Annu. Rev. Pharmacol. Toxicol.* **48**, 495–535 (2008).
20. Boudvillain, M., Dalbiès, R., Aussourd, C. & Leng, M. Intrastrand cross-links are not formed in the reaction between transplatin and native DNA: Relationm with the clinical inefficiency of transplatin. *Nucleic Acids Res.* **23**, 2381–2388 (1995).
21. Wheate, N. J., Walker, S., Craig, G. E. & Oun, R. The status of platinum anticancer drugs in the clinic and in clinical trials. *Dalt. Trans.* **39**, 8113 (2010).
22. Kelland, L. The resurgence of platinum-based cancer chemotherapy. *Nat. Rev. Cancer* **7**, 573–584 (2007).
23. Kostrhunova, H., Kasparkova, J., Gibson, D. & Brabec, V. Studies on cellular

- accumulation of satraplatin and its major metabolite JM118 and their interactions with glutathione. *Mol. Pharm.* **7**, 2093–2102 (2010).
24. Banfic, J., Legin, A. A., Jakupec, M. A., Galanski, M. & Keppler, B. K. Platinum(IV) complexes featuring one or two axial ferrocene bearing ligands - Synthesis, characterization, and cytotoxicity. *Eur. J. Inorg. Chem.* 484–492 (2014).
 25. Wang, X. & Guo, Z. Targeting and delivery of platinum-based anticancer drugs. *Chem. Soc. Rev.* **42**, 202–224 (2013).
 26. Dougherty, T. J. *et al.* Photodynamic Therapy. *JNCI J. Natl. Cancer Inst.* **90**, 889–905 (1998).
 27. Dolmans, D. E. J. G. J., Fukumura, D. & Jain, R. K. Photodynamic therapy for cancer. *Nat. Rev. Cancer* **3**, 380–387 (2003).
 28. Shaili, E. Platinum anticancer drugs and photochemotherapeutic agents: Recent advances and future developments. *Sci. Prog.* **97**, 20–40 (2014).
 29. Yano, S. *et al.* Current states and future views in photodynamic therapy. *J. Photochem. Photobiol. C Photochem. Rev.* **12**, 46–67 (2011).
 30. Hockel, M. & Vaupel, P. Tumor Hypoxia: Definitions and Current Clinical, Biologic, and Molecular Aspects. *JNCI J. Natl. Cancer Inst.* **93**, 266–276 (2001).
 31. Mayhew, S., Vernon, D. I., Schofield, J., Griffiths, J. & Brown, S. B. Investigation of Cross-resistance to a Range of Photosensitizers, Hyperthermia and UV Light in Two Radiation-induced Fibrosarcoma Cell Strains Resistant to Photodynamic Therapy In Vitro. *Photochem. Photobiol.* **73**, 39–46 (2001).
 32. Gomer, C. J. *et al.* Photodynamic therapy-mediated oxidative stress can induce expression of heat shock proteins. *Cancer Res.* **56**, 2355–2360 (1996).
 33. Kratochwil, N. A., Zabel, M., Range, K.-J. J. & Bednarski, P. J. Synthesis and X-ray crystal structure of trans,cis-[Pt(OAc)₂I₂(en)]: a novel type of cisplatin analog that can be photolyzed by visible light to DNA-binding and cytotoxic species in vitro. *J. Med. Chem.* **39**, 2499–2507 (1996).
 34. Vogler, A., Kern, A. & Hüttermann, J. Photochemical Reductive trans-Elimination from trans-Diazidotetracyanoplatinate(IV). *Angew. Chemie Int. Ed. English* **17**, 524–525 (1978).

35. Müller, P. *et al.* Nucleotide cross-linking induced by photoreactions of platinum(IV)-azide complexes. *Angew. Chemie - Int. Ed.* **42**, 335–339 (2003).
36. Mackay, F. S. *et al.* A photoactivated trans-diammine platinum complex as cytotoxic as cisplatin. *Chem. - A Eur. J.* **12**, 3155–3161 (2006).
37. Farrer, N. J., Woods, J. A., Munk, V. P., MacKay, F. S. & Sadler, P. J. Photocytotoxic trans-diam(m)ine platinum(IV) diazido complexes more potent than their cis isomers. *Chem. Res. Toxicol.* **23**, 413–421 (2010).
38. Mackay, F. S. *et al.* A potent cytotoxic photoactivated platinum complex. *Proc. Natl. Acad. Sci.* **104**, 20743–20748 (2007).
39. Westendorf, A. F. *et al.* Trans,trans,trans-[Pt^{IV}(N₃)₂(OH)₂(py)(NH₃)]: a light-activated antitumor platinum complex that kills human cancer cells by an apoptosis-independent mechanism. *Mol Cancer Ther* **11**, 1894–1904 (2012).
40. Farrer, N. J. *et al.* A potent trans-diimine platinum anticancer complex photoactivated by visible light. *Angew. Chemie - Int. Ed.* **49**, 8905–8908 (2010).
41. Venkatesh, V., Wedge, C. J., Romero-Canelón, I., Habtemariam, A. & Sadler, P. J. Spin-labelled photo-cytotoxic diazido platinum(IV) anticancer complex. *Dalt. Trans.* **45**, 13034–13037 (2016).
42. Butler, J. S., Woods, J. A., Farrer, N. J., Newton, M. E. & Sadler, P. J. Tryptophan Switch for a Photoactivated Platinum Anticancer Complex. *J. Am. Chem. Soc.* **134**, 16508–16511 (2012).
43. Mackay, F. S., Moggach, S. A., Collins, A., Parsons, S. & Sadler, P. J. Photoactive trans ammine/amine diazido platinum(IV) complexes. *Inorganica Chim. Acta* **362**, 811–819 (2009).
44. Zhao, Y. *et al.* De Novo Generation of Singlet Oxygen and Ammine Ligands by Photoactivation of a Platinum Anticancer Complex. *Angewandte* **125**, 13878–13882 (2013).
45. Halliwell, B. Oxygen and nitrogen are pro-carcinogens. Damage to DNA by reactive oxygen, chlorine and nitrogen species: Measurement, mechanism and the effects of nutrition. *Mutat. Res. - Genet. Toxicol. Environ. Mutagen.* **443**, 37–52 (1999).
46. Wiseman, H., Kaur, H. & Halliwell, B. DNA damage and cancer: Measurement and mechanism. *Cancer Lett.* **93**, 113–120 (1995).

47. Butler, J., Land, E. J., Prütz, W. A. & Swallow, A. J. Charge transfer between tryptophan and tyrosine in proteins. *Biochim. Biophys. Acta (BBA)/Protein Struct. Mol.* **705**, 150–162 (1982).
48. Land, E. J. & Prütz, W. A. Reaction of azide radicals with amino acids and proteins. *Int. J. Radiat. Biol. Relat. Stud. Phys. Chem. Med.* **36**, 75–83 (1979).
49. Chung, K. T. & Gadupudi, G. S. Possible roles of excess tryptophan metabolites in cancer. *Environ. Mol. Mutagen.* **52**, 81–104 (2011).
50. Solar, S., Getoff, N., Surdhar, P. S., Armstrong, D. A. & Singh, A. Oxidation of tryptophan and N-methylindole by N₃·, Br₂·-, and (SCN)₂·- radicals in light- and heavy-water solutions: a pulse radiolysis study. *J. Phys. Chem.* **95**, 3639–3643 (1991).
51. Buscemi, N. *et al.* Melatonin for Treatment of Sleep Disorders: Summary. (2004), AHRQ Evidence Report Summaries: Agency for Healthcare Research and Quality (US). Available from: <http://www.ncbi.nlm.nih.gov/books/NBK11941/>.
52. Cardinali, D. P. & Pévet, P. Basic aspects of melatonin action. *Sleep Med. Rev.* **2**, 175–190 (1998).
53. Arendt, J., Skene, D. J., Middleton, B., Lockley, S. W. & Deacon, S. Efficacy of Melatonin Treatment in Jet Lag, Shift Work, and Blindness. *J. Biol. Rhythms* **12**, 604–617 (1997).
54. Reiter, R. J. & Tan, D.-X. What constitutes a physiological concentration of melatonin? *J. Pineal Res.* **34**, 79–80 (2003).
55. Rodriguez, C. *et al.* Mechanisms involved in the pro-apoptotic effect of melatonin in cancer cells. *Int. J. Mol. Sci.* **14**, 6597–6613 (2013).
56. Turjanski, A. G., Rosenstein, R. E. & Estrin, D. A. Reactions of melatonin and related indoles with free radicals: A computational study. *J. Med. Chem.* **41**, 3684–3689 (1998).
57. Roberts, J. E., Hu, D. N. & Wishart, J. F. Pulse radiolysis studies of melatonin and chloromelatonin. *J. Photochem. Photobiol. B Biol.* **42**, 125–132 (1998).
58. Tomás-Zapico, C. *et al.* Melatonin protects against δ -aminolevulinic acid-induced oxidative damage in male Syrian hamster Harderian glands. *Int. J. Biochem. Cell Biol.* **34**, 544–553 (2002).
59. Marshall, K.-A., Reiter, R. J., Poeggeler, B., Aruoma, O. I. & Halliwell, B. Evaluation

- of the Antioxidant of Melatonin in Vitro. *Free Radic. Biol. Med.* **21**, 307–315 (1996).
60. Hill, S. M., Blask, D. E., Hill, S. M. & Blask, D. E. Effects of the Pineal Hormone Melatonin on the Proliferation and Morphological Characteristics of Human Breast Cancer Cells (MCF-7) in Culture. *Cancer Res.* **48**, 6121–6126 (1988).
61. Farriol, M., Venereo, Y., Orta, X., Castellanos, J. M. & Segovia-Silvestre, T. In vitro effects of melatonin on cell proliferation in a colon adenocarcinoma line. *J. Appl. Toxicol.* **20**, 21–24 (2000).
62. Guardiola-Lemaître, B. Toxicology of Melatonin. *J. Biol. Rhythms* **12**, 697–706 (1997).
63. Lissoni, P. *et al.* A randomized study of chemotherapy with cisplatin plus etoposide versus chemoendocrine therapy with cisplatin, etoposide and the pineal hormone melatonin as a first-line treatment of advanced non-small cell lung cancer patients in a poor clinical state. *J. Pineal Res.* **23**, 15–19 (1997).
64. Maharaj, D. S., Glass, B. D. & Daya, S. Melatonin: New places in therapy. *Biosci. Rep.* **27**, 299–320 (2007).
65. Lack, B., Daya, S. & Nyokong, T. Interaction of serotonin and melatonin with sodium, potassium, calcium, lithium and aluminium. *J. Pineal Res.* **31**, 102–108 (2001).
66. Stoll, S. & Schweiger, A. EasySpin, a comprehensive software package for spectral simulation and analysis in EPR. *J. Magn. Reson.* **178**, 42–55 (2006).
67. Makino, K., Suzuki, N., Moriya, F., Rokushika, S. & Hatano, H. A Fundamental Study on Aqueous Solutions of as a Spin Trap. *Radiat. Res.* **86**, 294–310 (1981).
68. Kremers, W., Koroll, G. W. & Singh, A. Spin trapping of the azide radical with nitroso compounds. *Can. J. Chem.* **60**, 1597 (1982).
69. Lion, Y., Kuwabara, M. & Riesz, P. Spin-Trapping and ESR studies of the Direct Photolysis of Aromatic Amino Acids, Dipeptides, Tripeptides and Polypeptides in Aqueous Solutions—III. Tryptophan and Related Compounds. *J. Photochem. Photobiol.* **35**, 43–52 (1982).
70. Pailthorpe, M. T. & Nicholls, C. H. Indole N-H Bond Fission During the Photolysis of Tryptophan. *Photochem. Photobiol.* **14**, 135–145 (1971).
71. Buettner, G. R. Spin Trapping - Electron-Spin-Resonance Parameters of Spin Adducts. *Free Radic. Bio. Med.* **3**, 259–303 (1987).

72. Elias, R. J., Andersen, M. L., Skibsted, L. H. & Waterhouse, A. L. Key factors affecting radical formation in wine studied by spin trapping and EPR spectroscopy. *Am. J. Enol. Vitic.* **60**, 471–476 (2009).
73. Yates, Z. *et al.* Histidine residue mediates radical-induced hinge cleavage of human IgG1. *J. Biol. Chem.* **285**, 18662–18671 (2010).
74. Navaratnam, S. & Parsons, B. J. Reduction potential of histidine free radicals: a pulse radiolysis study. *J. Chem. Soc. Faraday Trans.* **94**, 2577–2581 (1998).
75. Harriman, A. Further Comments on the Redox Potentials of Tryptophan and Tyrosine. *J. Phys. Chem.* **91**, 6102–6104 (1987).
76. DeFelippis, M. R., Faraggi, M. & Klapper, M. H. Redox potentials of the azide and dithiocyanate radicals. *J. Phys. Chem.* **94**, 2420–2424 (1990).
77. Reszka, K., Kolodziejczyk, P. & Lown, J. W. Photosensitization by antitumor agents. 5. daunorubicin-photosensitized oxidation of NAD(P)H in aqueous and N,N-dimethylformamide/aqueous solutions— an electron paramagnetic resonance study. *Free Radic. Biol. Med.* **5**, 63–70 (1988).
78. DeFelippis, M. R., Murthy, C. P., Faraggi, M. & Klapper, M. H. Pulse radiolytic measurement of redox potentials: the tyrosine and tryptophan radicals. *Biochemistry* **28**, 4847–4853 (1989).
79. Tan, D. *et al.* Chemical and Physical Properties and Potential Mechanisms: Melatonin as a Broad Spectrum Antioxidant and Free Radical Scavenger. *Curr. Top. Med. Chem.* **2**, 181–197 (2002).
80. Poeggeler, B. *et al.* Melatonin-A Highly Potent Endogenous Radical Scavenger and Electron Donor: New Aspects of the Oxidation Chemistry of this Indole Accessed in vitro. *Ann. N. Y. Acad. Sci.* **738**, 419–420 (2006).
81. Zang, L. Y., Cosma, G., Gardner, H. & Vallyathan, V. Scavenging of reactive oxygen species by melatonin. *Biochim. Biophys. Acta - Gen. Subj.* **1425**, 469–477 (1998).
82. Dellegar, S. M., Murphy, S. A., Bourne, A. E., DiCesare, J. C. & Purser, G. H. Identification of the Factors Affecting the Rate of Deactivation of Hypochlorous Acid by Melatonin. *Biochem. Biophys. Res. Commun.* **257**, 431–439 (1999).
83. Claustrat, B., Brun, J. & Chazot, G. The basic physiology and pathophysiology of melatonin. *Sleep Med. Rev.* **9**, 11–24 (2005).

84. Dallmann, R., Brown, S. A. & Gachon, F. Chronopharmacology: New Insights and Therapeutic Implications. *Annu. Rev. Pharmacol. Toxicol.* **54**, 339–361 (2014).
85. Lyon, D. E., Walter, J. M., Starkweather, A. R., Schubert, C. M. & McCain, N. L. Tryptophan degradation in women with breast cancer: a pilot study. *BMC Res. Notes* **4**, 156 (2011).
86. Capuron, L. *et al.* Association between decreased serum tryptophan concentrations and depressive symptoms in cancer patients undergoing cytokine therapy. *Mol. Psychiatry* **7**, 468–473 (2002).
87. Stubbe, J. & Van Der Donk, W. A. Protein Radicals in Enzyme Catalysis. *Chem. Rev.* **98**, 705–762 (1998).
88. Sigel, H. & Sigel, A. *Metal Ions in Biological Systems: Volume 30: Metalloenzymes Involving Amino Acid-residue and Related Radicals.* **30**, (CRC Press, New York, 1994).

Chapter 7

Conclusions and Future Work

This thesis focused on the investigation of novel applications of electron paramagnetic resonance (EPR) spectroscopy in the pharmaceutical field. The versatility of this powerful biophysical technique presents a wide range of possible uses for EPR in all the very different phases of pharmaceutical research and development, from drug design to drug development and product formulation. These are all areas where to date EPR has been much underutilised. In the first part of this work, EPR has been used to study the effects of γ -irradiation for the sterilization of pharmaceutical excipients as an alternative to the classic sterilization methods. The radicalic degradation products formed upon irradiation of the excipients were characterised and their reactivity was evaluated. These studies showed the great potential of EPR in assessing the stability of pharmaceutical products. In the second part of this work, the spin trap methodology was applied to investigate the reactivity of photo-irradiated platinum(IV) complexes. The mechanism of action of a promising candidate of this class of anticancer drugs was at the centre of this investigation, contributing to the overall understanding of the reactivity of this compound and its generated photo-products.

7.1 Conclusions

Chapter 4 focuses on the investigation of the effects of γ -radiation sterilization on the pharmaceutical excipient L-histidine (L-his). This amino acid is typically used in pharmaceutical and biopharmaceutical formulations as a buffering agent and a stabiliser. The analysis of the γ -irradiated solid powders at r.t. highlighted the formation of persistent C-centred radical species at a concentration of approximately 2.5 mM at 25 kGy. The influence of a different irradiation source was also evaluated by studying the effects of X-rays on L-his. X-irradiation of the powder was found to produce the same main paramagnetic species, with only small spectral differences that were attributed to the dissimilar irradiation conditions, resulting in the formation of minor radical species at different concentrations. Single crystal analysis confirmed the main radical species to be the product of deamination, as previously reported,¹ being a common degradation pathway for amino acids. The analysis of the EPR

spectra of an L-his single crystal also highlighted the presence of secondary species, as suggested by the powder spectra. Simulations of the roadmaps were performed, combining previously published hyperfine coupling tensors and g-tensors extracted from simulation of the powder spectra, achieving reasonably good agreement with the experimental data. Multi-frequency analysis (9–263 GHz) highlighted the anisotropic feature of the g-value of the deamination radical, but the presence of secondary minor species interfering with the analysis prevented the extraction of the Hamiltonian parameters through global fitting of the multi-frequency data. Low temperature irradiation was performed to characterise the (assumed) primary radical species formed as a result of the irradiation process, and to study the evolution of the said species into the ones persistent at r.t. This is a necessary step to assess the compatibility between the various ingredients forming multi-component systems, in particular to avoid transient radical-driven degradation of the active pharmaceutical ingredient (API). Indeed, not only direct degradation of the API(s) due to irradiation, but also indirect degradation brought by interaction with the excipients' radical species must be considered. The analysis of the low temperature irradiated L-his single crystal at 80 K showed the presence of a three-line EPR spectrum, which was ascribed to a previously reported L-his carboxyl anion.¹ At 120 K, such radical species were found to irreversibly evolve into the L-his deamination radical from both the L-his crystal and powder samples. The annealing in steps of low temperature irradiated L-his highlighted the formation of an unreported transient paramagnetic species, which quickly disappeared upon further heating.

Finally, the reactivity of the radicals in solution was assessed by means of spin trapping experiments. Histidine-containing formulations are often of the parenteral type, meaning that the product needs to be solubilised prior to administration to the patient. Thus, assessing the behaviour of the radicals in solution is paramount to assess the safety of the irradiated drug. The solid state persistent radicals were found to have a short lifetime in solution, as expected for this type of C-centred radicals. Spin trapping with the nitroso spin trapping agent MNP allowed trapping and characterisation of the L-his deamination radicals. Interestingly, the same L-his radical species could still be trapped when the spin-trap was added minutes after dissolution of the powder, in apparent contrast with the short lifetime of the radicals. It was therefore proposed that the deamination radicals are regenerated through a Fenton-type reaction involving the presence of trace metals and strong oxidant species, leading to the generation of reactive oxygen species (ROS) responsible for the regeneration of the radicals. This supposition was supported when a chelating agent was added to the sample mixture, the regeneration of the radicals was found to cease. The source of the metals needed for the Fenton chemistry was attributed to the metal needle of the syringe used to transfer the sample solution into the EPR tube for analysis, a characteristic confirmed by XRF analysis. Indeed, by using a glass Pasteur

pipette in place of the syringe and needle, the regeneration of the radical was not observed. The fact that similar medical needles might be used for the administration of the parenteral formulation confers great relevance to these findings. Avoiding the regeneration of the radicals in solution is necessary not only to eliminate the potential of radical-induced degradation of other drug components, but also to avoid direct toxicological issues due to unintentional injection of free radicals into patients. The characterisation of the degradation products of L-his through widespread techniques such as electron spray ionisation mass spectroscopy (ESI-MS) and proton nuclear magnetic resonance (^1H NMR) was also attempted, but failed in detecting the additional species formed upon irradiation of the samples previously studied with EPR spectroscopy because of the limited sensitivity of these techniques compared to EPR.

Chapter 5 focuses on the study of the effects of γ -irradiation sterilization on D-mannitol. Mannitol is the most used excipient in lyophilised formulations where it is utilised as a bulking agent and as such can constitute up to 90% w/w of the drug product. Knowing the effects of radiation sterilization on mannitol is therefore of great importance. To the best of our knowledge, studies identifying the radicalic degradation products formed upon irradiation of D-mannitol have not been reported to date, nor have spin trapping experiments of mannitol radicals in solution been described. In this work, the evolution of the primary radical species formed upon irradiation of D-mannitol at 77 K into the r.t. persistent species has been studied by CW EPR. Liquid nitrogen temperature irradiation of D-mannitol was found to induce the formation of a C-centred radical characterised by a large isotropic hyperfine coupling, *radical I*, which was assigned to the abstraction of a proton from either C3 or C4. Annealing of the samples to 120 K was found to induce the formation of a second, O-centred radical species, *radical II*, possibly formed upon abstraction of a proton from the hydroxyl bound to either C1 or C6. Further annealing to 170 K resulted in the formation of a third radical species, *radical III*, which was suggested to arise from the abstraction of a proton from the carbon atom in position 1 or 6. By further annealing to 200 K and 240 K, an additional, unidentified radical species characterised by a large isotropic doublet was found to become more dominant in the EPR spectrum, while decreases of the other radical species were observed. The mutation of the EPR spectra first at 260 K and then at 295 K (r.t.) was interpreted as indicating the formation of new paramagnetic species, with at least three different radicals believed to be persistent at r.t. However, the complexity of the spectra in this temperature range did not allow a complete characterisation of the newly formed species. Interestingly, quantification of the r.t. persistent radical species showed an almost three times higher radical concentration for D-mannitol compared to L-his for a 25 kGy irradiation dose.

The spin trapping methodology was applied to assess the reactivity of the radicals in solution. As for L-his, the r.t. radicals persistent in the solid state were not detected in solution in the

absence of a spin trapping agent. Although direct dissolution of the irradiated powder in a spin trap solution of MNP resulted in the detection of a radical spin-trap adduct, the regeneration process that was witnessed for L-his was not observed for D-mannitol. These findings suggested such radical regeneration mechanism to be characteristic for L-his, and possibly related to the antioxidant properties of this amino acid that make it more susceptible to attacks from ROS. ESI-MS analysis of the D-mannitol irradiated powders resulted in the detection of a species with a molecular mass of 2 m/z units lower than the unaltered mannitol molecule, a species that was not observed in the MS spectrum of the non-irradiated powder. Such species was suggested to be the result of a C-centred radical formed by proton abstraction, subsequently rearranging through beta-elimination of a second proton and consequent formation of a double bond. ^1H NMR spectra of the irradiated samples also highlighted the presence of degradation products formed upon irradiation, though a thorough characterisation of such species was not possible due to the low signal-to-noise and the overlap of the signals from the unaltered D-mannitol.

Chapter 6 investigates the mechanism of action and the intracellular targets of the anticancer photo-activable platinum(IV) anticancer complex *trans,trans,trans*-[Pt(N₃)₂OH₂(pyridine)₂] (complex **13**). It has been previously reported that complex **13** exerts its anticancer activity through a dual mechanism of action, involving both platination of DNA induced by the photo-reduced Pt^{II} centre and the oxidative attack carried out by photo-released azidyl radicals ($\bullet\text{N}_3$).^{2,3} The simultaneous presence of L-tryptophan (L-trp) was found to have a photo-protective effect in cancer cells.² This effect was previously ascribed to the quenching of the azidyl radicals from the indole derivatives, which has been suggested to take place through a one-electron oxidation of the indoles with the consequential formation of a transient indole radical species. However, such species have not been detected before. Accordingly, it was also suggested that the cellular target of the above mentioned reactive nitrogen species (RNS) could be biological structures containing aromatic amino acids. In this work, the transient indole species formed from quenching of the azidyl radicals were successfully detected by means of CW EPR spin trapping experiments with the nitroso spin trap MNP. Photo-activation of complex **13** with blue (465 nm) LED light in the presence of L-trp resulted in the detection of the MNP-trp radical adduct. Similarly, blue light irradiation of complex **13** in the presence of the indole derivative melatonin (MLT) and MNP resulted in the trapping of a similar indole radical, but to a much higher (~ 30 times) extent compared to L-trp. Interestingly, irradiation at longer wavelengths (528 nm green LED light) allowed the detection of the indole spin trap adduct only for L-trp. Irradiation of complex **13** in the presence of the hydroxyl radical ($\bullet\text{OH}$) scavenger ethanol resulted in the trapping of a α -hydroxy-ethyl radical, implying an alternative photo-activation pathways for complex **13** that involves the release of hydroxyl radicals. Additionally, to investigate the

intracellular target of photo-released RNS/ROS, complex **13** was photo-activated in the presence of the L-trp containing peptide pentagastrin. Although spin trapping with MNP did not result in the detection of an indole radical, spin trapping of $\bullet\text{N}_3$ with the nitron spin trap DMPO highlighted a reduced formation of the DMPO- N_3 spin adduct in the presence of pentagastrin, suggesting the ability of the peptide to quench $\bullet\text{N}_3$ radicals.

7.2 Future work

The first part of this work was concerned with the characterisation of the degradation products formed upon irradiation of two common excipients, L-histidine and D-mannitol. Assessing the behaviour of single ingredients of pharmaceutical products is the necessary first step towards the study of multi-component systems. Hence, a sample of the most common pharmaceutical excipients from all the classes used in the parenteral formulation of pharmaceutical products could be tested applying the same experimental procedures utilised in this work, which provided extremely valuable information on the identity and reactivity of the radicalic degradants. Future investigation could then focus on determining the effects of radiation sterilization on a complete pharmaceutical product, including one or more active pharmaceutical ingredients (APIs). In fact, it is known that the effects of ionising radiations cannot be predicted beforehand.⁴ Indeed, it has been shown that APIs can both be protected from the irradiation⁵ and have a protective effect towards other drug components.⁶ Thus, the production of a dataset illustrating the effects of radiation sterilization on the most recurrent single drug components would enormously facilitate the following study of complete drug products, and allow the formulation of pharmaceuticals according to a *quality by design* approach. EPR is surely the technique of choice for the study of paramagnetic degradation products formed upon irradiation. Nevertheless, this work showed that techniques such as NMR and MS can produce extremely valuable complementary information for the characterisation of the degradants. The weak point of such techniques is that, differently from EPR, they are not selective towards the degradants, thus the signal of such impurities is often hidden by the signal of the unaltered compound. Therefore, the use of separation techniques such as High Performance Liquid Chromatography (HPLC) should be tested in combination with MS and NMR to overcome this issue.

The second part of this work focused on the investigation of the mechanism of action and the intracellular target of the photo-activable anticancer compound complex **13**. Our findings suggested the intracellular targets for the RNS/ROS released upon photo-activation of the compound to be aromatic amino acid-containing biological structures. This work suggested that

the photo-protective effect induced by L-trp is still present when L-trp is incorporated into a small peptidic chain. Future investigations will aim to prove that this effect can still be observed in the presence of more complex structures, i.e. proteins. Additionally, the presence of multiple photo-degradation pathways for complex **13** was confirmed by indirect detection of hydroxyl radicals. Further work is required to reach a thorough understanding of the degradation pathways of such platinum complex. An additional method for the determination of the source of OH• radicals involves the synthesis of ¹⁷O-labelled (*I* = +5/2) complex **13**. Trapping of the ¹⁷OH• radical with DMPO would therefore produce an alternative EPR spectrum, providing valuable information on the release of the hydroxyl ligands from the above-mentioned platinum(IV) complex.

7.3 References

1. Westhof, E., Flossmann, W., Ludemann, H.-D. & Muller, A. ESR and INDO study of radical conformations in irradiated single crystals of L-histidine free base. *J. Chem. Phys.* **61**, 3376–3381 (1974).
2. Butler, J. S., Woods, J. A., Farrer, N. J., Newton, M. E. & Sadler, P. J. Tryptophan Switch for a Photoactivated Platinum Anticancer Complex. *J. Am. Chem. Soc.* **134**, 16508–16511 (2012).
3. Farrer, N. J. *et al.* A potent trans-diimine platinum anticancer complex photoactivated by visible light. *Angew. Chemie - Int. Ed.* **49**, 8905–8908 (2010).
4. Schulman, S. G. & Achey, P. M. *Encyclopedia of Pharmaceutical Technology*. **6**, (Marcel Dekker, New York, 2007).
5. Abuhanoğlu, G. & Özer, A. Y. Radiation sterilization of new drug delivery systems. *Interv. Med. Appl. Sci.* **6**, 51–60 (2014).
6. Montanari, L. *et al.* Gamma irradiation effects on stability of poly(lactide-co-glycolide) microspheres containing clonazepam. *J. Control. Release* **75**, 317–330 (2001).